RECONSTRUCTING THE EAST ASIAN MONSOON RESPONSE TO MAJOR VOLCANIC ERUPTIONS: A TEST OF MODEL SKILL WITH INSTRUMENTAL AND PALEOCLIMATE DATA

A Dissertation Presented

by

JAMES A. BRADBURY

Submitted to the Graduate School of the
University of Massachusetts Amherst in partial fulfillment
of the requirements for the degree of

DOCTOR OF PHILOSOPHY

September 2006

Department of Geosciences

RECONSTRUCTING THE EAST ASIAN MONSOON RESPONSE TO MAJOR VOLCANIC ERUPTIONS: A TEST OF MODEL SKILL WITH INSTRUMENTAL AND PALEOCLIMATE DATA

A Dissertation Presented

by

JAMES A. BRADBURY

Approved as to style and content by:

_____
Raymond S. Bradley, Chair

_____
Robert M. DeConto, Member

_____
Mathias Vuille, Member

_____
David Ahlfeld, Member

_____
Wei-Chyung Wang

_____
Michael Williams, Department Head
Department of Geosciences

DEDICATION

To my wife, family and friends who believed in me.

I had a dream, which was not all a dream.

The bright sun was extinguish'd, and the stars

Did wander darkling in the eternal space,

Rayless, and pathless, and the icy earth

Swung blind and blackening in the moonless air;

Morn came and went--and came, and brought no day,

And men forgot their passions in the dread

Of this their desolation; and all hearts

Were chill'd into a selfish prayer for light:…

Extract from “Darkness” by Lord Byron (July, 1816)

ACKNOWLEDGEMENTS

This research was funded in large part by the United States Department of Energy. I want to thank my advisor, Ray Bradley, for providing me with invaluable guidance and inspiration. Frank Keimig proved indispensable by providing good humor and sound technical support for everything from e-mail to data acquisition to programming. I also want to thank the University of Massachusetts Department of Geosciences and the Climate System Research Center students and faculty, particularly Mathias Vuille, Carsten Braun, Ted Lewis and Mark Besonen, for their friendly support and technical help.

Caspar Ammann, from the National Center for Atmospheric Research, deserves a great many thanks for providing me with model output from the Millennium simulations as well as a series of other shorter CSM1.4 runs that were subsequently used as input for ReCM simulations. I am also thankful to NCAR for granting me time on their supercomputers and processing machines as well as travel and lodging assistance during three separate trips to the CCSM workshops. Wei Chyung, Wei Gong and Caiming Shen, from the State University of New York, Albany are also thanked for providing output from their East Asian RCM. The folks at SUNYA were also very generous with their time, computing expertise and resources throughout this project.

Michael Chenoweth was very kind to share daily adjusted marine air temperature measurements from the South China Sea. Mary Davis and Lonnie Thompson are thanked for sharing annual resolution water equivalent snow accumulation and $d^{18}O$ data from their Tibetan Plateau Dasuopu and Dunde ice cores.

ABSTRACT

RECONSTRUCTING THE EAST ASIAN MONSOON RESPONSE TO MAJOR VOLCANIC ERUPTIONS: A TEST OF MODEL SKILL WITH INSTRUMENTAL AND PALEOCLIMATE DATA

SEPTEMBER 2006

JAMES A. BRADBURY, B.A. THE COLORADO COLLEGE

M.S., UNIVERSITY OF NEW HAMPSHIIRE

Ph.D. UNIVERSITY OF MASSACHUSETTS AMHERST

Directed by: Professor Raymond S. Bradley

Global and regional-scale climatic changes caused by volcanic eruptions are difficult to discern conclusively based on limited 20th century climate records. Analyses of paleoclimate records and global climate model (GCM) simulations indicate that a significantly increased volcanic signal occurs in East Asia in response to historical eruptions, many of which were much larger than those experienced in the 20th century. Records of historical floods vs. drought in eastern China suggest that major eruptions over the past millennium typically led to a relatively wet north and a dry south. The GCM simulates a 10% reduction in the strength of tropical Hadley circulation and significantly decreased precipitation throughout the tropics under Tambora-like volcanic forcing conditions. The volcanic-induced weakening of the West Pacific sub-tropical high apparently contributes to a decrease in modeled precipitation throughout northeastern China. Meanwhile a general decrease in tropical precipitation resulting from

reduced incoming solar radiation and lower evaporation is hypothesized to have caused observed (and modeled) decreases in summertime precipitation in southeastern China.

TABLE OF CONTENTS

LIST OF TABLES

LIST OF FIGURES

LIST OF ABBREVIATIONS

A_n	Annual net accumulation (water equivalent)
AO	Arctic Oscillation
AOGCM	Atmosphere-ocean GCM
AR4	IPCC Fourth Assessment Report
CMAP	Climate Prediction Center merged analysis of precipitation
CMB	Central Meteorological Bureau of China
COADS	Comprehensive Ocean-Atmosphere Data Set
CRU	Climate Research Unit
CCM3	NCAR Community Climate atmosphere Model
CCSM	NCAR Community Climate System Model
CSM	NCAR Climate System Model (generic)
CSM1.4	NCAR Climate System Model version 1.4
$d^{18}O$	Isotopic ratio of oxygen-18 to oxygen-16
DI	Drought/Dryness index
DJF	December, January and February
DVI	Dust veil index
EA	East Asia
EAM	East Asian Monsoon
EAJSI	East Asia jet strength index
ECMWF	European Center for Medium-range Weather Forecasting
ENSO	El Niño/ Southern Oscillation
GCM	General circulation model/ global climate model (generic)
GFDL	Geophysical Fluid Dynamics Laboratory
GHCN	Global historical climatology network
GHG	Greenhouse gas
GISS	Goddard Institute for Space Studies
GJSI	Global jet strength index
GPCP	Global Precipitation Climatology Project
GPH	Geopotential height
HCINsf	Hadley Cell Index (NH) - stream function
HCINvs	Hadley Cell Index (NH) – vertical shear
HCISsf	Hadley Cell Index (SH) - stream function
HCISvs	Hadley Cell Index (SH) - vertical shear
hPa	Hecto-Pascal
IPCC	Intergovernmental Panel on Climate Change
ITCZ	Intertropical convergence zone
IVI	Ice-core volcanic index
JJA	June, July and August
LIA	Little Ice Age (~1250 – 1850 AD)
LSTD	Land – sea surface temperature difference index
MAM	March, April and May
MAT	Marine air temperature
NASA	National Aeronautics and Space Administration
NCAR	National Center for Atmospheric Research

NCEP	National Centers for Environmental Prediction
NEC	Northeastern China
NINO3.4	SSTs averaged over central tropical Pacific region: 5°N–5°S, 170°–120°W
NH	Northern Hemisphere
NOAA	National Oceanographic and Atmospheric Administration
NOAA-ER	NOAA Extended Reconstructed SST dataset
OKHI	Okhotsk high index
PC	Principal component
PCA	Principal component analysis
PDO	Pacific Decadal Oscillation
PRUDENCE	Prediction of Regional scenarios and Uncertainties for Defining EuropeaN Climate change risks and Effects
QBO	Quasi-biennial oscillation
RCM	Regional climate model (generic)
ReCM	SUNYA regional climate model (MM5-based)
SAGEII	Stratospheric Aerosol and Gas Experiment (version 2)
SAOD	Stratospheric aerosol optical depth
SAT	Surface air temperature
SCS	South China Sea
SEC	Southeastern China
SH	Southern Hemisphere
SLP	Sea-level pressure
SMI	Summer monsoon index
SOI	Southern Oscillation index
SON	September, October and November
SUNYA	State University of New York at Albany
SST	Sea-surface temperature
TOA	Top of the atmosphere
TOMS	Total Ozone Mapping Spectrometer
VEI	Volcanic Explosivity Index
WI	Wang/ wetness intensity/index
WNPMI	West North Pacific monsoon index
WPSH	West Pacific subtropical high pressure system
WPSHz	WPSH zonal displacement index
YRV	Yangtze River Valley

CHAPTER 1

INTRODUCTION

Large-scale tropical volcanic eruptions have occurred with a frequency of roughly 10 per century over the past 600 years (Ammann and Naveau, 2003), with catastrophic consequences for those within close proximity to eruption sites and climatologic effects lasting for several years. Immediate societal impacts caused by volcanic eruptions usually include the significant loss of life, infrastructural damage and disruption to air-travel, even when eruptions are forecast well in advance by geologists (Robock, 2001b). Future relief efforts to mitigate disaster and respond to explosive volcanic eruptions, particularly on the scale of the 1815 Tambora eruption, will be faced with global-scale challenges and an array of regional impacts during the months and years following each event.

1.1. Volcanic eruptions and climate change

Examining the global- and regional-scale climatic response to major volcanic eruptions is helpful for advancing several aspects of modern-day climate research (Robock, 2000). While the greatest changes in 21st century climate are expected to result from anthropogenic greenhouse gas emissions, it is necessary to also study natural and anthropogenic forcing factors that cause climate perturbations on different temporal and spatial scales. This is because the portion of climate change that is caused by anthropogenic forcing occurs against a background of internal variability in the coupled ocean atmosphere system as well as continual natural radiative forcing from volcanic activity and solar variability. The climatic response to volcanic eruptions has been

studied extensively through both observational (e.g., Robock and Mao, 1995; Hansen et al., 1996; Kelly et al., 1996; Briffa et al., 1998) and model-based studies (e.g., Stenchikov et al., 2002; Stenchikov et al., 2004; Shindell et al., 2003; Shindell et al., 2004), most of which have focused on large-scale, mean air temperature effects.

Quantifying the extent to which solar and volcanic forcing contribute to decadal- to century-scale climate variations during the pre-industrial era is a necessary prerequisite to making reliable projections of future climate change based on projected anthropogenic forcing (Free and Robock, 1999; Ammann, et al., 2006). Thus, recent studies have attempted to test our knowledge of this subject by forcing atmosphere-ocean general circulation models (AOGCM) with the best available radiative forcing estimates (Hansen et al., 2002; Ammann et al., 2003). Then, results from these model simulations are compared with direct or reconstructed observations of past variations in surface air temperature. For example, Figure 1.1 shows results from one such study (Ammann et al., 2006) comparing output from the National Center for Atmospheric Research (NCAR) paleoclimate model (CSM1.4; Boville et al., 2001) with independent proxy-based reconstructions of northern hemisphere temperatures over the past 1,000 years (Jones et al., 1998). Note that output data from the modeling component of that study – the so-called "Millennium Simulation" with the Paleo-CSM1.4 – were also used as the basis for AOGCM analyses conducted for the present study (see Chapters 2, 3 and 6 for more details).

In addition to global scale climate studies, an increasing amount of attention is being focused on the study of regional-scale climate change and variability because societal impacts of climate change result from relatively localized changes in the system.

Furthermore, advancing the development of reliable decision support tools, seasonal forecasting products and longer-term future climate projections to benefit society requires rigorous testing of dynamical climate models on a variety of temporal and spatial scales and under a range of boundary conditions and forcing scenarios. Model-observation comparisons provide a necessary test of the ability of AOGCMs to realistically simulate the climate system's thermodynamic sensitivity to radiative forcing.

One final motivation for gaining a better understanding of the climatic response to volcanic eruptions relates to the similarity between this naturally occurring radiative forcing and certain proposed geo-engineering projects aimed at mitigating global warming. A National Academy of Sciences report (NAS, 1992) – noting that aerosols injected into the stratosphere by the recent El Chichon and Pinatubo eruptions caused a negative radiation balance and global-scale cooling – suggested that humans could physically inject volcanic-like back-scattering aerosols into the stratosphere to effectively dampen or reverse observed surface and tropospheric temperature increases caused by rising greenhouse gases (Teller et al., 2002). Also, a recent editorial comment in the August issue of the journal, Climatic Change revisits this issue (MacCracken, 2006). Thus, the present study could provide insights into some of the regional-scale hydroclimatic implications of a global-scale geo-engineering project of this sort, were its implementation ever to be seriously considered.

1.2. Hypothesis, objectives and strategy

This dissertation employs available historical documentary evidence, the geologic record, early instrumental measurements and modern climate models to better understand

the effects of major tropical eruptions on climate in the densely populated East Asian Monsoon region and, to a lesser extent, tropical climate in general. The research strategy employed here has three main parts. First, historical, instrumental and reanalysis data are used to characterize key components of synoptic-scale climate in Eastern China and to identify the response of the East Asian monsoon (EAM) system to major volcanic eruptions. In addition, the likely mechanisms for this response are assessed by examining the processes by which large-scale stratospheric aerosol forcing could influence global- to synoptic-scale climate in eastern China on interannual to decadal time-scales. Second, a coupled AOGCM is used in conjunction with a limited-area regional climate model (RCM) to examine the extent to which these models are capable of realistically simulating the regional-scale processes and boundary conditions considered in part one, without volcanic forcing. The objective of this portion of the study is achieved by comparing output from global and regional models with respect to observations – using both station and reanalysis data – to identify model biases. The third and final part of the study – which represents the most rigorous test of the models – involves a comparison between the observed and modeled climatic response to stratospheric aerosol forcing from major volcanic eruptions. Unfortunately, the RCM simulation run with volcanic forcing was still not complete at the time of this writing, so those results are not included here.

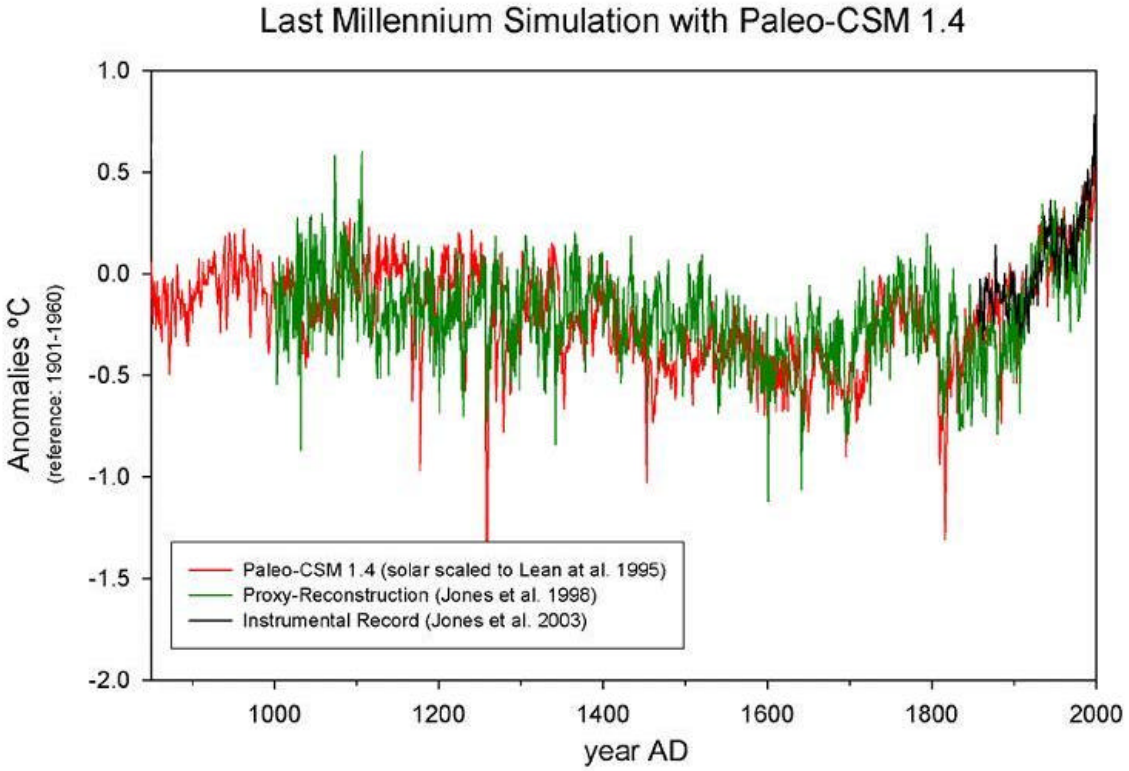

Figure 1.1. Comparison between Northern Hemisphere temperatures from observations (black), proxy-based reconstructions (green) and the "Millennium" climate simulation (red), by Caspar Ammann, which provides the basis for the modeling aspect of this study. The good agreement between these time-series on decadal to centennial time-scales suggests that the relative forcing from natural and anthropogenic sources has been estimated with some skill.

CHAPTER 2

LITERATURE REVIEW

The first objective to this study is achieved in part through a literature review of peer-reviewed publications (*in English*) on a wide range of topics. First, a brief overview of both modeling and observational studies of the East Asian monsoon (EAM) system is provided, with a particular focus on climate in eastern China. Large scale atmospheric circulation patterns, such as the El Niño Southern Oscillation and the Arctic Oscillation, are also discussed in the context of their relevance to climate in China and/or volcanic eruptions. Next, previous observation- and model-based studies focused on the climatic effects of volcanic eruptions are summarized. Finally, possible links between hydroclimate in East Asia and forcing from volcanic eruptions are hypothesized. The chapter concludes with a brief discussion of why paleoclimate records and multi-century climate model simulations are so vital to this study's objectives.

2.1. Introduction to climate in East Asia

Eastern China (Figure 2.1) is an exceptional location to examine the regional-scale skill of climate models due to its dense network of both instrumental and paleoclimate data, which are uniquely abundant in this region. The EAM system is also widely recognized as an important component of the global climate system, with high interannual variability, the strongest subtropical jet on Earth and teleconnections to remote locations in both hemispheres (Chang et al., 2000a,b; Huang et al., 2003; Lau and Wang, 2006). The EAM system dominates inter-seasonal hydroclimate variability throughout much of eastern China, South Korea and Japan. With the economy, industry,

agriculture and daily lives of one third of the world's population affected, the EAM system continues to be a subject of intense study by the global climate research community (e.g., Liang et al., 2001; Kang et al., 2002; Wang et al., 2004; Fu et al., 2005).

In eastern China, the seasonal evolution of precipitation occurs through a series of processes that essentially facilitate the delivery of moisture from the South China Sea (SCS) and Bay of Bengal (Figure 2.1), through a low-level southwesterly jet, to the north (Luang et al., 1999). This occurs through the sequential passage of the Mei-yu front in early summer, the intensification of the West Pacific subtropical high (WPSH) and mid-latitude frontal activity in mid-summer and tropical cyclones/ typhoons (in the south) in late summer (Ding, 1994; Chang et al., 2000a,b; Chen et al., 2004). The withdrawal of summer monsoon rains over eastern China is relatively rapid, beginning from north to south in late August. Generally, by early- to mid-October the winter monsoon has set in for southern China (Ding, 1994).

The timing of the onset, withdrawal, the length of the breaks, plus the intensity and duration of the summer rains vary greatly on interannual to decadal time-scales depending on a range of factors affecting synoptic disturbance activity. The most important of these factors, include: the strength, persistence and longitudinal position of the WPSH (Riyu, 2002, Wang et al., 2002), the strength and location of the subtropical jet (Wang, W.-C. et al., 2000), the phase of the El Niño/ Southern Oscillation (Wang, B. et al., 2000; Chang et al., 2000a; Hu et al., 2005), winter and spring snow depth over the Tibetan Plateau (Qian et al., 2003b; Zhang et al., 2004), and sea-surface temperature (SST) variations in the West Pacific warm pool (Huang et al., 2003) and the South China Sea (Chang et al., 2000a). Of course, all of these components are interrelated (see

chapter 4), plus they interact with regional-scale atmospheric circulation and land surface conditions (Fu, 2002). However, little attention has been given to the focus of this study: the EAM response to global-scale volcanic forcing.

To briefly introduce the precipitation climatology over eastern China, Figure 2.2 plots a 23-year average of the annual cycle of monthly mean CMAP precipitation (section 3.1.1) at each latitude (10 – 50°N), averaged across the region (from 105° - 123°E). These Hovmoller diagrams highlight the seasonality of precipitation (left panel) and illustrate that most precipitation falls in the non-winter months. North of 40°N, nearly all precipitation falls between June and August (right panel), making these months of critical interest to this study. Figure 2.2 also illustrates the sequential passage of the quasi-stationary Mei-yu rainband, which makes a series of sequential transitions, or jumps, from ~25°N to 40°N through eastern China from early May to late July (Liang and Wang, 1998).

2.1.1. A longer view of past climate change in East China

Geologic evidence is in general agreement with paleoclimate modeling results, which suggest that the East Asian summer monsoon was relatively stronger and spatially more extensive during the mid-Holocene – due to differences in orbital forcing relating to the precession cycle – resulting in a wetter and more densely vegetated China at 6 ky (Zheng at al., 2004). Since that time, there appears to have been a gradual decline in regional precipitation, particularly in continental regions to the west and north, leading to a steady southward advancement of the Gobi Desert through recent millennia. Additionally, vegetation changes throughout China have accelerated since the 11th

century due the significant expansion of agricultural and other land uses (Fu, 2002; Wang, H. et al., 2003). Currently, roughly 80% of land area in China is categorized as a man-made ecosystem (Fu, 2002). Modeling studies suggest that recent vegetation declines are part of a positive feedback cycle that reduces regional precipitation, water vapor flows, runoff and soil moisture along with a general weakening of the strength of the summer monsoon in China (Fu, 2002; Gao et al., 2003; Gordon et al., 2005). In the winter, increased albedo and decreased surface roughness associated with this long history of deteriorating vegetation cover creates more intense high pressure systems over the mainland (Wang, H. et al., 2003), stronger northwesterly surface winds and colder conditions over the entire region (Fu, 2002).

Historical reconstructions of hydroclimate variability in China, based on historical documents, from 1470 – 1999 AD, contain low frequency 80-year oscillations whereby flood vs. drought conditions in the north and southeast vary in phase with one another and both vary out of phase with low-frequency variations in hydroclimate in central eastern China, or the Yangtze River Valley region (Zhu and Wang, 2002). Liang et al. (1995) noted low-frequency, cyclical variability in the same data, with spectral peaks decreasing from ~47 years in the north to ~21 years in the south. Examining extended reconstructions of wet vs. dry periods from 952 AD to present, Qian et al. (2003a) also noted dominant modes of variability on time scales from 20 to 70-80 years.

2.1.2. Modeling the East Asian summer monsoon

Regional hydroclimate variability in eastern China is controlled by a complex array of multi-scale interactions and processes, some of which are reasonably well

resolved by global models (e.g., large-scale atmospheric circulation), while others are better suited for higher-resolution regional models (e.g., precipitation and land surface-atmosphere interactions). In recent decades, a large amount of climate research has been dedicated to the development and testing of global and regional climate models to improve our understanding of the climate system and to develop appropriate tools for regional-scale climate change impacts assessments and seasonal climate forecasting. To complement and provide a basis for advancing these efforts, a series of model intercomparison projects have been conducted to assess the skill of climate models in comparison with a variety of benchmarks. The following two sections (2.1.2.1. and 2.1.2.2.) summarize a few key findings from some of these intercomparison projects, plus results from several modeling studies of particular relevance to the present study are highlighted and discussed. Additional discussions of the EAM system and the dynamical mechanisms controlling seasonal and interannual climate variability in China can be found in Chapter 4.

2.1.2.1. Global climate models and East Asian hydroclimate

Kang et al. (2002) assessed the skill of 10 atmospheric general circulation models (AGCMs) with respect to Asian summer monsoon precipitation. Overall, the study found that composites of modeled *mean* precipitation over Asia show spatial patterns similar to those observed, however, most models are particularly unskillful over East Asia where they generally produce anomalously weak average rainfall over the subtropical western Pacific and eastern China. This precipitation bias is common among models and appears to be associated with an abnormally strong West Pacific subtropical high pressure cell

that extends into the South China Sea (SCS) region; thus, diminishing southerly winds and effectively cutting off a primary moisture source for the eastern China summer monsoon (Kang et al., 2002). Another particularly dramatic precipitation bias that is common to many models – including ECMWF reanalysis data and the CCM3 (Yu et al., 2000; see Chapter 6) – is a pronounced summer rainfall peak in the lee of the Tibetan Plateau (~30-35°N, 105°E; Kang et al., 2002), where observations show very dry continental conditions.

A complementary analysis by Wang et al. (2004) assessed model precipitation *variability* during the exceptional 1998 El Niño event. For that study, ten-member ensemble simulations were run with 11 AGCMs, each with observed SSTs for the 2-year period from September 1996 – August 1998. Analysis of model results found "extremely poor" model performance over most of Asia and the authors attributed most of the models' poor performance to problems in the East Asia region (5° - 30°N, 80° - 150°E). In particular, nearly all of the models simulated a positive correlation between local precipitation and prescribed SSTs anomalies over the Bay of Bengal, SCS and tropical western North Pacific, while this relationship is actually opposite in nature (Wang et al., 2004).

Confirming results from the above two studies (Kang et al., 2002; Wang et al. 2004), Liang et al. (2001), noted that the CCM3 – an uncoupled AGCM with prescribed SSTs – performed particularly poorly over the East Asia region, while the fully coupled CSM was relatively skillful. Liang et al. (2001) suggested that, despite some notable SST biases in the CSM, realistic air-sea interactions – including negative radiative feedbacks from increased convective cloud formation in response to positive SST

anomalies, etc – were critical to more accurate simulations of rainfall in the EAM region. Still, while the coupled CSM is more skillful than the CCM3 with respect to seasonal and interannual precipitation variability, the former still displays significant regional biases with respect to summer mean precipitation patterns over eastern China (Dai et al., 2001; see section 3.4 for model description and Chapter 6 for more detailed discussions of these biases).

2.1.2.2. Regional climate models and East Asian hydroclimate

As was apparent from studies cited in the previous section, regional-scale biases in modern-day climate simulated by global AOGCMs vary widely from region to region and across models. For example, Giorgi and Francisco (2000) noted GCM inter-model ranges for seasonal area-averaged regional temperature biases from <1°C to 6°C; while precipitation biases generally range from <10% to >100%. Thus, much attention is being paid to improving regional-scale skill of global model output by increasing horizontal resolution and through the development of statistical and dynamical downscaling techniques. This section summarizes results from several dynamical regional modeling studies that have focused on climate over East Asia.

The most comprehensive assessment of regional climate model skill in East Asia is currently underway through the Regional Climate Model Intercomparison Project (RMIP) for Asia (Fu et al., 2005). RMIP for Asia has published results from the first phase of their assessment, which primarily involves regional model intercomparisons over a one year annual cycle for a recent period during which a number of extreme climatic events – heatwaves, drought and flooding – occurred (from March 1997 to

August 1998). Phase two will assess the RCMs' ability to realistically capture other statistical behaviors of observed Asian monsoon climate, during a ten year simulation period (January 1989 – December 1998). Both phases one and two use initial and lateral boundary conditions from the National Centers for Environmental Prediction (NCEP)-reanalysis data. RCM simulations in phase three, on the other hand, will use output from the CSIRO coupled AOGCM as driving boundary conditions (Fu et al., 2005). This final phase most closely resembles the experiment design of the present study; unfortunately, it will not be completed in time for its findings to be compared with results found here.

Nevertheless, initial findings from phase one of RMIP for Asia (Fu et al., 2005) reveal that all nine of the RCMs are able to realistically reproduce seasonal averages of daily mean, maximum and minimum temperatures in terms of their spatial patterns and general annual cycles. However, cool temperature biases are common over land and are particularly strong over arid regions of northern China. Seasonal area-averaged temperature biases for the Japanese Islands, the Korean Peninsula and mainland China range mostly from +1°C to –5°C and from –1°C to –4°C, in winter and summer respectively. The spatial distribution and annual cycle of RCM simulated precipitation across Asia also compares well with observations, except in western arid regions. Seasonal area-averaged precipitation biases over Japan, Korea and China range mostly from –25% to +25% and from –65% to +40%, in winter and summer respectively.

So, the biases in regional temperature simulated by nine RCMs in RMIP for Asia are generally comparable to those simulated in five coupled AOGCMs (compare with results from Giorgi and Francisco, 2000, mentioned above). Meanwhile, regionally averaged precipitation biases in the RCMs appear to be slightly better than biases in

AOGCMs. The causes for these biases – which exist despite the fact that all RCM simulations were driven with observed/reanalysis data boundary conditions – are still under investigation (Fu et al., 2005).

Another intercomparison project conducted with reanalysis-driven RCMs examined three regional models' (SUNYA-ReCM; PNNL-RCM; NCAR-RegCM) ability to simulate extreme Mei-yu rains and flooding over the Yangtze River valley in the summer of 1991 (Leung et al., 1999). This study found that simulated energy and hydrological cycles over cloudy regions of south and central China were very different among the RCMs because modern regional models treat clouds and radiation very differently. Nevertheless, the PNNL-RCM and the SUNYA-ReCM captured the general spatial pattern, strength and location of the Meiyu rainband (May-July), which is a prominent regional feature of summer precipitation that stretches from the Yangtze River Valley to the southern-central Japanese Islands (Leung at al., 1999; Wang, W.-C. et al., 2000).

In their surface energy budget analysis of the regional models, Leung et al. (1999) noted that the SUNYA-ReCM's surface physics scheme, which determines the model's partitioning of energy at the surface, may be particularly unsuitable for long-term climate simulations. This scheme uses the MM5 "force restore" slab model with a single soil layer that transfers energy from the surface to the substrate too quickly. The result is a cold bias in surface air temperatures that increased from near zero to –5°C over central China during the course of a 90-day simulation (Leung et al., 1999). This problem with the SUNYA regional model was also recently noted by Wei Gong (personal communication) when a simulation was conducted for a one year period – using CSM1.4

boundary conditions – and a cold bias in surface air temperature grew steadily throughout the experiment, particularly during winter. The existing surface physics scheme has since been adjusted to reduce this model deficiency (Wei Gong, personal communication); however, an entirely different scheme may prove more suitable for year-round climate simulations in the future.

In parallel with the intercomparison project summarized by Leung et al. (1999; above), Wang, W.-C. et al. (2000) and Gong and Wang (2000) conducted sensitivity experiments and further diagnostic analyses of the SUNYA-ReCM to assess model skill with respect to the Mei-yu system. While the ReCM captured the secular precipitation trends observed during the summer of 1991, the spatial patterns were slightly less well simulated. The model simulated the Mei-yu rain belt slightly too far south, compared to observations. The rain belt position was attributed to the model's cold bias (noted above), which effectively prevented the West Pacific subtropical high, westerly jet at 200 hPa and the associated Mei-yu front from making their natural northward progression after the middle of July. Also, the model's overall underestimation of precipitation totals (dry moisture bias), was partially attributed to the lack of a vegetation-soil scheme in the land surface model (Wang, W.-C. et al., 2000). However, despite these problems, the ReCM compares well with observations in terms of its dynamical internal consistency, particularly with respect to interrelationships between the primary components of the EAM system: the West Pacific subtropical high, the East Asian jet at 200 hPa, and the Mei-yu rainband (Wang, W.-C. et al., 2000).

2.2. Global-scale teleconnection patterns

The interrelationships between climate in eastern China, the EAM system and large-scale modes of climate variability are complex and variable on a variety of spatial and temporal scales. Past studies of these topics have generally grown out of an interest in developing improved empirical and dynamical models for the purpose of forecasting monsoon behavior on seasonal time-scales. Also teleconnection patterns are of interest because they generally reflect inherent modes of natural climate system variability and thus provide a structural context within which any region's climate can be viewed and studied. Understanding this context helps us see the processes that generally govern interannual variability in the EAM system. In the context of the present study, these processes are important because they could contribute to the climatic noise that masks a volcanic signal or they could effectively provide the mechanism for a regional-scale climatic response to a global-scale radiative forcing.

2.2.1. Arctic oscillation (AO)

The Arctic Oscillation (AO; also referred to as the Northern Hemisphere annular mode, or NAM) is a statistical description of the leading mode of atmospheric pressure variability in the Northern Hemisphere. The AO index is simply defined as the first principal component (PC) of wintertime monthly gridded mean sea-level pressure (SLP) anomalies poleward of 20°N; though it can be defined throughout the year and at nearly all levels of the atmosphere, from the surface to 50 hPa (Thompson and Wallace, 1998). Since atmospheric circulation is more vigorous during the winter and the AO explains a larger portion of total pressure variance during this season, most studies focus on the AO

during December, January and February. The AO index essentially measures the strength of the westerlies and the circumpolar vortex; the positive AO phase is associated with zonally (west-to-east) symmetric negative pressure anomalies over the Arctic polar region and positive pressure anomalies over mid-latitudes (particularly over the Atlantic and Pacific Oceans; see section 3.1.3).

The AO resembles – and is highly correlated with – the North Atlantic Oscillation (NAO), which is the dominant mode of atmospheric pressure variability in the North Atlantic region (Hurrell, 1995). The NAO index, defined as the standardized monthly SLP difference between the Azores High and the Icelandic Low (Rogers, 1984), describes the steepness of a north-south atmospheric pressure gradient across the North Atlantic Ocean. Variability in the AO and NAO each strongly relate to heat and moisture transport throughout the extratropical Northern Hemisphere (Thompson and Wallace, 1998), with positive index values associated with stronger circumpolar westerlies and warm surface air temperatures (SATs) throughout North America and Eurasia. Furthermore, not only do these relationships hold up on monthly and seasonal timescales, but Thompson and Wallace (2001) documented anomalous daily winter weather events associated with daily anomalies in the AO (NAM) index at locations throughout the Northern Hemisphere.

It is worth noting that there was a fairly consistent multi-decadal upward trend in the AO index through the end of the 20th century and a significant component of that trend was consistent with the average Northern Hemisphere SAT trend over the same time period (Hurrell, 1995). Some recent studies have employed models to consider mechanisms for an anthropogenic cause for this recent positive AO trend (e.g., Gillett et

al., 2003; Rind et al., 2005). However, most current AOGCMs, forced with historical trends of greenhouse gas and aerosol concentrations, are not able to simulate observed low-frequency variations, or trends, in the AO index (Scaife et al., 2005; Stenchikov et al., 2006). Furthermore, Cohen and Barlow (2006) noted that the observed positive trend in the AO appears to have reversed in the early 21st century – while northern hemisphere temperatures have continued to trend in the positive direction – further indicating that recent AO variability may not be attributable to anthropogenic greenhouse gas forcing.

2.2.1.1. Arctic oscillation signal in China

Throughout most of China, average winter temperatures are positively correlated with the AO index (Thompson and Wallace, 1998), with significant correlations in the north ($r > +0.4$) and in coastal regions as far south as Shanghai ($r > +0.3$; Gong et al., 2001; Gong and Wang, 2003). The frequency of extremely cold days in northeastern China is also significantly related to the phase of the AO (Thompson and Wallace, 2001). Over the Yellow River valley, winter precipitation (which is very rare) is positively correlated with the AO (Gong and Wang, 2003).

The mechanism for a link between the AO and the East Asian winter monsoon is likely tied to the Siberian High; in winter, a significant out of phase relationship exists between the intensity of the Siberian high and the AO index ($r = -0.48$; Gong et al., 2001). Sea level pressures (SLP) over Siberia tend to decrease by roughly 1-3 hPa when the AO index increases by 1 standard deviation (Thompson and Wallace, 2000). As a result, during negative AO conditions the upstream Siberian high anticyclone is strengthened, and the surface pressure gradient is increased between the northern

continental and southern coastal regions of China. With an enhanced upstream anticyclone, there are more frequent cold air surges and lower average winter temperatures throughout northeastern China (Gong and Wang, 2003).

Additionally, Gong and Ho (2003) investigated a possible relationship between the AO and observed summer precipitation in China but did not find any correlations at zero lag. However, they did identify a spatially coherent and statistically significant lagged relationship between the AO in May and JJA precipitation in the Mei-yu/Baiu rainband, from the Yangtze River valley to the southern Japanese Islands ($r < -0.40$; Gong and Ho, 2003). A clear mechanism for this 1-4 month lagged teleconnection between regional hydroclimate and the phase of the AO remains unclear, however the strength and location of the East Asian jet core apparently shares a common signal (Gong and Ho, 2003).

2.2.1.2. Arctic oscillation response to volcanic eruptions

Robock and Mao (1992) noted anomalously warm surface air temperatures over most of North America and Eurasia – with cooling over the oceans and Middle East – following the 12 largest volcanic eruptions of the past century. Robock and Mao (1995) attributed the majority of this warming to *tropical* eruptions, in particular. Examining gridded SAT and SLP anomaly composites following the five largest recent tropical eruptions, Kelly et al. (1996) observed that the "winter warming" noted by Robock and Mao (1992; 1995) was associated with SLP anomaly patterns that are very similar to those associated with the positive phase of the NAO (Hurrell, 1995). Kelly et al. (1996) further noted SLP anomalies in the vicinity of the Aleutian Low that were consistent with

an overall strengthening of the circumpolar vortex in response to major tropical eruptions.

It follows that the final and most important reason for considering the AO in the present study is that several previous studies have noted that the AO tends toward the positive phase during winters following large tropical eruptions (Shindell et al., 2001a; Robock et al., 2000; Stenchikov et al., 2002; Shindell et al., 2004; Stenchikov et al. 2006). Thus, the AO is an inherent mode of global-scale climate variability that essentially provides the mechanism for a regional-scale climatic response. Most previous studies have highlighted the resulting climatic impacts in Europe (e.g., Písek and Brázdil, 2006), but little attention has been given to the climatic implications for other regions. Further details regarding the mechanisms responsible for this dynamic climatic response to tropical volcanic eruptions are discussed below, in section 2.3.4.

2.2.2. El Niño/ Southern Oscillation (ENSO)

The terms El Niño and La Niña refer to anomalous SST events in the equatorial Pacific Ocean. El Niño represents the warm phase, and La Niña the cold. These SST anomalies are associated with a Walker circulation cell over the tropical Pacific known as the Southern Oscillation, which is statistically defined by the SLP seesaw between Tahiti and Darwin, Australia (Trenberth and Caron, 2000). Pacific SSTs throughout the tropics are intricately coupled with the atmospheric Southern Oscillation and together they form the El Niño/ Southern Oscillation (ENSO), which, through distinct teleconnection patterns, is linked to significant variations in tropical and extratropical climates worldwide (Rasmusson, 1985; Ropelewski and Halpert, 1987; Trenberth and Caron,

2000). The effect of the ENSO on mid-latitude regional climates is typically most pronounced during the winter season (Hoerling and Kumar, 2000).

2.2.2.1. ENSO signal in China

Several studies have attempted to characterize the nature of the climatologic link between the EAM system and ENSO (e.g., Wang et al., 2000; Hu et al., 2005). However these efforts are significantly complicated by the fact that the nature of the EAM-ENSO relationship has changed over time, particularly in the late 1970s (Chang et al., 2000a; Wu and Wang, 2002; Lau and Wang, 2006), when the North Pacific Ocean appears to have experienced a major climatic shift (Trenberth and Hurrell, 1994). Nevertheless, summer rainfall over eastern China and variability in the East Asian monsoon system has been shown to have significant seasonally lagged correlations with SSTs in the eastern tropical Pacific (Chang et al., 2000a; Yu et al., 2001).

Yu et al. (2001) noted that rainfall from April to August over the Yangtze River Valley has significant positive correlations with SSTs in the Niño3 region (5°S - 5°N, 150°W - 90°W) during the previous winter. Summer rainfall in this region is also inversely correlated with Niño3 SSTs during the following year, suggesting a causal role for the East Asian monsoon system with respect to the phase of ENSO (Lau and Wang, 2006). To summarize, exceptionally wet summers in the Yangtze River Valley are often preceded by El Niño conditions during winter, while La Niña conditions commonly begin in the following fall (Yu et al., 2001; Chang et al., 2000a). In northeastern China, wet summers (April to August) often accompany below normal Niño3 SSTs (La Niña), which tend to persist into the following spring (Yu et al., 2001).

The mechanisms for an anomalously wet summer rainfall response in the Yangtze River Valley (YRV) to El Niño conditions were best defined by Chang et al. (2000a) as follows. The Walker and Hadley circulation response to an El Niño event creates a stronger western North Pacific subtropical high that extends further to the west in summer, beginning during the previous winter and extending into the fall. This prominent high pressure system contributes to a stronger lower-level pressure gradient over the Mei-yu region and a more stationary front with more persistent rainfall over the YRV. The presence of a prominent anticyclone to the south and east of China also leads to anomalous warming over the SCS, which contributes to greater southwesterly moisture advection to the rainfall region.

2.2.3. Pacific decadal oscillation (PDO)

The Pacific Decadal Oscillation is the leading mode of North Pacific SST variability north of 20°N. The PDO index is highly positively correlated with eastern tropical Pacific SSTs. Also, extratropical atmospheric pressure anomalies associated with the opposite phases of the PDO are similar to those associated with ENSO extremes (Mantua et al., 1997). Thus, in many cases, the phase of the PDO can effectively either dampen or enhance ENSO-related teleconnections patterns.

Variability in the PDO index is associated with decadal-scale variations in summer precipitation over East Asia, with significant negative correlations over northeastern China (NEC) and southeastern China (SEC) and positive correlations over the YRV (Shen at al., 2006). Thus, the “warm phase” of the PDO (SSTs anomalously cold in the western North Pacific and anomalously warm in the tropics) is associated with

relatively dry decades in the north and south, with wet conditions prevailing in central eastern China. This rainfall pattern is typical of a West Pacific subtropical high that is stronger and positioned further to the west, favoring southerly moisture advection to the middle and lower reaches of the Yangtze River Valley. Furthermore, an abrupt positive shift in the PDO index occurred, in 1977, in phase with what Gong and Ho (2002) noted to be a significant increase in YRV precipitation, warmer tropical Pacific SSTs, and a a long-term climatologic shift toward a stronger West Pacific subtropical high.

Results from proxy-based reconstructions extending the PDO record back to the 15th and 16th centuries (Shen et al., 2006; D'Arrigo and Wilson, 2006) display some multi-decadal shifts on the order of those observed during the 20th century (e.g., in 1925, 1947, and 1977). Other paleoclimate reconstructions of the PDO – mostly based on tree-ring chronologies from mountain areas east of the Pacific (e.g., Bondi et al, 2001) – also display some degree of multi-decadal variability, yet they are not in very good agreement with each other (see section 3.2.2). As would be expected, this is particularly true when comparing PDO index reconstructions that are based on proxy series from opposite sides of the Pacific Ocean. D'Arrigo and Wilson (2006) suggest that one reason for the generally poor agreement between various PDO reconstructions could result from the different regional/local responses of individual proxy series to relatively independent forcing from strong ENSO events or volcanic eruptions.

2.3. Stratospheric aerosols from tropical volcanic eruptions

Episodic volcanic eruptions inject into the stratosphere (from 10 to 50 km altitude) several megatons (1 Mt = 10^9 kg) of sulfuric gases that, on weekly time-scales,

convert to sulfate aerosols, which remain in the upper atmosphere for up to 3 years following individual events. During the weeks immediately following each eruption, SO_2 and – to a lesser extent – HS_2, react with OH, O_2 and H_2O to form H_2SO_4 aerosols, which is what produces the dominant radiative effect caused by volcanic eruptions (Robock, 2000; Oman et al., 2006). These sulfate aerosols in the stratosphere typically circle the globe within 2-3 weeks of the eruption, and over this time period the particles become relatively evenly distributed zonally, particularly at latitudes closest to the source (Robock, 2000). The primary removal processes for stratospheric aerosols from the atmosphere include winter subsidence over the poles and mid-latitude tropospheric folding. The later process is the primary mechanism for aerosol removal, while large-scale polar subsidence accounts for roughly 25% of removal (Hamill et al., 1997). The decay of aerosol loading appears to also depend in part of the phase on the Quasi-biennial Oscillation (QBO). Lidar measurements of stratospheric aerosol backscatter from the Mona Loa observatory suggest that volcanic aerosols from the El Chichón and Pinatubo eruptions decayed more rapidly during the westerly QBO phase (Barnes and Hofmann, 1997).

The best available measurements of the spatial distribution, time evolution and optical properties of stratospheric sulfate aerosols are derived from remote sensing measurements. The Total Ozone Mapping Spectrometer (TOMS; e.g., Bluth et al., 1992), available since 1979, measures backscattered ultraviolet radiation and has serendipitously provided useful information on total column amounts of SO_2 and O_3 (Robock, 2000). NASA'a Earth Radiation Budget Satellite, launched in 1984, hosts the Stratospheric Aerosol and Gas Experiment (SAGE II) instrument, which measures

atmospheric extinction within a range of wavelengths (from 0.385 µm to 1.02 µm,) sufficient to define the effective radius of the size distribution of stratospheric aerosols (Hansen et al., 2002). This information is critical for estimating radiative forcing (Andronova et al., 1999). SAGE has proven particularly useful for detailed studies of the 1991 eruption of Mount Pinatubo (Yang and Schlesinger, 2002), the largest tropical eruption in modern history.

For explosive tropical eruptions close to the equator – the primary focus of this study – the typical aerosol cloud reaches both hemispheres within months and polar regions within a year, but the bulk of the aerosols tend to remain at low latitudes (although the actual distribution of the cloud depends significantly on the circulation of upper level winds at the time of eruption) (Robock, 2000). This uneven global distribution of aerosols causes non-uniform radiative heating and cooling respectively in the stratosphere and the troposphere, creating anomalous temperature gradients that set the stage for indirect climatic effects, through dynamical changes in large-scale atmospheric circulation. On the other hand, aerosol clouds from extratropical eruptions typically remain at high latitudes, causing significant radiative cooling at the surface but little dynamical climatic response (Oman et al., 2005)

It should also be noted that not all volcanic eruptions are climatologically significant, especially if they produce a small amount of sulfate gases. Alternatively, if the bulk of the sulfate gases and aerosols are not projected into the stratosphere, then they are subjected to tropospheric weather, providing suitable cloud condensation nuclei and effectively washed out of the atmosphere within 2-3 weeks (Robock, 2000). Thus, less explosive eruptions, or those with a significant horizontal component to the ejecta (e.g.,

Mt. St. Helens, Washington U.S.), typically have a minimal impact on the global climate system.

2.3.1. Direct climatic response to aerosol forcing

The persistent stratospheric aerosol cloud described above directly affects incoming solar radiation because the sulfate particles have a typical effective radius equivalent to the wavelength of visible light (~0.5 µm) and a single-scatter albedo of 1 (Robock, 2000). Through the forward and backscattering of sunlight, these aerosols have two fundamental effects on the earth's radiative balance. First, they effectively increase optical depth of the stratosphere, reflecting incoming solar radiation back into space and thereby limiting the amount of shortwave radiation reaching the lower atmosphere, thus causing cooling at the surface (Briffa et al., 1998). Second, the aerosols absorb both shortwave and longwave radiation, causing heating in the stratosphere (Labitzke and McCormick, 1992), which is reradiated out to space and back toward Earth (Robock, 2000).

While volcanic aerosols from even the largest eruptions remain in the stratosphere for 3-years at most – thus causing a sub-decadal climate response – there is growing evidence that sequential eruptions over relatively short periods of time can cause climate change on longer time-scales (Zielinski, 2000; Ammann et al., 2003). For example, a persistent climate response could be caused by the occurrence of multiple eruptions within a closely spaced time period, creating an increase in the decadal-scale mean stratospheric optical depth, leading to negative heat balance in the ocean (Gleckler et al., 2006) and other atmosphere-ocean feedbacks (Robock, 2000). Furthermore, recent

studies comparing climate modeling results with paleoclimate reconstructions of global temperature have suggested that low-frequency variations in both solar and volcanic forcings have contributed significantly to observed decadal- to century-scale climate changes in the past (Ammann et al., 2003), including global-scale cooling during the so-called "Little Ice Age" (Free and Robock, 1999; Shindell et al., 2003; Ammann et al., 2006).

Another relevant point, in the context of this paleoclimate study, is that the diffuse daylight created by volcanic eruptions is favored by trees to direct sunlight. Thus, global tree-growth is enhanced in the months and years following major eruptions, despite negative temperature anomalies caused by negative radiative forcing. The enhanced tree growth, in turn, results in the increased uptake of atmospheric carbon into the biosphere, as evidenced by the diminished rate of growth in atmospheric CO_2 concentrations during years following Agung, El Chichón and Pinatubo (Robock, 2005). Furthermore, analyses of proxy-based global-scale temperature reconstructions have found that tree-ring only reconstructions indicate less global cooling in response to the Tambora eruptions, compared with other temperature proxies (Robock, 2005). Remarkably, this occurs despite the fact that tree-ring proxies are inherently biased toward recording summer/growth season conditions, which is the season when radiative cooling from eruptions is greatest. This discovery has many implications, but chief among them is that global temperature reconstructions based entirely on indices of tree growth (e.g., Free and Robock, 1999; Briffa et al., 1998; see section 2.6) are likely to underestimate the magnitude of the actual cooling that occurred in response to volcanic forcing (Robock, 2005).

2.3.1.1. Observed temperature response

On time-scales of hours to days, there are significant climatic impacts caused by volcanic ash in the areas downwind and closest to the eruption site (Robock et al., 2000). For example, to estimate the climatic impact of the May 1980 eruption of Mt. Saint Helens in downwind towns, Robock and Mass (1982) compared actual temperature measurements with temperatures predicted by forecast models that did not include ash or aerosols. In Yakima, Washington (~135 km east of Mt. Saint Helens) they found a 16°C reduction in the diurnal temperature range, which only lasted for a few days.

On time-scales of weeks to months, once the sulfur gases have circled the globe in the stratosphere and converted to sulfate aerosols, a direct tropospheric cooling effect is generally detectable (Robock, 2000). Using a simple energy balance model, Hansen et al. (1978) accurately modeled the global surface air temperature (SAT) cooling following the 1963 Agung eruption. However, observational studies attempting to quantify the volcanic signal in the instrumental or paleoclimate record have achieved the best results through superposed epoch analyses centered on January, year-one of an eruption (e.g., Bradley, 1988; Kelly et al., 1996). Other studies have sought to statistically remove the ENSO signal to offset the tropospheric heating effect of El Niño events and, thus, to more clearly examine the volcanic signal in spatial and seasonal SATs (Robock and Mao, 1995; Yang and Schlesinger, 2001).

Results from Robock and Mao (1995) – using superposed epoch analysis and an ENSO-signal removal technique – showed that the maximum cooling generally occurs in the year following the eruption. They also found that SAT cooling is most consistently observed in the tropics – generally following solar declination – with the strongest mid-

latitude seasonal signal in the summer hemisphere. Also, since the land surface responds more quickly to radiative perturbations, Robock and Mao (1995) noted that maximum cooling typically occurs in the Northern Hemisphere, which is consistent with results from modeling studies (Kirchner et al., 1999; Robock, 2002).

To examine the spatial pattern of the SAT response to major tropical eruptions – individually and collectively – Shindell et al. (2004) used an updated version of the Mann et al. (1998) multi-proxy Northern Hemisphere temperature reconstruction (Rutherford et al., 2003), from 1600 to present. As noted previously, temperature anomalies in winters (October – March) following tropical eruptions reflect a dynamical climatic shift into the positive phase of the naturally occurring AO pattern. This response is quite consistent following individual eruptions and is clearly apparent in multi-year composites. On average, there is winter warming over much of northern Eurasia and the eastern United States, while China, the Middle East and North Africa experience winter cooling. This spatial pattern is clearly apparent and statistically significant during the first and second winters following the tropical eruptions listed in Table 2.1 (Shindell et al., 2004).

2.3.1.2. Radiative forcing & climate sensitivity

By definition, climate sensitivity is the change in atmospheric temperature (?T) in response to a given change in radiative forcing (?F), or ?T/?F (°C/Wm^{-2}). While average global temperature variations can be measured with reasonable accuracy (e.g., Jones and Moberg, 2003), there are significant uncertainties associated with estimations of radiative forcing. The magnitude of volcanic forcing depends on visible optical depth, which depends on the quantity and properties of the stratospheric aerosols – particularly

the effective radius of the aerosol size distribution (Andronova et al., 1999; Yang and Schlesinger, 2002). For simplicity, it is common for modeling studies to assign a fixed aerosol size distribution (e.g., ~0.42 µm; Ammann et al., 2003) when estimating stratospheric optical depth, particularly for pre-satellite era eruptions for which detailed measurements of aerosol properties are not available. Once the effective aerosol particle radius has been fitted to the best available measurements of this parameter, stratospheric optical depth can be estimated and used in conjunction with models to calculate radiative forcing (Hansen et al., 2002).

Models with radiation transfer schemes are useful for tracking the impact of a given forcing on the energy balance of the planet. For example, instantaneous changes (?) in radiation are calculated by subtracting the radiative flux during a control (no forcing) simulation from the same flux when a climate forcing is applied to the model. A standard methodology for calculating the net change in the total radiative flux (?N), is as follows:

Equation 2.1 $$?N = ?S - ?R$$

where net outgoing longwave radiation is ?R and net incoming solar (shortwave) radiation is ?S (Yang, 2000). This procedure is most frequently done at three primary levels: at the top of the atmosphere (1 hPa), at the tropopause (~200 hPa) and near the surface. Thus, Hansen et al. (2002) forced a global climate model with uniform stratospheric aerosol optical depth t = 0.1 (wavelength ? = 0.55 µm) and estimated an adjusted radiative forcing equal to 2.1 Wm^{-2}. From this (2.1 Wm^{-2}/ 0.1) Hansen et al. inferred the following general relationship:

Equation 2.2 $$F\ (Wm^{-2}) = -21 \times t$$

Andronova et al. (1999) used a radiative transfer model to come up with a similar solution:

Equation 2.3 $$F\ (Wm^{-2}) = -25.4 \times t$$

Finally, climate model simulations that are forced with realistic radiative forcing estimates and agree well with observed changes in temperature are used to estimate global climate sensitivity. Recent studies along these lines suggest that for most forcings (e.g., greenhouse gases, solar irradiance or stratospheric aerosols) global climate sensitivity at the tropopause is somewhere between 0.75°C to 1°C per Wm^{-2} of forcing (Hansen et al., 2002).

In summary, accurate reconstructions of past forcings provide a foundation for realistic simulations of past climate. These simulations, in turn, provide a basis for reliable quantitative estimates of the global climate system's sensitivity to both natural and anthropogenic forcing. However, while relatively simple climate models may be employed for the purpose of exploring these broad-scale issues, more complex models with dynamic oceans and high resolution stratospheres are necessary for realistically simulating the regional-scale response to radiative forcings (Hansen et al., 2002).

2.3.1.3. Observed precipitation response

Most research into the climatic effects of volcanic eruptions has focused on the air temperature response (Robock, 2000); meanwhile, much less attention has been given to the global- and regional-scale effects on precipitation and hydroclimate, which is the focus of this study. Robock and Liu (1994) – comparing model results with observations – noted reductions in tropical precipitation for 1-2 years following eruptions. They

attributed this to reduced evaporation caused by tropospheric cooling and also suggested that the 1982 El Chichón eruption led to enhanced drought conditions in the African Sahel region, although the latter result was considered somewhat preliminary. Satellite derived tropical averages of monthly precipitation over land also show marked negative anomalies following the El Chichón and Pinatubo eruptions (Adler et al., 2003). However, Adler et al. (2003), noting the negative correlation between the Niño 3.4 index and tropical land precipitation from 1979 – 2001 (also see: Trenberth and Caron, 2000), attribute these anomalies primarily to the 1983 and 1992 El Niño events. Adler et al. (2003) also note that tropical precipitation over the oceans, which typically varies in phase with the Niño 3.4 index, only increased slightly during the 1983 and 1992 Niño events, suggesting – though not definitively – that the volcanic eruptions immediately preceding these events may have dampened this signal.

The sequential northward transitions in the Mei-yu front each year are known to occur in part due to intense summer heating of the landmass, particularly in the north (Samel et al., 1999). Furthermore, the Clausius-Clapeyron equation predicts an increase in the saturation vapor pressure accompanying an increase in air temperature. It is logical, then, that a reduction in global tropospheric heating would lead to a decrease in global precipitation, thus dampening summer rainfall in China. In fact, a recent model-data intercomparison study concluded that shortwave radiative forcing from volcanic eruptions is detectable in 20th century global-scale precipitation but longwave radiative forcing from anthropogenic greenhouse gases (GHGs) was not (Gillett et al., 2004). Also, using simple linear regression techniques, Lambert et al. (2004) found that the influence of shortwave forcing on interannual variations in both modeled and observed

precipitation was detectable at the 90% level, which was not true for long-wave forcing. Lambert et al. argue that these results can be explained through simple tropospheric energy budget considerations; shortwave forcing should have a larger degree of influence on global precipitation than GHG longwave forcing, per degree of warming.

2.3.2. Dynamic response to volcanic aerosol forcing in the stratosphere

One of the biggest challenges to any climate analysis stems from the limitations of the observational record. This is particularly true when a study is restricted to a limited number of events, such as tropical volcanic eruptions. To grapple with these limitations, climatologists are 1) taking fuller advantage of the available paleoclimate records (see section 2.6) and 2) making greater use of global climate models. Both of these techniques effectively increase the sample size for analysis, while the later has become an indispensable tool for testing theoretical knowledge and improving our understanding of how the climate system responds dynamically to changes in forcing and boundary conditions. This section discusses how both of these analysis methods have contributed to our current knowledge of the global- and regional-scale climatic response to volcanic forcing.

2.3.2.1. Modeling the AO response

The tendency for atmospheric circulation in the Northern Hemisphere to favor the positive phase of the AO during the two consecutive winters following explosive tropical eruptions is well documented (Shindell et al., 2004) and modeling studies have been particularly helpful for understanding why this might happen due to stratospheric aerosol

optical depth (SAOD) forcing (Kirchner et al., 1999; Shindell et al., 2001a). While there appear to be multiple radiative and dynamical mechanisms responsible for this climatic response, the primary factor seems to result from volcanic aerosol heating in the equatorial lower stratosphere. This heterogeneous heating increases the south-north temperature gradient in the lower stratosphere and strengthens the circumpolar vortex, thus triggering positive AO conditions through the so-called "stratospheric gradient" mechanism (Stenchikov et al., 2002). This mechanism is enhanced by chemical reactions initiated by the presence of volcanic aerosols, which cause ozone depletion in the lower stratosphere (Oman et al., 2005) and further cooling in the polar stratosphere during late winter and spring (Stenchikov et al., 2002).

The positive AO pattern produced in winter through the stratospheric gradient mechanism also becomes self-reinforcing. Both observations and dynamical modeling studies confirm that the positive phase of the AO leads to cooling in the polar stratosphere (Stenchikov et al., 2006), thus increasing the equator-pole temperature gradient. This is because a strong polar vortex tends to inhibit, or deflect, the propagation of planetary waves into the polar stratosphere, which strengthens tropospheric westerlies and further promotes a stronger polar vortex via the so-called "wave feedback" mechanism (Stenchikov et al., 2002).

Another significant contributor to the dynamical AO response to radiative forcing from tropical eruptions involves tropospheric cooling at low-latitudes and a decrease in the meridional (south-to-north) temperature gradient near the surface (Stenchikov et al., 2002). Through this so-called "tropospheric gradient" mechanism, the meridional temperature gradient is diminished most significantly between 30° and 60°N, causing a

decrease in zonal-mean energy and a dampening of the amplitude of mid-latitude Rossby waves. This should cause a decrease in vertical wave activity and diminish friction between the troposphere and the lower stratosphere; which, in turn, allows the polar vortex to accelerate, thus triggering the aforementioned wave feedback mechanism through tropospheric thermodynamics (Stenchikov et al., 2002).

Much of what is understood about these theoretical mechanisms for the climatic response to volcanic forcing has been learned though modeling studies (e.g., Kirchner et al., 1999; Stenchikov et al., 2002). Thus, it is important to note that the most comprehensive dynamical model intercomparison project on the subject, to date, has found that modern AOGCMs significantly underestimate the magnitude of the observed AO response (Stenchikov et al., 2006). AOGCM output used in that study were taken from "historical" simulations (late 19th century to 2000 AD) prepared for the pending fourth assessment report (AR4) by the Intergovernmental Panel on Climate Change (IPCC). Stenchikov et al. (2006) concluded that the AOGCMs consistent underestimation of the AO response is likely due to their coarse vertical resolution, which limits their ability to fully capture the magnitude of the wave feedback mechanism; also noting that increased horizontal resolution did not appear to provide any significant added advantage in this regard.

The importance of vertical resolution for realistically simulating the observed AO response was illustrated in an earlier study by Stenchikov et al. (2004), using the Geophysical Fluid Dynamics Laboratory (GFDL) SKYHI model. Greater vertical resolution in the middle and upper atmosphere provides for more realistic simulations of tropopause dynamics, interactions between the troposphere and stratosphere and the wave

feedback mechanism, in particular (Stenchikov et al., 2006). Furthermore, including atmospheric layers beyond the stratosphere and into the mesosphere makes it possible for the model to realistically simulate the Quasi-biennial Oscillation (QBO), which is important for reasons that are briefly outlined below.

The QBO is a wind oscillation in the equatorial lower stratosphere (centered at ~20-30 hPa) that switches between easterly and westerly phases roughly every two years. Kirchner et al. (1999) were among the first to document the role of the QBO in modulating the magnitude of the positive AO response to tropical volcanic eruptions. When the QBO is in its easterly phase stratospheric temperatures in the tropics decrease by roughly 1°C, thus dampening radiative heating caused by aerosol loading. In contrast, the westerly QBO phase has the opposite thermal effect and thus amplifies the stratospheric gradient mechanism. For example, at the time of the 1991 Pinatubo eruption, the QBO was in its easterly phase and during the following winter the AO response was less than expected; but in the winter of 1993, the QBO phase had reversed and the model calculated AO response was closer to the observed signal (Kirchner et al., 1999).

On slightly longer time-scales, Shindell et al. (2003) used the Goddard Institute for Space Studies (GISS) GCM – with a slab/mixed-layer ocean – to model the climatic response to volcanic aerosols during the pre-industrial era, from 1600 to 1850 AD. Results were compared with Shindell et al. (2001b) – where the climatic response to changes in solar irradiance (Lean et al., 1995; Figure 2.4) were modeled over the same time period – and with Northern Hemisphere temperature reconstructions, which are significantly more skillful after 1600 AD (Mann et al., 1998). Shindell et al. (2003)

concluded that both of these natural forcing factors contributed substantially to northern hemisphere cooling during the Maunder Minimum (Figure 2.4.), while solar forcing was the dominant factor influencing regional-scale climate over annual and longer time-scales.

While acknowledging that volcanic forcing can induce a significant regional climatic response on seasonal time-scales, Shindell et al. (2003) concluded that long-lasting temperature effects are minimal on these spatial-scales, especially for more than two years following individual eruptions. They explained this by noting that the frequently observed continental warming brought on by positive AO conditions in winter is often offset by summer season cooling from stratospheric aerosols. On the other hand, the cooling effect of reduced solar irradiance was consistent year-round and lasted for decades at a time (Shindell et al., 2003).

2.3.2.2. The confounding ENSO factor

As alluded to above, one of the most significant challenges to understanding both global and regional climatic effects of recent eruptions (e.g., Agung (Feb 18, 1963); El Chichón (Mar 28, 1982); Pinatubo (Jun 15, 1991)) stems from the fact that these events have all occurred during El Niño years (Robock, 2000; Adler et al., 2003). The fundamental problem with this is that both temperature and precipitation teleconnection patterns associated with El Niño are significant enough to effectively mask or unduly amplify the volcanic signal, particularly on regional-scales. This concern applies to East Asia, where ENSO is associated with regional temperature and precipitation variability

through various dynamical mechanisms throughout the year (Chang et al., 2000a, 2000b; Huang et al., 2003).

It remains unclear as to whether or not there is a causal link between volcanic activity and El Niño events. Results from a recent paleoclimate study (1649 AD to present; Adams et al., 2003) have reignited a controversial debate over this question. Adams et al. (2003) found that an explosive volcanic eruption roughly doubles the chance of an El Niño event occurring during the following winter, which certainly hints at cause and effect. A separate analysis of a six-century reconstruction of ENSO found that reduced radiative forcing – periods of low solar activity and increased volcanism – are associated with increased ENSO *variability*, and visa versa (D'Arrigo et al., 2005). This is consistent with early instrumental observations and historical records from the Pacific Basin during the Tambora era (Chenoweth, 1996) showing La Niña conditions during the first half of 1816; while 1814 and 1817 were both characterized as El Niño events. Quinn et al. (1987) and Ortlieb (2000) confirmed the timing of these El Niño events. Meanwhile, modeling studies aimed at determining a physical mechanism for a link between ENSO and volcanic forcing are conflicting (Robock et al., 1995; Mann et al., 2005; see the following section). This issue remains a confounding factor for studies examining the climatic response to volcanic forcing, especially during the period of instrumental record.

Thus, efforts have been made to statistically separate from the instrumental temperature record the spatial and temporal patterns associated with El Niño so that a more "pure" volcanic signal can be identified and studied (Robock and Mao, 1995; Kirchner and Graf, 1995; Yang and Schlesinger, 2001). Meanwhile, others have argued

that statistical removal of an ENSO signal from monthly datasets on a grid-point basis – especially in regions with non-stationary (e.g., East Asia; Chang et al., 2000a) or insignificant teleconnections with respect to ENSO – is problematic and could unnecessarily add confusion when interpreting results (Kelly et al., 1996; Shindell et al., 2004). Additionally, if a physical link does exist, as Mann et al. (2005) suggest, then this would at least partially call into question the physical basis for previous efforts to statistically separate the ENSO and volcanic signals.

To help clarify this matter, Robock (2000) noted that the El Chichón and Pinatubo eruptions appear to have occurred following the onset of the 1982-1983 and 1991-1992 El Niño events, respectively, which suggests that volcanic forcing could not have *caused* these recent events. Regardless, these late 20th century volcanic eruptions are likely to have modulated the global and regional climatic signals caused by concurrent ENSO conditions. So, notwithstanding the caveats listed above, the present study applies a simple regression technique to linearly remove the monthly ENSO signal from various regional monsoon indices and some gridded datasets during the instrumental period of record (after Robock and Mao, 1995). The regional-scale volcanic signal is then assessed based on analyses using both raw and ENSO-filtered climatic data, to test the sensitivity of the climatic response to the ENSO factor (Chapter 5).

2.3.2.2.1. A volcanic trigger for ENSO?

As discussed earlier, modeling studies have produced conflicting results with regard to whether or not volcanic forcing can induce an El Niño event or amplify its magnitude. Using a simple linear steady state atmosphere model, Hirono (1988)

proposed a mechanism by which the *tropospheric* aerosol cloud from the El Chichón eruption caused the trade winds to fail in the eastern equatorial Pacific, thus triggering the 1982-1983 El Niño event. Robock et al. (1995), investigating the plausibility of Hirono's mechanism with a non-linear AGCM, confirmed that the tropospheric aerosol cloud produced by El Chichón likely led to a trade wind collapse in their vicinity. However, Robock et al. (1995) also noted that El Niños are generally caused by trade wind collapses in the *western* equatorial Pacific, and that the oceanic component of the 1982-1983 El Niño event was already underway before the eruption of El Chichón. Based on this and other empirical data, Robock (2000) concluded that there is no evidence for volcanic-induced El Niño events.

Also mentioned above was the fact that recent empirical paleoclimate analyses by Adams et al. (2003) and D'Arrigo et al. (2005) – in addition to results from a modeling study by Mann et al. (2005) – have reignited the debate over a link between tropical eruptions and ENSO. To focus their analysis directly on the question at hand, Mann et al. (2005) employed a simplified Zebiak-Cane model to explore the potential impacts of volcanic forcing on the ENSO system and the coupled ocean-atmosphere in the tropical Pacific Ocean. Their results indicated that volcanic forcing can indeed trigger El Niño events, through an "ocean thermostat" mechanism, which arises due to the differences between the thermodynamic response to radiative forcing in the eastern vs. the western tropical Pacific. Basically, when radiative forcing is positive, the response in the western tropical Pacific is generally greater (due to the climatologically deeper thermocline), thus increasing the west-east SST gradient, which enhances the trade winds, leading to more upwelling in the east and warmer surface waters in the west. Thus, according to the

model, the result of positive radiative forcing is a positive feedback cycle that leads to a La Niña climatic state. Meanwhile, the opposite is true of negative radiative forcing (e.g., volcanic eruptions; solar minima), wherein El Niño conditions would be favored (Waple et al., 2002; Mann et al., 2005).

2.3.3. Practical applications for our improved understanding of volcanic forcing

One final point worth mentioning in this section addresses practical applications for dynamical modeling of volcanic forcing. Robock (2001d) concluded that the general circulation and regional-scale surface climatic response to Pinatubo and other recent eruptions was large enough to warrant the inclusion of stratospheric aerosols from future eruptions of similar scales into dynamical seasonal climate forecasting models (Robock, 2001d). The thermodynamic significance of volcanic forcing is also illustrated by the fact that the next generation of ECMWF reanalysis products will be generated by models that include stratospheric aerosols from volcanic eruptions, to more realistically reproduce the observed climate in the months and years following those events.

2.4. Hypothesized global and regional-scale response to aerosol forcing

To achieve this study's objectives, diagnostic analyses focus mainly on the processes by which synoptic-scale changes in the EAM system occur in response to global-scale changes in general circulation, with a particular focus on processes that are apparently sensitive to variations in stratospheric volcanic aerosol forcing. Thus, the processes to be considered in this study include changes in both regional and large-scale climatic boundary conditions. Regional-scale processes include changes in regional

SSTs and Tibetan Plateau snow cover – from direct radiative forcing – and dynamical changes in the West Pacific subtropical high and the East Asian jet. Large-scale processes include tropical Hadley circulation, the global upper-tropospheric subtropical jet stream and coupled atmosphere-ocean circulation patterns such as the Arctic Oscillation and the El Niño/ Southern Oscillation, each of which has important influences on regional climate variability (Liang and Wang, 1998; Chang et al., 2000a) and may also respond to global-scale volcanic forcing (Robock, 2000; Stenchikov et al., 2002; Shindell et al., 2003; Adams et al., 2003; Mann et al., 2005).

2.4.1. The global Hadley cell

The Hadley Cell may be best described as the dominant large-scale meridional overturning of the atmosphere that occurs due to latitudinal heating gradients throughout the earth's lower latitudes (Webster, 2005). Though the exact location of the cells changes with the seasons, there is typically rising air close to the equator and sinking air in the vicinity of the Tropic of Capricorn and Tropic of Cancer. Tropical regions with the greatest rainfall are closely linked to areas with rising atmospheric motion and frequent convective rainfall, while the great subtropical deserts are typically found where subsidence occurs.

Oort and Yeiniger (1996) noted that the strength and character of global Hadley circulation is significantly related to the phase of ENSO (1964-1990). Smoothed indices for tropical Eastern Pacific SSTs and Northern Hemisphere Hadley Cell strength have an in-phase relationship ($r = 0.49$); while Eastern Pacific SSTs are inversely related with variations in the Southern Hemisphere Cell ($r = -0.54$). In both cases, El Niño events

apparently increase the meridional overturning circulation associated with the Hadley cell, particularly in the Pacific Ocean region (Oort and Yeiniger, 1996). However, it has been noted in subsequent studies that meridional Hadley circulation in the Pacific region is somewhat inseparable from the Walker Cell, which has an implicit meridional component (Tanka et al., 2003). On the local- and regional-scale, meridional Hadley circulation is directly linked with lower level winds over the SCS and rainfall in southeastern China (Liang and Wang, 1998). The subject of synoptic scale links between the EAM system and Hadley circulation will be revisited in section 4.3.

As noted above, volcanic forcing measurably modifies atmosphere and ocean temperature gradients and causes a noticeable decrease in tropical SATs (Robock, 2000), evaporation and precipitation rates (Robock and Liu, 1994). It is hypothesized here that the latter changes relate to a decrease in global Hadley circulation, which could lead to significant regional climate anomalies around the globe, including East Asia, where the monsoon trough is embedded in the western Pacific intertropical convergence zone (ITCZ; the convective component of the Hadley cell) at various times during the summer (Chen et al., 2004).

Estimates of the near-equatorial energy balance associated with the Hadley circulation (Webster, 2005) suggest that a net surface solar radiation gain of 200 Wm^{-2} essentially comprises the engine that drives meridional overturning of tropical air. A simple calculation of the maximum instantaneous forcing averaged over the tropics (24°S – 24°N), from the 1815 Tambora eruption, estimates a maximum 21 Wm^{-2} reduction in solar radiation at the surface (based on a climate sensitivity of -21 t (Hansen et al., 2002)

and subject to the limitations of the volcanic forcing dataset), which could theoretically dampen the tropical Hadley circulation by up to 10%.

It is hypothesized that the theory of a volcanic-dampened Hadley cell may be tested in observational data by examining the relative strength of northern vs. southern hemisphere Hadley circulation following tropical eruptions with uneven aerosol distributions. For example, volcanic aerosol forcing caused by the March, 1982, El Chichon (17°N, 93°W) eruption was estimated to have been twice as strong in the northern hemisphere (NH) compared with the southern hemisphere (SH), while the relative forcing from the February, 1963, Agung (8°S, 115°W) eruption was reversed (Andronova et al., 1999; Hansen et al., 2002). Meanwhile, Oort and Yeiniger (1996) noted that they were unable to explain why, during the 1982-83 El Niño event, the normal in-phase relationship between tropical Pacific SSTs and Northern Hemisphere Hadley circulation was dampened, while the Southern Hemisphere Hadley cell responded normally. This question will be revisited in Chapter 5.

2.4.2. The global sub-tropical jet

While a weakening in tropical Hadley cells would have direct implications for evaporation and precipitation in the vicinity of the ITCZ, it is also hypothesized here that a modified Hadley circulation, acting in conjunction with extra-tropical changes in the circumpolar westerlies and the Arctic Oscillation, is likely to dynamically affect the strength and structure of subtropical high pressure systems and associated upper tropospheric jets. It is well established that the strong meridional circulation in the western tropical Pacific – with ascending motion largely driven by high SST's in the

West Pacific Warm Pool – strongly influences the West Pacific subtropical high (WPSH) (Huang et al., 2003) and the exceptionally fast subtropical jet over eastern Asia (Hou, 1998; Trenberth et al., 2000).

Stenchikov et al. (2006) examined the response of the winter season Northern Hemisphere tropospheric jets using both observations and IPCC AR4 coupled AOGCM "historical" simulations. Using 200 hPa geopotential heights (GPH) as a proxy for meridional changes in the jet, observational analyses noted northward movement over the North Atlantic, North America and Eurasian sectors while a southward shift was observed in the Pacific during winters following low-latitude eruptions. The zonal-mean structure of this response is generally consistent with a strengthening and contraction of the circumpolar vortex, as would be expected under positive AO conditions. Using the GISS AGCM, Hansen et al. (2005) noted that an acceleration of the Northern Hemisphere westerly jet was simulated in response to volcanic forcing. While many models reasonably simulate this observed jet response, most of the models underestimated its magnitude and failed to consistently capture regional-scale details (Stenchikov et al., 2006).

2.4.3. Temperature, precipitation, SSTs and snow cover

Anomalies in regional-scale boundary conditions, such as SSTs and snow cover, are likely to respond to surface cooling from diminished incoming solar radiation caused by increased stratospheric optical depth. The high heat content of the oceans make them a logical place to look for climate anomalies caused by persistent reductions in solar radiation (Gleckler et al., 2006), especially in partially closed basins like the South China

Sea where extensive advection and mixing from other basins would be relatively limited on monthly to interannual time-scales. In fact, average marine air temperature (MAT) measurements from 0° – 20°N (including measurements from the North Atlantic, Bay of Bengal and SCS) indicate that annual average cooling from 0.5° to 1.0°C occurred following the 1809 unknown and 1815 Tambora eruptions (Chenoweth, 2001). The significance of this is made clear by the fact that SSTs in the SCS are known to influence both the timing of the seasonal monsoon onset date as well as the intensity of the summer monsoon in eastern China (Chang et al., 2000a; Huang et al., 2003; Ding et al., 2004).

The persistence and depth of Tibetan Plateau snow cover during the winter and spring seasons may also be sensitive to reduced radiation and cooler tropospheric temperatures. Snow depth over the Tibetan Plateau during these seasons has been shown to affect regional atmospheric circulation and hydroclimate in eastern China through mechanisms related to heat, moisture and energy fluxes between the land surface and the atmosphere (Qian et al., 2003; Zhang et al., 2004).

2.4.4. Regional monsoon indices

During the past decade, an increasing number of studies have employed the use of climate indices to represent various components of the East Asian monsoon system. This provides one way of examining local or regional surface climate variability in the context of synoptic-scale variations in the atmosphere-ocean system. Through these studies, it has become clear that no single index is necessarily ideal for the purpose of characterizing variability in this complex regional monsoon system (Wu and Chan, 2005a). So, this study considers a wide array of such indices to gain the broadest

possible view of the EAM system and possible volcanic influences on regional/ local climate change.

Section 4.2 defines a number of published dynamic and thermodynamic global- and regional-scale climate indices and describes their significance in terms of their relationships with surface climate variability in East Asia. The regional-scale indices used for the present study include: 1) the West Pacific Subtropical High zonal displacement index (Riyu, 2002), 2) the Okhotsk High Index (Wang, Y. et al., 2003), 3) the Western North Pacific Monsoon Index (Wang et al., 2001; Wu and Wang, 2002), to characterize the lower level jet in the EAM region, 4) the Summer Monsoon Index (Wu and Chan, 2005), to measure the east-west sea-level pressure (SLP) gradient between eastern China and the western North Pacific, 5) the Land Sea-Surface Temperature Difference Index (Wu and Chan, 2005), to capture the zonal and meridional thermal contrast between eastern China and surrounding seas and, finally, 6) the East Asian Jet Strength Index (at 200 hPa; this study). In addition to the AO, ENSO, and the PDO, other global-scale indices include a global subtropical Jet strength index (this study) and two global Hadley Cell indices (based on the meridional stream function and vertical wind shear; Oort and Yienger, 1996).

2.5. Eruptions of the past

Table 2.1 lists the largest explosive tropical volcanic eruptions of the past 600 years (Briffa et al., 1998; Simkin and Siebert, 1994), all of them rating over 5 on the Volcanic Explosivity Index (VEI) scale (Newhall and Self, 1982; see below). Each of these eruptions appear to have had significant impact on global and regional climate

(Robock and Mao, 1995; Kelly et al., 1996; Shindell et al., 2004) making them of particular interest to the present study. Note that 1902 was a particularly active year for tropical eruptions; in addition to the Santa Maria event, both Pelée and Soufriere St. Vincent erupted (both VEI = 4), likely contributing to the climatic impacts noted by several researchers (Robock and Mao, 1995; Kelly et al., 1996; Shindell et al., 2004).

2.5.1. Indices for past volcanism

Several different methods have been used to compile histories of explosive volcanic eruptions for the purpose of examining their climatic effects. Lamb (1970) created the Dust Veil Index (DVI) based on a number of factors, including: historical reports of eruptions, optical phenomena, radiation measurements, and published estimates of the volume of ejecta. The most common criticism of the DVI is that the size of eruptions is based in part on the scale of observed climatic effects in response to each eruption, which leads to circular reasoning if the DVI is used as an independent index of volcanism for climate studies (e.g., Zielinski, 2000). However, Robock (2000) points out that the contribution of temperature effects to the derivation of the DVI is small and does not have a significant effect on most index values. Still, as noted by Bradley (1988), the observations of temperature, optical and radiation effects that are used to derive the DVI were largely acquired from mid-latitude locations, making this index potentially less suitable for studies in other regions.

The VEI rates eruptions on a scale of one to eight, with eight being the most explosive. As implied by its name, the VEI was developed to classify eruptions according to their eruptive power based on geological – as opposed to atmospheric – data

(Newhall and Self, 1982). The source data, spanning the past 8,000 years were collected and complied by Simkin and Siebert (1994) and contain no explicit climatic references or considerations. However, Newhall and Self (1982) note that plinian, or highly explosive, eruptions with VEI values greater than or equal to 4 are definitely powerful enough to inject sulfuric gases into the stratosphere. However, as noted by Robock (2000) and Zielinski (2000), Mt Saint Helens had a VEI value of 5 but had no discernible climatic effect beyond the immediate region because the blast trajectory was mostly lateral – as opposed to vertical. Compared with other indices, the VEI has been noted to correlate relatively poorly with global and hemispheric mean temperatures (Briffa et al., 1998; Robock, 2000). Still, the VEI is positively correlated with other volcanic indices (Robock and Mao, 1995) and it has been successfully used for climatic studies (e.g., Adams et al., 2003).

To more directly measure sulfuric emissions from volcanic eruptions, Robock and Free (1995) developed the ice-core volcanic index (IVI) using data from polar ice cores from 1850 to present. The IVI is based on sulfate ion content and acidity recorded at annual to sub-annual resolution in 6 ice-cores from the Southern Hemisphere and eight ice-cores from the Northern Hemisphere. Using additional ice core data from the past 2000 years, Robock and Free (1996) attempted to extended the IVI, acknowledging that the reliability of volcanic forcing reconstructions diminished significantly further into the past (e.g., pre-1200 AD in the northern hemisphere and pre-1850 in the southern hemisphere).

Robock and Free (1995) also discuss in considerable detail the inherent difficulties associated with using ice-core sulfate ion content and acidity as proxies for

volcanic forcing. Their primary concerns included: 1) non-volcanic sources for sulfate and acids, 2) dating uncertainties attributed to any number of factors, including the timing of sulfur transport from eruption source to deposition, 3) sulfate biases associated with local eruptions, which may or may not have entered the stratosphere, 4) sulfate transport processes from the stratosphere to the ice sheet, 5) the stochastic nature of dry deposition and snow accumulation through drifting vs. direct snowfall, all of which can vary dramatically on multiple temporal- and spatial-scales, and 6) uncertainties associated with acidity readings, which are sensitive to the ice temperature and measurement techniques sometimes vary from group to group.

Ultimately, for the purpose of climate studies, the perfect volcanic index accurately quantifies the timing, spatial distribution and magnitude of the radiative forcing, which is most closely related to the characteristics of the sulfate aerosol cloud in the stratosphere (Robock, 2000). Thus, since the publication of the IVI (Robock and Free, 1996) most attempts to quantify radiative forcing from volcanic eruptions have relied on proxy data from ice cores collected in high latitude regions (e.g., Crowley, 2000; Robertson et al., 2000; Zielinski, 2000; Ammann et al., 2003; Shindell et al., 2004; Mann et al., 2005; Ammann et al., 2006; Gao et al., 2006), where stratospheric sulfate aerosols decay most efficiently (Hamill et al., 1997). Still many of the seminal works acknowledge that a combination of indices, based on several independent data sources (e.g., VEI and IVI), may provide the best representation of pre-instrumental volcanic activity for use in climate studies (Robock and Free, 1995; Briffa et al., 1998; Free and Robock, 1999; Adams et al., 2003). The reader is referred to Robock (2000) for a more

thorough review of these and other volcanic indices (e.g., Sato et al., 1993; Mitchell, 1970).

2.5.2. Eruptions during the period of instrumental record

The most recent explosive tropical eruptions (Table 2.1.) have been the focus of a greater number of climatological studies because of their occurrence during the period of instrumental record and the abundance of available observational data for analysis. Agung (Indonesia; February 18, 1963), El Chichón (Mexico; March 28, 1982), and Pinatubo (Philippines; June 15, 1991) all had noticeable radiative and dynamic effects on global climate, despite the fact that these eruptions were all relatively small compared with earlier historical events, like Tambora.

The plinian column from the 1991 Pinatubo eruption reached up to 40 km in height and injected an estimated 17 to 20 Mt of SO_2 into the stratosphere (Self et al., 1996; Bluth et al., 1992), thus, producing roughly one third of sulfur gas yielded by Tambora and about twice that from El Chichón (~7 Mt; Bluth et al., 1992). The resulting stratospheric aerosols produced the highest global stratospheric optical depths since the eruption of Krakatau over a century earlier, in 1883 (Gao et al., 2006). For details regarding the climatic implications of the Pinatubo eruption, the reader is referred to extensive recent literature on the subject (e.g., Labitzke and McCormick, 1992; Hansen et al., 1996; Stenchikov et al., 1998; Kirchner et al., 1999; Yang, 2000; Robock, 2001b; Yang and Schlesinger, 2001; Stenchikov et al., 2002; Yang and Schlesinger, 2002; Stenchikov et al., 2004).

2.5.3. Tambora era climate

Tambora era climate is a logical time period on which to focus for a couple primary reasons. Firstly, a great number of previous studies have explicitly studied the climate of this era and thus there is a relative abundance of literature and paleoclimate data upon which to draw (e.g., Stommel and Stommel, 1982; Eddy, 1992; Harrington, 1992; Zhang et al., 1992; Chenoweth, 1996, 2000, 2001; Oppenheimer, 2003; Wagner and Zorita, 2005). Also, the Tambora eruption was enormous and as a result the climatic signal was also apparently very large. Thus, it is logical that if a region's climate may be susceptible to volcanic forcing then this response would have most likely been apparent following Tambora.

The year 1816 is famously known as "the year without a summer," for the global climatic disruptions following the eruption of the Tambora volcano on Sumbawa island, Indonesia (Stommel and Stommel, 1983). This event took place in 1815 and was the largest known eruption during the past 500 years (Briffa et al., 1998). The prominent plinian explosion on April 10 produced ash plumes up to 43 km high, injecting roughly 60 megatons of SO_2 well into the stratosphere (Oppenheimer, 2003). Over 71,000 people died on Sumbawa and the neighboring Lombok islands in the wake of Tambora. Many were killed immediately from ash fallout and pyroclastic flows, while thousands perished from hunger and disease in the months that followed (Oppenheimer, 2003). Broad-scale environmental and socioeconomic impacts related to this eruption ranged from climatological, to agricultural, to epidemiological (Pang, 1991; Harrington, 1992; Oppenheimer, 2003).

When considering the ensuing climatic impacts cause by the Tambora eruption, it is important to also note that this event was apparently preceded by an exceptionally large eruption of unknown origin in 1809 (Dai et al., 1991; Gao et al., 2006). Based on the existence of high sulfate levels measured in multiple bi-polar ice-cores, the 1809 eruption is very likely to have occurred in the tropics. It is also estimated to have produced roughly even stratospheric sulfate aerosol loading in each hemisphere (Gao et al., 2006), with total forcing ranging from half (Robertson et al., 2001) to more than three quarters the size of Tambora (Crowley, 2000; Ammann, 2006). Also, both Tambora and the 1809 unknown eruption occurred coincidently with the so-called "Dalton Minimum," a period between about 1790 and 1830 when solar activity was at a relative minimum (Eddy, 1992; Figure 2.3). Thus, some antecedent cooling caused by the Dalton Minimum and possibly from the preceding unknown eruption are likely to have contributed to the exceptionally anomalous global climatic conditions that followed Tambora.

A calibrated proxy-based annual reconstruction of April – September surface air temperatures suggests that the Northern Hemisphere (NH) was roughly 0.5°C and 0.75°C below modern climatology (1961 – 1990) during the year following the 1809 unknown and 1815 Tambora eruptions, respectively (Briffa et al., 2001). A multi-proxy reconstruction of NH annual temperatures by Mann et al. (1998) shows a relatively weak response to these eruptions. As noted earlier, Shindell et al. (2004) attribute the lack of a strong annual volcanic signal to the fact that the winter warming response observed over NH continents largely offsets the summer cooling response, leading to a minimal net annual effect.

However, compilations of over 43, 000 marine air temperature (MAT) measurements from 98 ships in the South China Sea, Atlantic and Indian Oceans during the period from 1807 to 1827 AD (Chenoweth, 2001) confirm that significant global-scale cooling occurred on a magnitude comparable to that noted by Briffa et al. (2001). Chenoweth also concluded that the NH annual average temperature response to the 1809 and Tambora eruptions was greater than the response to any subsequent eruptions, including Krakatoa (1883) and Pinatubo (1991). Interestingly, MAT measurements from the NH indicate that 1809 was actually the coldest year during this two-decade period of record (Chenoweth, 2001). Another interesting result from the Chenoweth (2001) study was that he dated the so-called "1809 unknown eruption" to spring (March – June) of 1808. He did this based on the occurrence of maximum global MAT anomalies during the year of 1809 and also from evidence for rapid, then sustained, cooling recorded in July, 1808, by two independent Malaysian temperature observers.

In New England, snow fell during every month of the "year without a summer" (Robock, 2001a). Worse yet, there were severe precipitation shortfalls and multiple killing frosts that drastically shortened the 1816 growing season, combining to cause near total crop failure throughout the region (Stommel and Stommel, 1983; Baron, 1992; Oppenheimer, 2003). Europe also experienced severely stunted agricultural productivity, but their problems came from below average temperatures coupled with anomalously high rainfall and cloudiness. The crops grew slowly and were subject to mold and fungus, which led to widespread famine throughout Europe (Stommel and Stommel, 1983). As a point of cultural interest, the deep red sunsets and unusually wet and dreary weather during the summer of 1816 inspired a contest between friends Lord Byron, Mary

Shelly and Percy Shelly to see who could write the best ghost story. On the shores of Lake Geneva, inspired by an environment changed due to a volcanic eruption half a world away, Mary Shelly won the competition by writing her famous novel, *Frankenstein* (Robock, 2001a)

Based on available historical records and early instrumental observations, there is also substantial evidence for unusually cold and stormy weather, below normal crop production and other anomalous weather patterns throughout eastern China (Zhang et al., 1992). For example, near modern extreme minimum temperature measurements were noted following Tambora on two occasions by ship merchants located at Canton, China (23°N, 113°E): 6.7°C and 4.5°C, in November and December of 1815, respectively (Chenoweth, 1996). Tibet saw three days of heavy snowfall in June, 1816 (Zhang et al., 1992), causing severe hardship to local populations and slowing W. Webb's survey of the Himalayas (Chenoweth, 1996). Using extensive quantitative harvest information collected from 66 different localities in China, Zhang et al. (2006) noted significant summer and fall crop reductions through the early 19th century, particularly in north and central regions. Zhang et al. (1992) also noted below normal crop production in the same regions during the summers of 1816 and 1817.

A comprehensive analysis of dryness/ wetness data from sites in the lower basins of the Yellow and Yangtze River valleys found that 1816 was the wettest year during the period from 1811 to 1820 (Huang, 1992). In fact, all of the 20 sites examined in that study experienced flooding or severe flooding in 1816. Reconstructed estimates of the strength of the West Pacific subtropical high (Huang and Wang, 1985) indicate this high pressure system was extremely weak during the decade from 1811-1820 and only weaker

during one other decade between 1470 and 1980 AD. Huang (1992) associated this weakening of the subtropical high with observed flooding in northern China during the summer of 1816. Furthermore, since wet summers are generally also cold summers, Huang (1992) inferred that the lower basins of the Yangtze and Yellow rivers were likely to have been exceptionally cold during that year. Of course, it is important to note that below normal regional temperatures during the summer of 1816 were unlikely to have been merely coincidental, since most abnormally cold and extremely cold summers since A.D. 1500 apparently occurred 0-2 years after large volcanic eruptions (Qun, 1988).

A recent study comparing global-scale proxy-based temperature reconstructions with results from coupled AOGCM simulations of the early 19th century climate indicated that volcanic forcing dominated the temperature signal during this era (Wagner and Zorita, 2005). That study noted that the regional-scale temperature response (in Europe) to volcanic forcing was much noisier, less consistent across multiple model ensemble members, and generally less statistically significant than the global signal. These results could highlight a potential shortcoming of the present study's experimental design, which aims to discern a regional-scale volcanic signal based on climate simulations with a single AOGCM realization (see section 3.4). However, Wagner and Zorita's (2005) experiment design was poorly suited for effectively resolving regional-scale volcanic-climate signals, since their volcanic forcing was prescribed as annual averages at the top of the model atmosphere, equally at all latitudes, through simple perturbations of the solar constant. Such a volcanic forcing method is, for example, unlikely to realistically reproduce the tropospheric and stratospheric temperature gradient

mechanisms that are believed responsible for the consistently observed (Shindell et al., 2004) positive AO response in winter (Stenchikov et al., 2002).

2.5.4. Superposed epoch analysis

Many previous studies have explored the effect of explosive volcanic eruptions on regional- and global-scale temperatures using compositing or superposed epoch analysis (e.g, Adams et al., 2003; Mann et al., 2005). This procedure is designed to assess the climatic response to a number of specific events, which are *a priori* expected to influence climate (i.e., volcanic eruptions), while reducing climatic noise that may be caused by a range of other influences. Bradley (1988) employed superposed epoch analysis by identifying a series of eruptions and then averaging monthly temperature anomalies during the three years before and the three years after the month of the eruption. Since eruptions can occur at any time of year and temperature means and variances change through the course of the seasonal cycle, data were standardized on a monthly basis prior to averaging. This analysis technique is problematic because the temperature response to high forcing has since been shown to change depending on the season (e.g., "winter warming"; Robock and Mao, 1992).

Another approach to accounting for these seasonal effects yet while also taking into account the possibility of different responses during different seasons is to composite data relative to January in the year of the eruption (Kelly et al., 1996). However, the problem with this approach is that the climatic response to an eruption in January could be different from the climatic response to an eruption several months later (e.g., in the fall season), particularly if the response season of interest occurs in between these events

(e.g., the summer monsoon). The seasonal timing of an eruption will also affect the magnitude of the radiative forcing and the spatial distribution of the stratospheric aerosols during a specific season of interest subsequent to the eruption (Ammann et al., 2003). These issues are further discussed in the context of this study's objectives in Chapter 5.

2.5.5. The importance of the paleoclimate perspective

The complexity of the dynamic general circulation response to volcanic eruptions coupled with unresolved questions regarding a causal link between ENSO and volcanic forcing underline the primary reasons for this study's focus on pre-instrumental eruptions. For one, the geologic record contains ample evidence for several well-dated tropical eruptions during the last millennium that were significantly larger than anything observed during the period of instrumental record (Crowley and Kim, 1999; Crowley, 2000; Zielinski, 2000; Bauer et al., 2003). Focusing on larger eruptions (e.g., Tambora) is advantageous because greater forcing presumably increases the climatic signal relative to that observed following smaller, more recent eruptions (e.g., Pinatubo). Also, analyzing the regional-scale climatic response to multiple large pre-instrumental eruptions increases the sample size of the analysis, provides an opportunity to test for signal stationarity under a variety of different boundary conditions and, therefore, increases confidence in the physical and statistical significance of the results. This may be particularly important with regard to this study's focus on the regional-scale hydroclimatic response.

The availability of annual resolution 510-year historical reconstructions of flooding and drought from multiple locations in eastern China (Central Meteorological

Bureau, 1981; Wang, 1988) provides a unique opportunity to explore the regional climatic response to multiple large eruptions under a wide variety of boundary conditions. These data also provide an opportunity to use a very unique high spatial resolution paleoclimate dataset to compare with results from AOGCM and RCM paleoclimate simulations. Additionally, this study's use of historical records from China as a proxy for paleoclimate avoids one problem that previous studies have faced by relying largely on tree-ring data (e.g., Shindell et al., 2004), which have been shown to underestimate the volcanic signal with respect to temperature, compared to other climate proxies (Gu et al., 2003; Robock, 2005).

Table 2.1. The largest explosive tropical volcanic eruptions between 1400 and present (Briffa et al., 1998; Simkin and Siebert, 1994). The year and season of each eruption is listed. Asterisks note 1 year adjustments to the timing of the eruptions originally published by Briffa et al. (1998), as suggested in an updated version of Crowley (2000), published by Mann et al. (2005). Question marks reflect uncertainty in the actual explosivity of a given eruption (Simkin and Siebert, 1994).

Year	Season	Volcano and region	Lat.	Long.	VEI
1453*	–	Kuwae, Vanuatu, SW Pacific	16.8S	168.5E	6
1580	–	Billy Mitchell, Bougainville, SW Pacific	6.1S	155.2E	6
1586	–	Kelut, Java	7.9S	112.3E	5(?)
1593	–	Raung, Java	8.1S	114.0E	5(?)
1601*	–	Huaynaputina, Peru	16.6S	70.9W	6(?)
1641	DJF	Parker, Philippines	6.1N	124.9E	6
1660	–	Long Island, New Guinea	5.4S	147.1E	6
1674*	MAM	Gamkonora, Halmahera	1.4N	127.5E	5(?)
1681*	–	Tongkoko, Sulawesi	1.5N	125.2E	5(?)
1815	MAM	Tambora, Lesser Sunda Is	8.3S	118.0E	7
1835	DJF	Cosiguina, Nicaragua	13.0N	87.6W	5
1883	JJA	Krakatau, west of Java	6.1S	105.4E	6
1902	SON	Santa Maria, Guatemala	14.8N	91.6W	6(?)
1963	MAM	Agung, Lesser Sunda	8.34S	115.51E	5
1982	MAM	El Chichon, Mexico	17.4N	93.2W	5
1991	JJA	Pinatubo, Philippines	15.1N	120.4E	6

Figure 2.1. Geopolitical map of China and the greater East Asia region.

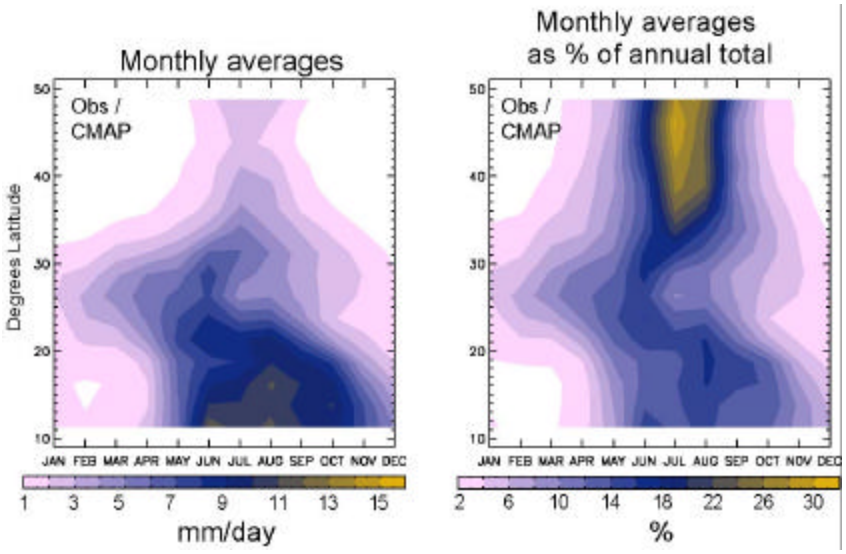

Figure 2.2. Hovmoller diagrams of the annual cycle of monthly CMAP precipitation, zonally averaged at each latitude across eastern China (105° – 122°E). Latitude-month precipitation values are presented as averages (left; mm/day) and as percentages of annual means (right), to highlight the seasonality of precipitation at each latitude.

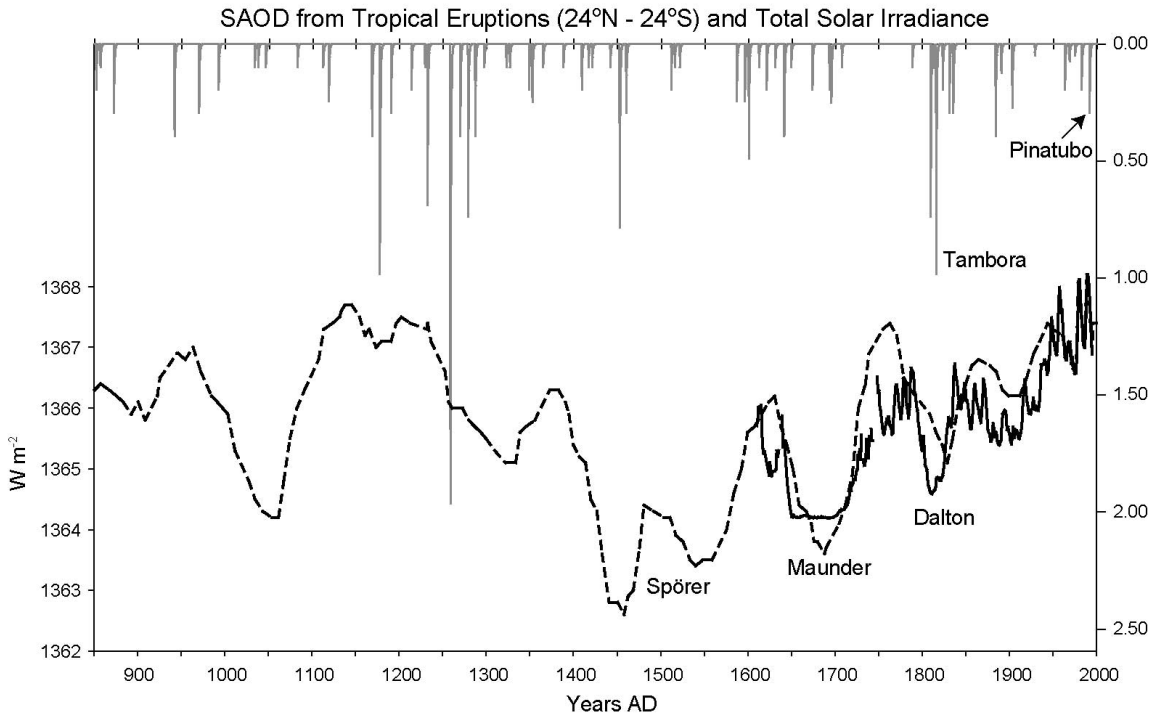

Figure 2.3. Estimates of monthly natural climatic forcing factors for the period from 850 to 2000 AD. Stratospheric aerosol optical depths (SAOD) (Ammann et al., 2006; grey) from tropical eruptions (average SAOD from 24°N – 24°S), with reverse scale y-axis at right (units = t). Total solar irradiance (W m^{-2}) based on sunspot observations calibrated with respect to direct satellite measurements beginning in 1980 (Lean et al., 1995; solid black), with y-axis at left. Total solar irradiance based on ^{10}Be from ice cores and scaled to total irradiance based on Lean et al. (Bard et al, 2000; dashed black). The Spörer, Maunder and Dalton solar minima are labeled, as well as the Tambora and Pinatubo volcanic eruptions.

CHAPTER 3

DATA AND METHODS

3.1. Observational datasets: station data and reanalyses

3.1.1. Surface parameters

Instrumental observations of monthly precipitation and temperature over East Asia have been acquired from several sources. First, global historical climatology network (GHCN) stations with fewer than 5 missing months from 1961-1990 were selected after determining that these screening criteria provide the best regional coverage from stations with the most complete temperature and precipitation records. To extend data coverage through the early 20th century, Climate Research Unit (CRU) gridded (0.5° × 0.5°) monthly temperature and precipitation data (1902 – 2002) are also used (Mitchell and Jones, 2005).

Two gridded global monthly precipitation datasets, derived from combined satellite and gauge observations, are also used because they are generally more directly comparable with modeled precipitation, due to their gridded format (2.5° × 2.5°) and the fact that their coverage extends over the oceans. First, the NOAA Climate Prediction Center (CPC) merged analysis of precipitation (CMAP) data (Xie and Arkin, 1997) are available from 1979 – 2001 and were provided by the JISAO at the University of Washington. Second, the Global Precipitation Climatology Project (GPCP) combined precipitation data (Adler et al., 2003) are available from 1979 – 2005 at the GPCP website.

A late 20th century monthly resolution history of Northern Hemisphere snowcover is derived from National Oceanographic and Atmospheric Administration (NOAA)

satellite data, from 1972 – 1999. Initially, daily visible satellite imagery was used to produce a weekly product depicting the presence or absence of snowcover within 89 × 89 gridpoints on a polar stereographic projection covering the Northern Hemisphere (Dewey and Heim, 1982; Robinson et al., 1993). The weekly data were later converted to a latitude-longitude grid at 2° × 2° resolution. To make these data comparable with other data used in this study, a monthly percentage value is assigned to each grid point for each month, indicating the frequency with which weekly snowcover was present at each location. Also, an annual time series of spring season snowcover extent over the Tibetan Plateau is calculated by averaging March and April percentages within the region: 91° – 105°E, 27° – 37°N. Station-based monthly observations of the total number of days with snowcover were available from eleven stations throughout the northeastern Tibetan Plateau region. Monthly data from these sites are generally available, with only occasional missing values, from 1954 – 1993 and were acquired from the Carbon Dioxide Information Analysis Center website (Shiyan et al., 1997).

NOAA Extended Reconstructed sea-surface temperature (SST) data (Smith and Reynolds, 2004), available globally at 2.5° × 2.5° resolution from 1854 to present, were also acquired from NOAA-CIRES Climate Diagnostics Center, Boulder, Colorado (http://www.cdc.noaa.gov/). These gridded data are interpolated from the most recently available Comprehensive Ocean-Atmosphere Data Set (COADS) SST dataset, which consists of ship-of opportunity observations. The strength of the analyzed signal is relatively consistent over time; however, due to sparse data availability, prior to 1880 the signal is significantly damped.

3.1.2. Upper-air data: reanalysis and sea-level pressure

Gridded monthly observations of upper air variables and surface temperature are represented by NCEP-NCAR reanalysis data. In most cases, these data are available at 2.5° × 2.5° – or finer-scale – resolution and are provided by the NOAA-CIRES Climate Diagnostics Center, Boulder, Colorado (http://www.cdc.noaa.gov/). In addition to the NCEP-NCAR reanalysis data, monthly gridded sea level pressure (SLP) data were provided by the National Center for Atmospheric Research (http://dss.ucar.edu/datasets/ds010.0/). This particular SLP dataset covers most of the northern hemisphere at monthly time steps from January, 1899, to December, 2005, at 5° × 5° resolution (Trenberth and Paolino, 1980).

3.1.3. The Arctic oscillation

The observed monthly AO index data were taken from the University of Washington JIASO website (http://jisao.washington.edu/analyses0302/), as prepared by Thompson and Wallace (2000). To be consistent with previous studies (e.g., Gong and Ho, 2003), the methods of Thompson and Wallace (2000) and the NOAA Climate Prediction Center (CPC) were employed to compute AO values from global climate model output. Specifically, for each model run, a principal component analysis (PCA) was performed on the covariance matrix of unstandardized monthly mean 1000 hPa geopotential height (GPH) anomalies north of 20°N. A monthly time series for the first principal component score was retained as the Arctic Oscillation index (Figure 3.1). Prior to analysis, the seasonal cycles were first removed from the data at each grid point.

Also, to ensure equal area weighting in the PCA, all data were weighted by the square root of the cosine of latitude.

All AO analyses are based on monthly mean height anomalies for all calendar months. Note, given that pressure level variance is greatest in winter months and the PCAs are based on the temporal covariance matrix from unstandardized data, the loading patterns are slightly dominated by winter season circulation patterns. However, when the same PCA technique was conducted on annual time series (CSM 1.4) with respect to each month separately, the results were nearly identical (e.g., June R^2 values = 0.99). AO loading patterns with respect to observed 1000 hPa GPH anomaly fields are shown in Figure 3.2.

3.1.4. The Pacific decadal oscillation (PDO)

Observed monthly PDO index data were taken from the University of Washington website (http://jisao.washington.edu/pdo/PDO.latest), following the methodology described by Mantua et al. (1997). Consistent with observations, the modeled PDO was derived through PCA of the temporal covariance matrix of monthly SST anomalies in the North Pacific Ocean, north of 20°N. A monthly time series for the first principal component score is retained as the Pacific Decadal Oscillation index (Figure 3.1). Prior to analysis, monthly mean global average SST anomalies were subtracted from anomalies at each grid-point to separate the North Pacific pattern of variability from any global signals (e.g., warming) that are present in the data. Figure 3.3. shows spatial correlation patterns between interannual variability in seasonally averaged SSTs and the seasonal

PDO index. Notice the strong out-of-phase relationship between SSTs in the North Pacific and those in the tropical Eastern Pacific/ ENSO region.

3.1.5. The El Niño/ Southern Oscillation (ENSO)

Observed monthly Southern Oscillation Index (SOI) data were taken from the Climatic research Unit website (http://www.cru.uea.ac.uk/cru/data/soi.htm) following the methodology described by Ropelewski and Jones (1987). The SOI is defined as the normalized SLP difference between Tahiti and Darwin, Australia (1866 – 2004 AD). Grid cells from locations closest to these sites were used to similarly define the SOI in the CSMv1.4, from 850 – 1999 AD. Positive SOI values indicate below average pressures over the western tropical Pacific Ocean and above average pressures over the central-eastern Topical Pacific (La Niña). Negative SOI values indicate the opposite pressure anomalies and signify El Niño conditions. Figure 3.1 compares winter averaged time-series for the SOI, PDO and AO indices during the period from 1901 – 2000 AD.

Figure 3.4 shows spatial correlation patterns between interannual variability in seasonally averaged SSTs and the seasonal SOI. Consistent with previous studies (Trenberth and Caron, 2002) interannual SOI variations correlate most strongly ($r > -0.8$) with SSTs in the central equatorial Pacific, the so-called NINO3.4 region (5°N–5°S, 170°–120°W), making these two indices for ENSO variability somewhat interchangeable. Also, notice clear similarities between these SST patterns and those shown in Figure 3.3, with respect to the PDO. Also note that while interannual variability in the SOI and PDO indices are significantly inversely correlated ($r = -0.35$; Mantua et al., 1997), their dominant time-scales of variability differ (Figure 3.1).

3.2. Paleoclimate datasets and record validation

During the period prior to instrumental records, a suite of proxies are used to quantitatively and qualitatively deduce paleoclimate conditions. The archive of historical data from East Asia is particularly rich, paralleled in scope only by similar early records from the European region. However, whether they are based on historical writings or the geologic record, any proxy-based index for paleoclimate variability must first be compared with direct observations in order to properly understand their climatic significance (Jones et al., 1998). This section introduces paleoclimate datasets used in this study and provides a basis for their use and interpretation in subsequent analyses.

3.2.1. Hydroclimate reconstructions based on historical writings in China

A wide array of historical Chinese manuscripts has been used to generate a number of paleoclimate reconstructions for Eastern China. Unfortunately, the vast majority of these manuscripts have never been translated into English; therefore the present study only uses quantitative and, in some cases, qualitative interpretations of the original documents, as presented in previous publications. While these records are of varying quality and reliability, many of them date back centuries and provide adequate spatial and temporal representation to examine the regional- and local-scale hydroclimatic response to past volcanic eruptions.

The range of historical documents from China includes local gazettes, official histories, memos to the Emperor and personal diaries (Zhang et al., 1992). Local gazettes are official histories written at the local and provincial level by prominent citizens or government officials. Compiled at intervals of several decades, these histories include

descriptions of geography, hydrology, agriculture and climate, in addition to political and social developments. Traditionally, each new dynasty of emperors also compiled official histories of the previous dynasty, coordinated through a large central government bureau in Beijing. Additionally, designated officials from various branches of government frequently sent to the central government, through several independent channels, memoranda that contained information on agriculture, weather and moisture. The final source of climate information came from personal diaries, where weather or phenologic observations were recorded with regularity by prominent citizens throughout China (Zhang et al., 1992).

Based on these historical documents, paleoclimate reconstructions of flooding and drought in eastern China were generated by the Central Meteorological Bureau (CMB; 1981) and Wang (1988) and are used here as proxy indicators of annual (summer-season) hydroclimate variability across the region. The CMB (1981) data – otherwise known as the drought/flood index (DI) – were available for this study at annual resolution for the period from 1470 – 1979 AD at up to 121 locations. For each year and each location a DI value from 1 to 5 is assigned such that 1 equals severe flooding while 5 equals severe drought. While time series from many sites have several years of missing data, records from roughly 30 locations are 100% complete and another 30 have at least 75% complete records (Figure 3.5).

The means by which written documentary records were used to assign individual years a DI value and the calibration of that index with respect to modern rainfall records deserves further explanation. The occurrence of severe flooding, flooding, drought or severe drought was usually recorded with regularity in local gazetteers in each of the

counties throughout eastern China. The frequency with which flooding or drought occurred was used to assign a grade to each location during a given year. Recent studies have shown that occurrence frequency is well correlated with the percentage of the rainfall anomaly at a given location (Wang and Wang, 1994). Table 3.1 outlines the basic rubric used for assigning index grades (1 – 5), the associated rainfall anomaly for each grade and the frequency with which years are generally assigned these grades.

However, the frequency distribution of DI value occurrences can vary significantly from site to site (Song, 2000). A cursory look at frequency distribution plots from all sites indicates that the occurrence of drought or severe drought is very rare at some locations, accounting for a combined total of 15% of all years, whereas at other sites drought or severe drought can account for 40% to 50% of all years on record, although this occurs at only a couple locations. Thus, the frequencies shown in Table 3.1 represent the typical range of DI values from most locations. To further justify the use of DI as a proxy for rainfall, Figure 3.6 shows scatter plots of regionally averaged CRU precipitation vs. DI values from sites within the same three regions in eastern China.

Another useful historical records-based dataset of pre-instrumental hydroclimate are the Wang (1988) Indices (WI), which reconstruct annual flood vs. drought conditions in three commonly studied regions of eastern China: the lower Yellow River, the lower Yangtze River and, southeast China. Incorporating flood-drought data (CMB, 1981) from locations within these regions (Figure 3.5), the WIs extend the DI hydroclimatic history for eastern China to the period 950 – 1999 AD (Qian et al., 2003a). However, note that the scale of this hydroclimatic index is opposite to that of the DI, which means

that higher WI values represent relatively wetter years, while lower WI index values reflect dryness.

3.2.2. Temperature reconstructions from historical records

Historical records described in the previous section contain relatively less information that can be used to develop quantitative temperature reconstructions (Zhang et al., 1992). In fact, the paucity of such data has meant that most available provincial temperature reconstructions are generally only available at decadal or longer time-scales (e.g., Wang and Wang, 1990; Wang, 1991; Ge et al., 2003). Unfortunately, decadally averaged datasets are of relatively limited use to the present study of monthly to annual volcanic signals in regional climate. Nevertheless, a few of the available regional temperature indices are used in the present study to get a general sense for how their variability has historically been linked to volcanic forcing.

First, Wang and Wang (1990) developed provincial temperature reconstructions from historical records for southeastern China, with decadally averaged indices representing temperature variations during the various seasons (e.g., JJA, DJF) and also year-round (ANN). A similar set of seasonal and year-round decadally averaged temperature indices from the Beijing region of northeastern China were also used (Wang, 1991). These particular records were chosen because they were available through personal communications between the original authors (Wang and Wang, 1990; Wang, 1991) and Raymond Bradley. Of course, temperature reconstructions that are based mostly on written descriptions are often more subjective, may depend on the observers

age at the time of writing and are therefore generally not as reliable on decadal or longer time-scales (Jones et al., 1998).

On the other hand, historical records sometimes contain some relatively objective measures for temperature, such as phenology (plant budding or flowering dates) or weather specific observations, such as the total number of frost days. Thus, another recent reconstruction of decal mean winter-half year temperatures from the middle and lower reaches of the Yangtze and Yellow River Valleys was also used. This dataset, prepared by Ge et al. (2003) is based mostly on documentary records of phenologic events and winter snow day observations. The final decadal mean temperature reconstructions that are used in this study were developed by Yang et al. (2002) and are based on multiple climate proxies from throughout the East Asia region. The data that form the basis for the Yang et al. (2002) temperature indices were derived from ice-cores, tree-rings, lake sediments and historical records from the Tibetan Plateau, eastern China, Taiwan and Japan.

3.2.3. Pacific sea surface temperature reconstructions

An El Niño episode index was reconstructed by Quinn et al. (1987) and Ortlieb (2000) and made available at the University of Washington. The Quinn data do not explicitly account for La Niña conditions and rather focus solely on El Niño episodes, assigning each a rating from 1 – 6 indicating their relative strength. Each El Niño episode is also assigned a confidence level, from 1 – 5, which reflects the relative abundance of available evidence in support of El Niño conditions during a given year. While the Quinn data are available at annual resolution during the entire period from

1525-1988 AD, they are less reliable prior to 1791 (Henry Diaz, *personal communication*) and so only the later half of the record is used in subsequent analyses.

Several different multi-century reconstructions of the PDO index have been attempted; however, until recently most have relied entirely on climate proxies (generally tree-rings) from the North and South American continents (e.g., Bondi et al., 2001; Gedalof and Smith, 2001). Shen et al. (2006) recently reconstructed the PDO index for the period from 1470 to 2000 using DI data from eastern China. Also, D'Arrigo and Wilson (2006) recently published the first-ever paleoclimate reconstruction of the PDO index based entirely on tree-ring chronologies collected on the Asian continent, from locations in Bhutan to northern Siberia. Detailed analysis and discussion of these records is beyond the scope of this study; however it should be noted that temporal inconsistencies between the various reconstructed PDO indices highlight the need for additional research in this field (Figure 3.7). Specifically, the precise mechanisms responsible for controlling low-frequency changes in large-scale modes of climate variability – as well as the stationarity of related teleconnections patterns – remains somewhat poorly understood, particularly in the pre-instrumental era (D'Arrigo and Wilson, 2006).

3.2.4. Marine air temperature over South China Sea (1808 – 1827 AD)

While most so-called "paleoclimate" datasets used in this study are based on proxy climate indicators, one is derived from actual instrumental observations: early 19th century marine air-temperature (MAT) measurements from merchant ships' log books (Chenoweth, 1996, 2000, 2001). Michael Chenoweth was very generous to share with

me hundreds of daily MAT measurements that he painstakingly digitized from British Library archives and subsequently adjusted for time-of-day and other observational biases (Chenoweth, 2000). The specific data used for this study are from four grids within the South China Sea (SCS) basin: from 0 – 5°N, 5° – 10°N, 10° – 15°N, and 15° – 20°N. These records are available for the period from 1808 – 1827 AD, although they contain several missing values with significant sampling biases toward certain months of the year.

For example, Figure 3.8 plots the number of months during which at least one MAT measurement was made within each of the SCS grids. There is clearly significant under-sampling during the months of May, June and July, while the greatest total measurements were made during August and September; however these biases are basically common to all grids. To prepare these data for subsequent analysis, adjusted individual MAT measurements were averaged on a seasonal basis (Dec. – Feb.; Mar. – May; Jun. – Aug.; Sep. – Oct). Seasonal anomalies were initially calculated separately within each grid cell to remove the latitude-dependant seasonal cycle. Next, individual seasonal anomalies from all four grid cells (when available) were averaged to create a regionally averaged MAT anomaly index for the period 1808 – 1827 AD. To express anomalies relative to a benchmark period with relatively little volcanic forcing, a final adjustment was made by subtracting from them average MAT anomalies during the period from 1820 – 1825. Table 3.2 provides this final data product along with the associated total number of measurements included in each of the seasonally averaged values. It is noted that results from the South China Sea Monsoon Experiment support the use of MAT measurements as proxies for SSTs in summer, showing excellent

covariance between these two variables on daily to monthly times-scales (Ding et al., 2004).

3.2.5. Ice core records from the Dunde Ice Cap, Tibetan Plateau

Of the various boundary conditions of particular interest to this study, reliable estimates of pre-instrumental snowcover conditions over the Tibetan Plateau are perhaps the least well documented. However, Mary Davis has kindly provided me with unique records of $d^{18}O$ and water equivalent average annual net accumulation (A_n) from ice cores collected on the Dunde Ice Cap (38°N, 96°E, 5,325 meters above sea level), on the northeastern edge of the Tibetan Plateau (Davis et al., 2005; period of record: 1801 – 1986 AD). The A_n record contains water equivalent data from two separate cores (cores #1 and #3), while the annual $d^{18}O$ record is derived from core #1 only. Age dating for both cores was constrained by visible dust layers deposited each winter, a beta radioactivity signal from Soviet thermonuclear tests in 1963, as well as regular seasonal variations in $d^{18}O$. (The isotopic ratio of oxygen-18 to the relatively light and less abundant oxygen-16 is $d^{18}O = \{[(^{18}O/^{16}O)_{sample}/(^{18}O/^{16}O)_{SMOW}] - 1\} \times 1000$, where SMOW is the universal standard from mean ocean water; values are expressed in permil units). Dust layer counting and sub-annual $d^{18}O$ measurements allowed for the development of annually resolved A_n time-series in both cores throughout the available record. A_n records were initially derived from each core separately – prior to averaging – using a steady state flow model that accounts for down-core ice thinning. Each layer in the core was bound by winter dust layers; thus, annual data-points roughly correspond to

water equivalent net accumulation (A_n) or $d^{18}O$ over the course of each calendar year (Davis et al., 2005).

Noting several lines of independent evidence, Davis et al. (2005) demonstrate quite clearly that variations in $d^{18}O$ values on the Dunde Ice Cap are well representative of regional temperatures at the time of precipitation. Firstly, monthly averages of $d^{18}O$ in precipitation collected 150 km away are correlated significantly with local temperatures. Also, previous analyses of $d^{18}O$ from a nearby ice cap correlated significantly on decadal time-scales with 500 hPa temperatures during a relatively recent 30-year period. Finally, $d^{18}O$ values from the Dunde record show significant positive correlations with gridded NCEP reanalysis surface temperatures over a broad region of Eurasia.

The two-core averaged Dunde A_n record was validated for the purposes of the present study with respect to eastern Tibetan Plateau snow conditions using two independent indices for regional snowcover (snow depth data were not available). As noted earlier, observations from 11 climate stations located on the Tibetan Plateau contain roughly continuous monthly time series of the total number of days with observed snowcover. Data from November to April were used to generate annual resolution time series of total snowcover days during the period from 1954 to 1993. Each of these 11 time series was then correlated pairwise with the A_n record to identify those sites sharing significant (p-value <0.05) covariability with respect to the proxy record. This selection process eliminated eight sites whose snowcover variations were poorly correlated with the A_n record. Data from the remaining three sites (Figure 3.9) were effectively combined into a station-based regional snowcover index by performing PCA on their correlation matrix. The first principal component score was retained (PC1-snow)

and used, along with regionally averaged snowcover derived from satellite data (NOAA-snow), to validate the Dunde A_n record with respect to observations.

Figure 3.10 plots standardized time series of PC1-snow, NOAA-snow and A_n, illustrating reasonable agreement between these records. Simple correlation r-values were computed between A_n and PC1-snow during two separate 17 year periods (1954 – 1970; 1970 – 1986) and also over the entire 33 years of record overlap. The correlation between A_n and the independent NOAA-snow record was similarly measured during the 15-year period from 1972 – 1986. Results from these analyses – plotted in appropriate locations on Figure 3.10 – are all statistically significant (p-value <0.05), suggesting that the Dunde A_n record provides a good index for winter/ spring snowcover variability over the eastern/northeastern Tibetan Plateau.

Yet, some caveats are warranted. A closer look at Figure 3.9 reveals that there are a few climate stations closer to the Dunde Ice Cap than those that were included in the principal component analysis. Also, two of those selected are at a relatively low elevation (~1500m) compared to Dunde (~5300m). These observations are somewhat unexpected and could suggest that statistically significant correlations between PC1-snow and A_n are somewhat spurious. Another complicating factor is that recently observed long-term trends in snow accumulation days, temperature and precipitation on the Tibetan Plateau display considerable spatial heterogeneity throughout this topographically complex high elevation region (Niu et al., 2004). However, the fact that NOAA-snow – a regionally averaged index for snow cover – is also significantly correlated with A_n reinforces the stated interpretation of A_n for this study. Still, longer records from more sites across a broader region would have been beneficial for resolving

these questions. Thus, any general conclusions drawn from subsequent analyses of A_n must be treated as preliminary.

Finally, following the precedent of previous studies (e.g., Robock and Mao, 1995), a high-pass Lanczos filtering technique (Duchon, 1979) was used to remove low-frequency variations longer than 15 years from the Dunde A_n and $d^{18}O$ records. Low-frequency trends in A_n were exceptionally pronounced – compared to other datasets used for this study – and thus warranted removal prior to subsequent analyses, which are focused on deducing a high-frequency response to short-term volcanic forcing. The two panels in Figure 3.11 plot time series of the original raw A_n and $d^{18}O$ records (dashed lines) along with their respective linearly detrended, high-pass filtered time series (solid lines).

3.3. Volcanic forcing datasets

Though the seasonal timing of eruptions and the latitudinal distribution of optical depth variations can be critical to understanding the climatic response, reliable information regarding such details – particularly for the latter – is limited prior to the advent of satellite measurements in 1978 AD. For instance, the exact location, timing and magnitude of some volcanic eruptions as recent as 1809 can only be deduced from sulfate deposits in well-dated polar ice cores (Zielinski, 2000). The 1258 AD event is another eruption for which the source remains unknown; however, tephra layers and sulfate peaks in multiple ice cores from Greenland and Antarctica suggest this to have been the largest tropical eruption during the past 2 millennia and possibly the past 5,000 years (Langway et al., 1988). In other cases, where local populations existed at the time

of eruption, historical records have provided very reliable estimates for the timing of volcanic events as far back as Vesuvius, 79 AD (Zielinski, 2000). As a result, between the historical record, sulfate peaks from ice-cores (Robock and Free, 1995, 1996) and frost layers in tree-rings (Lamarche and Hirschboek, 1984), the timing of many large eruptions during the past millennium is well established with roughly annual precision (see Table 2.1; Briffa et al., 1998; Crowley, 2000; Gao et al., 2006).

3.3.1. The Ammann dataset

To represent pre-satellite-era volcanic eruptions realistically in the models, a monthly latitudinally varying dataset of zonally averaged stratospheric aerosol optical depth (SAOD) was developed using a simple off-line parameterization scheme by Ammann et al. (2003; 2006; Figure 3.12). Due in large part to the fact that stratospheric winds are dominantly zonal, modern satellite-based observations of stratospheric sulfate aerosols confirm that volcanic forcing is spatially well represented by global zonal means (Figure 5.1; Robock, 2000). Peak SAOD from each eruption was scaled relative to published estimates of total sulfate released by historic eruptions (e.g., Stenchikov et al., 1998) and sulfate levels in polar ice cores (e.g., Robock and Free, 1996; Gao et al., 2006). All aerosols are assumed to be spherical sulfuric acid droplets with uniform size distribution (r_{eff} = 0.42 micron) and composition of 75% H_2SO_4 and 25% H_2O, all of which is comparable to Pinatubo aerosols (Stenchikov et al., 1998). The SAOD data has a monthly resolution and the forcing from each eruption of known origin is set to start on the first day of the month in which it occurred. Forcing from eruptions of unknown origin (e.g., 1259 and 1809 AD) begins in January of the year in which they are estimated

to have occurred. Peak SAOD occurs 4 months after each eruption and aerosols decay at an e-folding time equal to 12 months in the tropics.

While recent studies based on direct observations of optical depth and sulfate loading from multiple bi-polar ice cores indicate that half to two thirds of volcanic aerosols from tropical eruptions tend to stay in the hemisphere of origin (Gao et al., 2006), prescribed SAOD from tropical eruptions are always assumed to be evenly distributed in each hemisphere, from 25°N – 25°S. Accounting for seasonal variations in upper-level winds, aerosols from tropical eruptions are then dispersed into the mid-latitudes during each hemisphere's respective winter, where they subsequently decay during summer. Aerosols from mid- to high-latitude eruptions remain completely poleward of 30° in the hemisphere of origin, in agreement with observational studies (Robock, 2000; Zielinski, 2000). Further discussion of this methodology and more detailed comparisons with observed aerosol distributions following individual eruptions are described in Amman et al. (2003).

3.4. Global and regional climate model experiment designs

3.4.1. Paleoclimate simulations with CSM version 1.4

To model paleoclimate variability and compare this output with independent reconstructions of past climate, "hindcast" simulations were carried out with a modified version of the National Center for Atmospheric Research (NCAR) Climate System Model (CSM; Boville and Gent, 1998). The CSM is a coupled global climate model with dynamic atmosphere (Community Climate System Model, CCSM3; Kiehl et al., 1998), ocean (NCAR CSM Ocean Model, NCOM; Gent et al., 1998), and sea-ice (Weatherly et

al., 1998) models, plus a land surface biophysics and basic hydrology model (Land Surface Model, LSM, Bonan, 1998). These various model components communicate with each other through a flux coupler (Bryan et al., 1996), which calculates the fluxes and controls the time coordination of model integrations. Boville et al. (2001) subsequently created CSM version 1.3 by modifying the basic CSM1 model configuration to reduce deep ocean drift and add capabilities that make the model suitable for multi-century transient paleoclimate simulations – with incremental changes in radiative forcing.

Finally, the AOGCM output used for this study were generated by CSM version 1.4 (CSM1.4), which includes a modified radiation code in the stratosphere (CCM3.6.6) such that time-latitude varying volcanic sulfate aerosols may be readily prescribed (Ammann et al., 2006). The primary benefit to this modification is that it improves the model's capacity to realistically simulate regional-scale impacts (Kelly et al., 1996) caused by indirect, dynamic climatic responses to volcanic forcing (Robock, 2001; Shindell et al., 2004). For example, the CSM1.4 configuration allows the model to capture the tropospheric cooling (caused by increased SAOD) and stratospheric heating (caused by the presence of sulfate aerosols) mechanisms that have apparently been responsible for the observed positive AO response to tropical eruptions in the past (Stenchikov et al., 2006; Chapter 2).

The specific "Millennium" simulation that provides the foundation for the modeling component of this study, the CSM1.4 was run for the period 850 – 1999 AD, at T31 resolution (~3.71° × 3.75°), with both natural and anthropogenic external forcing (Ammann et al., 2006). Forcing factors included low-frequency changes in solar

irradiance at the top of the atmosphere (Bard et al., 2000; scaled to Lean et al., 1995), volcanic aerosols prescribed at three vertical levels between 150 to 50 hPa (Ammann et al., 2006), and atmospheric greenhouse gas histories from ice-cores (CO_2, CH_4, N_2O, CFC-11 and CFC-12). Anthropogenic sulfate aerosols were also included, along with a recurring annual cycle of ozone and natural background sulfate aerosols. A companion 1,150-year long control experiment was also run, starting with the same initial conditions but with no external forcing. The control simulation is treated as a benchmark, representing internal, unforced, variability in the modeled climate system.

In all simulations, orbital forcing was set constant at 1400 AD conditions and vegetation/ land use changes were not included in the model (Ammann et al., 2006). Anthropogenic sulfate aerosols were specified in the CSM1.4 three-dimensionally in each global grid cell (T31; lat = 48, lon = 96, level = 18) at monthly time steps, from 1870 - present. A different, unchanging, three-dimensional 12-month field of the annual cycle of background tropospheric aerosols was specified annually for all simulation years prior to 1870. Atmospheric ozone is similarly specified by an unchanging 12-month forcing field that is cycled throughout the run, from 850 to 1999 AD. The inclusion of prescribed tropospheric aerosol forcing is unlikely to impact the results of this research, which focuses on large-scale volcanic eruptions, primarily in the pre-industrial era. However, the use of prescribed ozone could limit model's ability to capture the true sensitivity of the AO to volcanic forcing (Stenchikov et al., 2002), because the chemical reaction of stratospheric sulfate aerosols with O_2 reduces ozone concentrations in polar regions, thus contributing to the "stratospheric gradient" mechanism (section 2.3.4.2).

Otherwise, this CSM1.4 model configuration used here is as well suited as most other AOGCMs for the purposes of this study. By prescribing SAOD following explosive eruptions and by allowing for a prognostic radiative response to these aerosols in the stratosphere, the thermodynamic response to explosive tropical eruptions can be assessed on both global and regional scales. For example, this model is expected to realistically simulate the observed positive AO response via the tropospheric and stratospheric gradient mechanisms (Stenchikov et al., 2002), although the wave feedback mechanism may be somewhat muted due to a lack of high vertical resolution at the tropopause and in the stratosphere (Stenchikov et al., 2004; Stenchikov et al., 2006).

While most AOGCMs realistically simulate large-scale atmospheric circulation patterns and thus provide a reasonable basis for analyzing the processes by which the global climate system responds to volcanic aerosol forcing, the CSM's coarse spatial resolution contributes to the occurrence of some significant, though common (Kang et al., 2002; Liang et al., 2002), regional biases in surface hydroclimate – in the lee of the Tibetan Plateau, for example (see Chapter 6, Figure 6.1). However, this precipitation bias is known to improve in AOGCMs with much higher spatial resolution; as model topography becomes more realistic, so does the spatial distribution of regional precipitation (Kobayashi and Sugi, 2004; Ping Lu, personal communication). Thus, this study uses a limited area RCM – driven by boundary conditions from a the CSM1.4 – to test for its ability to alleviate these regional biases in surface climate (Chapter 7), while saving on the computational expense of having to run a full global model at increased horizontal resolution.

3.4.2. RCM simulations

Recognizing the obvious limitations of assessing local- to regional-scale climate change impacts based on spatially course GCMs, circa 1990 the first RCMs were developed by adapting mesoscale numerical weather forecasting models for simulations on climatic time-scales. Since the CSM generally simulates the primary large-scale boundary conditions and synoptic-scale controls on the East Asian monsoon system with reasonable accuracy (see Chapter 6, Figures 6.1 and 6.2), output from the CSM1.4 is used to provide the driving field for dynamical downscaling over East Asia, through limited area modeling with the SUNY Albany MM5-based regional climate model (SUNYA-ReCM; Wang, W.-C. et al., 2000; Gong and Wang, 2000). The ReCM uses 23 vertical levels, from the surface to 10 hPa, and a horizontal grid spacing of 60 km. The model domain is ~80° to 130°E, 15° to 45°N, with the Tibetan Plateau at the western lateral boundary (Figure 3.13). While regional model skill can be somewhat sensitive to the choice of lateral boundaries (Leung et al., 1999; Wang, W.-C. et al., 2000), these boundaries were chosen for this study somewhat arbitrarily: to maximize coverage in areas for which paleoclimate data are available and to minimize the size of the domain, thus reducing the total computational expense.

Both modern and paleoclimate simulations were run with the ReCM and CSM1.4 provided the lateral boundary conditions, or driving field, in every case. First, a four year modern run was conducted over a period with no major volcanic eruptions (from 1986 – 1989 AD), to validate this regional modeling scheme with respect to observations and confirm the extent to which the surface climatology simulated by the RCM represents a noticeable improvement over regional biases observed in the global model.

Subsequently, two paleoclimate simulations were conducted for the period 1808 – 1819 AD to study the simulated regional climate response to the 1809 eruption and the famous 1815 Tambora eruption. The first RCM paleoclimate simulation was conducted with the same natural (pre-industrial) external forcing that was used to drive the forced Millennium experiment and the second simulation was run under identical conditions, but without volcanic forcing. The second run is treated as a control simulation and is used to effectively isolate the volcanic signal relative to other forcings (e.g., solar) as well as internal regional-scale climate variability. However, as noted in the introduction, the paleoclimate simulations remain incomplete at the time of this writing and so results from those simulations are not included in this dissertation.

3.5. Caveats, uncertainties and experimental design limitations

This section details a few important caveats and uncertainties associated with the data and methods used in this study. While the following discussion may run the risk of undercutting certain conclusions presented in forthcoming analyses, it is important for the reader to be aware of these primary limitations because related issues frequently come up in discussions when results are interpreted. Furthermore, it is noted that several of the studies cited in this section are very useful general references.

The paleoclimate analyses conducted for this study, comparing coupled model simulations with pre-instrumental reconstructions, contain several fundamental sources of uncertainty. With regard to the study of paleoclimate reconstructions based on historical records and documents, there is obviously an inherent subjectivity to any qualitative written account or artist's rendering of past environmental conditions (Jones et al., 1998;

Bradley, 1999; Jones and Mann, 2004). Furthermore, even quantitative assessments of the geologic record contain errors due to uncertainties associated with precise dating, record interpretation and validation, as the many environmental conditions influencing characteristics of a given proxy may change through time (Bradley, 1999).

With any paleoclimate dynamical modeling simulations, significant sources of uncertainties come from the precise timing and magnitude of past changes in radiative forcing from solar irradiance and volcanic activity, in particular (Crowley, 2000; Waple et al., 2002; Hansen et al., 2002), both of which played significant roles in regional-scale climate variability, albeit on slightly different time-scales (Shindell et al., 2003). By comparing various published estimates of stratospheric aerosol loading from historical eruptions, Hansen et al. (2002) subjectively estimated uncertainties in the magnitude of aerosol forcing to be 15% for Pinatubo, 25% for El Chichon, 30% for Agung and 50% for other explosive eruptions from 1880 to 1915. This puts a lower bound of 50% uncertainty on the estimated magnitude of stratospheric aerosol forcing from pre-instrumental eruptions. Note that despite compelling indirect evidence – in the form of local and globally averaged temperature measurements (Chenoweth, 2001) – inferring a spring 1808 timing for the so-called "1809 eruption," the present study awaits further support for those findings and thus relies on the Ammann et al. (2006) dataset, which assigns a January, 1809, date for this event.

Also, quantifying the magnitude of low-frequency variability in solar irradiance is an unresolved scientific question. Thus, this issue remains a particularly important research priority for the purpose of quantitatively attributing natural vs. anthropogenic

contributions to global warming during the past one and a half centuries (Ammann et al., 2003; Stott et al., 2006).

This study makes a point of carefully considering ENSO dynamics for three primary reasons. First, ENSO is intricately coupled with the EAM system and, therefore, understanding hydroclimate variability in eastern China requires an understanding of their interrelationships (Liu and Wang, 2006). Second, given the first point, any comprehensive effort to test regional-scale model validation with respect to the EAM system necessitates the consideration of model skill with respect to ENSO teleconnections. Third, both modeling (Mann et al., 2005) and empirical studies (Adams et al., 2003) provide evidence for a physical relationship between volcanic forcing and the occurrence of El Niño events. However, as Cane et al. (1997) and subsequent researchers (Waple et al., 2002; Mann et al., 2005) have noted, most modern AOGCMs are run at resolutions too coarse to adequately simulate the dynamics of the "ocean thermostat" feedback mechanism, which is hypothesized to be responsible for inducing an El Niño response to SAOD forcing (Mann et al., 2005; see section 2.3.2.2.1). As a result, this study is unlikely to substantially address this third point. Nevertheless, as previous studies have shown (Robock and Mao., 1995; Kelly et al., 1996; Yang and Schlesinger., 2001), any empirical analysis of the observed regional-scale climatic response to volcanic forcing (Chapter 5) requires a thorough consideration of the ENSO factor.

With regard to this study's goal to make direct comparisons between coupled AOGCM output and regional-scale climate reconstructions, inherent differences between modeled vs. observed SSTs and land cover are inevitable. In the case of SSTs, the

primary and most obvious problem stems from the fact that ocean conditions are prognostic in AOGCMs; thus their variability will be different for every realization given unique initial conditions. This is a particularly confounding issue on the timescales of interest in this study because internal modes of interannual- to decadal-scale climate variability are known to be tightly coupled with modes of SST variability, particularly in the Pacific Ocean (Dai and Wigley, 2000). Furthermore, any limitations in the spatial-temporal representation of ENSO in the CSM (Meehl and Arblaster, 1998), however minor, would inevitably reflect on teleconnections with the monsoon climates and elsewhere (Liang et al., 2001). These issues are at least partially addressed through the use of composite analyses, which average the climate response to multiple large tropical eruptions. This procedure effectively increases the signal-to-noise ratio and thus increases the likelihood of deducing a "pure" volcanic signal that is unaffected by unrelated modes of climate variability.

On longer time scales, significant deforestation and intensive land use have been an important part of China's environmental history for at least 1,000 years (Fu, 2002; Elvin, 2004). Thus, the exclusion of an explicit representation of land cover change in the models could significantly limit their ability to realistically simulate observed long-term trends in paleoclimatic change over eastern China (Fu, 2002; Gao et al., 2003; Wang, H. et al., 2003; see section 2.1.1). On the other hand, given the short time-scales of interest in the present study, this may not pose any serious problems, particularly since holding vegetation constant throughout all simulations provides a control on this boundary condition, thus eliminating it as a possible source for variability in the models.

Another possible limitation of the global model configuration used for this study is that the CCM3's atmosphere has only 18 levels and a rigid lid at ~45 km altitude, which means that nothing above the stratosphere is resolved. Yet, as noted in Chapter 2, Stenchikov et al. (2004) showed that an atmospheric model with a high resolution stratosphere and mesosphere – with 40 atmospheric levels and a lid at roughly 80 km height – produces a more realistic spatial-temporal climatic response to volcanic forcing. On the other hand, it is noted that the Stenchikov et al. (2004) simulations were conducted with an atmosphere-only model (with prescribed SSTs) and that getting the correct phase of the QBO proved to be important for realizing the benefits of their high resolution upper atmosphere. Meanwhile, the actual phase of the QBO and the actual pattern of SST anomalies throughout the Pacific Basin at the time of pre-instrumental eruptions (e.g., Tambora in 1815) are unknown or poorly constrained boundary conditions. Thus, the fact that this study uses a coupled model with an atmosphere that does not resolve a mesosphere is not necessarily a drawback in terms of the overall experiment design, given the limitations of the existing paleoclimate record.

Regarding regional climate models, it is logical that models with higher spatial resolutions would be automatically more skillful in terms representing local-scale climatic effects in areas with complex topography, coastlines, and/or variable land cover. However, similar to global models, results from RCM simulations are highly sensitive to the physical parameterizations that are used to represent clouds, radiative transfer, and surface processes (Leung et al., 1999; section 2.1.2.2.). Additionally, depending on the complexity of the regional environs, RCM skill can also be significantly impacted by errors in the lateral boundary conditions that drive the model. This may be particularly

true for eastern China, where the Tibetan Plateau is somewhat unavoidably placed at the regional model's lateral boundary. Unfortunately, differences between the representations of surface topography in the RCM vs. the GCM can produce spurious weather features inside the regional model domain (Leung et al., 1999). As a result of these and other unresolved problems with physical parameterizations and lateral boundary condition errors, downscaling AOGCM output using a dynamical RCM is far from a panacea for the lack of regional-scale skill in relatively course global models.

Ideally, this regional modeling study would be conducted using several different global models, each run with a number of ensemble members. Several studies have shown that the use of multiple ensemble members effectively increases the volcanic-climate signal-to-noise ratio, particularly when regional effects are considered (Stenchikov et al., 2002; Shindell et al., 2003; Shindell et al., 2004; Stenchikov et al., 2006). Furthermore, since hydroclimate in East Asia is notoriously variable (Fu et al., 2005) ensemble simulations would have been particularly desirable for this study. Additionally, RCM intercomparison analyses have shown that regional-scale noise can be further reduced through the use of multiple AOGCMs providing a range of boundary conditions in a given region (Déqué et al., 2005). More specifically, results from the European PRUDENCE project illustrated that relatively minor differences were observed when comparing simulations from a several different RCMs that were driven by identical boundary conditions from a single global AOGCM. On the other hand, the biggest differences between RCM simulations occurred when multiple AOGCMs were used to provide boundary conditions for a single regional model (Déqué et al., 2005).

Table 3.1. Classification, description and rough calibration of drought vs. flood grades in the DI index from historical data at each site (adapted from Wang and Wang, 1994; Song, 2000).

Grades	Classification	Description	Percentage total rainfall anomaly	Occurrence of grade
1	Severe Flood	Extremely wet, long-lasting/ intense precipitation over large areas	=50%	5 - 15%
2	Flood	Wet, single season moderate lasting precipitation locally	=25%, <50%	20 - 35%
3	Normal	Normal, good harvest, no record of flood or drought	=-25%, <25%	25 - 50%
4	Drought	Dry, single season moderate drought locally	=-50%, <-25%	20 - 35%
5	Severe Drought	Extremely dry, long-lasting severe drought over large areas	=-50%	5 - 15%

Table 3.2 Seasonally averaged adjusted MAT anomalies (Chenoweth, 2000) from individual observations within all four grid cells in the South China Sea region (0 – 20°N), expressed relative to average seasonal MAT anomalies during the period from 1820 - 1825. See text for more details. The total number of measurements associated with each individual seasonal mean is listed in the columns on the right.

	Adjusted MAT anomalies (°C)				Total number of measurements			
YEAR	DJF	MAM	JJA	SON	DJF	MAM	JJA	SON
1808		-1.71	-0.55	-0.14	0	43	11	41
1809		-1.38	-1.32	-0.87	0	25	21	54
1810		-2.12		-0.07	0	32	0	81
1811	0.56	0.26	0.76	-0.11	13	46	13	21
1812	-1.63	-0.25	-1.14	-0.33	7	31	21	21
1813	-0.97		-0.23	-0.60	24	0	50	61
1814		-0.26	-0.75	-0.65	0	63	27	34
1815	-0.38		-0.70	-0.92	27	0	70	119
1816	-2.32	-0.74	-1.14	-1.71	65	60	81	98
1817	-1.03	-1.73	-0.45	-0.88	46	24	83	72
1818	0.49	-0.51	-0.45	-0.63	29	22	55	34
1819	-0.85	0.32	-1.41	-1.16	33	12	23	59
1820	0.62		-0.57	-0.90	39	0	43	63
1821	-0.40	1.11	-0.34	0.08	35	38	22	56
1822	0.53	0.28	-0.17	-0.55	10	32	80	48
1823	-0.61		0.33	0.04	31	0	35	40
1824	0.10			0.41	52	0	0	87
1825	0.00		0.28	-0.25	34	0	12	32
1826	-1.81	0.57		-0.81	7	14	0	24
1827	-0.92	-1.38	-0.86	-0.80	8	13	14	14

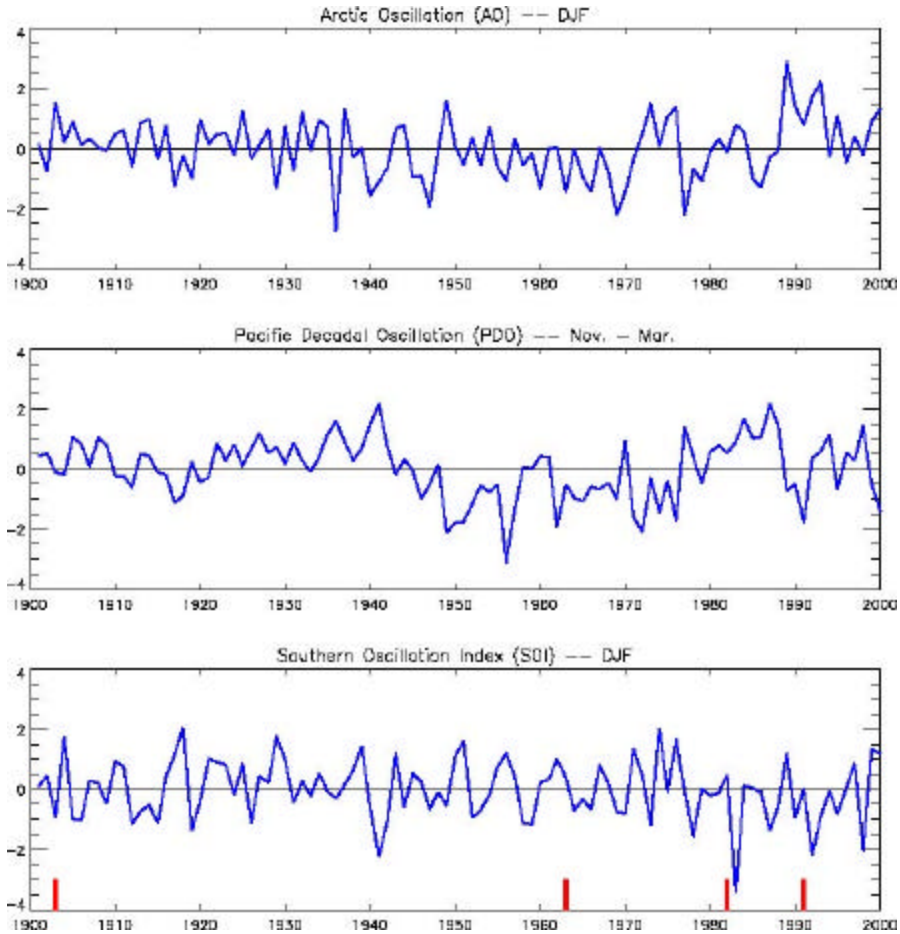

Figure 3.1. Time-series illustrating interannual variability in the observed standardized winter-averaged Arctic Oscillation (AO) (top, Dec. – Feb.), Pacific Decadal Oscillation (PDO) (middle, Nov. – Mar.), and Southern Oscillation Index (SOI) (bottom, Dec. – Feb.) from 1900 to 2000 AD. For reference, the timing of the Santa Maria (1902), Agung (1963), El Chichón (1982) and Pinatubo (1992) eruptions is marked by red vertical bars in the bottom panel.

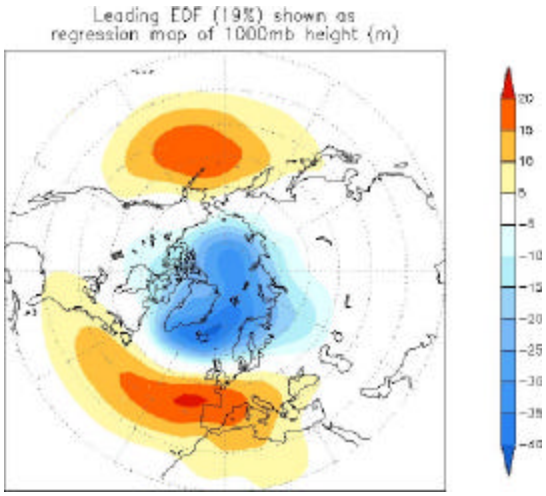

Figure 3.2. Regression map of the AO index on 1000 hPa geopotential height anomalies (units = m) north of 20°N (1979 – 2000). Image created by the Climate Prediction Center: http://www.cpc.noaa.gov .

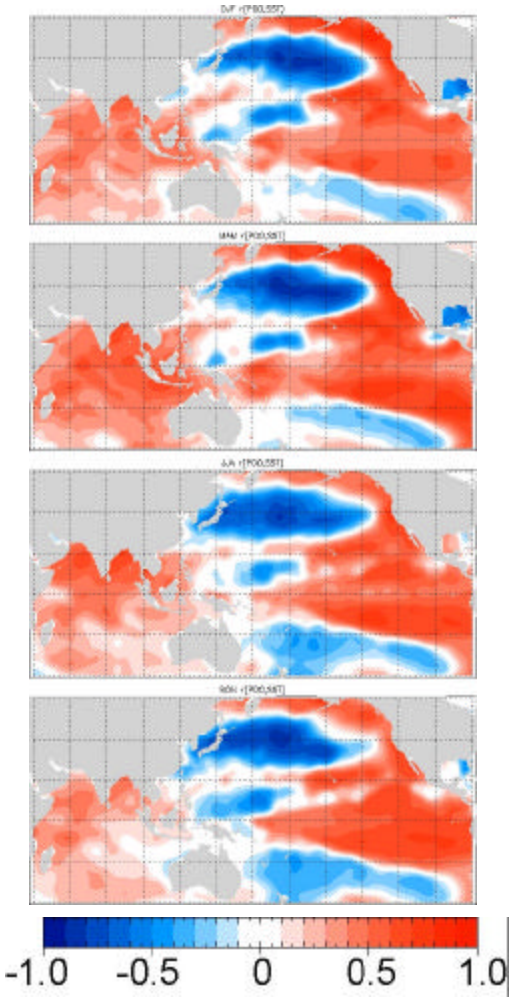

Figure 3.3. The seasonally averaged PDO indices correlated with respect to observed (NOAA-ER) SST anomalies (1900 – 2003). Rows represent the seasons, from top to bottom respectively: DJF, MAM, JJA, and SON.

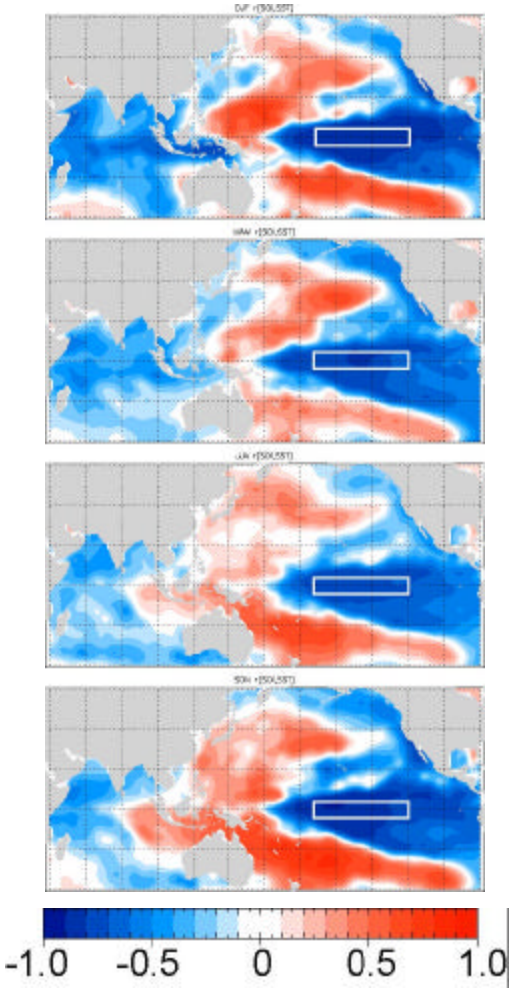

Figure 3.4. Similar to Figure 3.3, except that seasonally averaged SSTs are correlated with respect to seasonably averaged SOI values. The white boxes delineate the NINO 3.4 region (5°N–5°S, 170°–120°W).

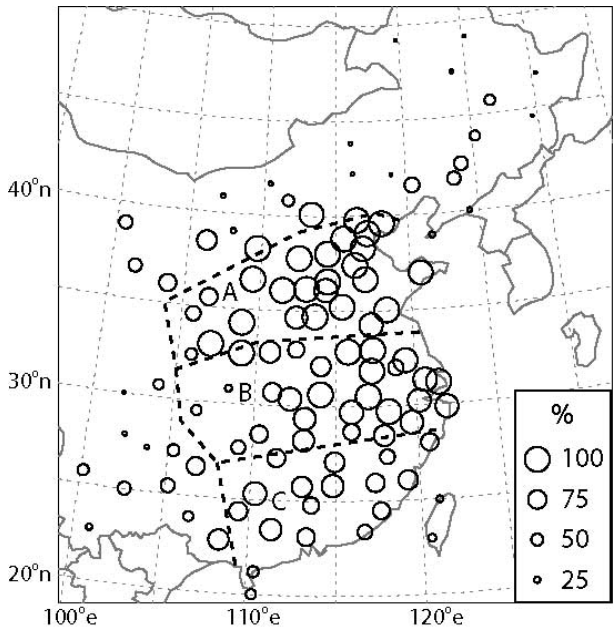

Figure 3.5. Circles show the locations for which DI data are available from the Central Meteorological Bureau (1981). In percentage units, the diameter of each circle corresponds to the completeness of the record from 1470 – 1979 AD. Bold dashed lines delineate regions defined by Wang (1988) as the (A) lower Yellow River, (B) lower Yangtze River and, (C) south China. Data from locations within A, B and C were used to develop the Wang (1988) Indices, from 950 – 1999 AD (Qian et al., 2003a).

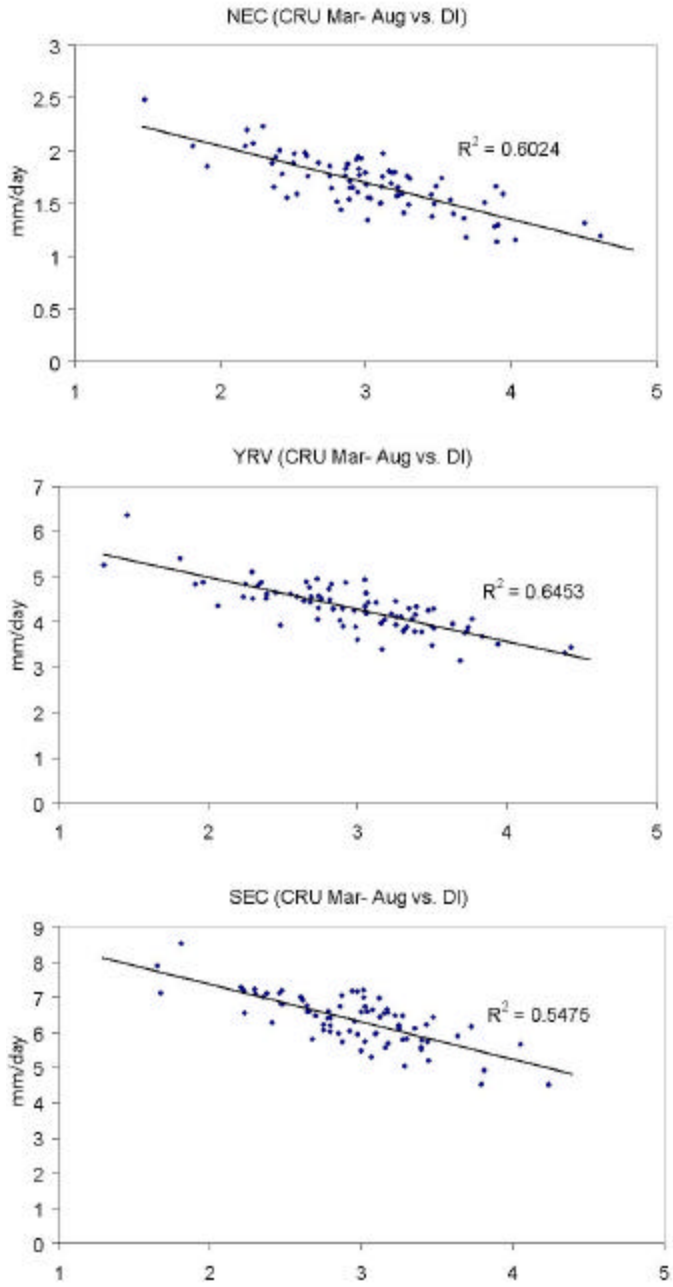

Figure 3.6. Scatter plots illustrate interannual correlations between March – August CRU precipitation (y-axis) and annual DI values (x-axis, 1902 – 1979 AD) averaged across three regions in eastern China (105 - 122°E), from top to bottom: northeastern China (NEC) (21 - 27°N), Yangtze River Valley (YRV) (27 - 35°N), and southeastern China (SEC) (35 - 44°N). See Section 4.1.2 and Figure 4.3 for objective regional definitions.

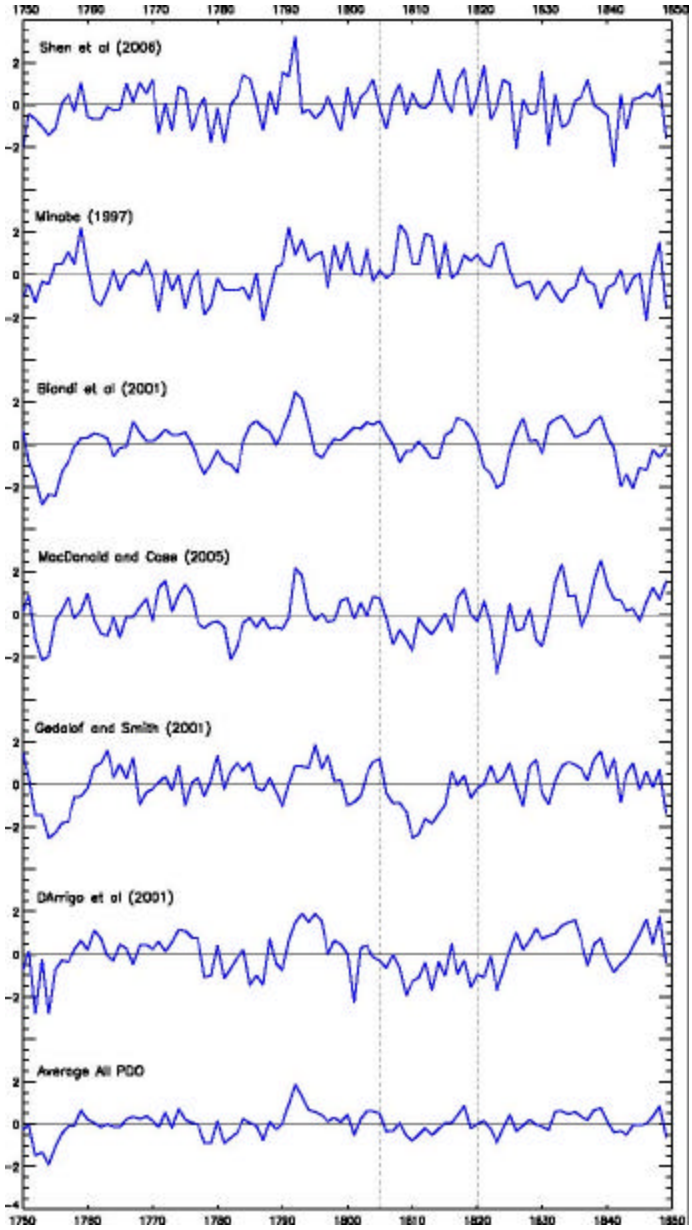

Figure 3.7. Time series of individual PDO index reconstructions, standardized and plotted during the period from 1750 to 1850 AD. The bottom line is an average of all indices shown here. Note that in some cases, general agreement between time series results from reconstructions that are based on identical paleoclimate data. Adapted from Shen et al. (2006).

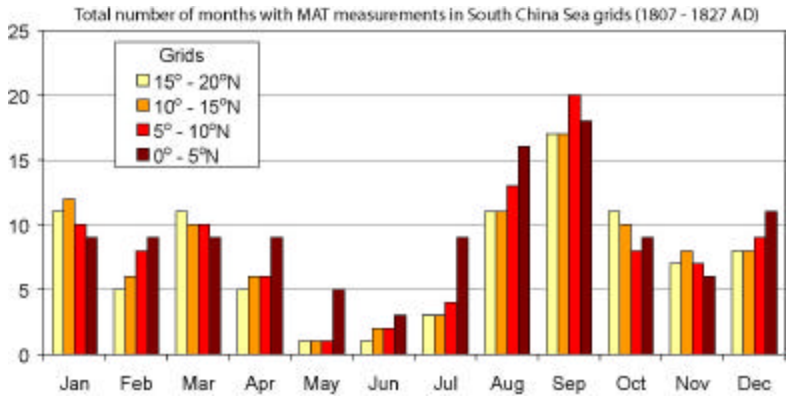

Figure 3.8. Histogram plot counts the total number of months within each grid containing at least one MAT measurement during the period from 1807 – 1827 (Chenoweth, 2000). Data were available from four grids within the South China Sea (see inset key), each spanning the full width of the basin.

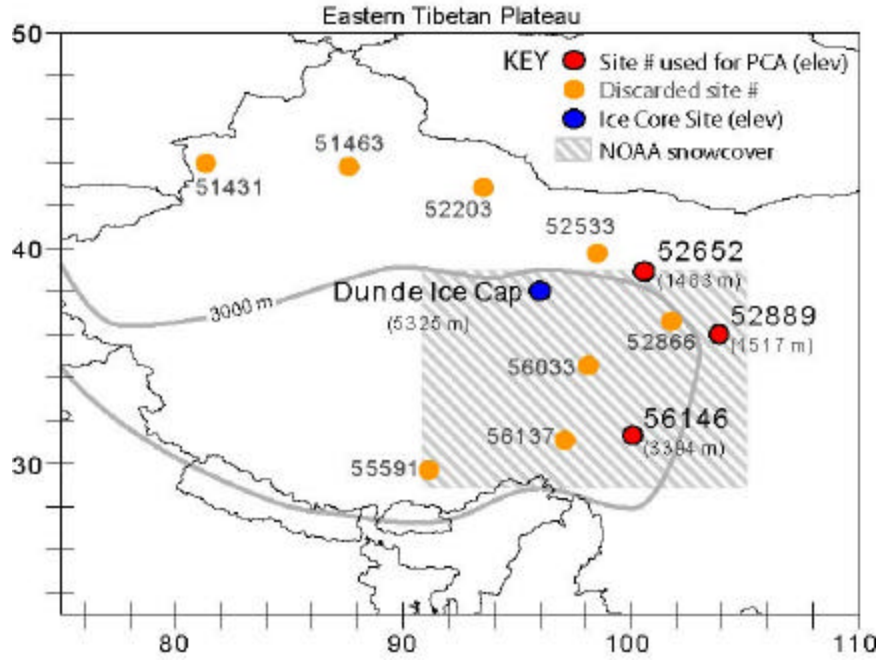

Figure 3.9. Tibetan Plateau regional reference map for snowcover analyses showing the locations of relevant climate observation stations and gridded NOAA satellite data. Records from sites marked by red circles were used for the purpose of validating the Dunde Ice Cap A_n record (Davis et al., 2005). Reference numbers correspond to stations in the Chinese instrumental climatic database. The Plateau itself is roughly outlined by the 3000 m contour line. Also, elevations at select climate stations as well as the Dunde Ice cap are included in parentheses (in meters above sea level). X- and y-axes respectively correspond to degrees longitude (east) and latitude (north).

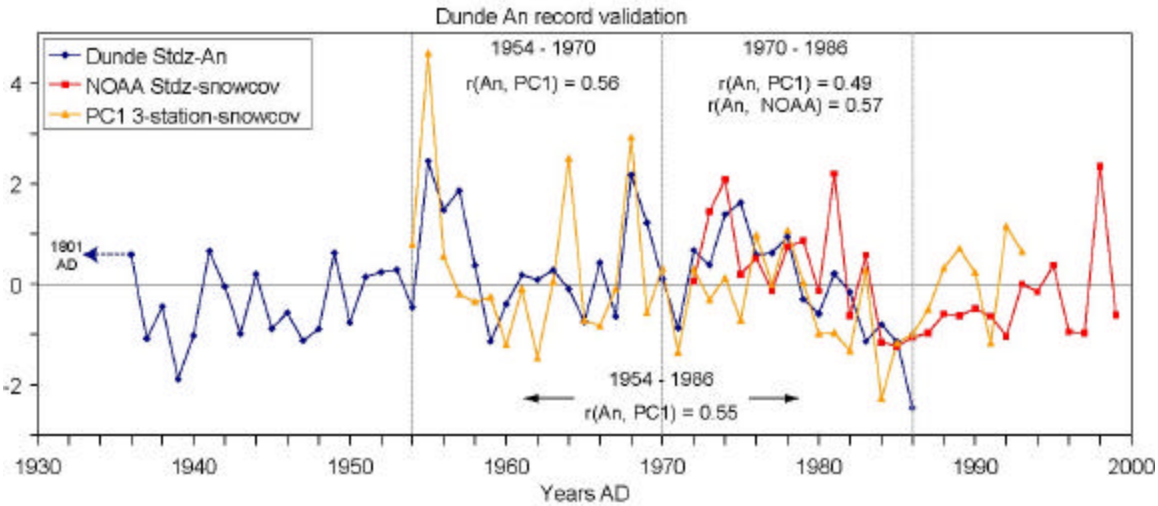

Figure 3.10. Record validation for the Dunde A_n record (shown here in standardized units) during the period of overlap with available observations. Comparisons between A_n and PC1-snow (the first principal component of snow cover observations from three stations on the eastern edge of the Tibetan plateau) are made during two 17-year eras: from 1954 – 1970 and 1970 – 1986 (separated by vertical dashed lines), and also over the entire period of overlapping record, from 1954 – 1986. Standardized average NOAA satellite data for snowcover are also compared with A_n from 1972 – 1986. Correlation r-values with respect to A_n during these different eras are shown as well (all are significant at the 95% level).

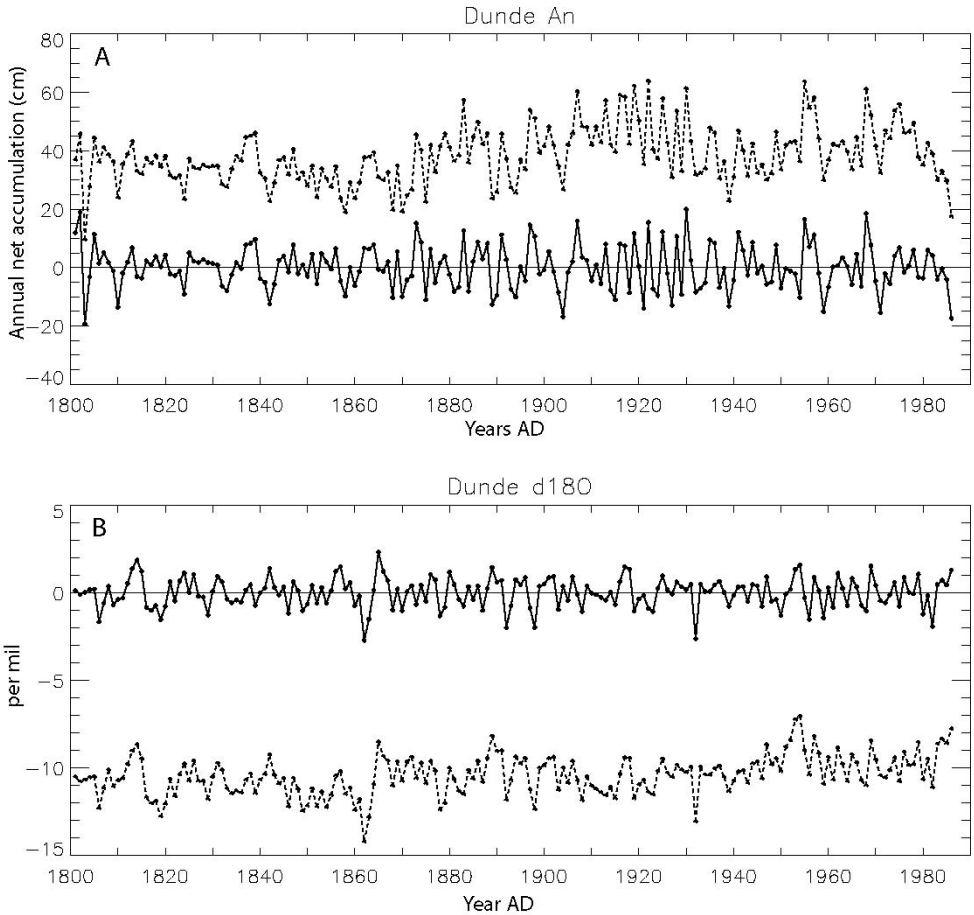

Figure 3.11. Average annual a) net accumulation (An) from two ice cores (water equivalent, expressed in cm units) and b) d18O from a single core collected from the Dunde Ice Cap. Time series shown here represent raw data (dashed) (Davis et al., 2005) and Lanczos filtered data with the long-term linear trend removed and low-frequency variations with periods greater than 15 years also removed (solid).

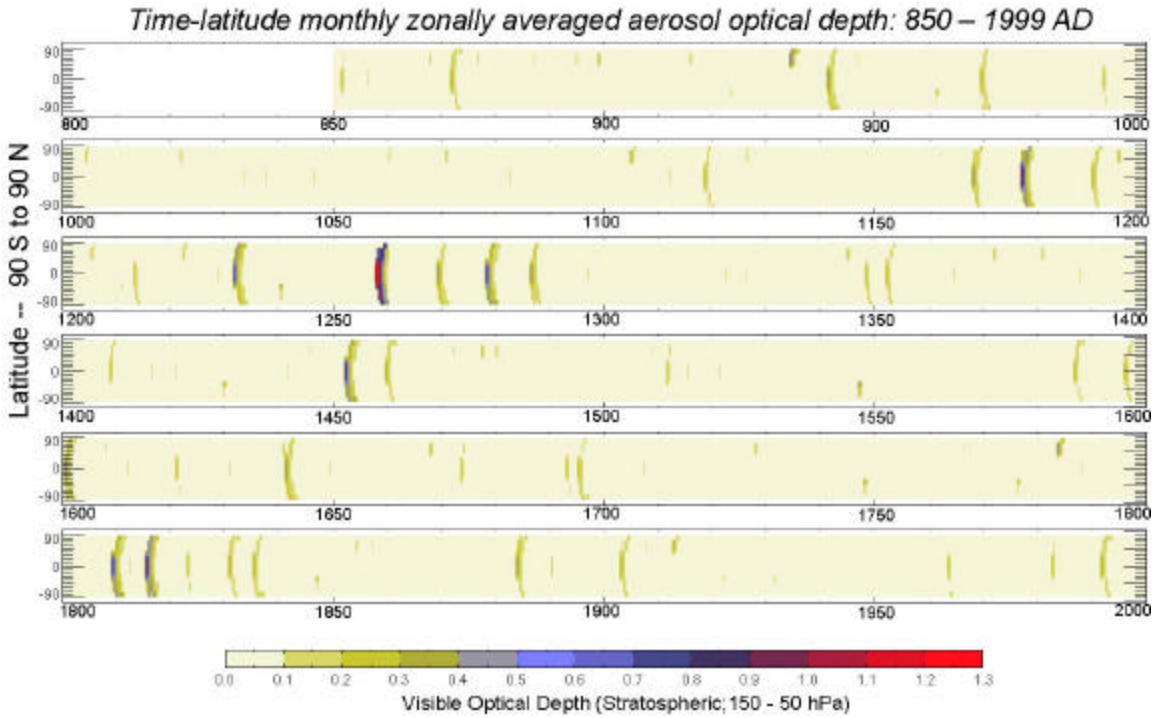

Figure 3.12. Hovmoller diagram of historical optical depth forcing at monthly temporal resolution (x-axis = years AD) and 3.71° spatial resolution (y-axis = degrees latitude) in the meridional dimension only (Ammann et al., 2006). Data shown here were used as volcanic forcing for both CSM1.4 and ReCM simulations. The same data were also used to identify significant tropical (24°N – 24°S) volcanic eruptions for composite analyses (see section 5.2.1).

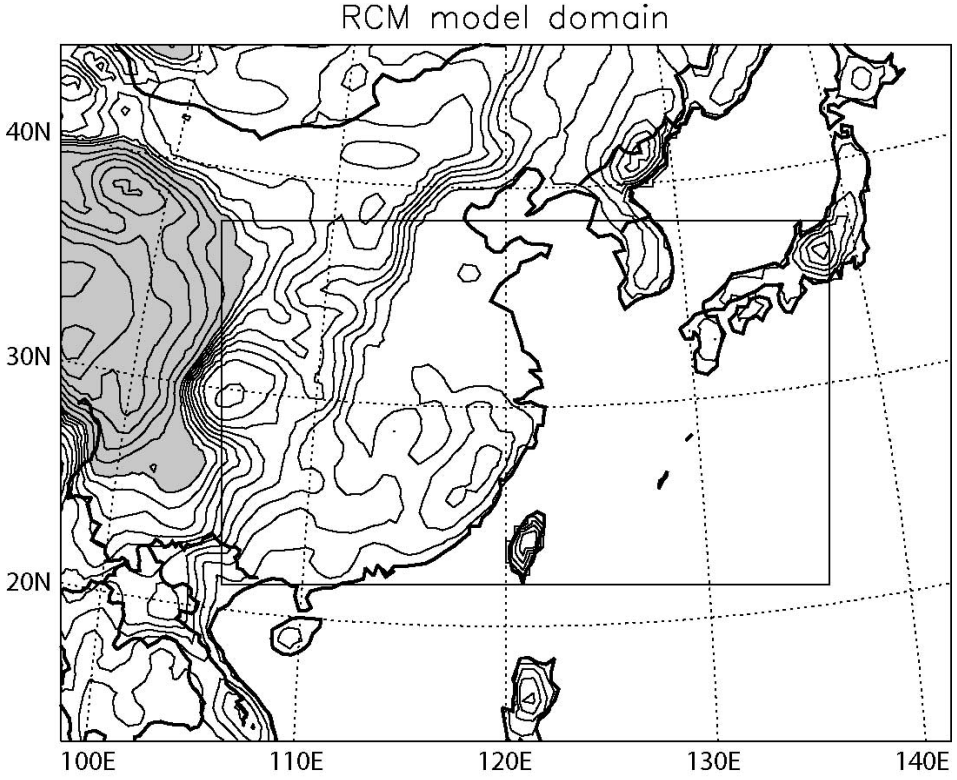

Figure 3.13. The entire region shown here represents the model domain for the SUNYA ReCM used in this study. The region between the outer margin of the plot and the inner box is the buffer-zone, where boundary conditions from the global model are relaxed. Model land surface elevation is illustrated by contour lines at 200m intervals, except over 2,000m (shaded regions), where contour intervals are 500m.

CHAPTER 4

DIAGNOSTICS AND ANALYSIS FRAMEWORK

As noted in the introduction, the primary objectives of this dissertation can be roughly separated into three main parts: 1) to identify the impact of major volcanic eruptions on hydroclimate in eastern China and explore possible dynamic mechanisms for this regional response, 2) to assess regional biases in the global and regional models and, 3) to compare the observed and modeled climatic response to major volcanic eruptions as a means to better understanding the hypotheses put forth in part one.

Achieving this study's objectives are predicated on a basic understanding of East Asian monsoon (EAM) climate through the available datasets that provide insight into this dynamic system. Furthermore, before climate models can provide any practical use, their simulations must first be compared with independent climate observations, to understand the strengths and weaknesses of each model. Thus, Chapter 4 provides a framework for subsequent observational and model-based analyses of the EAM system.

4.1. The context for climate in eastern China

This section is intended to more intimately familiarize the reader with the boundary conditions and geographical context for climate in eastern China. As general references, Figures 4.1 and 4.2 display several surface and upper-air variables, seasonally averaged and plotted over the greater East Asian region. Collectively, these plots illustrate most of the diagnostic variables that previous studies have shown to be important controls on surface hydroclimate change and variability in eastern China.

Noteworthy features in Figure 4.1 include the Tibetan plateau, which is much colder and generally drier than surrounding regions throughout the year. Also, note the Siberian high, which dominates the sea level pressure (SLP) field (Figure 4.1b) over the Asian continent throughout the winter season. Contrast this with summer SLP conditions, when a heat low presides over most of eastern Asia. These pressure fields are, of course, closely associated with the winter and summer monsoons. Precipitation plots (Figure 4.1c) illustrate that the majority of annual rainfall across Asia occurs in summer in the vicinity of these surface pressure lows. Average SSTs over the Pacific and Indian Oceans are shown in Figure 4.1d. Here, the West Pacific warm pool is a prominent feature, along with the relatively steep west-east temperature gradient between the warm pool and the cold tongue in the eastern equatorial Pacific. The influence of the Kuroshio western boundary current on regional mean SSTs is also apparent to the east of Taiwan and south of Japan.

At upper-levels, Figure 4.2a shows 500 hPa GPHs, illustrating a couple of notable features. First, a pressure trough is apparent during all seasons along the East Asian continental boundary. Also, the tight north-south mid-tropospheric pressure gradient in the vicinity of the trough is particularly striking during non-summer seasons. During summer, this meridional gradient is weakened and relatively weak upper-level westerlies prevail, while the West Pacific subtropical high (WPSH) pressure system becomes well defined to the southeast of China. The WPSH is a critical feature and is highlighted in the JJA panel only with an extra (bold) contour line at 5870 m. The prominent westerly jet is very clear in 200 hPa zonal-wind fields throughout the year, with easterlies prevailing in the south (Figure 4.2b). The 850 hPa wind vectors show a few prominent

lower-level jets and represent a critical index for the majority of atmospheric moisture transport (Figure 4.2c). For example, the summer panel shows a prominent westerly jet over India and the Indochina peninsula, plus the southwesterly flow of air into eastern China from the Bay of Bengal and, most importantly, the SCS. The northward redirection of the low-level westerly jet in the vicinity of the SCS is associated with the development of the aforementioned WPSH, as clockwise motion around the latter feature facilitates the advection of moisture into eastern China during the summer monsoon season.

Vertical velocity, at 500 hPa, is also shown to illustrate the general regions of ascending and descending air, contrasting the seasonal prevalence of convection vs. subsiding air masses and regional manifestations of Hadley circulation (Figure 4.2d). For example, during winter and spring tropical convection along the inter-tropical convergence zone (ITCZ; near the equator) is offset by subsiding air in the subtropics (~20°N) illustrating well the Hadley circulation cell (also notice the close correspondence between spatial patterns of vertical velocity and precipitation in lower latitude regions). However, the Asian monsoons clearly disrupt this classical conceptual model of Hadley circulation during the summer season, when extensive convection predominates for months over subtropical and extratropical land areas.

4.1.1. Precipitation dataset intercomparison

To validate observational data and consider long-term secular trends in regional hydroclimate, Figure 4.3 plots 12-panels of regionally averaged (unstandardized) precipitation in NEC, YRV, and SEC during all seasons [December - February (DJF),

March – May (MAM), June – August (JJA), September – November (SON)] from 1960 to 2001. As described in the figure caption, data from 4 different commonly used sources are displayed: GHCN, CRU, CMAP, and GPCP. For the most part there is good agreement between these various datasets when gridded and station data are averaged over broad regions. Yet, there are some notable exceptions, particularly in summer (JJA).

In the north, there is a fairly consistent dry bias to the CRU data, relative to GHCN, however these datasets are nearly identical in terms of variability, which is of primary interest to the present study. In the central eastern China region, there is very good agreement between all datasets prior to 1993, when the CRU (blue) time series diverges significantly from the CMAP and GPCP – satellite-based – time series. Still, all datasets consistently indicate a positive trend in YRV precipitation between the late 1970s and 2001, in agreement with the published literature (Gong and Ho, 2002; Wu et al., 2006). In the south, there is an apparent dry bias in the GHCN time series, relative to the other three datasets, however, again, interannual variability is quite comparable with respect all data sources.

4.1.2. Sub-regional precipitation definitions

To identify regions in eastern China (20° – 45°N, 105° - 123°E) with spatially coherent modes of summer (JJA) precipitation variability, principal component analyses (PCA) were applied separately to the correlation matrices of CMAP (1979 – 2001 AD) and GHCN station data (1961 – 1990 AD). Spatial loading patterns of the first PC of CMAP and GHCN precipitation – respectively explaining 22% and 16% of overall

regional variance – reveals three distinct zonal regions of covariability (Figure 4.4). These results are consistent with previous work in this region, where interannual precipitation patterns across eastern China are commonly partitioned zonally (e.g., Samel et al., 1999; Chang et al., 2000a,b; Liang et al., 2002). These results are also apparently insensitive to the period of analysis and even the time-scale of variability, as similar results have been found when examining regional interannual variations in flood-drought records over the past millennium (Zhu and Wang, 2001; Zhu and Wang, 2002; Qian et al., 2003).

Having objectively identified three regions with relatively coherent patterns of covariability, indices for regional rainfall are created by averaging standardized mean JJA precipitation from all grid-points (or stations) within each of the boxed regions (Figure 4.4). Thus, there is equal weight given to each grid-point, regardless of average summer precipitation at that location. These three indices of *observed* precipitation will hereafter be referred to, from north to south respectively, as northeast China (NECo), Yangtze River Valley (YRVo) and southeast China (SECo). Time series of precipitation in each of these regions are useful for exploring their statistical relationships with both local and remote SSTs and atmospheric circulation patterns, to reach a better understanding of what synoptic- to global-scale processes control interannual hydroclimatic variability in eastern China.

4.1.3. "Wet minus dry" maps

Previous studies have noted that warm season hydroclimate variability in E. China is strongly influenced by the lower-level tropical westerly jet, the West Pacific

subtropical high (WPSH) and the upper-level subtropical westerly jet (Wang et al., 2000; Chang et al., 2000a). Each of these atmospheric boundary conditions can be represented by 850 hPa winds (Figure 4.2c), 500 hPa GPHs (Figure 4.2a) and 200 hPa zonal winds (Figure 4.2b), respectively. As a way of demonstrating the relative hydroclimatic importance of each of these diagnostic variables, wind and GPH anomalies are computed by subtracting the average values during dry years from average values during wet years. Composite plots produced through this analysis are called "wet-minus-dry" maps (Chang et al., 2000a).

Wet-minus-dry maps are created based on the standardized regionally averaged time series of CMAP precipitation described in the previous section (NECo, YRVo and SECo; Figure 4.4). First, each of these time series are ranked to identify the wettest (top 25th percentile) and the driest (bottom 25th percentile) summers during the period from 1979 -2001 AD. Then, wet-minus-dry maps are generated for standardized values of precipitation and three key diagnostic variables by plotting the differences between each of these fields during the corresponding wettest and driest summers. Note that the same analysis was conducted using GHCN station data (from 1960 – 1990), yielding similar results, particularly over the YRV (not shown). Also, a somewhat complementary analysis is conducted below (section 4.3.1) where regionally averaged time series based on GHCN data are correlated with respect to global-scale 500 hPa gph. It should be noted that the satellite data were selected for this particular analysis so that wet-minus-dry precipitation patterns could be plotted over land and ocean regions, which is more directly comparable with model output (Chapter 6).

Results from wet-minus-dry map analyses are shown in Figures 4.5 – 4.7, including differences between standardized precipitation, 500 hPa GPH contours (with differences greater than one standard deviation shaded in grey), 200 hPa zonal winds, and 850 hPa wind vectors. In Figure 4.5, wet vs. dry summers in SEC are shown to be generally associated with drier conditions over central China, a diminished WPSH at 500 hPa, a weakened subtropical westerly jet at 200 hPa and weakened southerly lower-level winds, at 850 hPa. Also, at 500 hPa, a significant positive pressure anomaly is centered over Lake Baikal and the Okhotsk High is notably weakened (Figure 4.5b).

Figure 4.6, on the other hand, shows that wet vs. dry summers in the YRV region occur under conditions nearly opposite to those reflected by Figure 4.5. For instance, wet summers in the YRV occur when the subtropical jet is significantly enhanced at ~35°N, the WPSH is significantly stronger – particularly at 20°N and 120°E – and shifted west, while the associated 850 hPa southerly jet is enhanced, delivering moisture from the SCS to central eastern China. The Okhostk High is also strengthened, which has been noted to sharpen the Mei-Yu front temperature gradient (Samel et al., 1999) and stall the typical northward progression of the eastern China summer rainband, causing prolonged rainfall and flooding in the YRV (Wang, Y. et al., 2003).

In comparison with SEC and YRV, precipitation variability over northeastern China does not always appear to be driven by a consistent pattern; wet-minus-dry 500 hPa GPH differences barely exceed one standard deviation (Figure 4.7b). Still, consistent with results from Samel et al. (1999), a northwestward expansion of the WPSH at 500 hPa and slightly increased southerly 850 hPa winds in the vicinity of eastern China are apparently associated with greater precipitation in the north (Figure 4.7c).

4.2. Regional-scale monsoon indices

This section introduces a set of regional-scale monsoon indices, describes how they are defined and discusses their significance with respect to surface climate variability in eastern China. While several of these climate indices were originally derived for the purpose of studying the summer monsoon only, here the indices are defined for all months of the year to provide a basis for also considering the seasonal cycle of synoptic-scale atmospheric circulation. These indices have three primary uses in the context of this study. First, indices derived from observations are compared with those derived from CSM output as a way of testing global model skill with respect to the intraseasonal evolution of key components of EAM system (Chapter 6). Second, assessing model skill on this spatial scale, with regard to these particular variables, is considered particularly useful for assessing how well the CSM may provide realistic boundary conditions for the subsequent RCM simulations. Finally, and perhaps most importantly for the overall purpose of this study, these indices provide a simple and objective set of tools for exploring possible mechanisms for a dynamic synoptic-scale climatic response to tropical volcanic eruptions during all months of the year (Chapters 5 and 6).

Unless otherwise noted, each of the indices discussed in this section were derived from NCEP reanalysis data. For the sake of clarity, Table 4.1 provides a summary of the index calculation methodologies, while Figures 4.8 and 4.9 delineate the regions within which data were used to derive the indices. As a way of visually illustrating the regional climatic significance of each monsoon index, seasonal mean (DJF and JJA) time series plots are provided along with their spatial correlation patterns with respect to CRU

precipitation and temperature throughout eastern Asia (Figures 4.10 – 4.15). Note that DJF precipitation correlation patterns in northern China are relatively less meaningful, since very little precipitation falls in the north during winter. Also, Figure 4.16 shows monthly climatologies for each of the indices over the average annual cycle (1961 – 1990).

Interrelationships between the regional indices r(x,y) are also shown during the winter (DJF) and summer (JJA) seasons. Table 4.2 displays the JJA correlation values for the period from 1948 – 2002, while the stationarity of these interrelationships are assessed by conducting the same correlation analyses separately from 1948 to 1976 (Table 4.3) and from 1977 to 2002 (Table 4.4). Similarly, Table 4.5 presents DJF correlation values for the period from 1948 – 2002. For reference, these tables also include global-scale climate indices (e.g., AO, SOI & PDO), in addition to indices for regionally averaged rainfall in eastern China (NECo, YRVo, SECo). Thus, these tables provide a useful reference for gauging the statistical significance of spatial correlation patterns between regional precipitation and the various indices (Figures 4.10 – 4.15). To highlight interrelationships on interannual time-scales, note that long-term linear trends were first removed from each time series before calculating the correlation values displayed in these tables.

4.2.1. The West Pacific subtropical high zonal index

One of the most commonly referenced monsoon components is the West Pacific subtropical high (WPSH), which previous studies have indexed according to its overall intensity as well as its zonal and meridional displacement (Huang and Wang, 1985; Riyu,

2002; Wang et al., 2002; Wang, Y. et al., 2003). As noted in the previous section, interannual variability in the strength of the WPSH is closely linked to the strength of northward moisture transport from the SCS and, thus, to variations in precipitation throughout eastern China. Following the recommendations of Riyu (2002), the index used for this study captures the zonal (east to west) displacement of the WPSH and will hereafter be referred to as "WPSHz." The WPSHz is computed by averaging monthly GPHs at 850 hPa in the region 110° – 150°E, 10° – 30°N (Figure 4.10). More positive index values reflect higher pressure levels at 850 hPa and as well as a westward displacement of the WPSH in this region.

While some previous studies have derived WPSH indices from GPHs at 500 hPa, Riyu (2002) demonstrates that 850 hPa is a well suited atmospheric level at which to characterize this feature for several reasons. For example, at 850 hPa, the WPSH is more intense and stable, as well as being more directly associated with the low-level jet that transports large amounts of water vapor into the region. Also, Riyu (2002) found that WPSH indices from 850 hPa correlate more strongly with precipitation in E. China than do indices from other levels in the atmosphere. As a simple quality check, the Wang et al. (2002) WPSH intensity index was also computed (at 500 hPa) and was found to correlate significantly with the WPSHz index used here (not shown). Spatial correlation patterns between the WPSHz index and JJA precipitation (Figure 4.10) confirm results from wet-minus-dry map analyses, where precipitation over the YRV varies in phase – while precipitation in SEC, to a lesser degree, varies out of phase – with the WPSHz.

Summer precipitation over the YRV has been increasing for several decades (Li et al., 2004; Yang and Lau, 2004; Wu et al., 2006) and Figure 4.10 shows that the JJA

WPSHz index shows a concurrent and, perhaps, related upward trend (Gong and Ho, 2002). Upward trends in regional SSTs in the West Pacific warm pool and the Indian Ocean appear to also be related (Yang and Lau, 2004). Furthermore, correlation analyses (Table 4.2 – 4.4) confirm results from Gong and Ho (2002), that positive WPSHz anomalies in summer typically occur following negative SOI anomalies (El Niño conditions) during the previous winter ("SOI- DJF"), with no apparent relationship at zero-lag in summer. Also, during NH winter, a strong zero-lag teleconnection exists between these two variables (Table 4.5). However, as illustrated to some degree by correlation values in Tables 4.3 and 4.4 and discussed in Chapter 2 – as well as later in this chapter – ENSO-Asian monsoon teleconnections and are not entirely stationary through time and appear to have changed in conjunction with the North Pacific climate regime shift in the late 1970s (Trenberth and Hurrell, 1994; Trenberth and Caron, 2000). Additionally, the upward trend in the summer WPSHz index is apparently not linear; rather, most of the WPSH increase seems to have occurred step-wise in the late 1970s (Figure 4.10), coincidentally with the Pacific climate regime shift (Trenberth and Caron, 2000).

4.2.2. The Okhotsk high index

Compared to the WPSH, the Okhotsk high is a relatively impermanent blocking anti-cyclone, so-named for its frequent occurrence in summer over the Okhotsk Sea, adjacent to the northwest Pacific Ocean. Several previous studies have noted its importance to hydroclimate in eastern China (Samel et al., 1999; Wang, Y. et al., 2003); its statistical significance in relation to JJA rainfall is illustrated by SECo and YRVo wet-

minus-dry maps (Figures 4.5 and 4.6). Because of the relatively remote location of the Okhotsk high, its behavior is not considered to be a deterministic factor governing East Asian summer monsoon variability, but a strengthened Okhotsk high has been shown to contribute to summer flooding in the YRV (Samel and Liang, 2003). Following the methods of Wang, Y. et al., (2003), the Okhotsk high index (OKHI) was computed by averaging monthly GPHs at 500 hPa in the region 135° – 145°E, 55° – 70°N (Figure 4.8). More positive index values reflect higher pressure levels at 500 hPa over the region northwest of the Okhotsk Sea.

A clear long-term secular trend in the JJA OKHI is not apparent from Figure 4.11, however there does seem to be a rise in regional pressure levels through recent decades. The spatial patterns of correlations between the OKHI and regional summer precipitation indicates that YRV precipitation generally varies in phase – and SEC varies out of phase – with pressure levels over the Okhotsk Sea. Also, note that the zonal structure to the correlation pattern in Figure 4.11 (center-right panel) is very similar to the pattern observed with respect to the WPSHz (Figure 4.10); not surprisingly, the JJA WPSHz index and the OKHI are significantly correlated from 1948 – 2002 (Table 4.2; r-value = 0.36; p-value = 0.01).

4.2.3. The western North Pacific monsoon index

The western North Pacific monsoon index (WNPMI) characterizes the dominant mode of lower-level wind anomalies over the East Asian monsoon domain (Wang et al. 2001; Wu and Wang, 2002). The WNPMI has been used by other studies to characterize the intraseasonal monsoon cycle as well as the strength of the winter monsoon (Wang et

al., 2004; Zhu et al., 2005; Wu and Chan, 2005). The WNPMI is computed by subtracting 850 hPa zonal wind anomalies in the region 110° – 140 °E, 20° – 30 °N from the same variable in the region 100° – 130°E, 5° – 15 °N (Wang et al., 2001; Figure 4.8). Keeping in mind that westerly winds are positive, the sign of this index reverses from winter to summer (Figure 4.16), largely reflecting a late spring reversal of the lower-level jet over the SCS and Indochina peninsula. Thus, more positive index values correspond with a relative strengthening of this westerly jet over the SCS and a weakening of 850 hPa winds in the vicinity of Taiwan.

The significance of 850 hPa winds, in terms of controlling summer precipitation in eastern China, is discussed above and is apparent from the wet-minus-dry maps (Figures 4.5, 4.6, and 4.7). For example, the YRVo wet-minus-dry maps show that 850 hPa winds in the WNPMI regions (Figure 4.8) are intimately tied to the relative strength of the WPSH, where positive GPH anomalies centered over Taiwan are accompanied by a clockwise pattern of lower-level wind anomalies around the western edge of the subtropical high (Figure 4.6) and visa versa (Figure 4.7). Hence, it is not surprising that the summer WNPMI and WPSHz indices are inversely correlated with high statistical significance, particularly from 1977 – 2002 (Table 4.2 and 4.4). In summary, the JJA precipitation correlation plot (Figure 4.12) shows that a stronger low-level westerly jet over the SCS and a weaker jet to the north (more positive WNPMI value) is related to a weakening of northward moisture transport over eastern China and resulting drier conditions in the YRV and NEC regions.

4.2.4. The summer monsoon index

The summer monsoon index (SMI) quantifies the east-west surface pressure gradient between the East Asian continent and the western North Pacific Ocean and, thus, provides another measure of the winter and summer monsoons (Wu and Chan, 2005). The SMI is also routinely employed by the National Climatic Center (NCC) of China as a metric for the strength of the summer monsoon (Wu and Chan, 2005). The SMI is computed monthly by subtracting average SLP in the region 160°E, 20° – 50°N from average SLP in the region 110°E, 20° – 50°N (Figure 4.8). Both NCEP reanalysis and Trenberth and Paolino (1980) SLP datasets were used to derive the index. Concerns regarding the quality of SLP data in the NCEP reanalysis dataset have been raised in several previous studies (e.g., Trenberth and Caron, 2000; Smith et al., 2001; Wu and Chan, 2005). Time series plots illustrating secular changes in both summer monsoon indices during DJF and JJA SMI, from 1948 – 2003 (Figure 4.13), suggests that reanalysis SLP data prior to 1966 may be particularly suspect, especially in summer months. Thus, spatial correlation plots in Figure 4.13 are based on the SMI derived from SLP data by Trenberth and Paolino (1980). It is noted, however, that similar correlation patterns are observed when the NCEP reanalysis-based SMI is used, especially when the analysis is limited to the period from 1966 – 2003. Also, with the exception of apparent biases in the early decades of the NCEP reanalysis SLP data, there is very good agreement between the two JJA SMIs on interannual time scales.

The SMI reverses sign from winter to summer (Figure 4.16), which is largely driven by the development of the semi-permanent Siberian High in winter, which dominates lower tropospheric pressure fields over the Asian continent throughout the

cold season (Zhang et al., 1997; Gong and Wang, 2003). Also, sensible heating over the continent during warm-season months contributes to a surface pressure low over eastern Asia in JJA (Ding, 1994). Thus, the SMI may be considered a *thermodynamic* index for the EAM system, as opposed to most other indices discussed in this section, which are more strictly reflective of *dynamic* EAM characteristics (Wu and Chan, 2005).

The significance of the SMI in terms of regional precipitation is illustrated by Figure 4.13, where positive SMI values are associated with increased JJA precipitation over the YRV, decreased precipitation in NEC and visa versa. Thus, positive SLP anomalies over the northwestern Pacific and relatively negative SLPs over the continent (positive SMI values), in summer, creates an east-west pressure gradient in the lower troposphere that is conducive to the northward advection of tropical moisture from the SCS into eastern China, creating a stronger Mei-Yu front over the YRV (Lim et al., 2002). On the other hand, precipitation in NEC generally peaks in late July (Figure 2.2) when the Mei-Yu front shifts northward. Under these circumstances, negative SLP anomalies to the south and west are conducive to lower-level easterly water vapor advection from the East China Sea and West Pacific Ocean (Lim et al., 2002).

It is also noteworthy that winter temperatures and precipitation throughout East Asia – particularly over the Korean Peninsula and Japan – are significantly inversely correlated with the SMI (Figure 4.13). This most likely reflects the fact that cold-season anomalous high pressure over Siberia (more positive SMI) is associated with increased cold air surges advecting exceptionally cold and dry continental air from Siberia toward to coast (Ding, 1994; Zhang et al., 1997). While the SMI generally displays weak or inconsistent correlations with respect to regional monsoon and rainfall indices during the

summer season (Tables 4.2 – 4.4), the SMI is very well correlated with several of these variables in winter (Table 4.5).

4.2.5. The land sea-surface temperature difference index

The land sea-surface temperature difference (LSTD) regional climate index measures the north-south and east-west thermal contrast between land over eastern China and the adjacent oceans. To calculate the LSTD index, CRU temperature data were used over land areas, while NOAA-ER SST data were used over the oceans. Following the formula in Table 4.1, T_{YRV} and T_{SEC} represent average monthly land temperatures over the YRV (east of 105°E, 27°–35°N) and SEC (east of 105°E, south of 27°N) regions, respectively. Meanwhile, SST_{SCS} and SST_{NWP} represent average monthly SSTs over the SCS (105°–120°E, 5°–18°N) and northwest Pacific (120°–150°E, 15°–30°N) regions, respectively (Figure 4.9). Much like the SMI, the LSTD has been used in the Chinese meteorologic literature as a *thermodynamic* monsoon index (Wu and Chan, 2005). Hence, it is hypothesized to be particularly useful for assessing the impacts of volcanic forcing on boundary conditions in East Asia.

Due to the presence of the West Pacific warm pool, average monthly SSTs are always greater than air temperatures over eastern China and, as a result, the long-term mean monthly LSTD index values are always negative (Figure 4.16). Thus, more positive index values reflect a weaker thermal contrast associated with anomalously warm air temperatures over China and/or below normal regional SSTs. This condition is consistently and strongly associated with below normal JJA precipitation over the YRV and – to a lesser degree – above normal precipitation in the north (Figure 4.14; Tables 4.2

– 4.4). Conversely, when the thermal contrast is greater in JJA (warmer ocean; colder land) then it is generally much wetter over the YRV.

However, before reaching the conclusion that YRV rainfall is, in fact, directly *responsive* to this land-sea thermal contrast it should be noted that JJA precipitation variability is consistently out-of-phase with over-land air temperatures during this season (Figures 4.10 – 4.15). Based on this fact, it is logical to conclude that at least some of the variability in YRV precipitation that is explained by the LSTD index is a simple reflection of the fact that local cooling is generally caused by reduced sensible heating in the presence of abundant rain clouds, and visa versa. So, the LSTD index was also calculated based on the SSTs alone – with the same weights favoring SST_{NWP} (Table 4.1) – and results indicate that at least half of the YRV-LSTD signal is attributable to variability in SSTs, with significant positive correlations (0.3 < r-values < 0.45) between regional SSTs and YRV precipitation (not shown).

4.2.6. The East Asian and global jet strength indices

A jet stream is a relatively fast moving, narrow air current located at the tropopause level that circles the globe horizontally while making some high amplitude meanders along the way. Generally, the jet stream represents the existence of underlying enhanced baroclinicity (e.g., fronts) and potential energy available for cyclone formation. The strength and location of extratropical jets are directly related to upper-level divergence and confluence and have long been dynamically linked to surface cyclogenesis and anti-cyclogenesis (Koch et al., 2006). Figure 4.17a plots the global distribution of JJA zonal winds at 200 hPa, illustrating the predominantly zonal structure

of the Northern Hemisphere subtropical jet between 30° and 50°N. The same figure illustrates jet maxima centered over the eastern U.S., the northern Middle East and Western China, in addition to the well-known spiral-like structures (when viewed from a polar projection, not shown) that originate at lower latitudes over the Pacific and Atlantic Oceans then join the main stream over North America and Europe, respectively.

With consideration of the global zonal structure of volcanic forcing (Chapter 5) and to complement earlier studies (Oort and Yienger, 1996; Liang and Wang, 1998), two new jet indices were developed to explore the impact of volcanic eruptions on the global extra-tropical jet and the East Asian manifestation of the subtropical jet. The global subtropical westerly jet is exceptionally intense and well defined in the East Asia region, where it is associated with the WPSH and JJA precipitation throughout eastern China. Liang and Wang (1998) showed that when the regional jet at 200 hPa is displaced north of its climatological position precipitation increases in northern China; when it moves south, precipitation increases over southern regions. The East Asian jet is a particularly important feature of the Mei-yu front over China and the closely related Baiu front over Japan (Ding, 1994; Wang, W.-C., et al, 2000), which is apparent from the regional coherence and zonal structure of precipitation and upper-level wind differences in YRV wet-minus-dry maps (Figures 4.6a and 4.6c, respectively).

The East Asian jet strength index (EAJSI) measures average maximum zonal winds in the region 110° – 127.5 °E, 10° – 50°N (Figure 4.8). The EAJSI is computed by first identifying the maximum monthly zonal wind value at each longitude within the index domain and then by averaging these values. This approach allows for the strength of the regional subtropical jet to be calculated during each month of the year, as the jet

core migrates north-south over the course of the annual cycle. The global jet strength index (GJSI) is computed similarly, based on an average of maximum zonal wind values at all global longitudes and from 20° – 60°N.

Summer (JJA) averages of the two jet strength indices were correlated with respect to global fields of JJA 200 hPa zonal winds (1948 – 2003) and results are plotted spatially. Thus, Figures 4.17b and 4.17c illustrate global teleconnection patterns related to interannual variability in each of these indices and similarities between the two plots suggest that the global index is generally representative of the strength of zonal winds in the vicinity of East Asia. Furthermore, monthly correlations between the two jet strength indices (Figure 4.18) indicate that the GJSI explains roughly ~25 to 35% of interannual variability in the EAJSI during summer months and significant – though slightly lesser – amounts of variability during the remainder of the year.

Figure 4.15 shows that the EAJSI is most strongly anti-correlated with summer rainfall in southern China, although the lower basin of the YRV is also apparently affected (as confirmed by Table 4.2). This suggests that weaker westerlies at 200 hPa are generally more conducive to greater precipitation in south and central eastern China. Tables 4.2 – 4.4 also suggest hints of a positive correlation between the EAJSI and rainfall in NEC; however this relationship is generally not statistically significant or stationary. The GSJI is not significantly correlated with most JJA monsoon indices or summer rainfall over eastern China; however, it does generally show year-round stationary and significant positive correlations with respect to the PDO. As a final caveat, it should be noted that several of the interrelationships between the EAJSI, GJSI, and other indices are generally non-stationary (Tables 4.3 and 4.4), suggesting that

caution should be used before drawing broad-based conclusions based on these experimental indices.

However, as a final and more positive note, these indices appear to be relatively more climatically important during the non-summer seasons. For instance, the GJSI is strongly positively correlated with NH Hadley Cell indices (defined below) during DJF. Also, additional analyses of *spring* climate indicate that both jet strength indices are positively correlated with precipitation in SEC (r = 0.4 – 0.5) during this transition season. Also in the spring, the EAJSI is significantly inversely correlated with precipitation throughout northern China and the Korean Peninsula (r = -0.4 to -0.5). Strong positive correlations also exist between the EAJSI and both NH Hadley Cell in the spring and fall seasons (though not in the winter and summer), which is generally consistent with results from Oort and Yienger (1996). Taken together, these findings suggest that the Jet Strength indices may have particular relevance during transition seasons, perhaps influencing the timing of EAM onset and withdrawal.

4.2.7. Regional monsoon climate discussion

Before proceeding directly to the analyses of the larger-scale climatic context for the EAM system, some additional discussion is warranted to summarize some important recurring themes that may carry over into subsequent sections and chapters. Primarily, it is certainly noteworthy that many of the results presented above indicate that an out-of phase relationship exists between precipitation variability in the YRV and NEC. This could be interpreted to mean that precipitation in one region occurs at the expense of precipitation in the other region. Indeed, Yang and Lau (2004) demonstrated that

summers with excessive rainfall over the YRV are generally associated with dry conditions in the north. They further noted recent decadal-scale trends of precipitation that are decreasing in the north and increasing in the YRV. To explain these patterns, Yang and Lau (2004) show that persistent local convection over the YRV occurs when 1) there are above normal SSTs over the SCS, West Pacific warm pool and Indian Ocean, 2) below normal SSTs in the northwest Pacific, 3) abundant warm moist air advected from the south, and 4) cooler dry air drawn in from the north. The convergence of these air masses creates instability and local convection at the Mei-Yu front, which, under the right conditions, can persist beyond the climatologic mean and cause flooding in the YRV. Meanwhile, the NEC experiences a weakened monsoon, as the region is subjected to a prolonged period of northerly cool and dry continental winds.

4.3. Global-scale modes of climate variability

Expanding on analyses from the previous section, this section explores East Asian climate in the larger context of large-scale modes of climate variability (e.g., ENSO) and global-scale teleconnection patterns. As with the previous section, this portion of the analysis provides a basis for assessing dynamical mechanisms for a regional climatic response to volcanic forcing (Chapter 5), as well as helping to inform later assessments of AOGCM skill (Chapter 6).

4.3.1. Global-scale teleconnections with the ocean and atmosphere

To generally illustrate the large-scale patterns of atmospheric pressure variability associated with summer (JJA) rainfall in eastern China, global 500 hPa GPHs are

spatially correlated with standardized time series of GHCN precipitation from NECo, YRVo and SECo (1960 – 1990; Figure 4.19). These correlation patterns complement the wet-minus-dry maps of 500 hPa gph presented in section 4.1.3.

Confirming results from earlier studies (Wu and Wang, 2002) and the wet-minus-dry map in Figure 4.6b, the center panel of Figure 4.19 illustrates that precipitation variability in the YRV region occurs in phase with pressure heights throughout the tropics, particularly in the vicinity of the WPSH (highlighted by rectangle). Meanwhile, global pressure patterns correlated with summer rainfall variability in NEC (top panel) are generally out of phase with those associated with rainfall in the YRV. These findings are slightly different from results shown in the wet-minus-dry map in Figure 4.7b, but they confirm findings from earlier studies (Lim et al., 2002) indicating that *local* low pressures to the west coupled with a local high pressure cell to the east, over the Sea of Japan, allow for southeasterly moisture advection from the North Pacific Ocean into NEC. With regard to JJA rainfall in SEC, 500 hPa gph correlation patterns (Figure 4.19, bottom panel) are mostly negative and somewhat similar to patterns associated with rainfall in NEC. Consistent with results from most previous sections in this chapter, Figure 4.19 generally confirms that atmospheric circulation most conducive to summer rainfall in the YRV is commonly opposite of conditions linked to rainfall in the other two regions.

Similar to Figure 4.19, SSTs in the Indian and Pacific Oceans are spatially correlated with respect to regionally averaged GHCN summer precipitation time series from NECo, YRVo and SECo (Figure 4.20). SST correlation patterns linked to precipitation in NEC are generally consistent with Pacific SST variations associated with

ENSO (Figure 3.3): negative r-values in the eastern tropics and positive r-values in the northern basin and the West Pacific warm pool. As for summer rainfall in the YRV, associated SST patterns in the equatorial East Pacific are also somewhat reminiscent of ENSO. Also, consistent with the LSTD index analysis (Figure 4.14) and published literature (Chang et al., 2000a; Ding et al., 2004), relatively local SSTs in the dominant moisture source regions – the Bay of Bengal, SCS and Philippine Sea – are all positively correlated with YRV precipitation. Meanwhile, SST correlations linked with summer rainfall over SEC are generally opposite to those associated with YRV rainfall, particularly in the aforementioned adjacent basins to the south and east.

4.3.2. The global Hadley cell indices

Global Hadley circulation represents a particularly important aspect of tropical climate that is expected to respond to a reduction in shortwave radiation caused by volcanic forcing. Furthermore, it is hypothesized that this may translate into some regional-scale climate impacts. While there is no universally accepted index for the intensity of global Hadley circulation, one of the most commonly used measures is based on the maximum mean meridional streamfunction in the tropics, north and south of the equator (e.g., Mitas and Clement, 2005; Quan et al., 2004). Meridional streamfunction essentially measures the overturning of mass and it is derived by integrating meridional winds vertically through the atmosphere. Figure 4.21 illustrates the annual cycle of this overturning, plotting monthly long-term zonal mean meridional streamfunction values from 90°S – 90°N and from the surface to the top of the atmosphere (TOA). From the figure, it is clear that the strongest clockwise circulation (positive values) occurs in

January and February, while the strongest counterclockwise meridional overturning (negative values) occurs during July and August. The major transition months are April-May in the northern hemisphere (NH) spring and October-November in the NH fall.

To quantitatively assess temporal variability in Hadley circulation, the *maximum* value of monthly zonal mean meridional stream function in the 0° – 30°N zone indexes the strength of the NH Hadley Cell, while the *minimum* value of the monthly mean stream function from 0° – 30°S indexes the southern hemisphere (SH) cell (Oort and Yienger, 1996). These monthly streamfunction-based measures of meridional overturning in the atmosphere (derived from NCEP-reanalysis data) are hereafter referred to as the northern and southern hemisphere Hadley cell indices, respectively (HCINsf; HCISsf). It is important to note for these Hadley cell indices – as well alternative Hadley cell indices, defined below – that positive NH index values reflect strengthening in meridional overturning while positive SH index values reflect dampening.

The other measure of meridional overturning in the global Hadley cells is mean meridional vertical shear, or, the upper-lower level differences in zonally averaged meridional wind velocity at 200 and 850 hPa (Quan et al., 2004). Figure 4.22 plots long-term mean monthly vertical shear values from 60°N – 60°S. To represent temporal variability in the northern and southern hemisphere tropical Hadley cells respectively, mean monthly vertical shear values at 10°N and 10°S are sometimes used (Oort and Yienger, 1996). However, to more accurately capture the core of the overturning cells during transitions and summer seasons, the maximum and minimum monthly vertical shear values between 0° – 30°N and 0° – 30°S are used for the northern and southern hemisphere cells, respectively (HCINvs; HCISvs). Similar indices have also been

applied at regional scales to index the Asian monsoon (Tanka et al, 2004) and Hadley circulation over the Pacific Ocean, from 120° – 280°E (Oort and Yienger, 1996).

Tables 4.2- 4.5 display r-values from seasonal correlations between global Hadley cell indices, EAM indices (section 4.2), and regionally averaged precipitation time series from NEC, YRV and SEC. Naturally, the streamfunction- and vertical shear-based Hadley cell indices are well correlated with one another within their respective hemispheres. However, Hadley cell indices from opposite hemispheres are not significantly correlated. The HCINsf and HCINvs indices are significantly positively correlated with the GJSI during winter. Meanwhile, the EAJSI displays relatively stationary and statically significant positive correlations with respect to NH Hadley cell indices during both summer and winter seasons, respectively (Tables 4.2). In winter, HCINsf is also highly positively correlated with the WPSHz index. These interrelationships with respect to the jet and subtropical high indices are entirely expected and consistent with the classic conceptual model of the Hadley cell (Webster, 2004) as well as previous observational studies (Oort and Yienger, 1996; Hou, 1998).

Of course, it is of particular interest to this study that summer rainfall in the YRV is inversely correlated with the HCINsf. A mechanism for this teleconnection may be indirectly associated with variability in the WNPSMI, which is positively correlated with both NH Hadley cell indices and, like HCINsf, also inversely correlated with YRV rainfall. While a thorough review of these questions is beyond the scope of this study, these apparent teleconnections will be revisited through analyses and discussions in following chapters.

4.3.3. ENSO and regional precipitation

As discussed in previous sections, the relationship between ENSO, the EAM system and hydroclimate in eastern China is complex and apparently not entirely stationary through time. Previous studies have noted that phase shifts in the PDO circa 1925, 1946, and 1976 (Mantua et al., 1997; Mantua and Hare, 2002) represented significant climate regime shifts throughout the Pacific Basin, from North America (Gedalof and Smith, 2001), to Asia (D'Arrigo and Wilson, 2006), to the tropics (Trenberth and Caron, 2002). The 1976 phase shift, in particular, has been linked to changes in the stationarity of the ENSO signal with respect to the monsoon climates in Asia (Chang et al., 2000a; Kinter et al., 2002). So, for the purpose of this simple test of ENSO stationarity, simultaneous (no-lag) correlation analyses between the SOI and precipitation across East Asia are separated into three epochs, according to the long-term phases of the PDO.

Figure 4.23 shows that, with a few exceptions, statistically significant teleconnections between the SOI and regional hydroclimate in eastern China can be fleeting from one period to the next. For example, from 1925 – 1946, r-values greater than 0.6 are found across a broad region of eastern China during JJA, centered on the middle reaches of the YRV. Yet, during the following two epochs, this apparently robust teleconnection pattern nearly disappears (1947 – 1976) or reverses (1947 – 2002), in some portions of the region. Wu and Wang (2002) noted that statistically significant positive (lagged) correlations existed between Niño3 SSTs during the previous winter and summer rainfall in NEC in the period from 1960s to 1970s; however this relationship completely reversed by the 1980s. When a simultaneous correlation analysis is

conducted for the entire period of available record (1902 – 2001; Figure 4.23, right column), a subtle and statistically insignificant pattern of positive correlations between the SOI and JJA precipitation is apparent in the north, indicating drier conditions in that region during El Niño years.

Meanwhile, some of the teleconnections displayed in Figure 4.23. appear to be relatively stationary throughout most of the century: such as the DJF signal in south eastern China (wet during El Niño) or the patters in SON (El Niños are wet in the south and dry in the north). However, in the spring and summer seasons – when the majority of annual rainfall occurs in China – simultaneous correlations between SOI and regional precipitation are apparently inconsistent through time. These results are not surprising, since ENSO is in its peak phase during SON and DJF (Hoerling and Kumar, 2000).

To also consider these relationships on a slightly longer time-scale, a simple paleoclimate analysis is conducted on annual reconstructions of drought vs. flooding (DI) during El Niño years. Figure 4.24 shows a composite of average DI values during "strong" and "very strong" El Niño years during the two-century period from 1791 to 1979. All El Niño years included in the composite were assigned this classification with the highest possible level of "satisfactory" confidence (Quinn, 1987; Ortlieb, 2000). These results (Figure 4.24), though only marginally statistically significant, are consistent with spatial correlation patterns noted above (Figure 4.23, in JJA and SON), suggesting that El Niño years are generally drier throughout most of northeastern China. These findings are also consistent with results by Song (1998), who compared the same DI values with an instrumental Southern Oscillation Index during the period from 1852 – 1986.

4.3.3.1. ENSO and regional monsoon indices

The final analysis conducted in this chapter sets the stage for subsequent assessments of the *observed* dynamical climatic response to volcanic forcing from explosive tropical eruptions. To partially account for the fact that each of the major tropical eruptions in the last half century occurred during El Niño events, this section attempts to estimate the relative influence of ENSO on each of the various regional- and global-scale climate indices and to then linearly separate the ENSO effect from them.

First, to visually examine the ENSO signal and estimate its statistical significance throughout the seasonal cycle of each index, the first step was to classify all months on record as representative of either El Niño, La Niña or neutral ENSO conditions – according to the CRU Southern Oscillation Index, from 1948 to 2003. Specifically, ENSO conditions were defined such that months with SOI values in the upper 25th percentile were classified as La Niña events while months with values in the bottom 25th percentile were classified as El Niño events; all other months, with near-normal conditions were excluded from this analysis. However, the drawback to using this high index threshold – and, thus, excluding a portion of the data – is that it limits the sample size for each given monthly event to only a dozen cases. As a result, the statistical significance of some results is marginal, but the analysis allows for a good estimate as to which indices are most sensitive to ENSO, the nature of the interrelationship and during which season the signals are evident.

Figure 4.25 shows average monthly regional climate index anomalies during all ENSO "event" months. Average index anomalies during La Niña months are plotted in red while index anomalies during El Niños are plotted in blue. The 95% confidence

intervals for the true mean in each month are also shown by red and blue translucent vertical bars. When there is space between these bars and/or the zero line then results are statistically significant. The regional monsoon indices that are apparently most closely related to variability in ENSO are the WPSHz, the WNPMI and possibly the EAJSI. During El Niño winters, the WPSHz index is clearly more positive and the EAJSI is slightly more negative; while the opposite is true for La Nina winters. However, the response of these and most other regional climate indices is relatively mute during the summer monsoon season. The one exception would appear to be the WNPMI, which is more positive during El Niño summers and negative during La Niña.

As discussed earlier, it is desirable in the context of this study to test if the observed regional-scale hydroclimatic response to recent volcanic eruptions may have been particularly sensitive to the occurrence of simultaneous El Niño events. This can be accomplished by following methods similar to those employed by Robock and Mao (1995), who used a simple linear model to statistically remove ENSO signals from gridded global climate data before attempting to discern spatial patterns in the temperature response to volcanic forcing. In the present study the ENSO signal is statistically removed on a monthly and seasonal basis from regional monsoon indices and gridded surface climate data, respectively. This is accomplished by retaining the residuals from linear regression analyses of each variable with the SOI during each month or season separately, from 1948 - 2002. In each case, the SOI is treated as the independent variable while monsoon indices are treated as the dependent variable (DEP):

Equation 4.1 $$DEP = a + b(SOI)$$

such that *a* and *b* are regression coefficients in the linear regression relationship.

Of course, the true dynamical nature of the relationship between ENSO and the EAM is complex and cannot be fully captured through a simple linear equation. For example, several previous studies (e.g., Wang et al., 2000; Chang et al., 2000a) have demonstrated the existence of lagged relationships between these two systems. Furthermore, Tables 4.2 - 4.4 show that some regional summer monsoon indices are more closely associated with SOI values during the previous winter, as opposed to simultaneously. Robock and Mao (1995) included a seasonal lag in their methodology to account for observed lags in the air temperature response to ENSO over land areas, but they acknowledged that this was somewhat problematic because not all regions respond on the same time and spatial scales. Also, many of the regional and global indices discussed in this chapter do not exhibit strong or stationary links with respect to the SOI and questions remain regarding mechanisms for these lagged teleconnections (Lau and Wang, 2006). Finally, results from a study similar to Robock and Mao (1995), using singular value decomposition to separate the ENSO signal from surface temperatures (Yang et al., 2001), found that ENSO had a relatively weak signal in regional temperatures over the Eurasian continent and that their relatively elaborate signal removal technique had little overall effect on their final composite analyses of the air temperature response to volcanic forcing in this region.

Table 4.1. Reference table for regional and global dynamic climate indices. All numbers in index formulae represent pressure levels in hPa units. Capital letters in index formulae refer to geopotential height (Z), zonal wind (U) and meridional wind (V) at their respective pressure levels in the atmosphere. The symbol ? represents the zonal mean meridional stream function (Oort and Yienger, 1996). See text for more details.

Index Name	Index Formula
Regional Climate Indices	
West Pacific Subtropical High zonal index	WPSHz = avg(Z850) †
Okhotsk High Index	OKHI = avg(Z500) †
Western North Pacific Monsoon Index	WNPMI = avg($U850_{SOUTHWEST}$) - avg($U850_{NORTHEAST}$) †
Summer Monsoon Index	SMI = avg(SLP_{WEST}) – avg(SLP_{EAST}) †
Land – Sea Surface Temperature Difference	LSTD =[(T_{YRV} - SST_{NWP}) * 4 + (T_{SEC}- SST_{SCS})]/ 5 ‡
East Asia Jet Strength Index	EAJSI = avg max(U200) †
Rainfall in northeast China (CRU data)	CRUnec = avg(stdz(precip))$_{110° – 122°E, 35° – 44°N}$
Rainfall in Yangtze R. Valley (CRU data)	CRUyrv = avg(stdz(precip))$_{110° – 122°E, 27° – 35°N}$
Rainfall in southeast China (CRU data)	CRUsec = avg(stdz(precip))$_{110° – 122°E, 21° – 27°N}$
Global-Scale Climate Indices	
Global Jet Strength Index	GJSI = avg max(U200)$_{20 – 60°N, GLOBAL}$
Hadley Cell Index (North) - stream function	HCINsf = max[avg(?$_{GLOBAL}$)]$_{0 – 30°N}$
Hadley Cell Index (North) – vertical shear	HCINvs = max[avg($V200_{GLOBAL}$) - avg($V850_{GLOBAL}$)]$_{0 – 30°N}$
Hadley Cell Index (South) - stream function	HCINsf = max[avg(?$_{GLOBAL}$)]$_{0 – 30°S}$
Hadley Cell Index (South) - vertical shear	HCINvs = max[avg($V200_{GLOBAL}$) - avg($V850_{GLOBAL}$)]$_{0 – 30°S}$
Southern Oscillation Index	SOI = stdz(SLP_{TAHITI}) – stdz(SLP_{DARWIN})
Arctic Oscillation	AO = 1st principal component(Z1000)$_{20° – 90°N, GLOBAL}$
Pacific Decadal Oscillation	PDO = 1st principal component(SST)$_{20° – 70°N, PACIFIC OCEAN}$

Notes

† see Figure 4.8 for specific index domain

‡ see Figure 4.9 for specific index domain

Table 4.2. Correlation matrix comparing interannual variability in regional and global climate indices during JJA, 1948 – 2002 AD. Note that linear trends were removed from all indices prior to calculation of r-values. Bold R-values that are significant at the 95th and 99th percent confidence levels are italicized and underlined, respectively (not accounting for autocorrelation or stationarity). See text, Table 4.1 and Figures 4.8 and 4.9 for details regarding index definitions.

Variables	WPSHz	LSTD	WNPMI	SMI	OKHI	EAJSI	GJSI	HCIN-sf	HCIN-vs	HCIS-sf	HCIS-vs	SOI	SOI-DJF	AO	PDO	CRUnec	CRUyrv	CRUsec
WPSHz	1	**-0.37**	**-0.65**	0.26	**0.36**	0.07	0.11	-0.23	-0.09	0.12	-0.07	0.00	**-0.44**	-0.02	***0.30***	0.05	**0.34**	-0.25
LSTD		1	**0.37**	-0.21	**-0.42**	***0.29***	0.05	***0.29***	0.08	-0.18	-0.04	0.02	-0.01	0.15	-0.16	0.26	**-0.69**	0.22
WNPMI			1	0.11	**-0.43**	0.05	-0.11	**0.36**	**0.49**	-0.24	***-0.29***	***-0.27***	**0.35**	0.02	-0.19	**-0.33**	**-0.34**	0.16
SMI				1	0.05	0.03	0.09	-0.15	0.22	0.21	-0.05	-0.09	-0.01	0.10	0.09	-0.20	0.12	-0.12
OKHI					1	-0.25	-0.01	**-0.34**	-0.16	0.08	-0.14	0.08	-0.16	-0.03	0.15	0.01	**0.37**	-0.15
EAJSI						1	**0.45**	**0.36**	0.19	0.23	***0.27***	-0.09	***-0.30***	0.09	0.25	0.25	***-0.29***	**-0.32**
GJSI							1	0.21	-0.01	0.14	***0.27***	-0.17	**-0.46**	-0.08	**0.36**	0.08	-0.24	-0.05
HCIN-sf								1	**0.63**	-0.02	0.22	0.08	-0.05	0.21	-0.10	-0.12	**-0.46**	-0.11
HCIN-vs									1	-0.03	-0.22	-0.11	0.04	0.21	0.00	***-0.28***	-0.10	-0.17
HCIS-sf										1	**0.66**	0.21	***-0.28***	0.09	0.04	***0.30***	0.01	-0.20
HCIS-vs											1	0.22	-0.22	0.01	-0.10	**0.38**	-0.15	-0.06
SOI												1	0.06	***0.30***	**-0.41**	0.18	-0.09	-0.09
SOI-DJF													1	0.03	**-0.44**	-0.16	0.08	0.19
AO														1	**-0.33**	0.09	0.05	0.12
PDO															1	0.02	0.05	-0.25
CRUnec																1	0.00	-0.03
CRUyrv																	1	-0.08
CRUsec																		1

Table 4.3. Same as Table 4.2, except for JJA, from 1948 – 1976 AD.

Variable	WPSHz	LSTD	WNPMI	SMI	OKHI	EAJSI	GJSI	HCIN-sf	HCIN-vs	HCIS-sf	HCIS-vs	SOI	SOI-DJF	AO	PDO	CRUnec	CRUyrv	CRUsec
WPSHz	1	-0.29	***-0.42***	***0.40***	***0.40***	-0.23	-0.02	-0.33	-0.08	0.10	-0.29	-0.13	-0.31	0.10	0.12	-0.02	***0.36***	-0.02
LSTD		1	0.34	-0.22	-0.35	**0.59**	0.18	0.33	0.10	-0.13	0.03	-0.14	-0.05	0.07	-0.11	0.11	**-0.74**	0.10
WNPMI			1	-0.08	***-0.39***	0.24	-0.13	**0.54**	**0.54**	-0.30	-0.14	-0.23	0.27	-0.06	-0.18	***-0.44***	**-0.47**	-0.09
SMI				1	0.22	-0.22	-0.08	***-0.37***	0.08	0.23	-0.11	0.07	0.12	0.22	-0.09	-0.22	0.14	0.01
OKHI					1	-0.30	-0.15	-0.32	-0.01	0.03	-0.22	-0.02	-0.18	0.11	0.22	0.30	***0.41***	-0.17
EAJSI						1	**0.54**	***0.36***	0.05	0.01	0.35	-0.24	-0.08	0.20	0.01	0.15	***-0.41***	-0.13
GJSI							1	0.20	-0.18	0.09	0.35	-0.13	-0.34	-0.09	***0.43***	0.17	-0.25	0.07
HCIN-sf								1	**0.63**	-0.22	0.16	0.07	0.13	0.11	-0.32	-0.18	***-0.44***	0.03
HCIN-vs									1	-0.07	-0.17	0.05	0.22	0.14	-0.32	-0.24	-0.16	-0.10
HCIS-sf										1	**0.69**	0.26	-0.26	0.25	-0.10	0.36	0.13	0.31
HCIS-vs											1	0.26	-0.14	0.11	-0.17	0.27	-0.09	0.24
SOI												1	0.14	0.27	**-0.46**	0.11	0.12	0.08
SOI-DJF													1	0.01	-0.30	-0.17	-0.02	-0.09
AO														1	**-0.46**	0.15	0.05	0.17
PDO															1	0.11	0.09	-0.14
CRUnec																1	0.14	-0.24
CRUyrv																	1	-0.30
CRUsec																		1

Table 4.4. Same as Table 4.2, except for JJA, from 1977 – 2002 AD.

Variable	WPSHz	LSTD	WNPMI	SMI	OKHI	EAJSI	GJSI	HCIN-sf	HCIN-vs	HCIS-sf	HCIS-vs	SOI	SOI-DJF	AO	PDO	CRUnec	CRUyrv	CRUsec
WPSHz	1	***-0.44***	**-0.82**	0.05	0.32	***0.38***	0.23	-0.12	-0.11	0.13	0.11	0.12	**-0.52**	-0.10	***0.42***	0.16	0.27	***-0.43***
LSTD		1	***0.41***	-0.21	**-0.50**	-0.05	-0.08	0.25	0.05	-0.24	-0.10	0.18	0.03	0.23	-0.21	***0.39***	**-0.63**	0.34
WNPMI			1	0.29	**-0.46**	-0.07	-0.09	0.27	**0.47**	-0.23	***-0.38***	-0.29	***0.42***	0.08	-0.23	-0.26	-0.27	0.34
SMI				1	-0.20	**0.49**	***0.38***	0.33	**0.48**	0.13	0.06	-0.31	-0.13	-0.01	0.28	-0.12	0.02	-0.29
OKHI					1	-0.21	0.12	***-0.38***	-0.31	0.12	-0.07	0.19	-0.14	-0.14	0.10	-0.23	0.33	-0.13
EAJSI						1	***0.36***	0.34	***0.37***	**0.48**	0.19	0.05	**-0.53**	-0.01	**0.49**	***0.36***	-0.16	**-0.53**
GJSI							1	0.22	0.19	0.19	0.20	-0.21	**-0.56**	-0.08	0.33	0.01	-0.23	-0.17
HCIN-sf								1	**0.65**	0.25	0.29	0.08	-0.26	0.32	0.13	-0.08	**-0.47**	-0.28
HCIN-vs									1	-0.02	-0.26	-0.29	-0.13	0.30	0.26	-0.27	-0.08	-0.24
HCIS-sf										1	**0.67**	0.20	-0.28	-0.03	0.12	0.28	-0.16	**-0.64**
HCIS-vs											1	0.18	-0.29	-0.07	-0.03	***0.41***	-0.17	-0.30
SOI												1	-0.03	0.31	***-0.36***	0.20	-0.27	-0.25
SOI-DJF													1	0.02	**-0.52**	-0.23	0.24	***0.41***
AO														1	-0.23	0.01	0.09	0.08
PDO															1	0.02	-0.05	-0.31
CRUnec																1	-0.13	0.06
CRUyrv																	1	0.20
CRUsec																		1

Table 4.5. Same as Table 4.2, except for DJF, from 1949 – 2002 AD.

Variables	WPSHz	LSTD	WNPMI	SMI	OKHI	EAJSI	GJSI	HCIN-sf	HCIN-vs	HCIS-sf	HCIS-vs	SOI	AO	PDO	CRUnec	CRUyrv	CRUsec
WPSHz	1	0.16	-0.25	-0.25	**-0.45**	**-0.36**	0.21	**0.52**	0.11	0.21	0.26	**-0.78**	0.20	***0.29***	0.11	0.26	**0.33**
LSTD		1	0.04	**-0.33**	-0.24	-0.26	**-0.35**	-0.03	-0.07	-0.01	-0.08	-0.07	0.17	-0.26	0.16	0.17	-0.14
WNPMI			1	-0.01	0.04	-0.10	**-0.36**	-0.19	-0.02	0.15	-0.09	**0.35**	0.23	-0.26	0.20	0.16	0.09
SMI				1	**0.59**	**0.66**	**0.34**	0.03	***0.29***	0.02	-0.04	0.26	-0.16	0.17	**-0.45**	**-0.49**	**-0.40**
OKHI					1	**0.41**	0.18	-0.05	0.25	-0.01	-0.01	**0.37**	0.00	-0.11	-0.09	-0.21	-0.19
EAJSI						1	**0.45**	0.17	**0.32**	-0.16	-0.12	**0.36**	**-0.32**	0.13	**-0.40**	**-0.35**	***-0.27***
GJSI							1	**0.60**	**0.42**	-0.06	0.11	**-0.36**	-0.18	**0.44**	-0.26	-0.21	0.18
HCIN-sf								1	**0.72**	0.03	0.09	**-0.44**	-0.01	***0.28***	-0.09	-0.02	0.22
HCIN-vs									1	-0.10	-0.04	-0.11	0.07	-0.01	-0.09	-0.24	0.16
HCIS-sf										1	**0.82**	-0.21	0.14	0.02	-0.02	0.16	0.12
HCIS-vs											1	***-0.30***	-0.01	0.15	-0.08	0.08	0.20
SOI												1	-0.01	**-0.44**	-0.07	-0.14	**-0.46**
AO													1	**-0.41**	0.24	**0.34**	0.23
PDO														1	***-0.27***	-0.21	-0.05
CRUnec															1	**0.65**	**0.51**
CRUyrv																1	**0.49**
CRUsec																	1

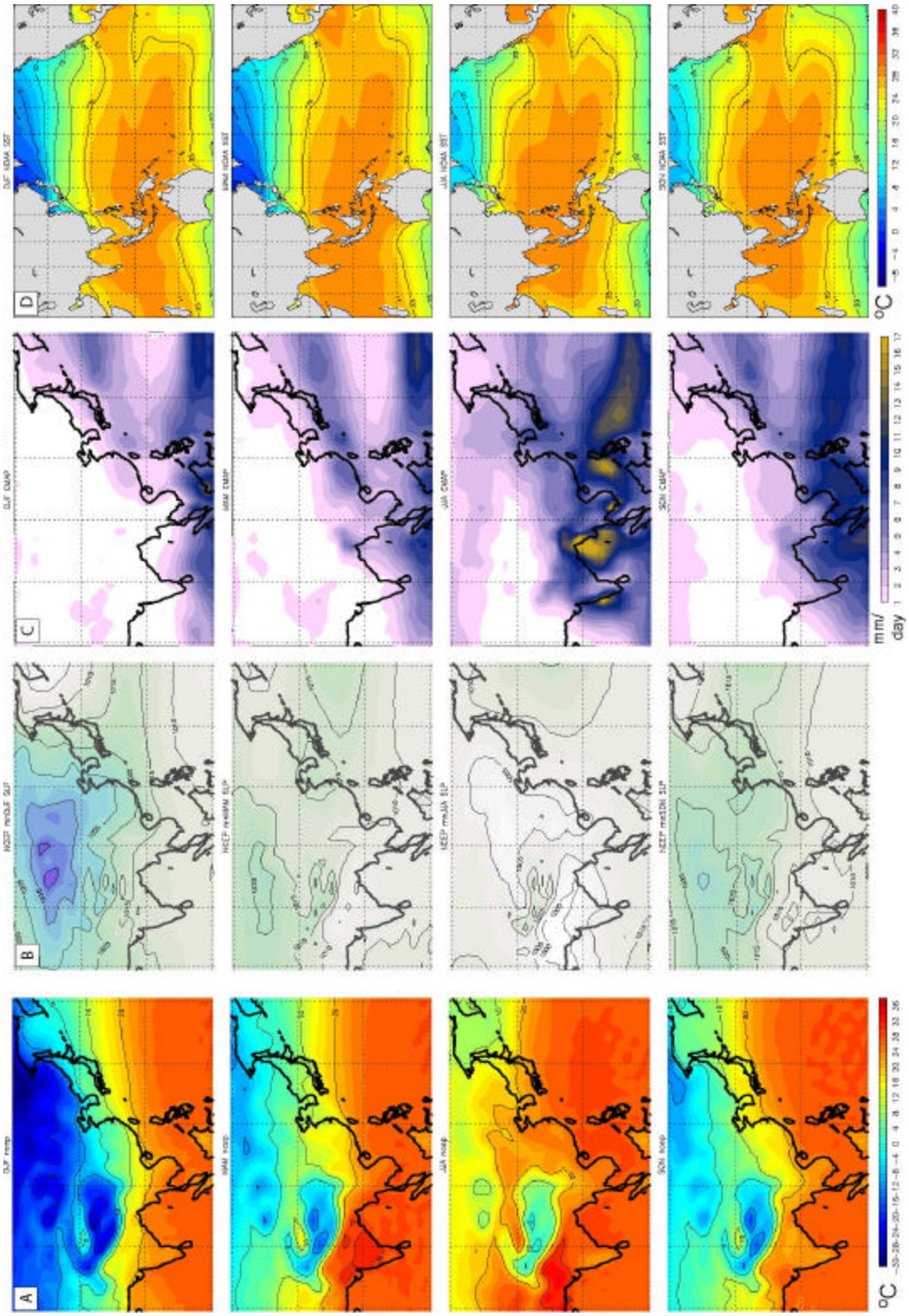

Figures 4.1. Plots show seasonal means of DJF, MAM, JJA and SON observed (a) reference height temperature (2m), (b) sea-level pressure, (c) precipitation (CMAP), and (d) sea-surface temperature (NOAA-ER SSTs) from 1961 to 1990 AD.

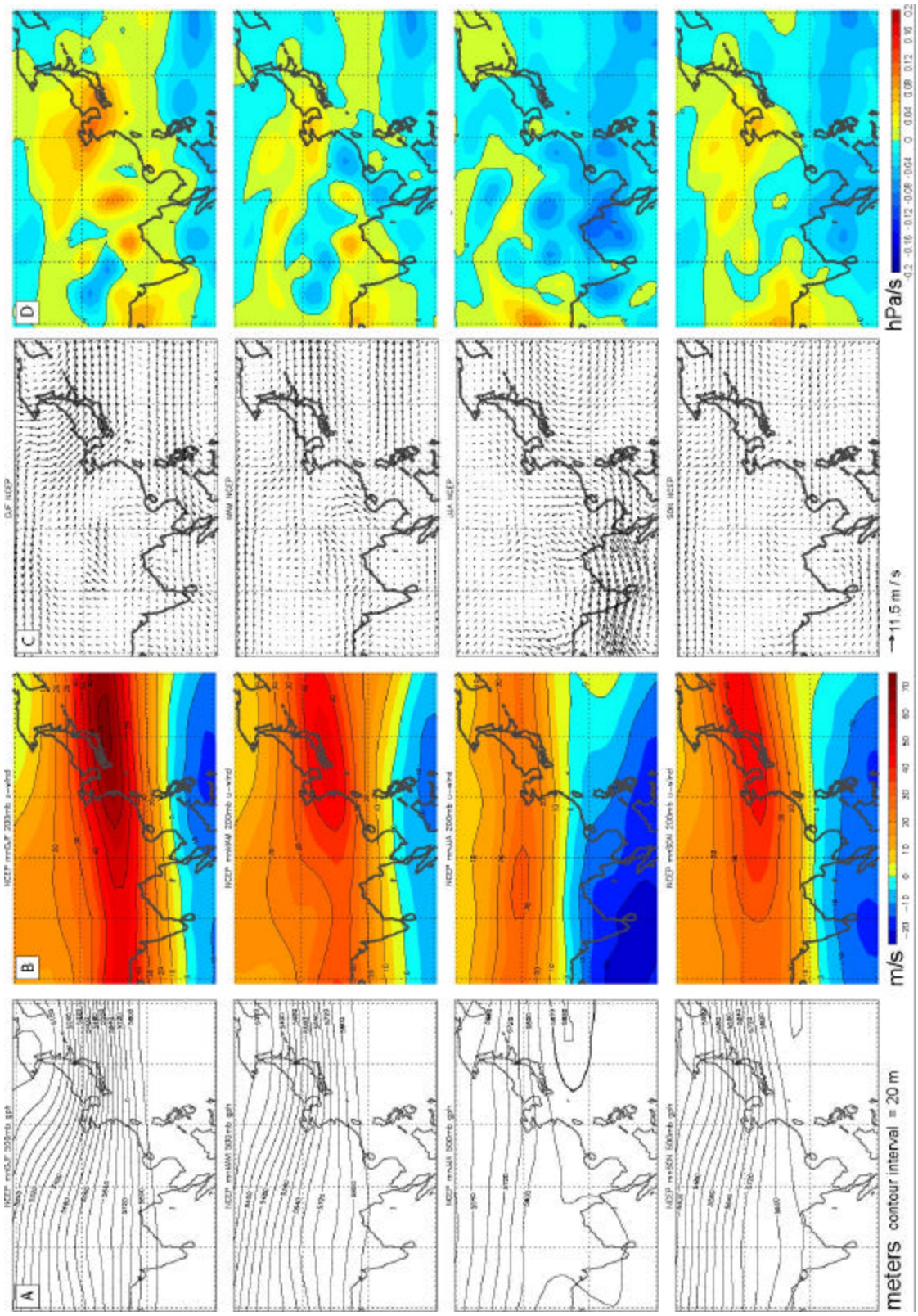

Figure 4.2. Same as Figure 4.1 but for (a) 500 mb geopotential heights, (b) 200 mb zonal wind, (c) 850 mb wind, and (d) 500 mb vertical velocity, or omega, from 1961 to 1990 AD.

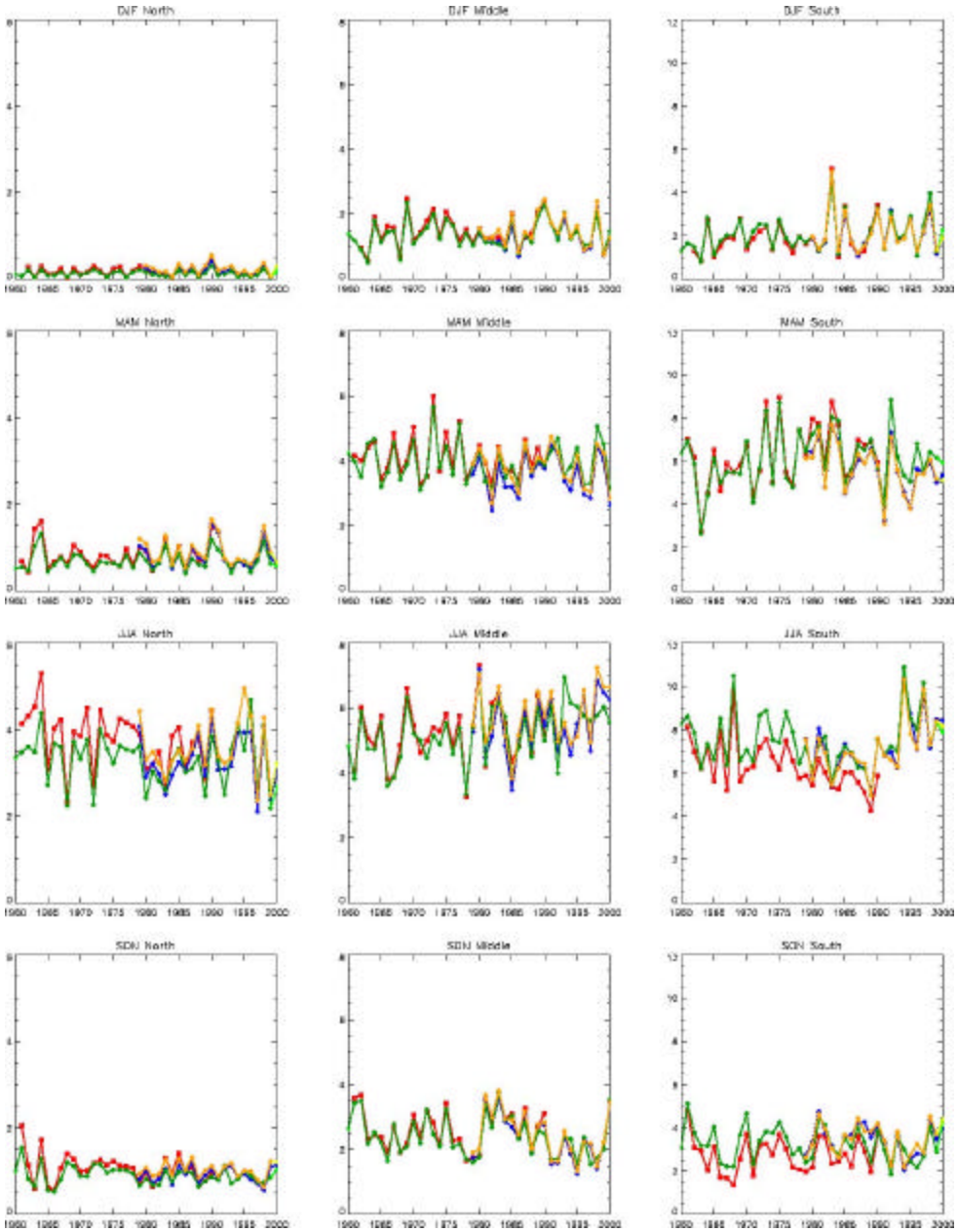

Figure 4.3. Seasonal time series of regionally averaged precipitation in NEC (left), YRV (center) and SEC (right) from 1960 – 2000; from top to bottom DJF, MAM, JJA, and SON. Plotted are data from four different sources: GHCN stations (red); CRU gridded (green); CMAP (blue); and GPCP (orange). Note different scales on the y-axes for each region.

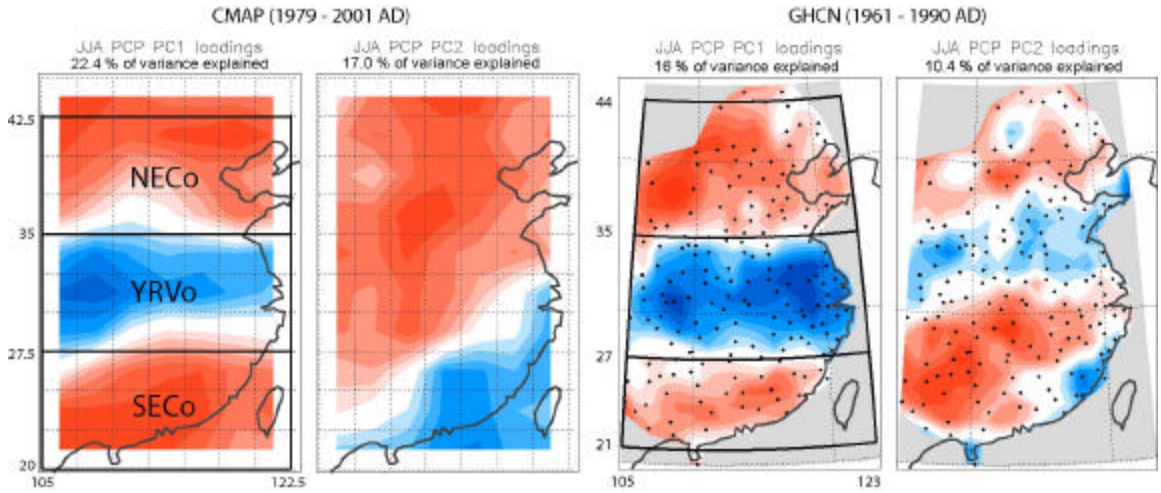

Figure 4.4. Loading patterns for the first and second principal components of interannual precipitation variability over eastern China (20° – 45°N, 105° - 123°E). Grid cells of the CMAP dataset are marked by light dashed lines (left two panels) and station locations for the GHCN data are marked with dots (right two panels). The boxes delineated in bold outline three zonal regions (labeled: NECo, YRVo, and SECo) with relatively coherent modes of observed interannual precipitation variability.

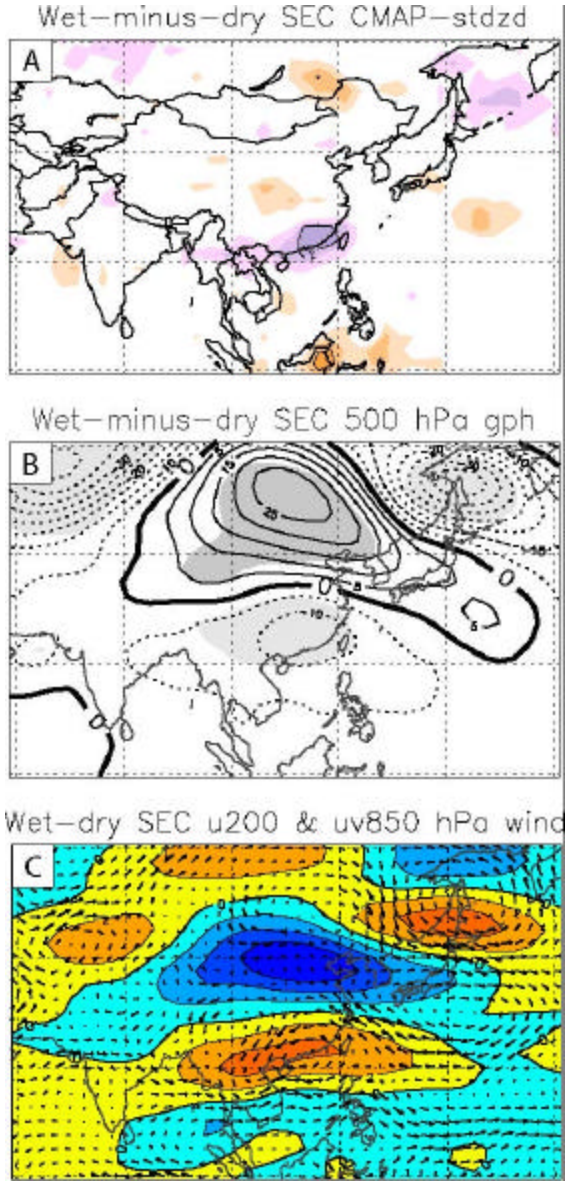

Figure 4.5. Wet-minus-dry maps based on SEC conditions showing (a) standardized CMAP precipitation, (b) 500 hPa geopotential heights, and (c) 200 hPa zonal winds (color contours) and 850 hPa wind vectors. Each plot reflects differences between observed conditions during the 5 wettest and the 5 driest summers (JJA) between 1979 and 2001. (a) Precipitation color contours occur at 0.5 standardized unit intervals while line contours occur at 2 standardized unit intervals (only differences exceeding one standard deviation are shown). (b) 500 hPa geopotential height contours occur at five meter intervals (solid = positive; dashed = negative; zero = bold) with lightly shaded regions highlighting differences less than one standard deviation below zero, while dark shading highlights differences greater than one standard deviation above zero. (c) 200 hPa zonal wind color contours occur at 2 m/s intervals with warm colors reflecting positive difference values while cool colors are negative.

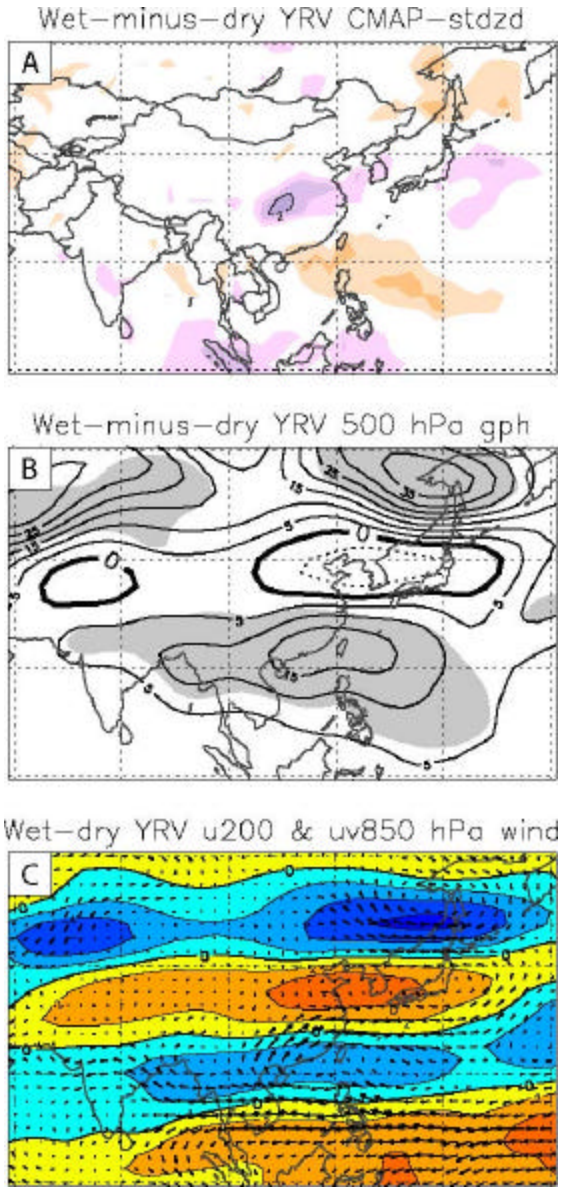

Figure 4.6. Same as Figure 4.5, except for YRV.

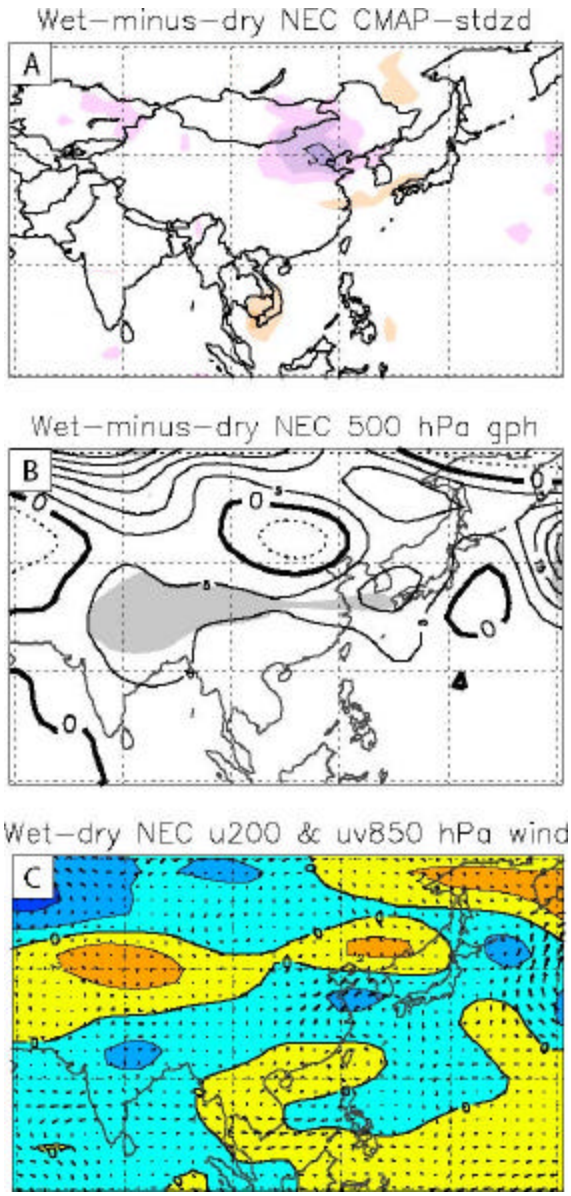

Figure 4.7. Same as Figure 4.5, except for NEC.

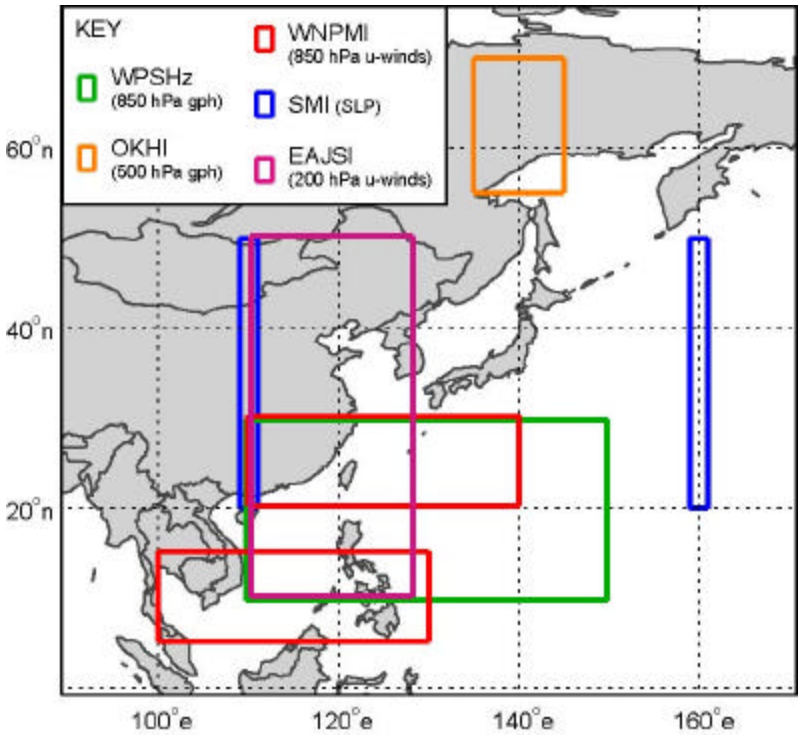

Figure 4.8. Boxes delineate the regions from which data were used in the process of computing the regional monsoon indices used for this study. Variables used to derive each of the indices are also included (in parentheses). See text and Table 4.1 for additional information.

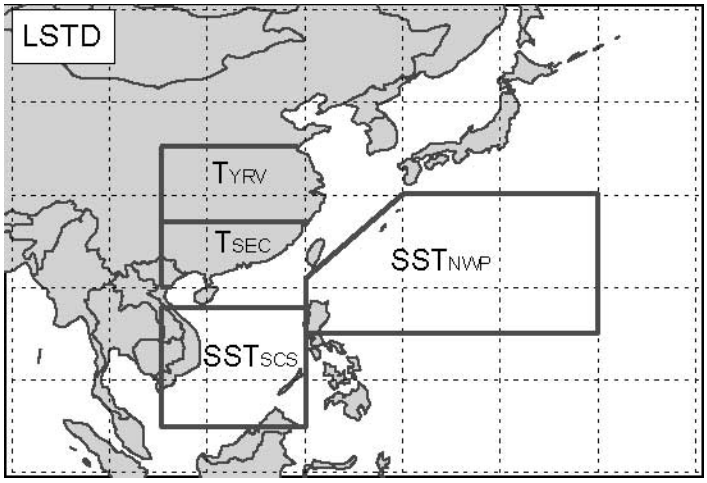

Figure 4.9. Boxes delineate regions from witch surface temperatures over land and SSTs were used to calculate the land-sea surface temperature difference (LSTD) index. See text and Table 4.1 for additional information.

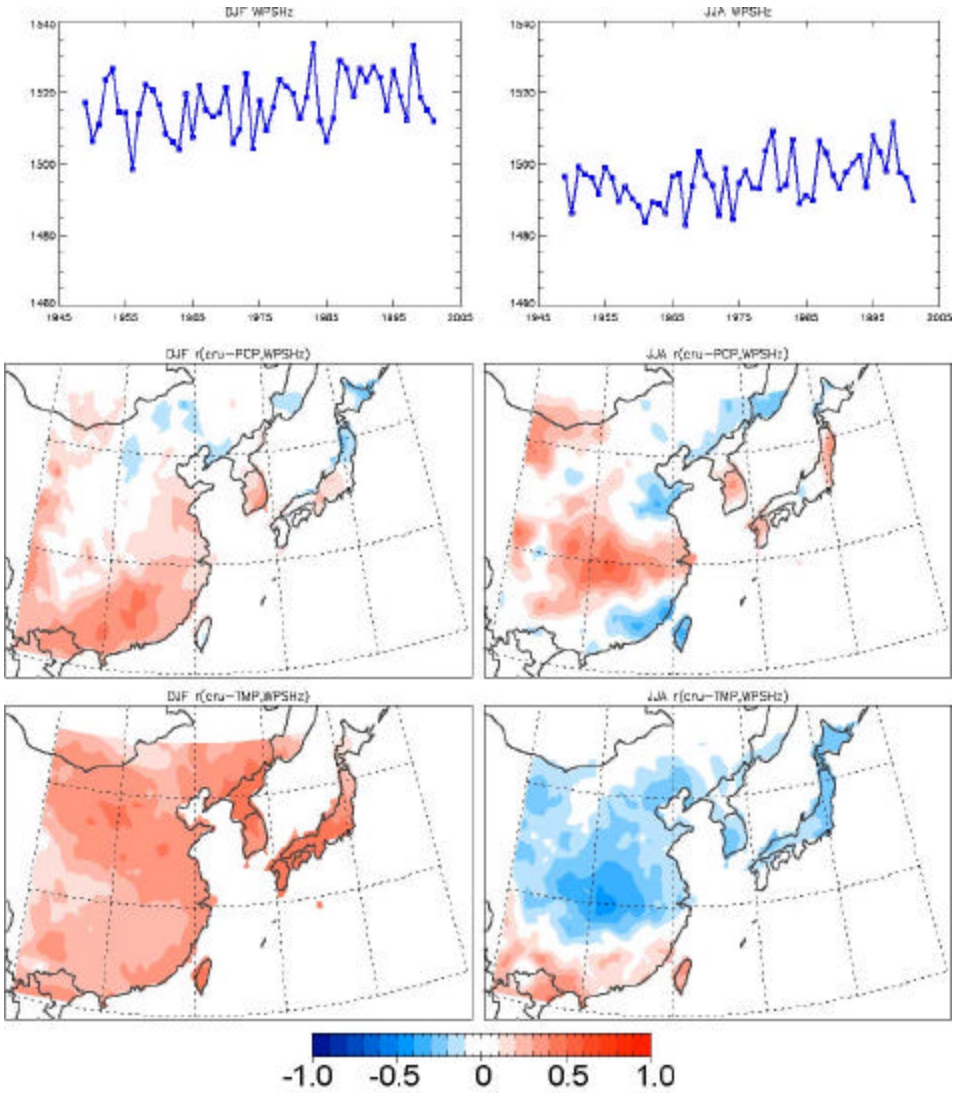

Figure 4.10. Plots illustrate temporal evolution and regional climate significance of the WPSHz index. The top two panels are time series of the WPSHz index during DJF (left) and JJA (right) from 1949 – 2003 AD. The bottom four panels spatially plot correlation values comparing the WPSHz during DJF (left) and JJA (right) with CRU precipitation (center) and surface temperature (bottom). The color bar is the key to correlation values in the bottom four plots (contour interval = 0.1). Individual correlation values greater than 0.3 (or less than -0.3) are significant with roughly 95% confidence (not accounting for multiplicity, the testing of multiple hypotheses).

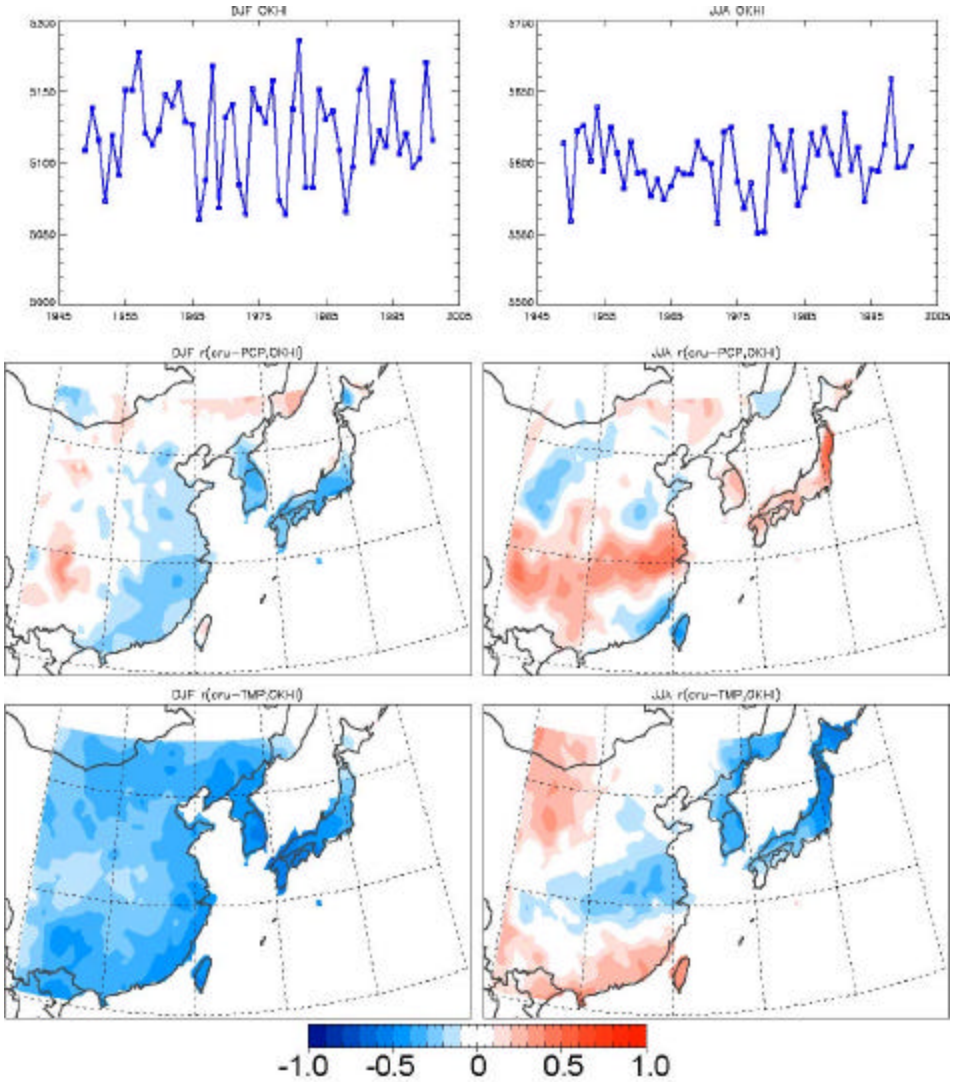

Figure 4.11. Same as Figure 4.10, but for the OKHI.

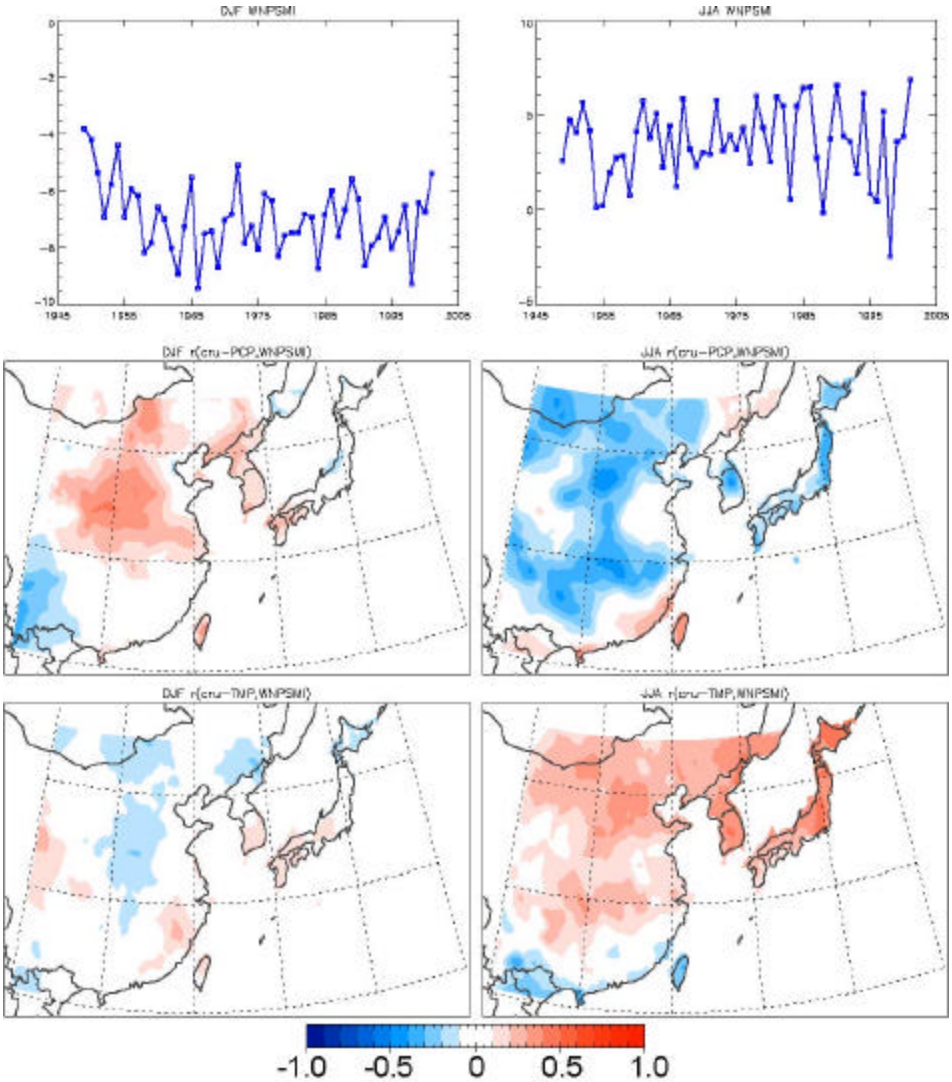

Figure 4.12. Same as Figure 4.10, but for the WNPMI.

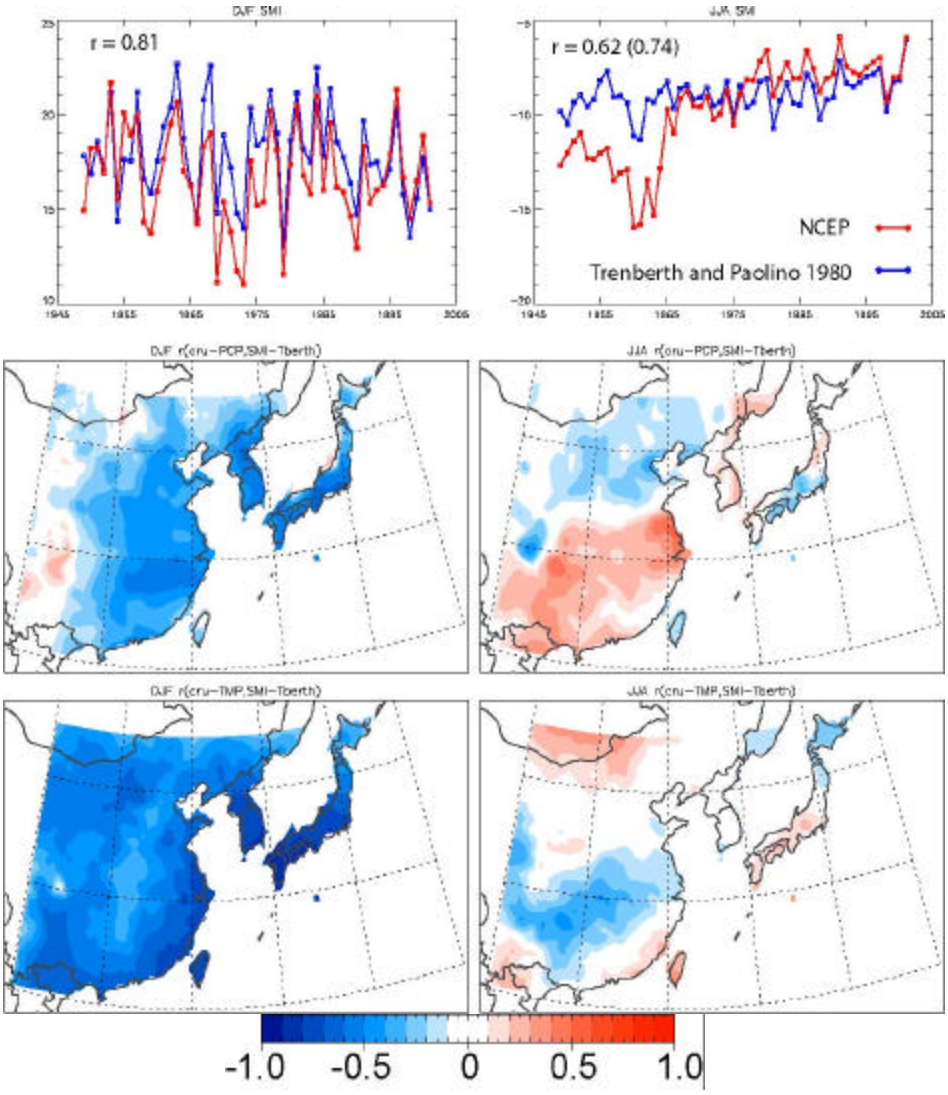

Figure 4.13. Same as Figure 4.10, but for the SMI. DJF and JJA time series plots compare SMI values derived from NCEP reanalysis (red) and Trenberth and Paolino (blue) SLP data. The top two panels include r-values from direct comparisons between the two indices during the period from 1948 – 2003 (or 1966 – 2003, in parentheses for JJA). Correlation maps illustrate relationships between regional temperature and precipitation with respect to the Trenberth and Paolino (1980) SMI time-series.

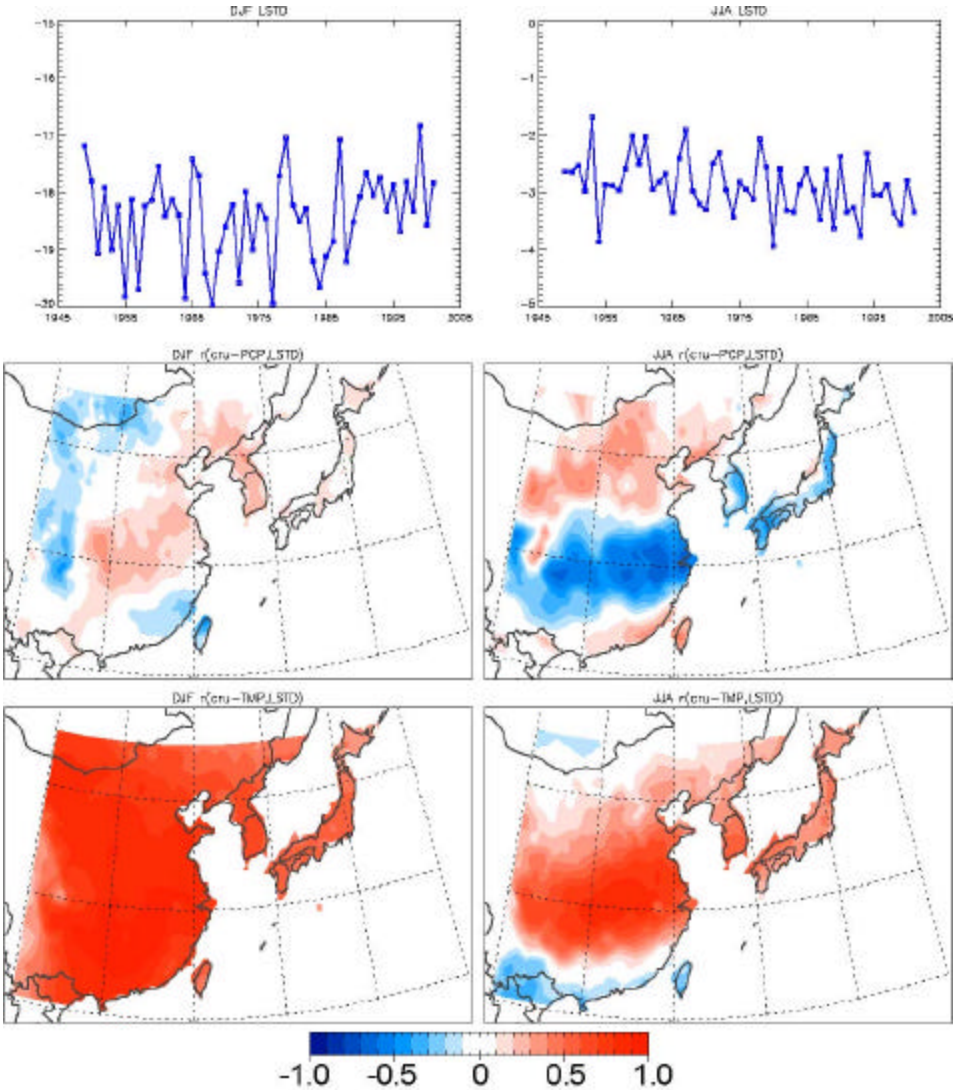

Figure 4.14. Same as Figure 4.10, but for the LSTD.

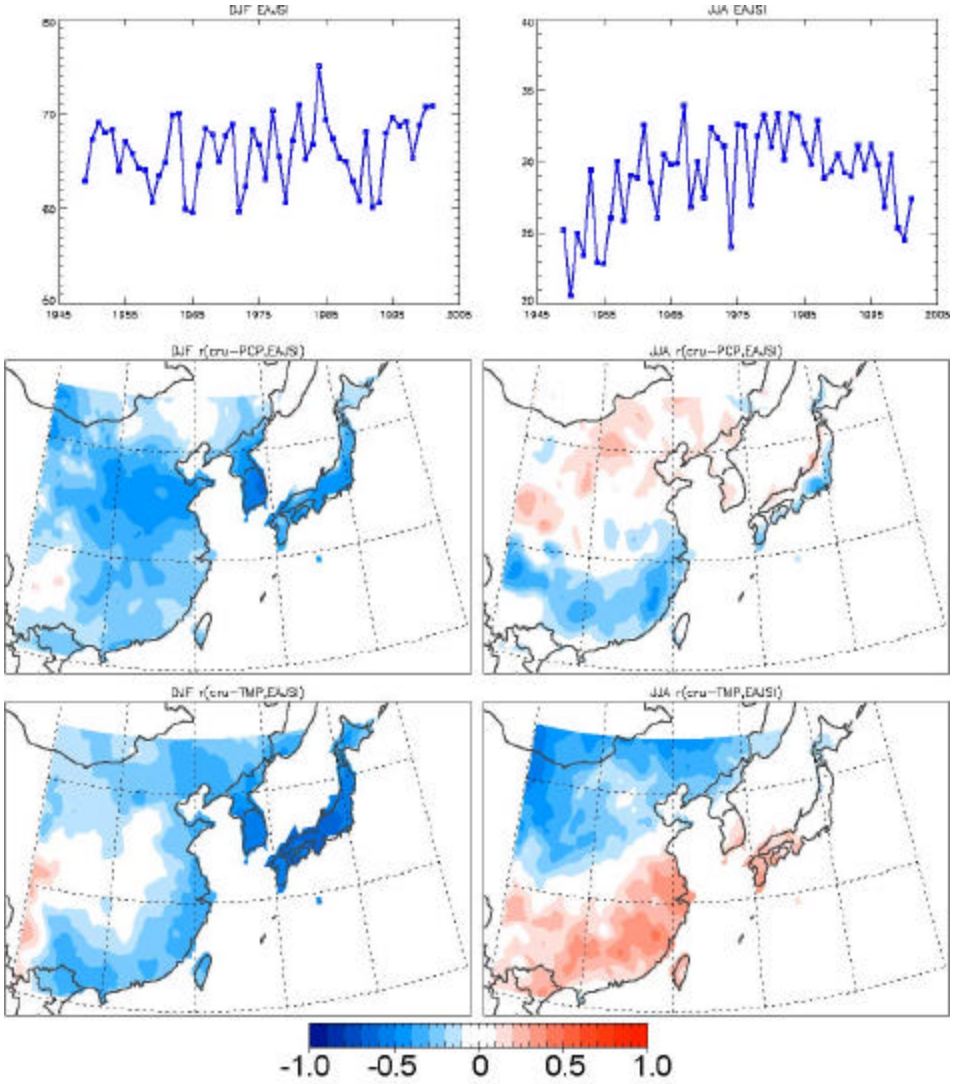

Figure 4.15. Same as Figure 4.10, but for the EAJSI.

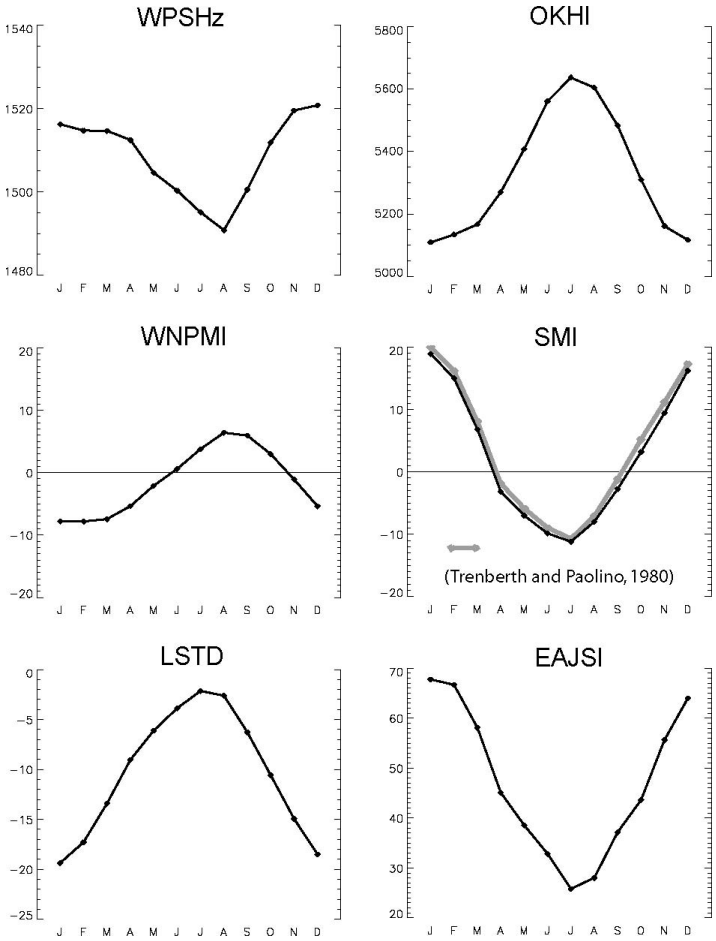

Figure 4.16. Long-term mean monthly climatologies for each of the regional climate indices (1961 – 1990). Note that the SMI includes two climatologies, one derived from NCEP reanalysis (dark) and one from Trenberth and Paolino (1980; grey). Units: WPSHz (m), OKHI (m), WNPMI (m/s), SMI (mb), LSTD (°C), EAJSI (m/s).

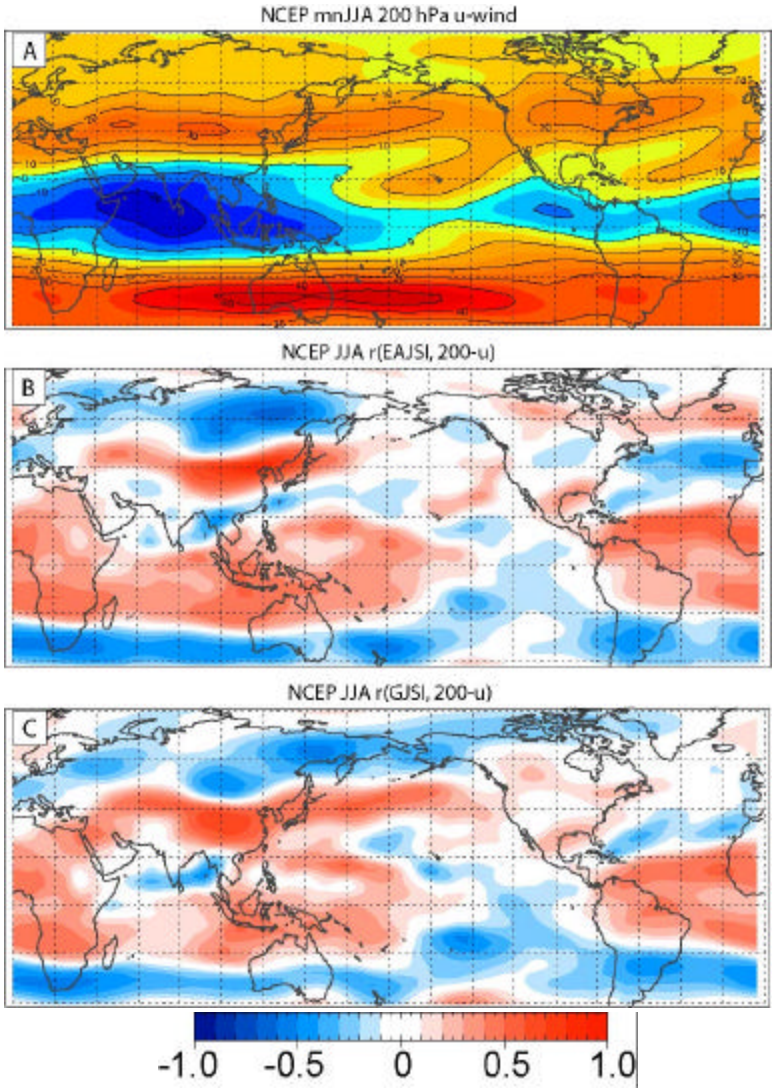

Figure 4.17. Observed (NCEP) zonal winds at 200 hPa (a) averaged for JJA from 1961-1990. The same wind global field is correlated from 1948 – 2003 with respect to (a) EAJSI, and (c) GJSI. In figures (b) and (c) positive and negative correlation r-values are plotted in red and blue, respectively, with contour intervals at 0.1 and no contour at zero. Individual correlation values greater than 0.3 (or less than -0.3) are significant with roughly 95% confidence (not accounting for multiplicity, the testing of multiple hypotheses).

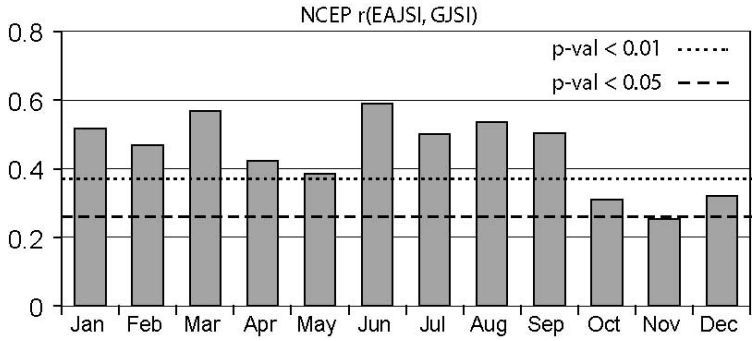

Figure 4.18. Monthly correlation r-values between EAJSI and GJSI (1948 – 2003).

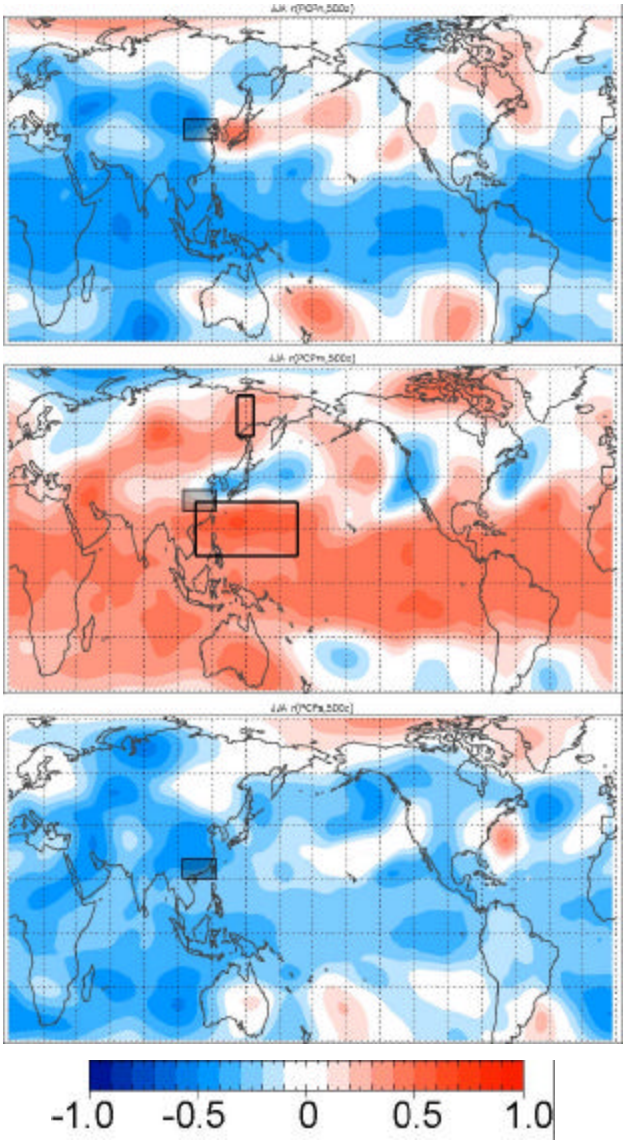

Figure 4.19. Map of correlations between 500 hPa geopotential heights and standardized regionally averaged precipitation in NEC (top), YRV (center) and SEC. For reference, precipitation regions are marked by translucent grey boxes, while the Okhotsk High and WPSHz index domains are also shown in the center plot. Individual correlation values greater than 0.4 (or less than -0.4) are significant with roughly 95% confidence (not accounting for multiplicity, the testing of multiple hypotheses).

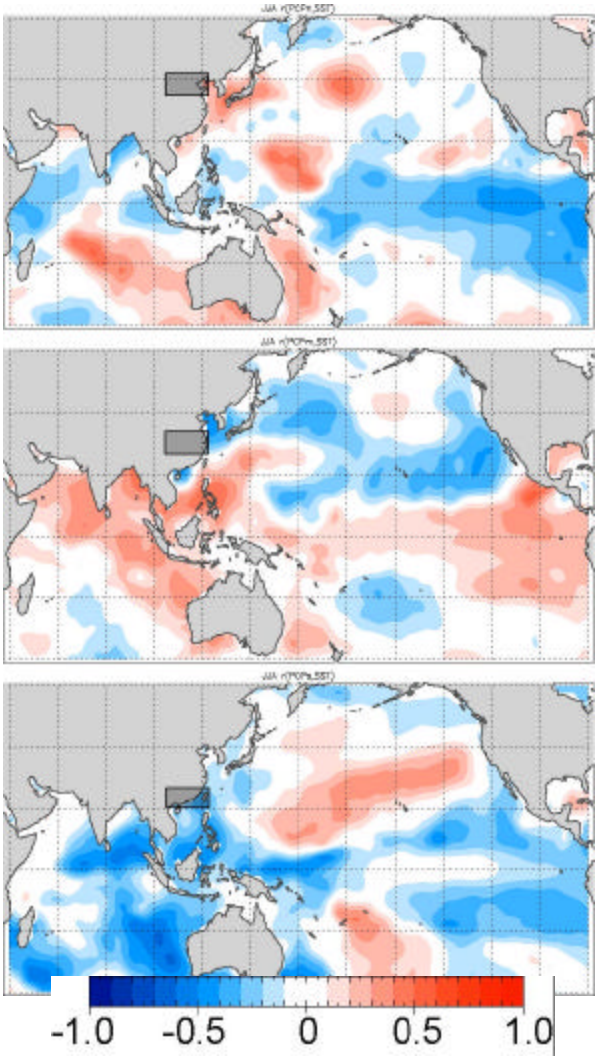

Figure 4.20. Map of correlations between SSTs and standardized regionally averaged precipitation in NEC (top), YRV (center) and SEC. For reference, precipitation regions are marked by translucent grey boxes. Individual correlation values greater than 0.4 (or less than -0.4) are significant with roughly 95% confidence (not accounting for multiplicity, the testing of multiple hypotheses).

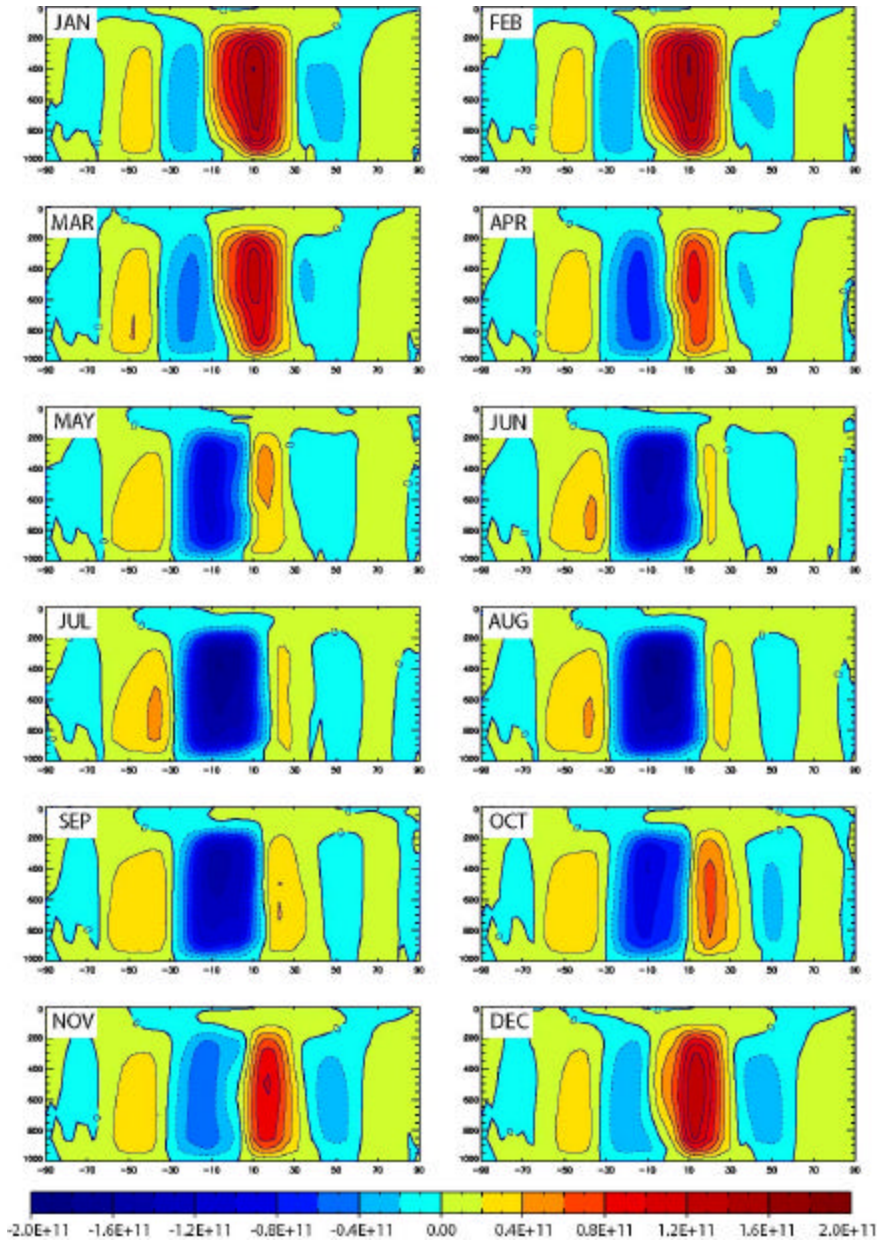

Figure 4.21. Observed monthly zonal mean meridional stream function at all latitudes and all levels of the atmosphere in units of kg s^{-1} (NCEP reanalysis data, 1948 – 2003). The x-axes range from 90°S to 90°N (left to right) and y-axes range from 0 to 1000 hPa pressure levels (top to bottom). Positive values (warm colors; solid contours) represent clockwise overturning circulation, while negative values (cool colors; dashed contours) represent counterclockwise overturning circulation.

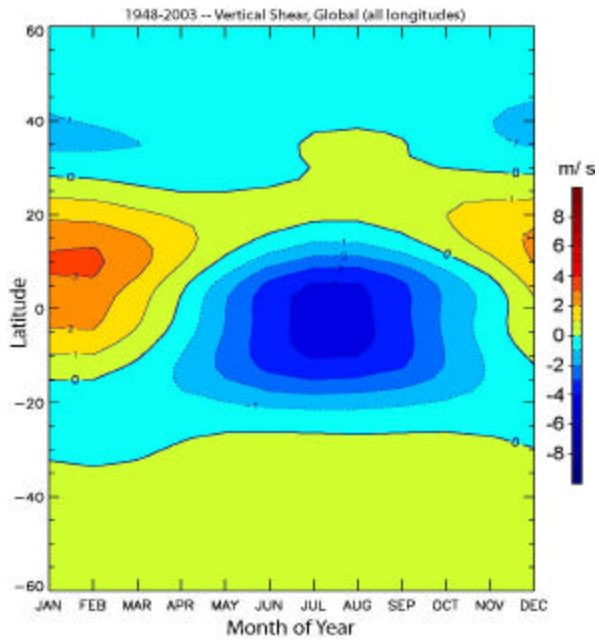

Figure 4.22. Hovmoller diagram of observed monthly zonal mean vertical wind shear from 60°N to 60°S, averaged over all longitudes (NCEP reanalysis data, 1948 – 2003). Vertical wind shear is defined as the difference between meridional wind velocity at 200 hPa and 850 hPa and is expressed here in units of m s^{-1}. Positive values represent anomalous northward wind anomalies at 200 hPa and/or anomalous southward wind anomalies at 850 hPa (and visa versa).

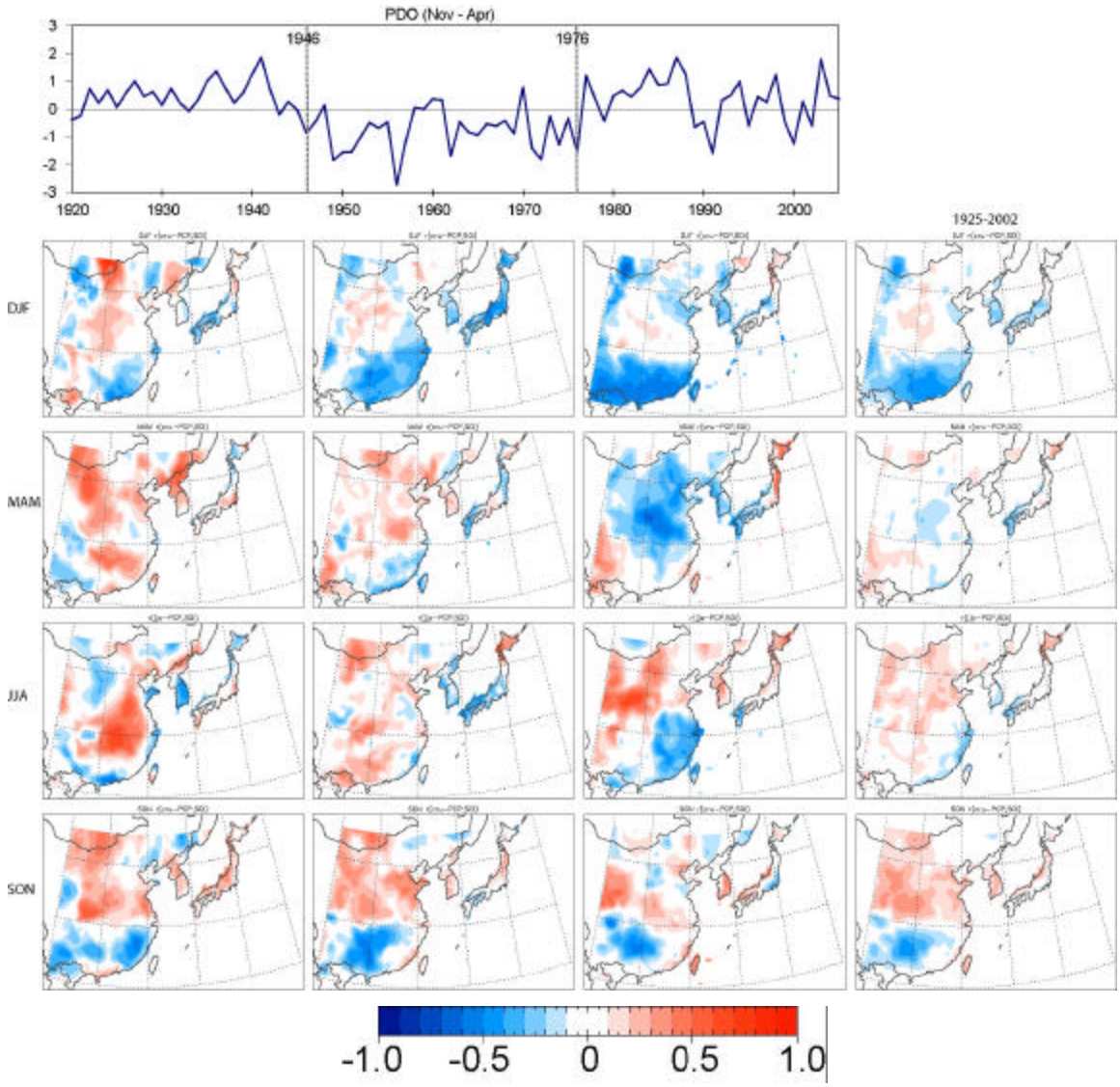

Figure 4.23. The stationarity of the ENSO signal in precipitation across East Asia is illustrated through correlation plots during three different eras. Time series at top plots the average PDO index from 1920 -2005 (Nov. – Apr.), with the two major transition points, at 1946 and 1976, marked by dashed vertical lines (Mantua et al., 1997). Bottom 16 panels show r-values from simultaneous correlation analyses between seasonally averaged CRU precipitation and the SOI index: 1925-1946 (left); 1947-1976 (center left); 1977-2002 (center right); 1925-2002 (right); from top to bottom DJF, MAM, JJA, and SON. Positive correlations signify wetter conditions during La Niña events, drier El Niños, and visa versa. Individual correlation values greater than 0.3 (or less than -0.3) are significant with roughly 95% confidence (not accounting for multiplicity, the testing of multiple hypotheses). N*ote: the time series of the PDO index is displayed for illustrative purposes only and was not used for any of the correlation analyses shown here.*

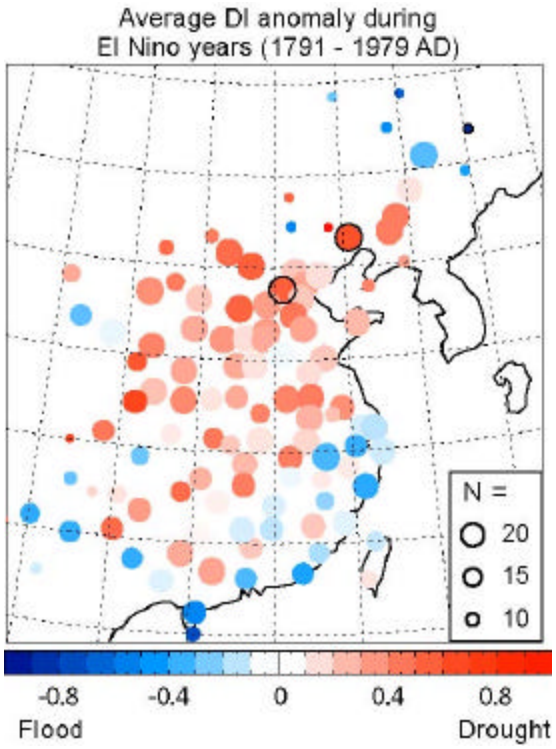

Figure 4.24. Average DI anomalies during El Niño events, for the period from 1791 – 1979 AD. As reflected on the color-scale, positive DI anomalies indicate more frequent drought (red) while negative DI anomalies indicate more frequent flooding (blue) during El Niño years. The diameter of each circle is proportional to the total number of years (N) during which DI data were available for this analysis (maximum N = 24). Circles with black perimeters are significant with at least 95% confidence, based on individual student t-tests.

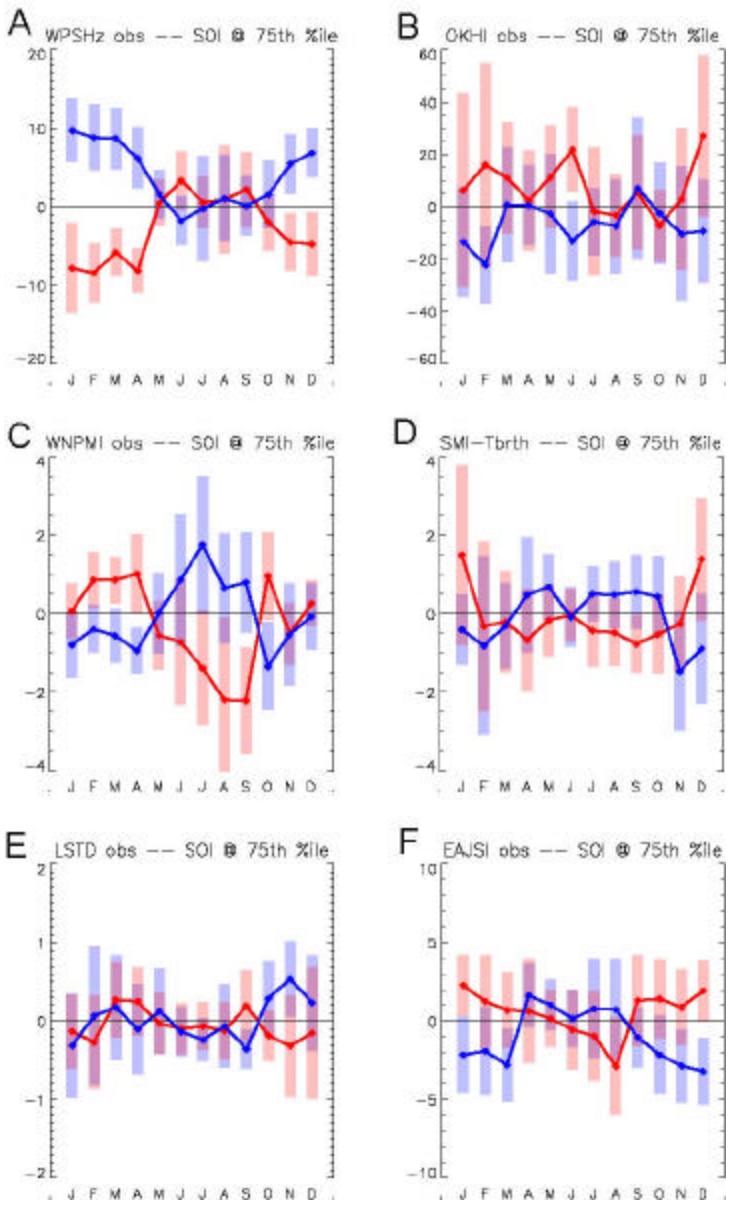

Figure 4.25. Composite monthly index anomalies through the annual cycle (January - December) during El Niño (blue) vs. La Niña (red) conditions. Composites are computed during months concurrent with the bottom 25th and top 25th percentiles of the SOI (n = 12/ month). Note that months with SOI values in between the 25th and 75th percentiles are excluded from the analysis. Color-coded error bars represent the 95 percent confidence intervals for the true mean during each month (based on 2× the standard error).

CHAPTER 5

ANALYSIS OF THE OBSERVED RESPONSE TO VOLCANIC FORCING

In the broadest sense, this study examines the effect of radiative forcing from stratospheric aerosols on climate with consideration to both direct and indirect, or dynamical, mechanisms. Unlike the vast majority of previous studies, the focus of this study is unique for exploring a precipitation – as opposed to temperature – response. While results from a limited number of studies have suggested that the influence of volcanic forcing on regional-scale hydroclimate is weak, these efforts have generally been confounded by the occurrence of simultaneous El Nino events and the short time period covered by the instrumental record.

The paleoclimate record provides an opportunity to explore these questions from a new perspective and, more specifically, to consider the effects of volcanic forcing of a greater magnitude than anything experienced during the 20th century. For example, early 19th century marine air temperature measurements taken on merchant ships across the globe suggest that the global cooling caused by Tambora and the unknown eruption of 1809 was significantly larger than the climatic response to either Pinatubo, in 1991, or Krakatoa, 1883 (Chenoweth, 2001). Under higher forcing and an increased climatic response, the signal to noise ratio in terms of regional hydroclimate is expected to increase.

5.1. Brief review of hypothesized mechanisms for a regional hydroclimatic response

As discussed in Chapter 2, previous studies have explored several dynamical mechanisms for regional climatic effects from volcanic forcing, including a possible

trigger for El Niño (Mann et al., 2005), the positive phase of the Arctic Oscillation in winter (Stenchikov et al., 2002), and the present study examines the possibility of a dampening of tropical Hadley circulation. Also, the previous chapter has demonstrated that variability in regional-scale summer rainfall associated with the EAM has exceptional global-scale teleconnections with respect to middle atmospheric pressure level heights and the strength of the subtropical jet.

In addition to these dynamical considerations, the most obvious mechanism for a direct response in precipitation over eastern China is through the blocking of short-wave radiation and a reduction in evaporation at the surface (Robock, 2000). This mechanism seems particularly likely given this study's focus on the summer season, when meridional temperature gradients are weaker and regional-scale precipitation variability is *generally* driven less by global-scale teleconnection patterns or large-scale organized weather systems (notwithstanding the global-scale teleconnections associated with the EAM system). Still, the vast majority of rainfall over eastern China occurs in the summer season when a significant portion occurs through convection from radiative surface heating and associated atmospheric instability (Ding, 1994). Furthermore, as noted in Section 2.3.3., precipitation is known to be measurably sensitive to direct short-wave forcing (Lambert et al., 2004). In comparison, the global *temperature* response considered in most studies (e.g., Briffa et al., 1998) is relatively persistent beyond the initial period of direct forcing, in part due to the high heat content of the oceans (Gleckler et al., 2006). Given these considerations, there is an *a priori* expectation for a direct and relatively immediate hydroclimatic response to concurrent – as opposed to lagged – SAOD forcing.

5.2. Zonal structure of global-scale volcanic forcing

Following the most explosive volcanic eruptions, volcanic aerosols are relatively quickly and efficiently distributed around the globe through advection from high velocity, predominantly zonal, stratospheric winds. Satellite observations taken with the SAGE II instrument reveal a stratospheric aerosol cloud from the Pinatubo eruption that was very well mixed zonally but had significant gradients in the meridional direction (Self et al., 1996; Stenchikov et al., 1998). Figure 5.1 shows that within a month of the June 15, 1991, Pinatubo eruption, significant quantities of stratospheric aerosols were already globally distributed. By September or October, the stratospheric aerosol optical depth (SAOD) was reaching its peak over the greater tropical region in both hemispheres. These measurements confirm that a global zonal mean representation of stratospheric aerosols from tropical or extra-tropical eruptions (e.g., Figure 3.12) is well justified for the purposes of most climatological studies on monthly, seasonal or longer time-scales (Hansen et al., 1978; Stenchikov et al., 1998; Robertson et al., 2000; Hansen et al., 2002; Ammann et al., 2003; Oman et al., 2005).

5.2.1. Event definitions: identifying "eruption years"

As noted in Chapter 3, most major eruptions from the past millennium are well dated with annual accuracy. Thus, the Ammann et al. (2006) SAOD dataset is considered appropriate for use in this observational study. Additionally, an updated version of Crowley's (2000) volcanic radiative forcing series, published by Mann et al. (2005) is used in conjunction with the Ammann et al. (2006) data as an independent check on the timing of tropical eruptions from 1000 – 2000 AD, since the timing for some eruptions

has been adjusted by one or two years (see Table 2.1). As such, for the purpose of studying the observed climatic response to tropical eruptions, appropriate adjustments were also made to the timing of some eruptions in the monthly Ammann et al. (2006) SAOD dataset.

After making these temporal adjustments, thresholds for peak SAOD loading intensity were chosen to select years, seasons or months with the highest forcing from tropical eruptions during a given period of analysis. As noted above, this study's interest in convective precipitation motivates a methodology that focuses on identifying a direct climatic response during months and seasons with maximum short-wave radiation forcing. For example, Figure 5.2 shows an annual time series of SAOD averaged from January to December over the tropical region (24°N to 24°S) and forcing years within the top 99th percentile are highlighted in red. Then composites of the observed (or modeled; see Chapters 6 and 7) climatic response to high volcanic forcing are created through the averaging of data anomalies during the years or seasons or months with maximum volcanic forcing. For example, when an analysis is focused on the summer season response, an annual-resolution forcing time series is created by averaging tropical SAOD values from May to September (or June to August) to identify the summers with the highest (e.g., 99th percentile) forcing over a given period of time. Then, data anomalies during those seasons with peak forcing are averaged into composites to deduce the typical climatic response.

It should be made clear that when a climatic response is considered on a monthly (or seasonal) basis that specific years selected for inclusion in each monthly (seasonal) composite depends in part of the seasonal timing of each eruption. For example, due to

the spring and summer timing of most major tropical eruptions during the period from 1900 to 2000, monthly composites for November would generally reflect average conditions during the calendar year of the eruption: 1902, 1963, 1982 and 1991 (selected based on the top 96th percentile of SAOD). On the other hand, January composites from the same analysis would include monthly data from the following calendar year: 1903, 1964, 1983, and 1992.

Due to the nature of the Ammann et al. (2006) parameterization scheme, this method is guaranteed to only select tropical eruptions, excluding years with even the largest extra-tropical events. Also, note that some eruptions are so large (e.g., Tambora) that high aerosol loading from a single eruption can persist into the following year such that consecutive years can be classified as "high forcing years." However, since each paleoclimate reconstruction generally has a unique record length and covers a slightly different era, not all analyses include the exact same eruptions – but nearly all include the events listed in Table 2.1.

To provide additional testing for the validity of certain results, some analyses in this chapter are also based on the IVI (Robock and Free, 1995, 1996). As noted in section 2.4.1., the VEI discretely rates the power of eruptions on the scale of 1 (lowest) – 8 (highest), while the IVI is a continuous index of radiative forcing derived from sulfate content and acidity from bi-polar ice-cores. Thus, to consider the climatic effects of multiple eruptions, Adams et al. (2003) discretized the IVI data on a scale parallel to the VEI so that individual years could be more easily categorized according to varying degrees of radiative forcing. Supplemental material from Adams et al. (2003) included Tables (S6 and S8) listing years with minimal and/or large radiative forcing according to

IVI data, and the present study occasionally employs these data to classify "high forcing years" (Table 5.3).

5.3. Zonal structure of the global-scale climatic response

As discussed in Chapter 2, the direct radiative effects of volcanic aerosols from tropical eruptions typically cause stratospheric warming (for up to two years) and global cooling in the troposphere (for up to three years), particularly in the northern hemisphere tropics and subtropics during summer (Briffa et al., 1998; Robock, 2000). In addition to these direct radiative impacts, stratospheric aerosol forcing causes indirect, or dynamic, climate perturbations on global to regional scales. For instance, both modeling and empirical studies have shown that the zonal structure of stratospheric aerosol forcing from tropical eruptions produce meridional temperature gradients – aloft and near the surface – that trigger Northern Hemisphere winter circulation patterns that favor the positive mode of the Arctic Oscillation (AO; Chapters 2, 3 and 4). Thus, despite the negative global energy balance caused by the aerosol cloud, the result is stronger mid-latitude westerlies that generally advect warm, moist marine air over extra-tropical northern hemisphere landmasses, bringing increased winter temperature anomalies to these regions, particularly northern Europe (Shindell et al., 2004; Stenchikov et al., 2006).

Figure 5.3. shows the observed monthly AO response to four major tropical eruptions between 1899 and present. Due to the small sample size most of the results are not statistically significant, though they generally confirm earlier studies that have found

a positive AO response in the winter season (Shindell et al., 2004) and no discernable dynamical response in summer (Robock, 2000).

5.3.1. Global tropical precipitation, Hadley circulation and the subtropical Jet

Previous studies have observed drying over tropical land areas following major 20th century eruptions but have also noted that this signal could be attributable to concurrent El Nino events, which also brings drought to many low latitude continental regions (Adler et al., 2003), particularly in the northern hemisphere. Generally confirming those results, Figure 5.4, plots global monthly zonally averaged land CRU precipitation beside composite anomalies during months with high volcanic forcing, from 1902 and 1999. While only a few monthly anomalies are statistically significant, this figure clearly shows a tendency for reduced tropical precipitation in the months with simultaneous high volcanic forcing. A parallel analysis of precipitation anomalies during El Niño years shows similar but not identical results (not shown).

However, in addition to any dynamical influences from ENSO, a plausible explanation for these negative low-latitude precipitation anomalies (Figure 5.4) could be that forcing from tropical eruptions has caused the blockage of short-wave radiation, reduced evaporation (Robock and Liu, 1994) and dampened tropical convection. If such a mechanism were at play on the global-scale then it would presumably also be reflected in changes in global Hadley cell circulation. This is because lower quantities of atmospheric moisture would decrease the amount of latent heat released from condensation through tropical lower-level convergence and this latent heat is an essential driver for Hadley Cell overturning (Webster, 2005).

Attempting to address this question, Figure 5.5 compares global monthly mean vertical wind shear (a) along with composites and individual anomalies during particular years of interest. To interpret the following results it is helpful to bear in mind that during the NH winter (~Dec. – Mar.) the convection that largely drives vertical motion in the NH cell is generally located in the vicinity of the Inter-topical Convergence Zone (ITCZ), south of the equator. Alternatively, during the SH winter (~Jun. – Sep.), convection driving the SH Hadley Cell is located north of the equator, as the ITCZ swings north during NH summer. To visualize these seasonal changes from another perspective, it is also instructive to review monthly streamfunction diagrams in Figure 4.21. Low-latitude precipitation changes in Figure 5.4 (left panel) also reflect this intra-annual cycle of tropical climate dynamics.

To further clarify the following analysis, Figure 5.5b is a composite of monthly vertical wind shear anomalies during 10 years with the lowest SOI values (El Niño conditions), for the period between 1948 and 2003. In agreement with results from Oort and Yienger (1996), this figure illustrates typical Hadley circulation behavior during El Niño years, where meridional overturning is strengthened in the NH cell and (to a much lesser degree) in the SH cell during their respective winters. This relationship is confirmed in part by the positive, highly statistically significant, negative correlation between HCIN-sf and SOI in the winter season ($r = -0.44$, p-value = 0.001). However, contrary to Oort and Yienger (1996), Tables 4.2 – 4.5 indicate that this is the only robust link between ENSO and any of the Hadley cell indices (NH or SH, DJF or JJA) during the period from 1948 – 2003.

Figure 5.5c is a composite of monthly vertical wind shear anomalies in response to three major tropical eruptions. Figures 5.5d, e and f plot individual monthly vertical wind shear anomalies during peak SAOD forcing from the Agung, El Chichón and Pinatubo eruptions, respectively (note, Figure 5.5c is the composite average of Figures 5.5d-f). Comparing Figures 5.5e-f, with Figure 5.5b, it is clear that tropical (and extra-tropical) Hadley circulation following the El Chichón (17°N) and Pinatubo (15°N) eruptions was anomalously strong in a manner very similar to typical El Niño conditions (as described above). Following both of these NH eruptions, the NH cell was anomalously strong during its dominant season for overturning (Dec. – Apr.), while the SH cell was also slightly stronger during its winter season (May – Oct.). However, it is remarkable that conditions following the Agung (8°S) eruption (Figures 5.5d) are nearly opposite to those in Figures 5.5e-f, apparently reflecting a weakening in both Hadley cells during their respective winters.

Thus, vertical wind shear anomalies during the year following the Agung eruption are generally consistent with the hypothesized Hadley cell dampening mechanism. However, some discussion is needed to explain why these anomalies occurred following Agung, but not in response to the El Chichón or Pinatubo eruptions. Firstly, it is noteworthy that the 1963 El Niño event was shorter than and not as strong as the 1982 and 1992 events (see Figure 3.1); so, the global-scale climatic "forcing" from the 1963 El Niño may have been relatively weak. Also, what made the Agung eruption unique – compared to other recent tropical eruptions – is that its' stratospheric aerosols remained primarily in the SH, causing much greater radiative forcing in that hemisphere (Andronova et al., 1999; Hansen et al., 2002). So, it may be significant that the NH cell

displayed a greater response during the winter season (Dec. – Apr.; Figure 5.5d), which is when SH convection drives Hadley circulation. It could also be that the uniquely robust link between the NH Hadley cell and the SOI during this season is particularly sensitive to short-circuiting caused by disproportionate SAOD forcing in the SH.

As discussed in Chapter 4, the velocity of the global subtropical jet streams (at 200 hPa) is positively correlated with the strength of the tropical Hadley circulation. This relationship is well established and true for both hemispheres (Oort and Yienger, 1996), so it is logical that any forcing that dampens or intensifies global Hadley Circulation would have a dynamical impact on subtropical climate. However, with the only apparent effect on Hadley circulation occurring in the NH winter, this type of response could be of relatively little importance to summer hydroclimate in East Asia.

5.4. Regional response in eastern China

The remainder of this chapter attempts to improve our understanding of how volcanic eruptions have historically affected climate in eastern China. The remaining sections draw upon the literature and from what was learned through analyses of the global climatic response with regard to the AO, Hadley circulation – despite the confounding ENSO factor. From the modern instrumental record a number of studies have examined spatial patterns in the temperature response throughout the northern Hemisphere (Robock and Mao, 1995; Kelly et al, 1996; Yang and Schlesinger, 2001; Shindell et al., 2004) yet few have identified particularly exceptional or noteworthy impacts in China. Largely confirming those findings, the top two panels of Figure 5.6 plot composites of winter and summer surface air temperature anomalies during high

forcing years between 1948 and 1999. Following a methodology similar to Robock and Mao (1995), the bottom two panels show the same analysis, but with the SOI signal removed on a grid-point by grid-point bases. Also, a Lanczos high-pass filter was applied at each grid-point to remove variability with periodicities longer than 10-years. Thus, Figure 5.6 shows the spatial distribution of the temperature response to late 20th century volcanic forcing while also providing a simple estimation of the sensitivity of these results to the occurrence of simultaneous El Niño events.

From the paleoclimate record, nearly all related research with specific relevance to China has focused on the aftermath of the Tambora eruption, which occurred only 6 years after an unknown eruption in 1809 and during the Dalton solar minimum. Huang (1992) noted persistent wetness, flooding and, by implication, cold conditions throughout China – particularly in the north – in the summer 1816. Zhang et al. (2006) found extensive evidence for summer and fall crop failures in central and northern regions, some of which Zhang et al. (1992) attributed to unusual early and late season frosts. There was also evidence for a strengthened winter monsoon, with unusual snow fall occurrences in the south and exceptionally strong northwesterly winds. Qun (1988) found that many of the coldest summers during the past 500 years occurred within 2 years of volcanic eruptions.

5.4.1. Precipitation and temperature

As noted above, the 20th century temperature response in East Asia was relatively subtle compared with some other regions. However, statistically significant negative anomalies were apparent during the winter and summer seasons over some part of the

East Asian region and these results do not appear to have been highly sensitive to the phase of ENSO (Figure 5.6). To explore this question in greater detail for eastern China specifically, using a longer dataset and with consideration to the hydroclimate response, the gridded CRU dataset (0.5° × 0.5°; land; Mitchell and Jones, 2005) is employed for the period from 1902 – 1999. This extended record is particularly useful because it also allows for consideration of the climatic response following the active volcanic year of 1902 (3 eruptions: Santa Maria, Pelée and Soufriere St. Vincent). This is additionally beneficial because El Niño conditions were apparently not prevailing throughout the period from 1902 to 1904 (Figure 3.1).

Following the same methodology used to generate Figure 5.6, the four panels of Figure 5.7 contain composite plots illustrating the magnitude of the regional temperature response during DJF and JJA, alongside the same analyses on gridded data from which the SOI signal and low-frequency variations were removed (Robock and Mao, 1995). From these results it is confirmed that winters during high forcing years are typically 0.5°C colder in western inland locations while the signal may be reversed in northeastern provinces and over the Korean Peninsula. Interestingly, this later result is also consistent with the fact that winter temperatures in Japan were relatively unaffected by the Tambora eruption (Harrington, 1992), suggesting a dynamical mechanism (e.g., positive AO response) could be contributing to this observed regional response in East Asia. Meanwhile, summer temperatures in eastern China were only marginally affected (Figure 5.7c), particularly when the SOI signal was removed (Figure 5.7d).

Similarly, Figure 5.8 illustrates the regional precipitation response during DJF and JJA, with and without SOI signal removal. In winter, when precipitation is sparse and

mostly confined to the south there is an apparent increase in rainfall in that region; however this response mostly vanishes after accounting for the ENSO factor (Figure 5.8b), which is not surprising given results from Chapter 4. In the summer, there is evidence for wetter conditions in central and northern regions (~1 mm/day; ~20% increase), particularly after the SOI signal is removed. In the south there is evidence for drying, although this is less obvious after accounting for ENSO. It should be noted that none of these results are statistically significant, in part due to the exceptionally high interannual variability that is typical for the region, but they provide some clue as to what might be expected through further analyses of the dynamical response and from the paleoclimate record.

5.4.2. Regional-scale monsoon indices

To better understand what regional-scale dynamical mechanisms might be responsible for the observed surface climate anomalies, this section examines the response by various regional monsoon indices described in Section 4.2. In Figure 5.9, monthly composites of monsoon index anomalies are plotted along with 95% confidence levels for the true mean in each month. Due to the small sample sizes of each composite (n = 3/ month) many of the results are not statistically significant, however general patterns can be observed and anomalies during consecutive months may be indicative of a response during a particular season. The clearest signal appears to be statistically significant positive WPSHz anomalies and accompanying slightly negative anomalies in the WNPMI during winter months. There is also evidence for a weakening in the EAJSI, also during winter. Otherwise, the responses are highly variable and generally not

statistically significant. Also, of particular interest to the present study is that there is little evidence for statistically significant or seasonally coherent responses during the summer monsoon season (May – Aug.). The one exception is consistently positive WNPMI anomalies, from June – September.

To test the sensitivity of these results to the ENSO factor, the SOI signal was linearly removed from each monsoon index during each individual month and the analysis was repeated. Figure 5.10 shows results clearly indicating that the SOI signal was the dominant factor contributing to all noteworthy results shown in Figure 5.9. So, while results from this section are generally inconclusive, they clearly illustrate the challenge of assessing the regional-scale dynamical response to volcanic eruptions from the available instrumental record – due to the confounding ENSO factor. This highlights the necessity to draw from the paleoclimate record and dynamical global climate model simulations to help answer the primary questions in this chapter.

5.4.3. The paleoclimate response in East Asia

To explore the observed climatic response to explosive tropical eruptions on longer time-scales, in response to relatively greater forcing, available paleoclimate data are examined. Before detailing the hydroclimate response, which is the primary focus of this study, following is a brief summary of the apparent temperature response in eastern China. As noted in Chapter 3, temperature reconstructions in this region are generally only available at decadal resolution. So, prior to making comparisons with those records, SAOD forcing data were averaged over equivalent time-scales (e.g., 1380 – 1389, 1390 – 1399… etc). Figure 5.11 plots available temperature time-series along with decadally

averaged tropical SAOD forcing to illustrate their covariability during the period from ~1380 to 1980 AD. Note that for illustrative purposes the SAOD data were first converted to Wm^{-2} units, based on the simple empirical formula (equation 2.2) established by Hansen et al. (2002). Thus, positive correlation r-values reflect the fact that decades with more negative radiative forcing from tropical eruptions generally accompany decades with lower average temperatures.

Results from simple pair-wise correlation analyses are displayed on Figure 5.11 and, as expected, all r-values are positive. Interestingly, the only statistically significant correlations between SAOD forcing and temperature are noted in the northeast region, in the vicinity of Beijing. Though the volcanic forcing index is derived from SAOD data in tropical regions only, the temperature response in southeastern China appears to be relatively weaker and statistically insignificant. The strongest example for this is the early 19th century, when there were three large tropical eruptions (1809, 1815, and 1835), northeastern China was consistently cold while a temperature response in the south is not apparent. While the decadal time-scale of this temperature analysis is problematic, given the time-scale of the forcing, possible explanations for these findings are proposed below, in the context of results from the paleo-hydroclimate analyses.

For the remainder of this chapter, paleoclimate reconstructions of drought vs. flooding, based on historical documentary records, are considered. For this part of the analysis, DI data from 120 sites across eastern China are averaged during high volcanic forcing years to examine the spatial distribution of the response. Then WI time series are used to estimate the statistical significance and stationarity of this volcanic signal in regional hydroclimate. Table 5.1 lists the summers (May – Sep) during which Ammann

et al. (2006) SAOD forcing was in the 98th percentile; thus, a total of 20 eruptions were selected for analysis during the period from 950 – 1999 AD. Notice that nearly all of the eruptions during the later half (1470 – 1999 AD) of the analysis are attributable to eruptions of a specifically known origin, while only one eruption during the early part of the record (950 – 1479 AD) has a known source. This highlights the fact that relatively little confidence can be placed in results and conclusions drawn from analyses of the response to earlier eruptions.

To further test the validity of these results the same analyses were carried out, except that the average DI and WI response was calculated from composites of high forcing years during which "large" IVI values were identified by Adams et al. (2003; Table 5.2). Using this approach, a total of 12 eruptions were selected for analysis during the period from 1650 – 1999 AD. While there is some overlap, seven out of the 12 years selected for analysis using the IVI data are independent of the eruption years identified using Ammann et al. (2006) SAOD data (compare Table 5.1. with Table 5.2). Finally, to consider the possibility of a lagged hydroclimatic response to high forcing, a superposed epoch analysis is employed at the end of subsection 5.4.2.1.

5.4.3.1. The Drought Index (DI)

Figure 5.12a. shows average DI anomalies at each site during the ten highest volcanic forcing summers – based on Ammann et al. (2006) SAOD – from 1470 – 1979 AD (Table 5.1). Figure 5.12b. shows results from the same analysis, except that composite years were selected based on the IVI (Table 5.2). Since DI reconstructions are generally incomplete at many locations (Figure 3.4), only sites with available data during

at least five eruption years are included; results reflect the average DI response during available years. As noted in the figure caption, larger circles represent sites from which more data are available and, thus, where results are generally more robust. Statistical significance is roughly estimated based on simple individual t-tests; circles outlined in black are significant with at least 95% confidence. However, it should be emphasized that the null hypothesis (that average anomalies during high forcing years are no different from the long-term mean) is being tested roughly 75 times in each panel, so, by random chance alone, one would expect to reject the null-hypothesis in 3 to 4 locations. Still, the response appears to be significant at 6 sites in Figure 5.12a and there is a spatial coherence to the average response in both panels that is suggestive of a clear signal. This somewhat marginal signal is suggestive of generally wetter conditions in the north and drier conditions in the south.

To quantify these findings in more detail, beyond simple averaging, the frequencies of drought vs. flooding are considered separately. Figures 5.13a and 5.13c plot the percentage of high forcing years with DI values equal to 4 or 5 (drought or severe drought), while Figures 5.13b and 5.13d plot the percentage of high forcing years with DI values equal to 1 or 2 (severe flooding or flooding). As above, separate analyses are carried out such that years included in Figures 5.13a and 5.13b were selected based on Ammann et al. (2006) SAOD data (N = 10; Table 5.1), while years included in Figures 5.13c and 5.13d were selected based on IVI data (N = 12; Table 5.2). Note that relatively darkly colored circles outlined in black highlight sites where drought was three times more likely than flooding under the high forcing conditions, or visa versa. For example, according to results in Figure 5.13a, for the southern region around Hunan province it can

be concluded that drought or severe drought occurred more than 50% of the time and was at least three times more common than flooding, in response to high volcanic forcing. Recall that under "normal" conditions, drought or severe drought can generally be expected to occur between 25% and 50% of the time at any given location (Table 3.1; Wang and Wang, 1994). The general conclusion that is reached here is obviously consistent with findings discussed earlier in this section, suggesting relatively wetter conditions in the north and drier conditions in the south.

5.4.3.2. The Wetness Index (WI)

To further estimate the statistical significance of results based on the DI record and to consider their temporal stationarity, the longer WI time series are analyzed and results are compared with the above findings. Recall from Chapter 3, the WI records consist of three annual time series, each representing drought vs. flood frequency in NEC, YRV and SEC. Derived from the same original data source, WI time series are directly comparable to the DI data during the latter halves of the WI records (from 1470 to 1999); so, the WI and DI datasets are somewhat redundant – although not identical – in this regard. Also, recall that the sign of the WI time series is reversed relative to the DI data (e.g., positive values indicate floods; negative values indicate drought).

Figure 5.14 shows the average WI response to peak SAOD forcing (98th percentile; see Table 5.1) during two eras from 950 to 1469 AD, from 1470 to 1999 AD, and over the entire period of the WI records (950 – 1999 AD). Only the Ammann et al. (2006) SAOD data are used for this portion of the analysis because they are available over the entire period of the WI record. Here, the 95% confidence for the true mean of

each response population (N=10) is estimated as two times the standard error for that population. Results indicate that summers with concurrently high volcanic forcing are generally wetter in the north and drier in the south, particularly when the entire period of record is considered (Figure 5.14), although this statement is also true in a relative sense during both halves of the WI records (compare Figure 5.14a with Figure 5.14b). Note that the response in the YRV region is generally neutral. Also, as expected, these results confirm findings presented above (Figures 5.12 and 5.13), indicating that roughly 95% confidence can placed in the conclusion that high volcanic forcing generally leads to drought in SEC and flooding in NEC during the last millennium.

5.4.3.3. An unconventional "epoch" analysis

The final stage in this section on the hydroclimatic response involves an unconventional form of epoch analysis that was designed to accommodate the limitations of the paleoclimate data while considering the possibility of a lagged response to SAOD forcing. Some specific issues that make the following methodology exceptional are that 1) the majority of annual precipitation in this region is generally limited to the summer season, thus making this season of paramount interest, 2) the paleoclimate data (WI) are only available at annual resolution, and 3) the SAOD forcing data are available at monthly resolution. Thus, given the relatively high resolution of the paleoclimate data and the fact that the nature of the climatic response is only desired for the summer season, the basic methodology was to hold the response season (summer) constant and to change the seasonal timing of peak radiative forcing relative to the summer response.

For instance, in the center of Figure 5.15 – inside the solid vertical rectangular box – one can see the mean WI response during the 10 years between 1470 and 1979 AD when radiative forcing was highest during the summer. This is basically the same result as Figure 5.13b, except that the Ammann et al. (2006) SAOD data were averaged from June to August – as opposed to May to September. Moving one step to the left of that box, the column labeled MAM shows mean WI composites from the 10 years with the highest radiative forcing during the spring season (March to May). Table 5.3 lists the actual years included in each off these composites and naturally, there is a good deal of overlap between the years included in the JJA and MAM examples explained above. However, due to the disproportionate representation of spring season eruptions during this time period (Table 2.1) and the fact that SAOD peaks 4 months after the time of eruptions (then decays relatively slowly), the columns marked JJA and SON actually include nearly all of the same years in their WI composites (as also reflected in their nearly identical responses). Outside of the center rectangle in Figure 5.15, years included in the WI composites are determined by simply adding or subtracting one or two years to the years included in the zero year composites (inside the rectangle). Please see the captions for Table 5.3 and Figure 5.15 for further details.

The confusing thing about this methodology is that most conventional epoch analyses are presented as time-series that are plotted relative to a "key date" (e.g., January in the year of an eruption). Thus, a lagged response to a given phenomenon is reflected by persistent anomalies to the right of this key date in the time series, moving forward through time. However, lagged responses in Figure 5.15 would be reflected by WI anomalies to the left of the center rectangle, because, in this case, it is the forcing

factor that is lagged relative to the response, as opposed to convention. The results presented here generally confirm the hypothesized response as well as findings from previous sections, providing little evidence for a lagged hydroclimate response to maximum forcing in prior seasons or years. These results further suggest that the timing and magnitude of eruptions are important factors to the process of resolving a hydroclimatic response in eastern China.

It should be noted that a more traditional superposed epoch analysis was also attempted, with composite plots of 10-year time series generated by averaging 10-year segments of WI and DI data relative to January of major eruption years (e.g., Kelly et al., 1996, Adams et al., 2003). However, results from these analyses were marginal and no apparent signals were noted. It is possible that this negative result reflects the fact that the summer season hydroclimatic responses resolved through the above analyses are truly most sensitive to maximum instantaneous radiative forcing. Perhaps the technique of creating annual composites relative to January of the eruption year – as opposed to the actual month or season of the eruption – is problematic for this study's focus on a summer season response. This is because late summer eruptions, such as Pinatubo, can create significant peak radiative forcing but if that forcing has diminished significantly by the time of the following summer monsoon season, then the overall impact could be minimal for the EAM.

5.5. Boundary conditions

5.5.1. Pacific SSTs as a context for Tambora era climate

Figure 3.7 plots six different (standardized) reconstructions of the PDO index during the century prior to instrumental records (1750 to 1850). The seventh time series, at the bottom of the figure, represents the average of all standardized indices and thus provides a measure of the level of agreement between these various reconstructions. With the exception of two decades 1) from 1750 – 1760 and 2) from 1790 – 1800, the all-index average is relatively flat and illustrates well arguments put forth by D'Arrigo and Wilson (2006) that PDO reconstructions based on data from limited portions of the Pacific Ocean basin are unlikely to realistically capture its true pre-instrumental climatic history. Still, the primary point of this brief discussion is to simply point out that the broad-scale context for the 1809 and Tambora eruptions – from the perspective of North Pacific SST boundary conditions – is not very well constrained despite numerous PDO reconstruction efforts (see Figure 3.7, between the vertical dashed lines).

As discussed briefly in Chapter 2, various historical records from the eastern tropical Pacific indicate that 1814 and 1817 were strong and moderate El Niño events, respectively (Quinn et al., 1987; Ortlieb, 2000). Also, based on sporadic early instrumental temperature and pressure observations, along with a wide variety of historical writings, Chenoweth (1996) concluded that La Niña conditions prevailed during the winter of 1815/1816. Given that summers following El Niño winters are generally drier in northern China (Chang et al., 2000a), an assumption of linearity in this teleconnection pattern suggests that wetter conditions could be expected in northern China following La Niña winters, including during the summer of 1816.

This issue of linearity deserves further discussion because most researchers studying teleconnections between ENSO and hydroclimate in eastern China pay particular close attention to the El Niño response but do not generally consider the regional response to La Niña. Yet, there is some compelling evidence in support of linearity. Primarily, statistically significant results in Figure 4.25 – wherein composites of monthly regional monsoon index anomalies were computed separately during opposite phases of the SOI – illustrate that the regional dynamical response to ENSO appears linear. For example, notice that indices with significant anomalies during El Niño years (e.g., WPSHz, Figure 4.25a) typically reflect an equal and opposite response during La Niña years. Furthermore, results from Song (1998) show that modes of wetness/dryness variability in eastern China correlate significantly with the Southern Oscillation Index (1851 – 1980), which obviously represents both cold (La Niña) and warm (El Niño) phases of the ENSO cycle. So, evidence for the occurrence of a La Niña event during the winter preceding the unusually wet summer of 1816 (Huang, 1992), is certainly worth noting in the context of the present study.

5.5.2. South China Sea marine air temperatures from 1808 - 1827

Available marine air temperature (MAT) observations from the South China Sea (SCS) provide the best available direct measurement of regional climate sensitivity to the 1809 eruption of unknown origin and the subsequent Tambora eruption in April, 1815. Figure 5.16 shows that seasonal mean cooling in the SCS region averaged between 1 to 2°C following each of these eruptions. This figure also plots the total number of temperature measurements corresponding to each seasonally averaged MAT anomaly.

Coincidentally, the greatest number of observations was made following the Tambora eruption, providing a relatively greater constraint on the actual MAT response to that event. These results are generally consistent with annually averaged MAT anomalies from thousands of individual measurements made throughout the tropics; however, not surprisingly, the magnitude of cooling in Figure 5.16 appears to be slightly greater than the average response calculated over larger regions (Chenoweth, 2001).

5.5.3. Tibetan Plateau snow cover and temperature

As noted in the Chapter 2, it is hypothesized that a decrease in short-wave radiation caused by increased SAOD could depress melting and effectively increase the persistence and average depth of snowcover on the Tibetan Plateau. This is important because recent studies have linked snow depth variability in the vicinity of the Dunde Ice Cap with spring and summer rainfall across eastern China. Specifically, variations in northeastern Tibetan Plateau snow depths during the winter and spring seasons are positively correlated with summer rainfall in the YRV and inversely correlated with summer rainfall in northeastern China – also, to a lesser degree, with rainfall in southeastern China (Quin et al., 2003; Zhang et al., 2004). The author is not aware of any published studies examining the effects of stratospheric aerosol forcing from volcanic eruptions on snowcover or snow depth on the Tibetan plateau.

To help answer this question, a composite analysis was conducted by averaging high-pass filtered Dunde A_n values during years (Jan. – Dec.) in which Ammann et al. (2006) SAOD forcing is in the top 96th percentile during the period from 1801 – 1986 (N=7). A parallel analysis was also conducted with respect to high-pass filtered $d^{18}O$

data. Figure 5.17 plots the filtered (a) A_n and (b) $d^{18}O$ time series along with reference markers for the high forcing years included in these composite analyses. Figures 5.17(c) and (d) respectively display composite analysis results, revealing a statistically significant decrease in net accumulation and a slight – though statistically insignificant – reduction in $d^{18}O$ values during high forcing years. To further test the significance and stationarity of this response, the same analyses were conducted separately during early (1801 – 1879) and later (1880 – 1986) sections of the ice core records (Figures 5.17(c) and (d)).

The year 1880 was chosen as a record bifurcation point because Davis et al. (2005) noted a "mode shift" in northeastern Tibetan Plateau climate around this time. During the Little Ice Age – prior to ~1880 – the Dunde A_n and $d^{18}O$ records varied largely out of phase with one another and exhibited significant differences in terms of their spectral frequencies. However, post ~1880 these records varied largely in phase with one another and their power spectra were in much closer agreement. Davis et al. suggested that the 1880 mode shift represented a transition from LIA to present-day conditions, where analyses of modern instrumental records confirm that cold years are generally also dry years on the Tibetan Plateau, and visa versa (Niu et al., 2004).

Results from the A_n and $d^{18}O$ composite analyses should be considered in the context of this mode shift. It should first be noted that, though statistically insignificant, the $d^{18}O$ response is generally negative (Figure 5.17(c)), indicating a weak tendency toward cooling following major tropical eruptions. Figure 5.17(c) suggests that annual net accumulation decreases significantly in response to volcanic forcing, particularly following the eruptions of Krakatau (1883) and Santa Maria (1902). Though contrary to the originally hypothesized response, this result is not surprising because, as noted above,

less precipitation generally occurs during colder years (Niu et al., 2004). Given the especially low average annual net accumulation rate on the Dunde Ice Cap (44 cm/yr, w.e.; Davis et al., 2005), it also makes sense that snowcover extent and persistence would be more limited by total snowfall than by average air temperatures. Finally, it is interesting to note that the A_n response was generally weaker and statistically less significant during the period prior to 1880, which is consistent with the notion that temperature and snowfall variations on the Dunde Ice Cap were relatively more in sync during the LIA (Davis et al., 2005).

5.6. Synopsis

Results from this study are in strong agreement with previous studies in finding that the occurrence of El Niño events during years following major tropical eruptions during the late 20th century significantly complicates efforts to deduce anything approaching a "pure" volcanic signal. Global-scale teleconnection patterns associated with ENSO include both zonal (e.g., Hadley circulation) and meridional (e.g., Southern Oscillation) components of global-scale atmospheric circulation.

Results from analyses of monthly zonal mean vertical wind shears (Figure 5.5) generally support the hypothesis that explosive tropical eruptions cause a weakening of global Hadley circulation. The overall strengthening of Hadley circulation that is characteristic of El Niño years was shown to be relatively dampened in the hemisphere in which the eruption occurred. This effect was most evident in the SH cell following the Agung eruption, whose short-wave forcing was relatively much greater in the Southern Hemisphere (Robock, 2000) and whose concurrent El Niño event was relatively weak.

Given the small sample size included in this observational portion of the study it will be beneficial to further explore this question using the CSM in Chapter 6. Unfortunately, since the SAOD forcing from tropical eruptions is always applied equally in both hemispheres in the CSM (Ammann et al., 2003) the apparent importance of the hemisphere-of-origin cannot be investigated explicitly.

The observed volcanic-hydroclimatic signal in northern China, based on DI and WI data is consistent with results from Huang (1992), who found that in 1816, one year after the Tambora eruption, flooding was common throughout the Yellow River Valley. Huang (1992) attributed this flooding to weaker subtropical high pressures in the western North Pacific during the 1811-1820 decade (Huang and Wang, 1985). The occurrence of frequent flooding in the YRV during the summer of 1816 (Huang, 1992) is consistent with the general hydroclimatic response to most eruptions – particularly over the northern half of the YRV region – based on analyses of the instrumental record (CRU, 1902 – 2002; Figure 5.8) and DI composites (e.g., Figure 5.13d). However, the tendency for drier conditions to prevail over the southern half of the YRV (Figures 5.8a,b and 5.12a,b) under high forcing conditions likely contributes to the apparently neutral response in regionally averaged WI data composites (950 AD and 1999). Meanwhile, analyses of DI, WI and modern instrumental records all agree that there is a tendency toward relatively drier conditions and drought throughout the SEC region. Finally, given the established inverse relationship between summer rainfall and SATs (Huang, 1992), this hydroclimatic response is consistent with results from analyses of reconstructed temperatures (Figure 5.11), wherein decades with higher volcanic forcing are typically cooler in NEC while relatively little response is noted in SEC.

Table 5.1. Summers (May – Sep.) with the 98th percentile of volcanic forcing (Ammann et al., 2006) from the early (950 – 1469), late (1470 – 1999) and entire past millennium (950 – 1999). Marked (×) are the years included in the computation of DI and WI average composites following explosive tropical eruptions (Figures 5.12, 5.13, and 5.14). The volcanic source of the forcing, when known, is also listed. Cases with no known specific source were chosen because relatively large sulfate peaks were measured, and tephra material observed, within annually layered ice cores extracted from both Northern and Southern Hemisphere polar regions, indicating the occurrence of an explosive tropical eruption during that year (Ammann et al., 2006).

Summer	950-1469	1470-1999	950-1999	Volcanic Eruption
969	×		×	---
1118	×		×	---
1168	×		×	---
1177	×		×	---
1232	×		×	---
1258	×		×	---
1259	×		×	---
1269	×		×	---
1278	×		×	---
1286	×		×	---
1453			×	Kuwae, Vanuatu, SW Pacific
1601		×	×	Huaynaputina, Peru
1641		×	×	Parker, Philippines
1674		×		Gamkonora, Halmahera
1695		×	×	---
1809		×	×	---
1815		×	×	Tambora, Lesser Sunda Is
1816		×	×	Tambora
1835		×	×	Cosiguina, Nicaragua
1884		×	×	Krakatau, west of Java
1963		×	×	Agung, Lesser Sunda

Table 5.2. List of eruption years included in Figures 5.12, 5.13, based on criteria established by Adams et al. (2003; from Tables S6 and S8 in their supplementary material).

Eruption Criteria	IVI M-L	IVI Large	VEI M-L	VEI Large
Time Period	1650-1980	1650-1980	1650-1980	1650-1980
# of eruptions	25	12	31	13
Eruption Years	1660	1665	1661	1671
	1665	1674	1665	1673
	1674	1694	1674	1680
	1694	1712	1680	1745
	1712	1747	1720	1768
	1721	1808	1745	1772
	1728	1815	1756	1812
	1747	1831	1760	1814
	1753	1835	1761	1815
	1775	1884	1764	1835
	1789	1903	1768	1869
	1795	1963	1791	1884
	1808		1793	1951
	1813		1803	
	1815		1808	
	1824		1812	
	1831		1813	
	1835		1814	
	1862		1815	
	1884		1818	
	1890		1823	
	1903		1835	
	1929		1884	
	1963		1899	
	1969		1902	
			1911	
			1917	
			1943	
			1951	
			1963	
			1968	

Table 5.3. WI years averaged into analyses presented in Figure 5.14 (1470 – 1979). For example, the WI response to simultaneous peak forcing is tested by averaging all WI values in column marked in bold (JJA), during the years with highest forcing in that season. The WI response to peak forcing during the prior summer is tested by averaging WI values during years listed in the column labeled "JJA+1" (just add one to each of the years included in the "JJA" composite).

DJF+2	MAM+2	JJA+2	SON+2	DJF+1	MAM+1	JJA+1	SON+1	DJF	MAM	**JJA**	SON	DJF-1	MAM-1	JJA-1	SON-1	DJF-2	MAM-2
1589	1598	1513	1513	1588	1597	1512	1512	1587	1596	**1511**	1511	1586	1595	1510	1510	1585	1594
1598	1603	1603	1588	1597	1602	1602	1587	1596	1601	**1601**	1586	1595	1600	1600	1585	1594	1599
1604	1643	1643	1603	1603	1642	1642	1602	1602	1641	**1641**	1601	1601	1640	1640	1600	1600	1639
1812	1697	1697	1643	1811	1696	1696	1642	1810	1695	**1695**	1641	1809	1694	1694	1640	1808	1693
1818	1811	1811	1811	1817	1810	1810	1810	1816	1809	**1809**	1809	1815	1808	1808	1808	1814	1807
1825	1812	1817	1817	1824	1811	1816	1816	1823	1810	**1815**	1815	1822	1809	1814	1814	1821	1808
1833	1818	1818	1818	1832	1817	1817	1817	1831	1816	**1816**	1816	1830	1815	1815	1815	1829	1814
1886	1837	1837	1832	1885	1836	1836	1831	1884	1835	**1835**	1830	1883	1834	1834	1829	1882	1833
1905	1886	1886	1837	1904	1885	1885	1836	1903	1884	**1884**	1835	1902	1883	1883	1834	1901	1882
	1905	1965	1885		1904	1964	1884		1903	**1963**	1883		1902	1962	1882		1901

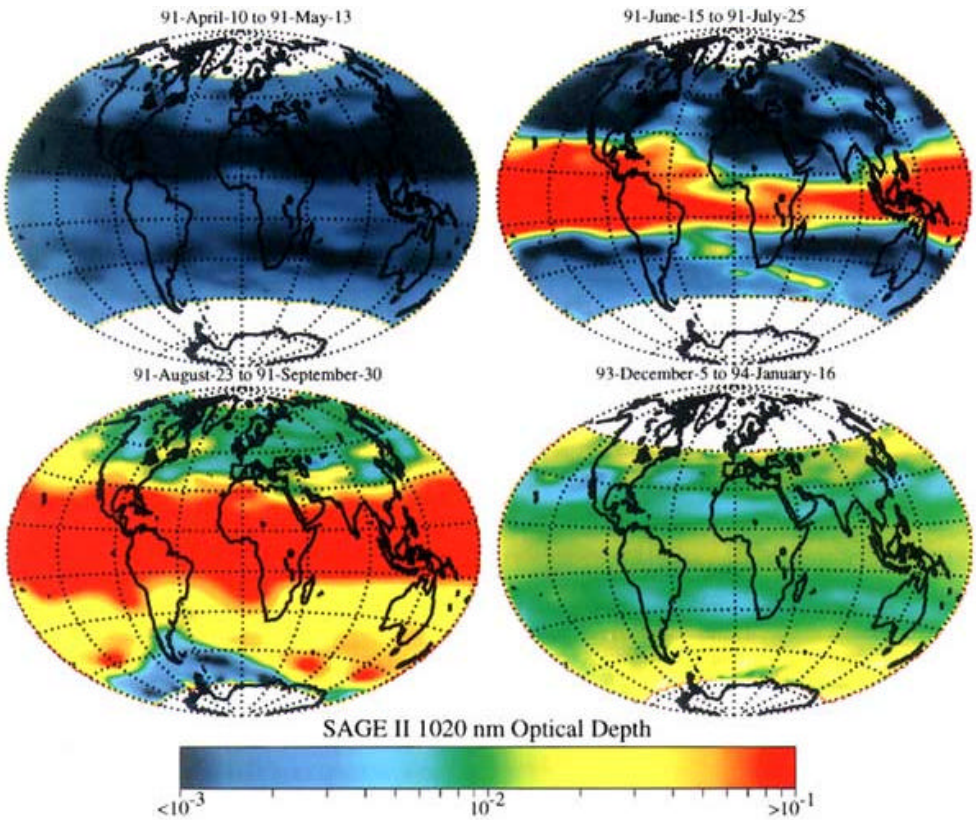

Figure 5.1. SAGE II Stratospheric aerosol optical depth measurements from the period before and after the eruption of Mount Pinatubo, on June 15, 1991 (Source: Self et al., 1996; public domain).

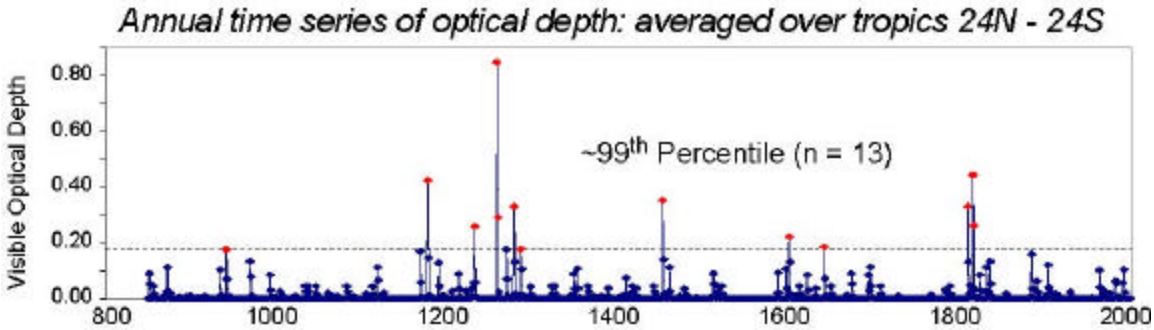

Figure 5.2. Annual time series of SAOD (from Figure 3.12) averaged from January to December over the tropical region (24°N to 24°S). The dashed line illustrates an arbitrary threshold (the 99th percentile) to select a sampling of years with high forcing, for subsequent model and observational composite analyses.

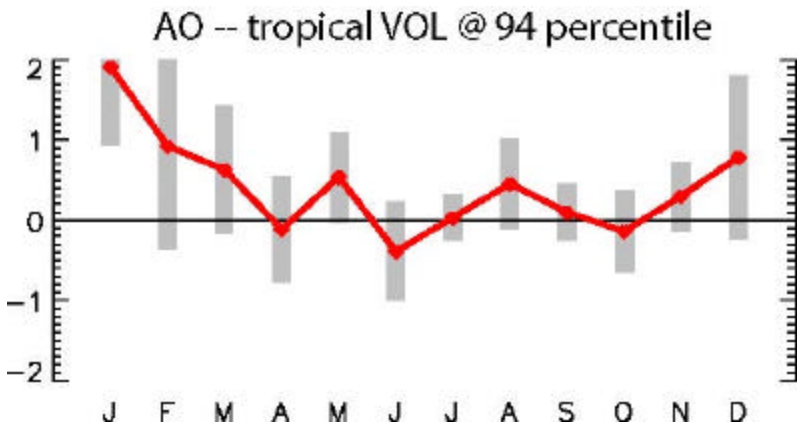

Figure 5.3. The observed monthly AO anomaly during high volcanic forcing months (1899 - 1999; n = 6/ month). Monthly composites include data from years following Santa Maria (1902), Agung (1963), El Chichón (1982) and Pinatubo (1991). Gray vertical bars represent the 95% confidence interval of the true mean in each month.

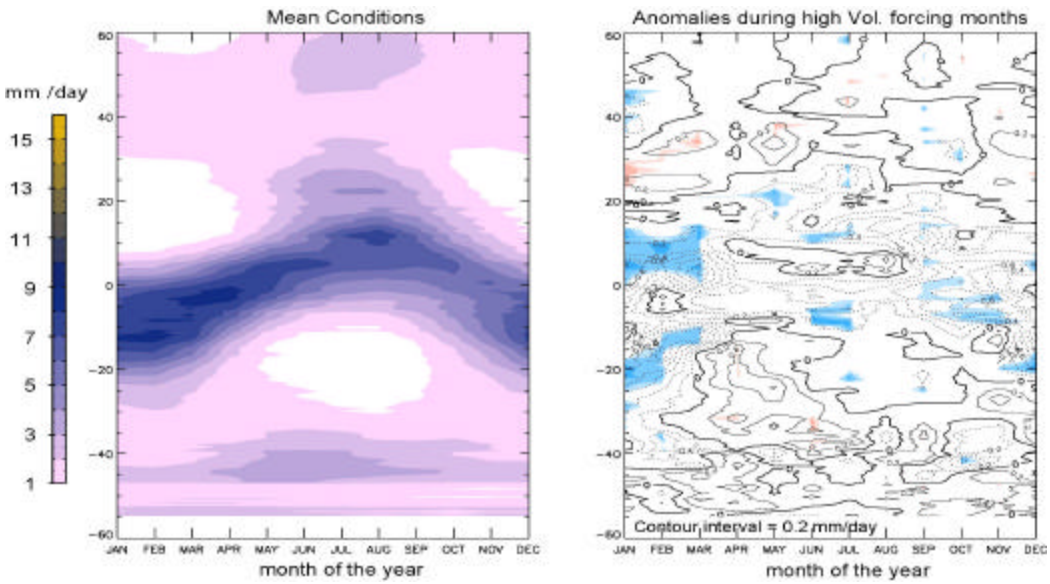

Figure 5.4. Global, monthly, zonally averaged land precipitation-rate (mm/day) from 60N to 60S (left) (CRU data). Composites of monthly precipitation-rate anomalies during the four months between 1902 and 1999 with the highest (96th percentile of SAOD; n = 4/month) forcing during this era (right). Based on individual student's t-tests, statistically significant positive and negative anomalies are highlighted with red and blue shading, respectively. The 90, 95 and 99% confidence levels are associated with the lightest, medium and darkest color shading, respectively.

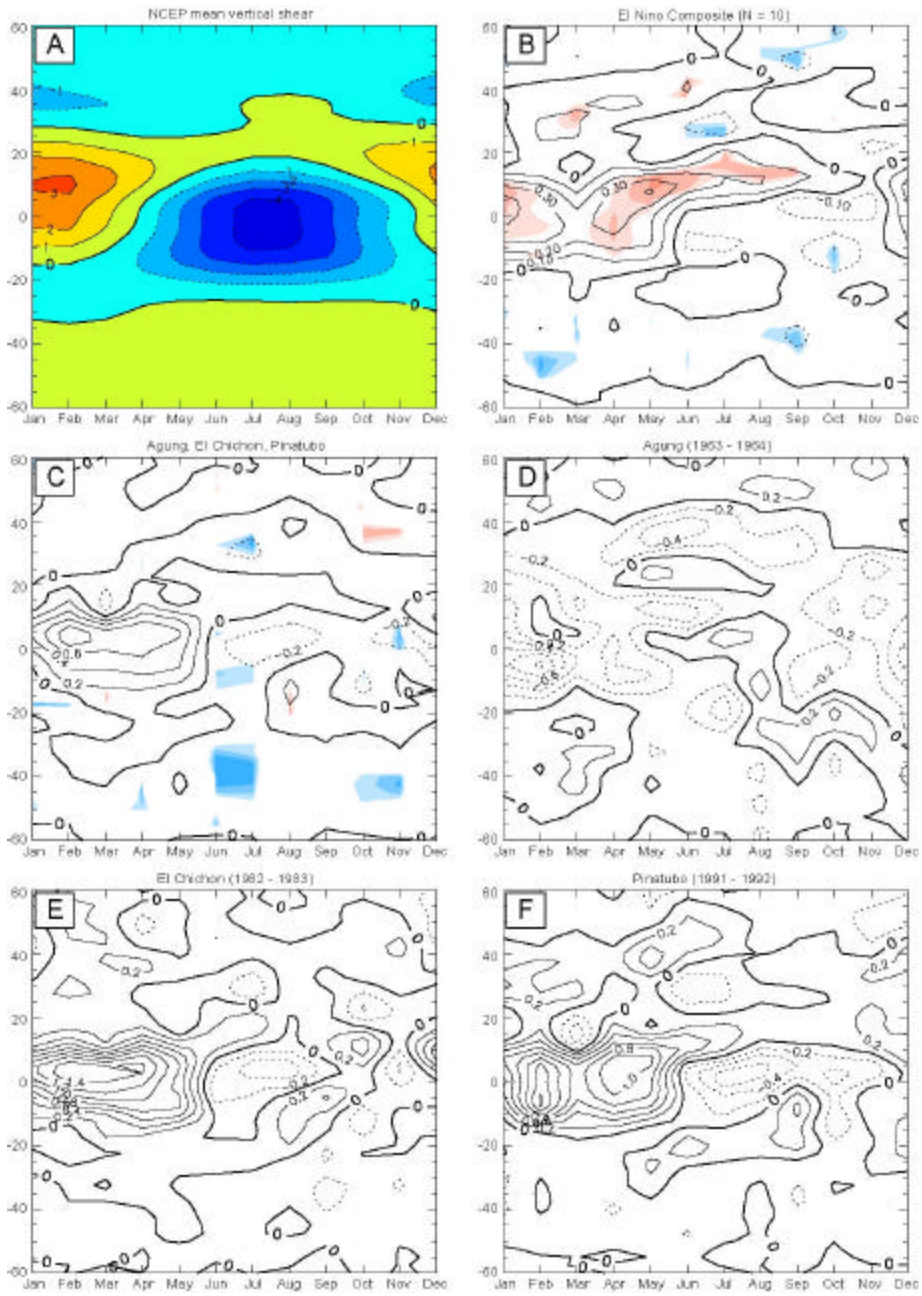

Figure 5.5. (a) Observed monthly zonal mean vertical wind shear from 60°N to 60°S, averaged over all longitudes (identical to Figure 4.22), in m/s units. Vertical wind shear is defined as the difference between meridional wind velocity at 200 hPa and the same at 850 hPa. (b) Zonal mean vertical wind shear anomalies during the 10 years between 1948 – 1999 with the lowest average SOI values (~El Niño conditions). (c) Composite mean vertical wind shear anomalies during high forcing months following the Agung, El Chichón and Pinatubo eruptions (n = 3/month). Monthly vertical wind shear anomalies are also plotted during individual years with high forcing following the (d) Agung, (e) El Chichón and (f) Pinatubo eruptions. Statistically significant results in (b) and (c) are highlighted by red and blue shading, as in Figure 5.4. Contour intervals are 0.1 m/s for (b) and 0.2 m/s for Figures (c – f).

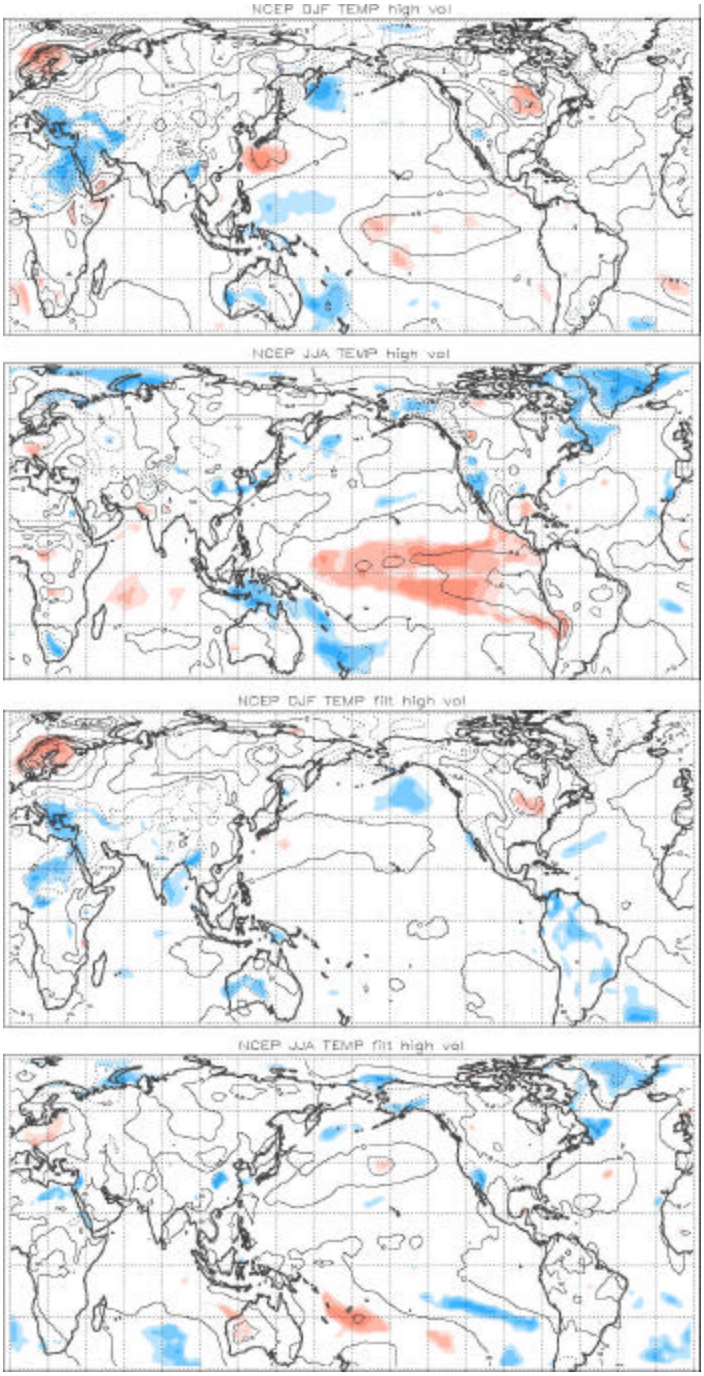

Figure 5.6. Contour plots show composites of winter and summer SAT anomalies during five high volcanic forcing years from 1948 to 1999, based on NCEP reanalysis data (top two panels). Positive, negative and zero anomalies correspond with solid, dotted and solid bold contours, respectively (intervals = 0.5°C). The bottom panels show results from an identical analysis, except that NCEP data were first filtered with a 10-year Lanczos high-pass filter and the SOI signal was linearly removed at each grid point (similar to Robock and Mao, 1995). Statistically significant anomalies are highlighted by red and blue shading, as in Figure 5.4.

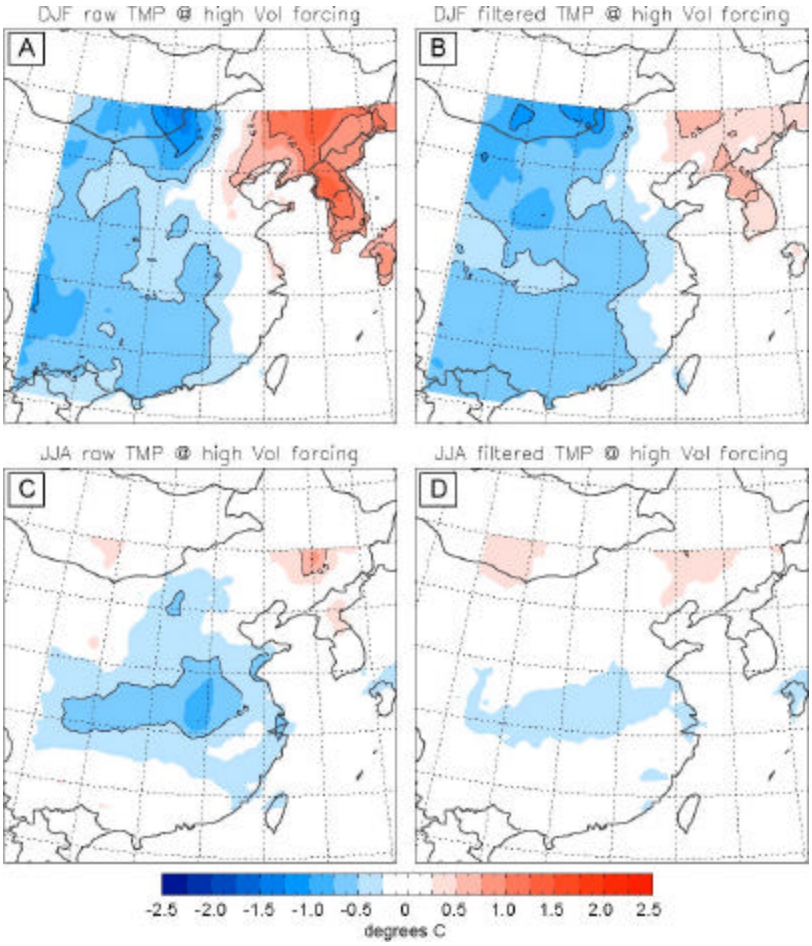

Figure 5.7. Composites of (a) winter and (c) summer surface air temperature anomalies during high volcanic forcing years during the period from 1902 and 1999, based on unfiltered CRU data. Panels (b) and (d) show results from an identical analysis, except that CRU data were first filtered with a 10-year Lanczos high-pass filter and the SOI signal was linearly removed at each grid point. See color bar for scale; solid contour intervals are added at 0.5°C intervals. DJF composites include: 1903, 1904, 1964, 1969, 1983 and 1992 (n = 6). JJA composites include: 1903, 1963, 1982, 1991, and 1992 (n = 5).

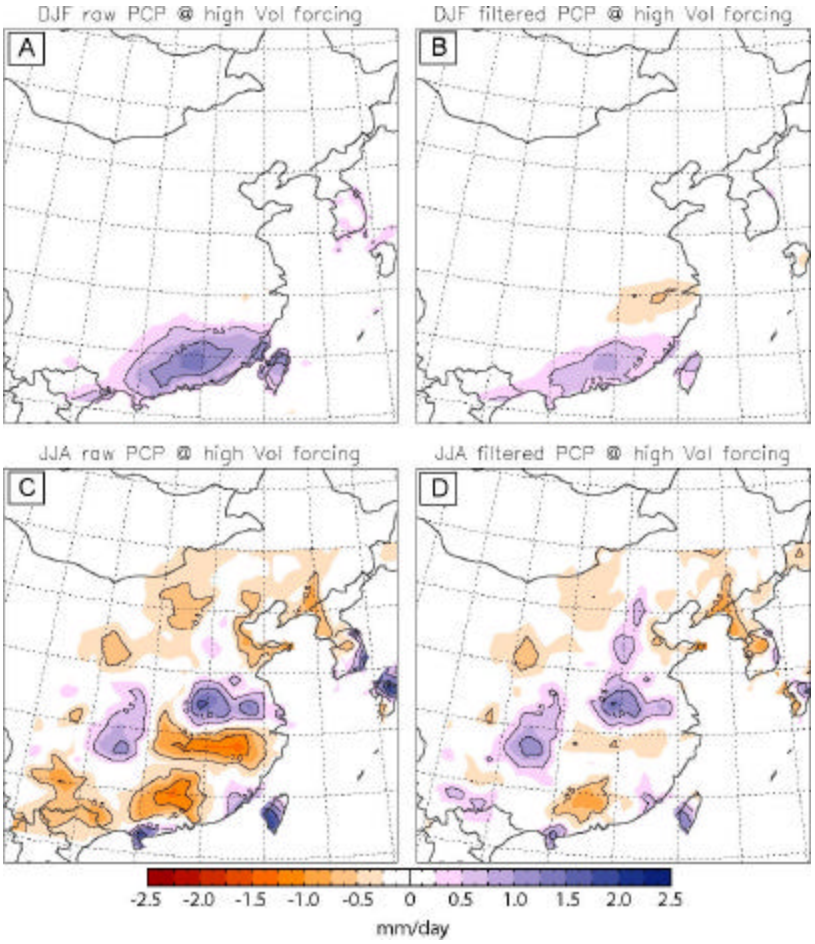

Figure 5.8. Same as Figure 5.7 except for precipitation rate, plus line contours were added at 0.5 mm/day intervals.

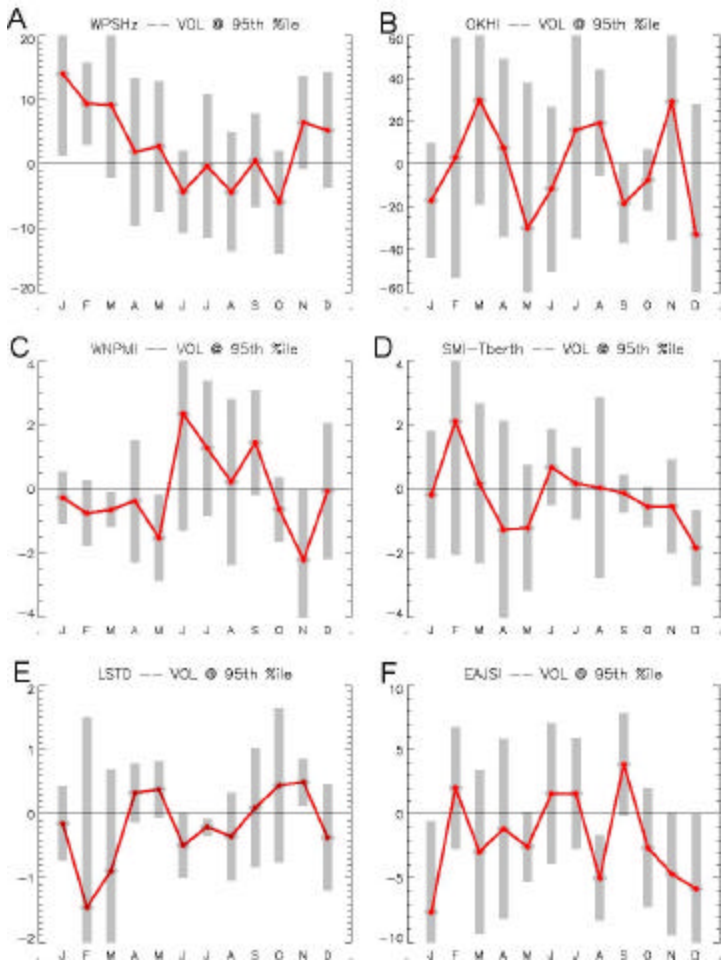

Figure 5.9. Composite monthly index anomalies throughout the annual cycle (January - December) during high volcanic forcing conditions. Composites are computed during months concurrent with the top 5th percentile of SAOD during the period from 1948 - 1999 (n = 3/ month). Vertical grey error bars represent the 95 percent confidence intervals for the true mean during each month (based on 2× the standard error).

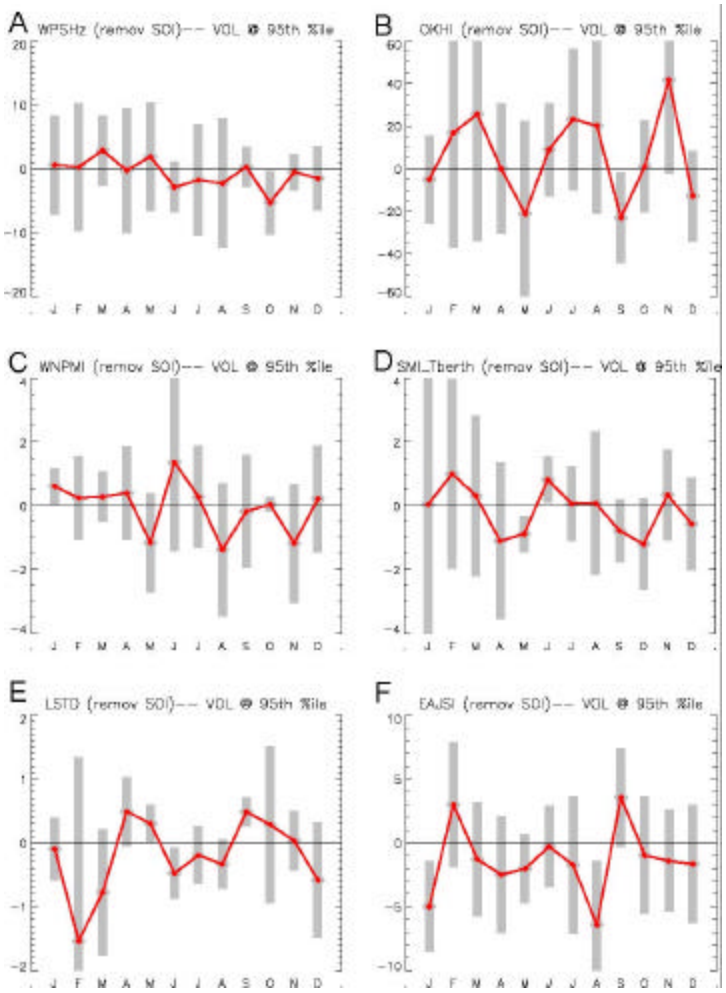

Figure 5.10. Same as Figure 5.9, but with the SOI signal linearly removed from each index during each month.

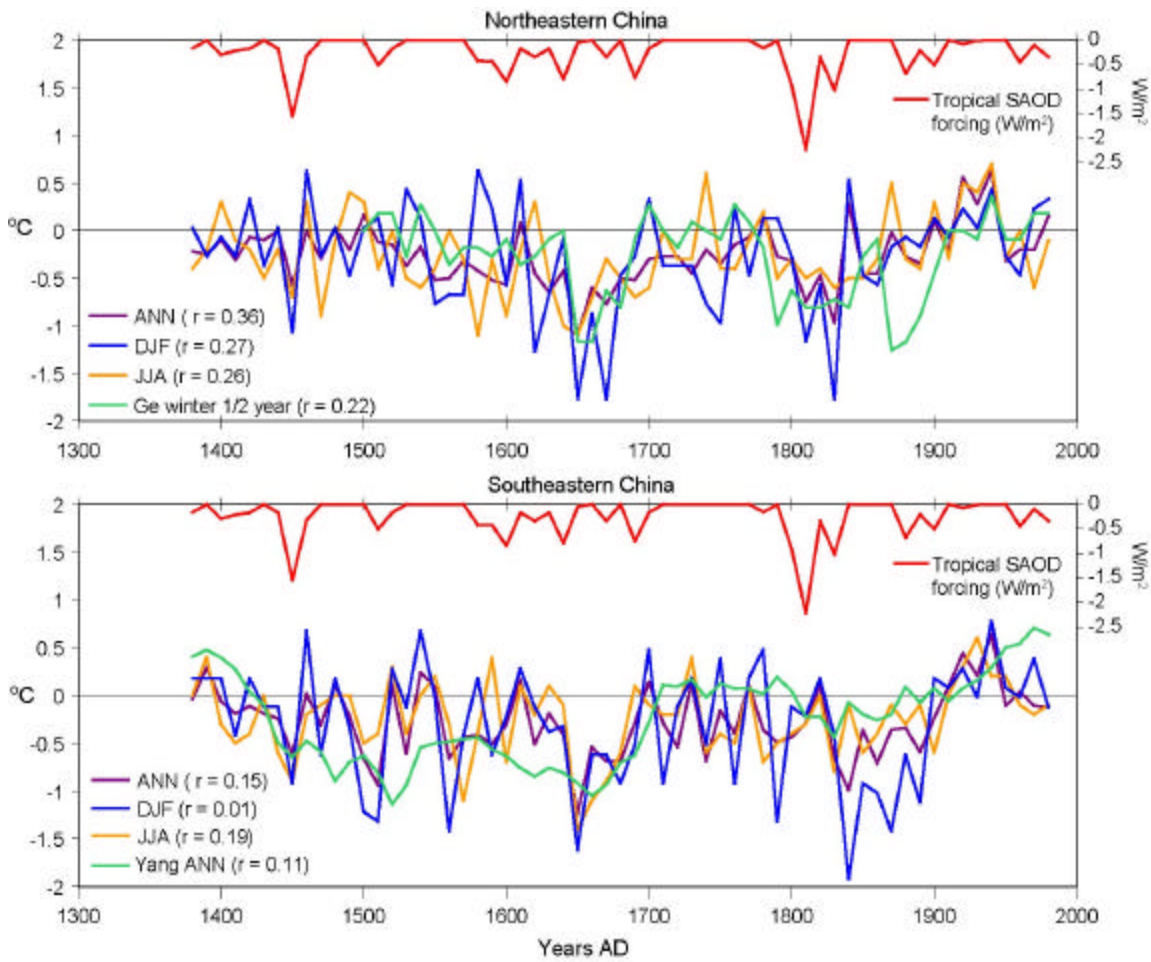

Figure 5.11. Time-series of decadally averaged tropical (24°N – 24°S) SAOD forcing (red) along with various temperature reconstructions for the East Asian region. Time-series in the top figure represent seasonal (DJF, JJA) and year-round (ANN) mean temperatures in the greater Beijing region (Wang, 1991, purple, blue, and orange), although one record (green) represents winter half-year temperatures throughout a larger area of northeastern China, including the middle and lower reaches of the Yangtze and Yellow River Valleys (Ge et al., 2003). In the bottom panel, three of the time series likewise represent seasonal (DJF, JJA) and year-round (ANN) mean temperatures throughout a relatively limited region of southeastern China (Wang and Wang, 1990, purple, blue and orange), while the fourth record (green) is based on an area-weighted multi-proxy year-round temperature reconstruction for the entire East Asia region (Yang et al., 2002). R-values show results from correlation analyses between each of the respective temperature series and the SAOD index at the top of each panel.

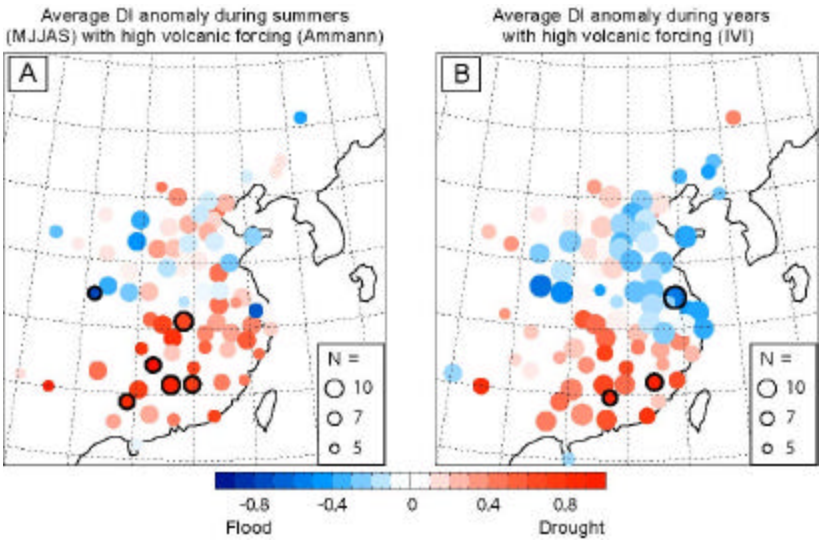

Figure 5.12. Average DI anomalies during (a) summers or, (b) years with high volcanic forcing. As reflected on the color-scale, positive DI anomalies suggest more frequent drought (red) while negative DI anomalies indicate more frequent flooding (blue). Panel (a) illustrates the DI response during eruption years defined by Ammann et al. (2006) SAOD data, during the period from 1470 to 1979 (N = 10; Table 5.1). Panel (b) illustrates the DI response during eruption years defined by IVI data, between 1650 and 1979 (N = 12; Table 5.2). The diameter of each circle is proportional to the total number of years (N) included in each composite. Only sites with data available for at least 5 eruptions are shown. Circles with black outlines are significant with at least 95% confidence, based on individual student t-tests.

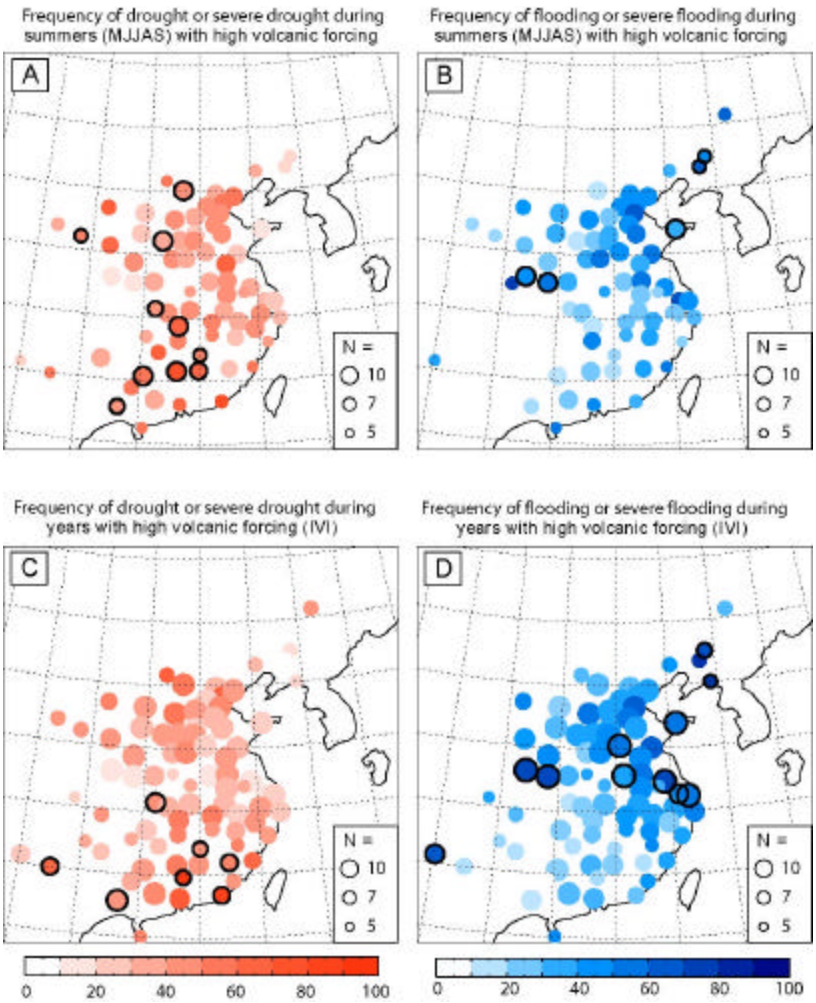

Figures 5.13. Frequency of drought (left) vs flood (right) occurrences during summers (top) (MJJAS) or years (bottom) with high volcanic forcing. Results are in percent units, expressing the frequency with which eruptions years are characterized by drought or severe drought (DI = 4 or 5) vs. flood or severe flood (DI = 1 or 2). The top two panels illustrate the DI response during eruption years defined by Ammann et al. (2006) SAOD data, during the period from 1470 to 1979 (N = 10; Table 5.1). The bottom two panels illustrate the DI response during eruption years defined by IVI data, between 1650 and 1979 (N = 12; Table 5.2). The diameter of each circle is proportional to the total number of years (N) included in this analysis. Only stations with data available for at least 5 eruptions are shown. Stations where drought (or flood) is at least three times as likely during high forcing years are outlined in black

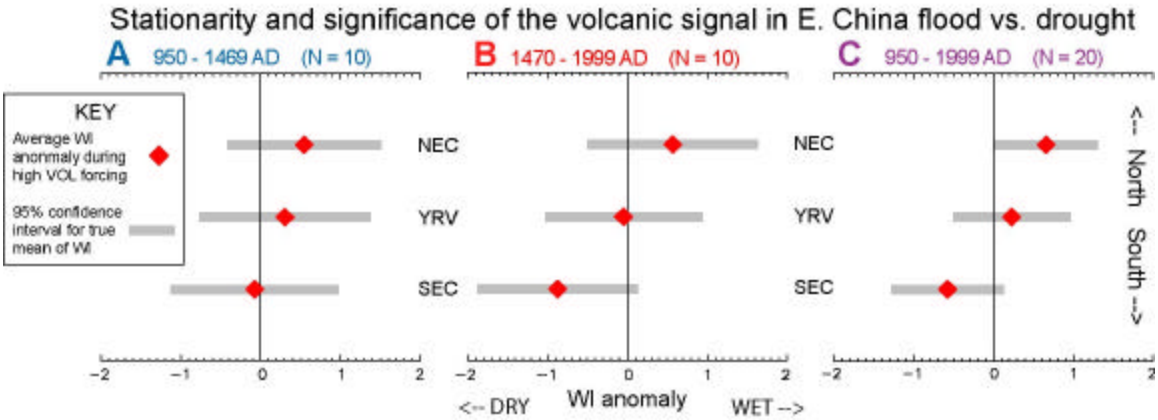

Figure 5.14. The stationarity and significance of the hydroclimatic response to the highest (top 98th percentile) summer (MJJAS) volcanic forcing conditions during the period from (a) 950 – 1469 AD, (b) 1470 – 1999 AD, and (c) over the entire period of the WI record. Composite WI anomalies (red diamonds) are shown for NEC (top), the YRV (middle), and SEC (bottom). Error bars (grey horizontal lines) represent 95% confidence intervals for the true mean of each composite. The specific years included in each WI composite are listed in Table 5.1

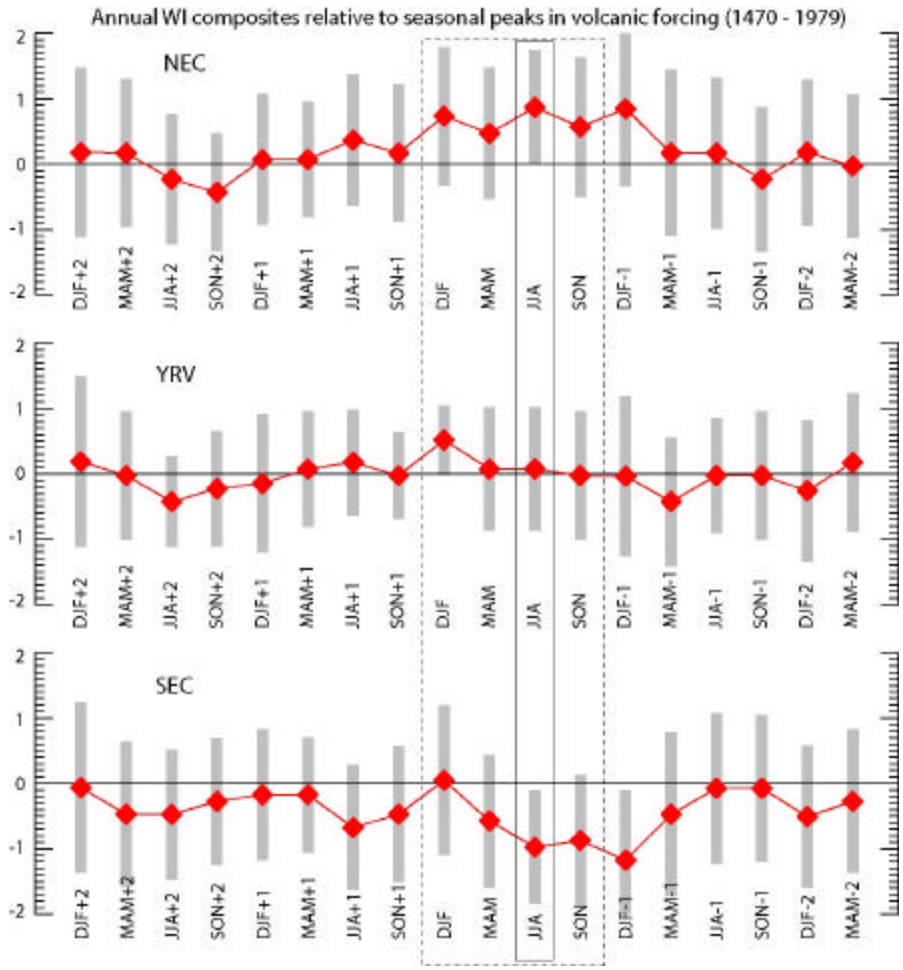

Figure 5.15. As in Figure 5.14, composite WI anomalies (red diamonds) are shown for three regions (NEC, YRV, and SEC) during years selected according to seasons with peak (top 98th percentile) Ammann et al. (2006) SAOD forcing. Composites highlighted by the solid vertical rectangle illustrate average WI anomalies during years with the highest SAOD forcing during the months of June – August (simultaneous with the response season). Within the dashed vertical rectangle, years included in WI composites were selected for having the top 98th percentile of SAOD forcing during each of the other three seasons (Dec. – Feb.; Mar. – May.; Sep. – Nov.; in the same year as the response season). Outside of the vertical rectangles, years selected for inclusion in WI composites are one or two years earlier (right) or later (left) than the years within the vertical rectangles. For example, all years included in WI composites marked "MAM+1" (left) are exactly one year after those included in composites marked "MAM," allowing an assessment of a possible one year lagged response to forcing in that season. Likewise, all years included in WI composites marked "MAM-1" (right) are exactly one year before the peak forcing and therefore generally before the eruptions (see text for more details). The specific years included in each WI composite are listed in Table 5.3.

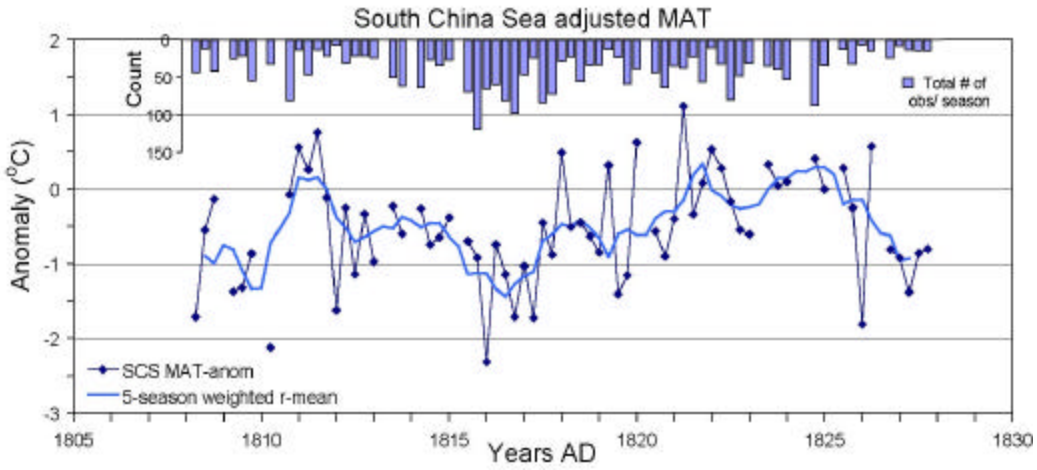

Figure 5.16. Time series line plots show adjusted MAT anomalies seasonally averaged and combined from four grid cells in the South China Sea (0° – 20°N). The histogram at top counts the total number of MAT measurements that were originally taken and then included into each seasonal average. Since less confidence can be placed in seasonal means containing fewer actual measurements, each point in the 5-season running mean (light blue line) was weighted by the total number of measurements in each of the respective individual season values (dark blue line). MAT anomalies are expressed in degrees Celsius relative to long-term seasonal mean anomalies during the period from 1820 and 1825 AD. See Chapter 3 and Table 3.2 for more details.

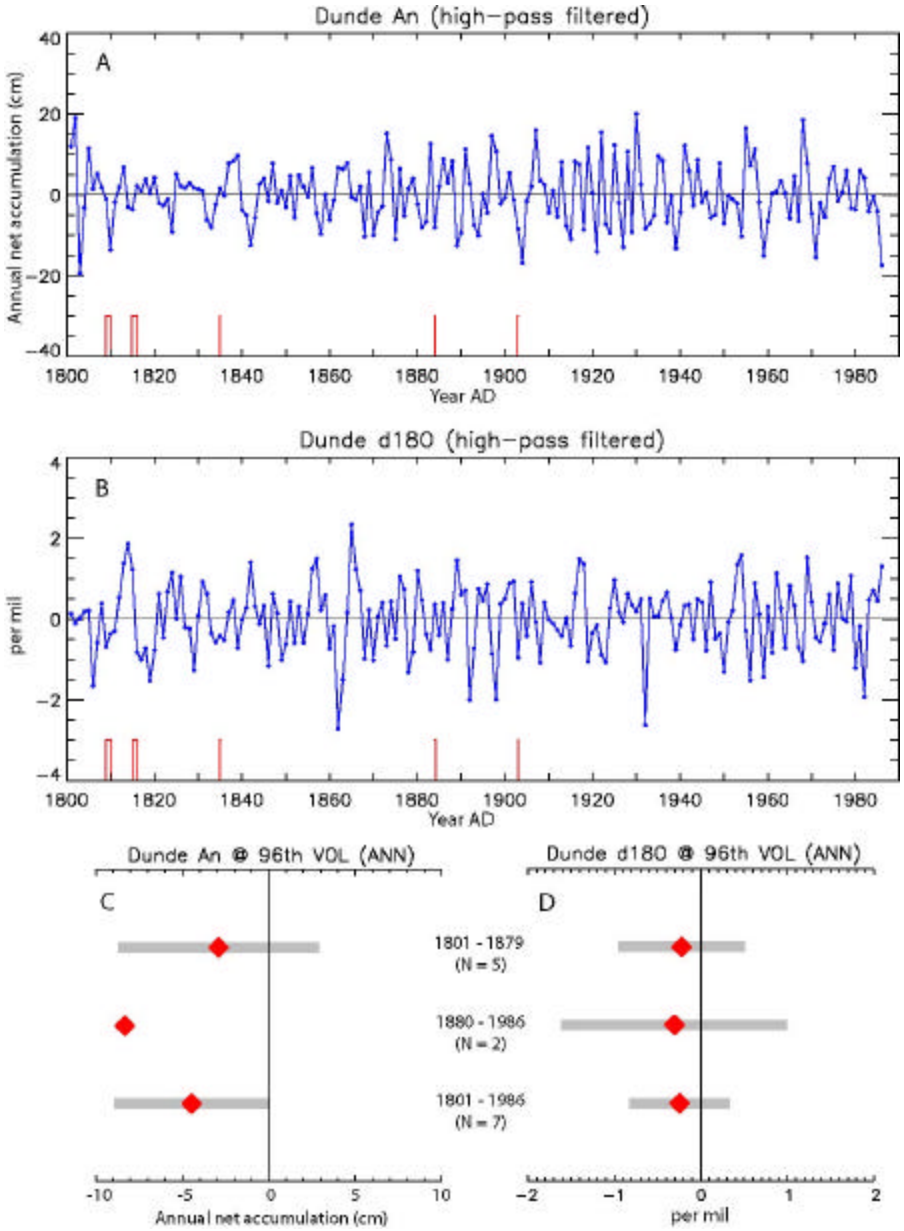

Figure 5.17. Four panel plots show Lanczos high-pass filtered time series for the a) A_n and b) $d^{18}O$ records from the Dunde Ice Cap (Davis et al., 2005) plus, a test of the c) A_n and d) $d^{18}O$ response to volcanic forcing. Red bars at the bottom of (a, b) mark years (Jan. – Dec.) in which Ammann et al. SAOD forcing is in the top 96th percentile during the period from 1801 – 1986 (eruptions: unknown, Tambora, Cosiguina, Krakatau, Santa Maria). Stationarity and statistical significance of the c) A_n and d) $d^{18}O$ response is shown in the bottom plots. Red diamonds show composite averages while grey horizontal lines represent 95% confidence intervals for the true composite means over the beginning (1801 – 1879), end (1880 – 1986) and entire period of record (1801 – 1986).

CHAPTER 6

GLOBAL CLIMATE MODEL ANALYSIS

This chapter has two main sections: model validation and the response to volcanic forcing. The first part is mostly focused on assessing the extent to which the CSM1.4 realistically simulates summer climate in eastern China. This includes some simple tests of model biases with respect to the observed mean climate state, but the emphasis is on the regional and large-scale processes and boundary conditions that control interannual hydroclimate variability. The second part considers how well the model is able to reproduce the observed EAM response to volcanic aerosol forcing. Through analyses and discussion the model is used as a tool for exploring possible mechanisms for observed responses.

The climate model simulations that form the basis for analyses in this chapter were originally run by Caspar Amman and results were kindly shared with the author for the purposes of this research. Two 1,150 year simulations were conducted – one control and one with full forcing – with the CSM1.4, which is a coupled AOGCM adapted from the NCAR CSM1 by Boville et al. (2001) for the purpose of transient paleoclimate simulations. The "Millenium Simulation" was run with incrementally-changing best estimates of radiative forcing from natural and anthropogenic sources for the period from 850 – 1999 AD (Ammann et al., 2006). A "control simulation" was also conducted over the same time period, starting with identical initial conditions but with no external radiative forcing. For additional details regarding the model configuration and forcing procedures, see section 3.4.

Recall from Chapter 1 (Figure 1.1) that output from the "hind-cast" Millennium simulation realistically replicated the observed time-evolution of global mean surface air temperatures from 1000 -1999 AD. Thus, analyses conducted with Millennium simulation output are considered more-or-less directly comparable with observed climate during this time period. Note that the control simulation was used as a baseline for natural, unforced climate variability. Thus, all t-tests computed in section 6.3 (response to volcanic eruptions) were conducted with respect to the long-term means and variations in the *control* simulation, over comparable periods of time for each analysis.

Finally, it should be noted that short portions of the Millenium and control simulations have been subsequently re-run and saved at 6-hour time steps to provide boundary conditions for regional paleoclimate simulations with the SUNYA ReCM (see Chapter 7 for details). These runs were initiated with boundary conditions from the Millennium and control simulations and thus replicate those experiments over their short simulation periods. Of particular interest, however, is that certain radiative flux data, which were not accessible to the author from the original Millennium run, were saved from a short Tambora-era simulation (1808 – 1819 AD). Thus, the radiation calculations conducted in section 6.3.1. were based on output from two shorter 12-year Tambora era simulations, one with full ("Millennium") forcing and one with only volcanic forcing removed (control).

6.1. Regional-scale CSM validation

Figures 6.1 – 6.4 compare observations with model output for mean-state climate, with a particular focus on summer conditions. To better illustrate the spatial distribution

of model biases with respect to several surface and upper-level diagnostic variables, differences were computed by subtracting observed seasonal mean values from simulated mean values. However, since these data are not from a common grid, the model data were first regridded (interpolating to a smooth quintic surface, using IDL software) to the same grids as observations.

6.1.1. Spatial biases at the surface

Model biases of JJA surface temperature (Figure 6.1(a)) are minor in central eastern China, with positive biases to the south and increasingly negative biases to the north. Also, the largest surface temperature biases occur over the Tibetan Plateau, where the relatively coarse model has a lower plateau elevation and does not generally capture the topographic detail found in nature, or in the NCEP reanalysis simulations. Modeled SST biases (Figure 6.1(c)) are relatively small, generally ranging from –2 to +2 °C in the Indian and Pacific Oceans. Biases in the SCS and subtropical Western Pacific – in closest proximity to China – are slightly positive.

Model biases in JJA precipitation rate (Figure 6.1(b)) – compared with CMAP precipitation – are very large in northern China, which is actually an arid to semiarid region. This is common for coarse resolution GCMs (Liang et al, 2001; Kang et al., 2002), where the spectral representation of regional topography induces unrealistic convective precipitation in the lee of the Tibetan Plateau. This problem is known to improve in models with higher spatial resolution; as the topography becomes more realistic, so does the spatial distribution of mean precipitation (Kobayashi and Sugi, 2004; Ping Lu, personal communication). There are also significant negative

precipitation biases throughout southern China, from 18° to 25°N, which is also true at most longitudes throughout this region.

Another important aspect of precipitation in eastern China is intra-annual variability which is dominated by the East Asian monsoon cycle. Figure 6.2 captures the average annual cycle of monthly mean precipitation in eastern China, comparing observations (CMAP) with model output. Here, monthly precipitation is zonally averaged, from 105° - 123°E, and then plotted from 10 – 50°N in Hovmoller diagrams. The top two panels show average mean precipitation as a rate (in mm/day) while the bottom panels present the same monthly data as a percentage of the long-term annual mean at each latitude. In terms of absolute values (top two panels of Figure 6.2), positive biases are apparent in the north while negative biases are apparent from 18° to 25°N. However, the bottom two panels are more similar, suggesting that the model captures the seasonal cycle of precipitation reasonably well, with peak rainfall in July throughout northern China. Also, the northward progression of maximum rainfall from spring through summer (i.e., the Mei-yu rain belt) is simulated realistically, although this happens a month or two too early and is shifted northward in the model (also noted by Liang and Wang, 1998).

Finally, Figure 6.3 compares monthly Eurasian snowcover from NOAA satellite observations with a similar product from the model. Note that the only saved snow-related model output variable is water equivalent snow depth. So, lacking model data that are directly comparable to observed snowcover, daily water equivalent snow depths were converted to monthly percent snowcover values for the purpose of this qualitative visual comparison. This was done by iteratively adjusting the minimum amount of daily

water equivalent snow depth that was required to assign, or not assign, snowcover to a grid cell during a particular day. Monthly percent snowcover values were then derived from the daily data. Results illustrate the simple point that snowcover over northern Eurasia is relatively well simulated by the model throughout the year, but warm surface temperature biases over the Tibetan Plateau result in the model significantly underestimating the length of the snowcover season in the later region.

6.1.2. Spatial biases in upper-air circulation

In Figure 6.4, the summer season (JJA) upper-level westerly Jet Stream, illustrated by 200 hPa zonal winds (200u), is shown to be well represented by the model in terms of its mean latitudinal location; however the strength of the Jet is overestimated by up to 10 m/s (~30%). The WPSH, defined here by the 500 hPa GPH (500z) 5870m contour, is resolved by the model however pressure levels in this region of the Pacific are generally overestimated. A lower-level westerly Jet, seen in the 850 hPa wind vector (850uv) field, is also captured by the model, including the northward redirection of this Jet in the vicinity of the SCS. This is a very important feature for the model to simulate correctly because these southerly winds are largely responsible for moisture transport from the SCS into eastern China and their strength is closely related to regional precipitation (Chapters 2 and 4). However, southerly lower-level water vapor transport in this region is associated with the intensity and location of the WPSH, and the exaggerated strength of this important boundary condition is very likely linked to the weakness of modeled precipitation in southeastern China and to easterly model biases, at 850 hPa, during the summer season.

Model biases with respect to vertical velocity (omega) are consistent with anomalously strong subtropical high pressure at 500 hPa, indicating that tropical Hadley Cell circulation is unrealistically strong in the CSM1.4 (Dai et al., 2001b). An overactive Hadley cell would also help explain the aforementioned negative precipitation at all longitudes from 18° to 25°N and positive anomalies closer to the equator, at ~10°N (Figure 6.1(b)). The question of model skill with respect to Hadley circulation is also revisited later in this chapter.

6.2. Regional-scale precipitation variability

Chapter 4 describes a principal component analysis (PCA) procedure that was used to objectively identify regions in Eastern China with common modes, or shared spatial patterns, of interannual variability. When the same PCA is performed on modeled (CSM1.4) precipitation the results (Figure 6.5) are similar to those found with respect to observations (Figure 4.4), except that the loadings from the first PC of observed precipitation are better matched with the second PC of precipitation in the model, and visa versa. These results are very encouraging, suggesting that spatial patterns of simulated and observed summer regional rainfall variability display a common zonal structure. It is interesting that this occurs despite the significant aforementioned model biases with respect to the mean state of summer precipitation in China. Thus, to reflect this zonal pattern of variability and to be consistent with the precipitation regions assigned for observational data analyses, the second PC of modeled precipitation was used to delineate three zonal regions for CSM data (Figure 6.5). For the following discussion, regional indices of *modeled* summer precipitation share similar nomenclature

as observations: southeastern China (SECm), Yangtze River valley (YRVm), northeastern China (NECm).

6.2.1. "Wet minus dry" maps

Following procedures described in section 4.1.3, composite plots are generated based on the differences between mean conditions during wet years minus dry years; results illustrate spatial patterns of upper air circulation associated with regional precipitation variability (Chang et al., 2000a). Figures 6.6, 6.7 and 6.8 show analysis results derived from standardized time series of regionally averaged JJA rainfall from SECm, YRVm and NECm, respectively.

For SECm, the CSM does very well compared with observations in the following regards (compare Figures 6.6 with Figure 4.5). Summer rainfall in SEC occurs when there is low-pressure aloft and high pressure anomalies centered over northern China, at 500 hPa. Local low-pressures are associated with a stronger lower-level westerly jet over the Indochina peninsula and cyclonic circulation in the immediate vicinity of SEC, at 850 hPa. Upper-level jet anomalies at 200 hPa are positive over the southern coast and slightly negative over NEC. However, beyond these somewhat local associations between SEC summer rainfall and atmospheric circulation, commonalities between simulated and observed wet-minus-dry maps diminish significantly.

Wet-minus-dry maps for the YRVm are remarkably similar to observations throughout most of this East Asian regional domain (compare Figures 6.7 with Figure 4.6). Firstly, the observed out of phase relationship between YRV rainfall and precipitation over Taiwan and the nearby tropical west Pacific region is well captured by

the model. Also, there is a clear strengthening of the WPSH at 500 hPa and an associated weakening of the westerly tropical jet at 850 hPa. These conditions favor stronger southerlies over SEC, increasing low-level moisture advection from the SCS. The spatial distribution of modeled 200 hPa zonal wind is also similar to observations, however the region-wide zonal structure of anomalies in this field are relatively more pronounced in observations.

For NECm, there are remarkably fewer commonalities with observation-based wet-minus-dry maps (compare Figures 6.8 with Figure 4.7). In observations there are only slight 850 hPa wind anomalies, hinting at moisture advection from the SCS and the immediately adjacent western Pacific. However, in the model there are relatively much greater southerly wind anomalies, perhaps reflecting that the model-simulated large positive precipitation biases in the north can only be maintained through extensive moisture advection from the SCS. However, it is also worth keeping in mind that *observed* wet-minus-dry maps for the NECo were generally not very spatially coherent; suggesting that there is relatively less year-to-year consistency in terms of the climatic conditions that control observed hydroclimate variability in the north, compared with the other two regions.

6.2.2. Regional-scale monsoon indices

Complementing wet-minus-dry map analyses, this section widens the scope of this study's validation of the CSM with respect to regional-scale climate variability. Beyond the somewhat local-scale processes that may contribute to surface hydroclimate variability in eastern China, the dynamics of the broader East Asian monsoon system are

also of considerable interest. Thus, the regional monsoon indices – introduced in Chapter 4 – provide a somewhat simplified but objective framework for considering model skill with respect to these various components of a very complex and dynamic system. In a generally qualitative manner, monsoon indices are used to test how well the CSM realistically simulates observed 1) monthly climatologies, 2) correlation patterns with respect to surface climate, and 3) interrelationships with other indices.

Figure 6.9 plots monthly climatologies of all six regional monsoon indices from observations (solid) and the CSM (dashed). Despite a few obvious year-round biases, it is clear that the model generally captures the timing and magnitude of the annual cycle of all six indices. For example, biases in the WPSHz and OKHI indices reflect of anomalously high atmospheric pressure heights in the tropics and subtropics and anomalously low pressures at high latitudes, respectively (Figure 6.4). Biases in the LSTD – an index based on the thermal contrast between the land and adjacent ocean – generally reflect slightly positive regional SST biases and negative land temperature biases (Figure 6.1). The seasonal transition from summer to winter monsoon conditions may be roughly measured by a shift in the SMI from negative to positive. Thus, it appears that this transition happens about one month too early in the model. One final noteworthy model deficiency is that the EAJSI plateaus near 40 m/s throughout the summer months while this jet weakens to 25 m/s during the peak of the summer monsoon, in July. This bias may be attributable to the anomalously strong meridional pressure gradient that exists during this season in the model, which may occur at most latitudes but appears to be particularly strong at these longitudes (120° – 150°E, Figure 6.4).

Figures 6.10 & 6.11 plot spatial correlation patterns between seasonally averaged time series of monsoon indices (DJF and JJA) and surface climate variables (surface air temperature and precipitation), illustrating the significance of each index with respect to regional surface climate. Note that the OKHI index is not shown here because analysis results from the model were exceptionally poor and not, otherwise, noteworthy. For comparison, results from observational analyses (CRU; Figures 4.10 – 4.15) are replicated in Figure 6.10 while results based on model output (CSM; 850 - 1999) are plotted in Figure 6.11.

Focusing first on winter (DJF) conditions over eastern China, the model simulation appears to be remarkably realistic, particularly with respect to temperature. With the exception of the WPSHz and WNPMI indices, the model simulates the correct sign of regional correlations and captures well many specific regional details in terms of the spatial distribution of observed correlation patterns. For example, the winter SMI is negatively correlated with precipitation throughout eastern China although a slight positive correlation pattern is apparent in the far southwest. Meanwhile the winter SMI is negatively correlated with temperatures region-wide, including the Korean Peninsula and Japan. Each of these details is replicated by the model.

In the summer season (JJA), success in terms of model skill is generally more mixed according to a few different measures (compare Figures 6.10 with 6.11). First, with regard to precipitation only, it could be argued that the model does get the correct sign of many regional correlation patterns; however, the spatial distributions of those patterns are often shifted to the north or south of their locations in observational analyses. For example, observed CRU precipitation in the YRV is positively correlated with the

WPSHz index; however, in the model this pattern is wider and expanded to include much of the YRV and NEC regions. On the other hand, observed negative correlations over SEC are reliably simulated by the model. Another example: observed CRU precipitation in NEC is negatively correlated with the SMI; meanwhile, in the model this pattern extends much further south and observed positive correlations in the south are not captured at all. Close visual inspection of results from the simulated LSTD and EAJSI indices tell a very similar story. Simulated summer correlation patterns with respect to the WNPMI are nearly identical (but of the opposite sign) to those for the WPSHz index; this is also basically true for observations.

However, a potentially more significant concern regarding simulated JJA surface hydroclimate is apparent from Figure 6.11, when results from the already-discussed precipitation analyses are compared with temperature analysis results. As discussed in Chapter 4, the observed JJA temperature correlation patterns track closely with observed precipitation patterns; typically, exceptionally wet conditions are accompanied by anomalously high cloud cover, which blocks incoming shortwave/ solar radiation, preventing surface heating and lowering air temperatures. Yet, the inverse relationship between precipitation and surface air temperature, which is consistently observed in nature throughout eastern China, is not really apparent in the model. This result likely reflects an endemic problem with AOGCMs, in which clouds and rainfall are necessarily parameterized and resulting impacts on radiation and surface air temperatures are notoriously problematic (IPCC, 2001).

The final test of model skill using the regional monsoon indices involves assessing interrelationships between them. To begin broadening the scope of this model

assessment even further, the regional indices are also compared with respect to Hadley cell and other global-scale climate indices. Tables 6.1 and 6.2 are correlation matrices displaying results from simple pair-wise correlation analyses during the summer (JJA) and winter (DJF) seasons, respectively (compare with Tables 4.2 and 4.5), covering the simulation period from 1948 – 1999. In general, it is found that observed index interrelationships are simulated with greater consistency during the winter season, compared to summer. While many of these results confirm conclusions reached earlier in this section, a few specific observations are noteworthy.

In both observations and the model, the winter WPSHz index is positively correlated with the Hadley Cell index (HCIN-sf) and inversely correlated with the SOI, with high levels of statistical significance (p-value <0.001). In both observations and the model, the two different Hadley Cell indices are highly correlated within their own respective hemispheres during the winter season. The model also correctly simulates high positive correlations between the Global and East Asian subtropical jet indices during winter and summer. It is worth noting – something that will be revisited later in this chapter – that the CSM captures the observed, inverse relationship between the PDO and SOI in the winter and summer seasons (although this relationship is notably weaker in the model). Also, interrelations between the WPSHz index, the WNPMI and summer precipitation in the YRV is apparently captured very well by the model.

Finally, some particular model deficiencies during summer are worth pointing out. Variations in the simulated OKHI index display none of the statistically significant teleconnections that are observed in nature. This result suggests that the model is not likely to correctly capture observed links between high latitude blocking patterns and

summer rainfall over eastern China (e.g., Samel and Liang, 2002). Also, the observed inverse correlation between a NH Hadley cell index (HCIN-sf) and YRV rainfall (r = -0.46) is completely missed by the model (r = 0.27).

6.3. Global-scale CSM validation

In the final stage of this global model assessment, regional rainfall variability from eastern China is considered in the broadest possible context through spatial correlation analyses with respect to global-scale pressure patterns and SST variability. Then the CSM is tested for its ability to realistically simulate some of the more prominent observed large-scale teleconnection patterns and global-scale modes of coupled ocean-atmosphere variability (ENSO, AO, and PDO).

6.3.1. Teleconnections

First, global-scale patterns of pressure variability are examined by correlating summer rainfall time series from NECm, YRVm and SECm with 500 hPa GPHs (Figure 6.12). Comparing these results with Figure 4.19 provides a qualitative gauge of how far beyond the immediate vicinity of East Asia the model can simulate observed atmospheric pressure-related teleconnection patterns. For NEC, it has already been established that the atmospheric circulation processes controlling precipitation variability in that region were somewhat tenuously defined by observational analyses conducted in this study. Thus, it is not particularly surprising that associated pressure patterns seen in observations do not match well with those simulated by the model. Still the dissimilarity between the top panels of Figure 6.12 and Figure 4.19 is somewhat striking.

On the other hand, the model appears relatively more skillful with respect to surface hydroclimate variability further to the south. For broad global regions, pressure variability linked to summer rainfall variations in the YRV are typically of the opposite sign to those linked with rainfall in SEC. This is particularly true for pressure variations at the western edge of the WPSH and throughout Eastern Asia, the North Pacific and North America. These interpretations generally apply for both modeled and observed climate variability.

Figure 6.13 spatially plots correlations between SST variability and summer rainfall time series from NEC, YRV and SEC. Comparing these results with Figure 4.20 provides a qualitative measure of how well the CSM simulates local and broad-scale SST anomaly patterns linked with precipitation variability in eastern China. For NEC, there are clearly several dissimilarities between the CSM simulation and observations. However, some of the broad-scale patterns agree, such as negative and positive correlations in the eastern tropical Pacific and North Pacific, respectively. For the YRV and SEC there are somewhat parallel broad-scale similarities between observed and simulated SST correlation patterns, some of which qualitatively suggest ENSO-like modes of SST variability in association with surface hydroclimate in East Asia.

On the more local-scale, simulated rainfall variability in the YRV is realistically positively correlated with SSTs in the SCS, but, unlike observations, inversely correlated with SSTs in the Philippine Sea. Similarly, SST variability in the SCS and northern Indian Ocean are realistically inversely related to SEC rainfall, but the sign of the correlations over the Philippine Sea is positive, contrary to observations. These results help to explain why highly significant observed correlations between E. China rainfall

variability and the LSTD index (which is preferentially weighted toward Philippine Sea SSTs) are not realistically captured by the model (compare Figure 6.10 with Figure 6.11).

6.3.1.1. Arctic oscillation

Figure 6.14 illustrates the loading pattern of the AO on 1000 hPa GPHs in polar projection based on CSM ouput from 850 – 1999. This result generally compares favorably with observations (Figure 3.2), indicating that the model captures well the basic structure of atmospheric-pressure variability associated with the computed AO. However, negative pressure loadings in the Arctic spread out further beyond the polar region in the model, compared with observations, particularly over the East Asia and Pacific regions. Another apparent discrepancy is that the observed AO explains less overall year-round variance than the model simulated AO. However, this is likely attributable to the relatively high resolution of the observed 1000 hPa gph dataset (2.5° x 2.5°), compared with the model (3.75° x 3.75°), which was also sub-sampled at every other grid point for this analysis (to increase computational efficiency).

6.3.1.2. PDO

As noted in Chapter 3, the PDO index was derived from the full forcing "Millennium" simulation and does display some multi-decadal variability; however, a clear low-frequency oscillation as pronounced as the one observed during the 20th century is not apparent throughout the 1,150 year simulation. However, since the exact mechanisms controlling multi-decadal changes in the PDO remain unclear and there is still considerable uncertainty regarding actual pre-instrumental variability (D'Arrigo and

Wilson, 2006), the significance of any apparent model shortcomings in this regard is difficult to ascertain. However, a more important and noteworthy model deficiency is its inability to realistically simulate the spatial SST loading pattern associated with observed PDO variability (Figure 6.15). Most notably, the strong out-of-phase relationship between North Pacific and tropical Pacific SSTs that is observed year-round in nature (Figure 3.2) is only marginally evident in the model. Also, the observed positive correlations between the PDO and both Indian Ocean and SCS SSTs are non-existent in the model.

6.3.1.3. ENSO

Figure 6.16 shows SST spatial correlation patterns associated with modeled SOI variability (compare with observations: Figure 3.4). There is generally good agreement between the model and observations, particularly in the NINO3.4 region; but there are also important differences. Primarily, as noted above, observed out-of-phase links between tropical and extra-tropical Pacific SSTs are resolved but they are relatively weak in the model. Also, of particular interest to this study, observed SSTs to the south and east of mainland China correlate negatively with the SOI during winter and spring, while the opposite is true for the model. These apparent deficiencies in the CSM could prevent realistic simulations of observed links between the SOI and rainfall in China; however, Figures 6.12 and 6.13 illustrate that some of these remote teleconnections may be slightly apparent in the model.

6.4. Response to volcanic eruptions

Following the precedent of the previous chapter, this section explores the global model response to volcanic forcing beginning on the global-scale and finishing on the regional-scale. This approach includes analyses that test how well the CSM is able to replicate certain results from previous studies (e.g., the AO response) but mostly provides original analyses of the Hadley circulation and East Asian monsoon response to volcanic forcing from 850 – 1999 AD.

6.4.1. Radiative forcing and climate sensitivity

Before exploring the simulated climatic response to volcanic forcing in detail, it is instructive to first compare the magnitude of the net radiative imbalance that is simulated by the model with independent published estimates of radiative forcing caused by a given increase in SAOD. This provides a first-cut basis for judging whether or not the magnitude of the CSM-simulated responses is realistic. Following the methodology described in Chapter 2.3.3.3, the average net change in incoming solar radiation and outgoing longwave radiation fluxes were first calculated based on the differences between these values in the forced vs. control simulations. Next, the change in the average global (40°N and 40°S) net outgoing longwave radiation (?R) was subtracted from net incoming solar radiation (?S) to estimate the total net change in radiative flux (?N). This procedure was followed based on CSM output from the surface and at the top of the atmosphere (TOA) during the period from 1808 – 1820 (data from the tropopause and other periods of time were not available).

Figure 6.17 presents results from the above calculations. Consistent with the findings of previous studies (Yang, 2000), radiative forcing at the TOA is less than forcing at the surface. For comparison, ?N was also computed directly from the Ammann et al. (2006) SAOD forcing dataset using a simple empirical relationship (Equation 2.2) established by Hansen et al. (2002). Results (Figure 6.17) clearly indicate that global mean CSM-simulated radiative forcing at the surface is nearly identical to published estimates derived from modeling and observational studies (Hansen et al., 2002).

Since the ?N value is shown to be equivalent to the change in radiative forcing (?F) at the surface (Figure 6.17), this value can be used in conjunction with the calculated temperature response (?T) to estimate global surface climate sensitivity (?T/?F) for the CSM1.4, from 40°N to 40°S. For the one year period beginning three months after the 1809 and 1815 eruptions, respectively, the average simulated ?N is -8.6 and -10.6 Wm^{-2}; while simulated ?T is -0.78°C and -1.0°C. Thus, the calculated surface climate sensitivity to the 1809 and 1815 eruptions is 0.091 and 0.093 $°C/Wm^{-2}$, respectively. These values are considerably lower than the typical global climate sensitivity noted by Hansen et al. (2002): 0.75°C to 1°C. However, values calculated by Hansen et al. (2002) were based on sensitivity experiments in which the forcing was held constant, which allows time for the climate to fully respond – unlike the transient forcing applied in the Millennium simulation.

6.4.2. Global-scale atmospheric circulation

6.4.2.1. The positive AO response

As discussed in previous chapters, the characteristically zonal structure of volcanic forcing from tropical eruptions typically causes NH atmospheric circulation to favor the positive phase of the AO during the winter season. Previous modeling studies (Stenchikov et al., 2002) have attributed this response to a combination of two primary thermodynamic mechanisms (section 2.3.4.1). The first is the so-called "stratospheric gradient" mechanism which occurs as a result of stratospheric heating at low-latitudes due to the presence of sulfate aerosols. This increases the equator-to-pole stratospheric temperature gradient and thus promotes stronger westerlies. The AOGCM used for this study should be able to realistically simulate this mechanism because the radiation scheme in the CSM1.4 stratosphere has been modified to thermally respond to increased SAOD, as if sulfate aerosols (effective radius = ~0.42 μm) were present in relative proportion to optical depth forcing (Ammann et al., 2003). The second thermodynamic mechanism is the so-called "tropospheric gradient" mechanism, which results from relatively greater tropospheric cooling at low latitudes, in response to the presence of increased SAOD from tropical eruptions. Since volcanic forcing is explicitly prescribed in the CSM1.4 as increased SAOD, there is little doubt that the model used here will realistically simulate this second mechanism, as well.

Previous studies have found that most AOGCMs (including the CSM) are able to realistically simulate the positive AO response, although they consistently underestimate its magnitude – perhaps due to their low vertical resolution at the tropopause and inability to realistically capture the "wave feedback" mechanism (Stenchikov et al., 2006). To test

if the CSM1.4 is able to realistically simulate the observed positive AO response, Figure 6.18, plots monthly composites of the AO during 13 years between 850 and 1999 with the highest SAOD forcing. Similar to observations (Figure 5.3) a statistically significant AO response is most consistently apparent in winter – keeping in mind that the CSM response is forced, on average by much greater increased optical depths (e.g., Tambora). This finding, along with results from a similar analysis of the CSM by Stenchikov et al. (2006), suggests that the coupled CSM is realistically able to capture the basic zonal-mean structure of the extra-tropical dynamical response to forcing from explosive tropical eruptions.

6.4.2.2. Global surface air temperature anomalies

In observations, a positive AO is associated with a general strengthening of upper-level zonal winds, an enhanced circumpolar vortex and increased extra tropical westerlies. This causes "winter warming" over mid-high latitude continents, particularly Europe (Shindell et al., 2004). Given the loading pattern of the AO on 1000h hPa GPHs in Figure 6.14 and the model's realistic positive AO response in winter (Figure 6.18), it is expected that the observed winter warming pattern will be correctly simulated by the model. Indeed, the top panel of Figure 6.19 clearly shows statistically significant positive temperature anomalies over Eurasia during high forcing winters. Furthermore, comparing this result with observations (Figure 5.6) and results from Shindell et al (2004, their Figure 1), it is remarkable how well the spatial distribution of the winter warming patterns agree over Eurasia. On the other hand, the model seems to underestimate the magnitude of the observed winter warming over eastern North America; although, a

realistic (weak) dynamical response is apparent over that continent as radiative cooling is relatively mild there, compared with other global regions at similar latitudes.

At lower latitudes, global cooling in response to volcanic forcing is very apparent. In summer, low-latitude cooling is strong, while the same high latitude regions that experienced winter warming were significantly colder than normal. Also, it is noteworthy that continental cooling is greater and more statistically significant, compared to oceanic regions; this is because the ocean's relatively high heat content means that it has a moderating effect on marine air temperatures. A final note on the summer composite plot: the only low-latitude regions without statistically significant cooling during this season are southern China and the ENSO region in the eastern tropical Pacific. While there is no clearly evident explanation for this (lack of) response in China, it is indeed interesting that warming (relatively less cooling) in the eastern tropical Pacific would be expected if the CSM were simulating an El Niño response to high volcanic forcing. This result should be considered preliminary but it is noteworthy because it is in qualitative agreement with recent modeling (Mann et al., 2005) and observational studies (Adams et al., 2003).

6.4.2.3. The global Hadley cell

In addition to the positive AO response, it is hypothesized that global-scale tropical rainfall and Hadley circulation are weakened by the blocking of incoming solar radiation caused by increased SAOD. A test of this hypothesis was conducted in the previous chapter using global zonally averaged CRU precipitation and vertical wind shear data; however, results were somewhat anecdotal and inconclusive, in part due to the

confounding ENSO factor. Here the same monthly compositing methods are used to test the Hadley cell dampening hypothesis based on results from the millennium simulation during three different eras: “modern”, “Paleo1” and “Paleo2.” For direct comparison with results from observations (Figures 5.4 and 5.5), “modern” periods used analyses of land precipitation (CRU) and vertical shear (NCEP reanalysis) from 1902 – 1999 (n = 4) and 1948 – 1999 (n = 3), respectively. The “Paleo1” analysis period is from 1800 – 1999 (n = 6) and the “Paleo2” analysis period spans the entire Millennium simulation, from 850 – 1999 (n = 13). Before discussing composite results, it should be noted that the CSM appears to be quite skillful at simulating global-scale monthly zonally averaged land precipitation (compare Figure 6.20a with left panel of Figure 5.4).

Figure 6.20a, which is directly comparable with the right panel of Figure 5.4, illustrates mean conditions and the simulated “modern” response to eruptions during the years 1902, 1963, 1982 and 1991. While the “modern” composite reflects both drier and wetter conditions in response to these tropical eruptions, the only (marginally) statistically significant results found at low latitudes are decreased precipitation rates. For the Paleo1 analysis (Figure 6.20c), the response throughout the tropics is much more clearly indicative of year-round drying. Also, relative to “modern,” results from Paleo1 are more statistically significant, which was expected due to the larger sample size and the higher average levels of forcing in the latter composite. Finally, results from the Paleo2 composite (Figure 6.20d) overwhelmingly reflect year-round drying with precipitation anomalies of greater magnitudes (10 - 15% decreases) and higher levels of statistical significance (>99% confidence). Another interesting result – though not apparent year-round – is that precipitation rate increases were commonly simulated at

subtropical latitudes (20° – 35°). Similar patterns are also apparent in observations (Figure 5.4), although they were not nearly as statistically significant.

To examine the response of a more direct measure of atmospheric meridional overturning in the tropics, composites of zonally averaged vertical wind shear are created. First, to consider model skill with respect to the observed climatology, a visual comparison between Figures 5.5a and Figures 6.21a suggests that the average seasonal cycle of model-simulated Hadley circulation is similar to observations. However, NH Hadley circulation is anomalously strong (nearly double) in the model, compared with observations. This bias in the CSM was also noted by Dai et al. (2001b), based on analyses of the zonal mean meridional streamfunction field. Also, recall that this model deficiency was also inferred from model biases in the tropical and subtropical Omega, or vertical velocity, field in the vicinity of East Asia (Figure 6.4). Nevertheless, the model is still considered useful for generally studying various aspects of Hadley cell *variability* and for exploring the dynamic climatic response to volcanic forcing in the tropics.

Figure 6.21b illustrates the model-simulated Hadley circulation response to volcanic forcing during the "modern" era and it is directly comparable to Figure 5.5c. Unlike the global precipitation analysis above, there is generally very little in common between the simulated and observed response in this circulation field. As discussed in Chapter 5, composites of the observed vertical shear response to volcanic forcing is actually very similar to the ENSO composite (Figure 5.5b), so it was suggested that the anomalies following Agung may be a better indicator for a response without the influence of ENSO (since 1963 was a relatively weak El Niño year). Indeed, a comparison between the modern model composite in Figure 6.21b is quite similar to Figure 5.5d.

However, as in the global precipitation composites (above; Figure 6.20), a much clearer signal becomes evident during the Paleo1 and Paleo2 eras, when the sample size and the average SAOD forcing in each composite is increased. The picture that begins to emerge in the Paleo1 composite is perfectly clear in Paleo2: vertical wind shear anomaly patterns in Figure 6.21d are recognizable as the very opposite of the long term mean pattern shown in Figure 6.21a. Thus, in response to forcing from the 13 largest tropical eruptions in the past Millennium, a statistically significant ~10% dampening of Hadley circulation is simulated in both the NH and SH cells during their respective dominant seasons of activity.

6.4.3. Regional-scale response

The regional-scale response is the final portion of this study's AOGCM analysis. First, simulated regional SATs are examined during three different eras of the Millennium run and then a seasonally averaged time series of observed Marine Air Temperature (MAT) measurements from the SCS are compared with comparable model output during the Tambora era. Next, the model-simulated East Asian summer season hydroclimatic response is assessed in the context of anomalies in a few key upper-air diagnostic variables. Finally, the EAM response is explored from the perspective of the regional-scale monsoon indices on a monthly basis throughout the mean annual monsoon cycle.

6.4.3.1. Surface air temperature anomalies

Figure 6.22 presents composite plots of the East Asian surface air temperature response during the aforementioned "modern," "Paleo1," and "Paleo2" eras. As in previous sections, the "modern" composite provides an opportunity to directly compare observations with the model-simulated response to identical eruptions. Results in the top row of Figure 6.22 bear little resemblance to the observed response to these eruptions (Figure 5.6); neither winter warming over Eurasia nor tropical temperature reductions are clearly apparent. This unrealistic model response has a couple of possible explanations, but the most likely reason for the lack of a realistic winter warming signal is that AOGCMs consistently underestimate the positive AO response in winter (Stenchikov et al., 2004), suggesting that greater forcing may be needed for the model to properly simulate this response. Also, as reflected by the low levels of statistical significance throughout the analysis domain, the signal-to-noise ratio in the "modern" composite is clearly quite low due to the relatively weak forcing and small sample size. Finally, the CSM1.4 could be responding to relatively higher greenhouse gases and increased tropospheric aerosols during this era, thus diminishing the volcanic signal.

On the other hand, results from the "Paleo" composites (Figure 6.22, bottom two rows), which contain more samples and greater average forcing, demonstrate the usefulness of the Millennium simulation for increasing the signal-to-noise ratio and thus helping to resolve more clearly the regional-scale temperature response to volcanic forcing. Both the Paleo1 and Paleo2 composites realistically capture the observed winter warming pattern over Eurasia as well as much greater cooling throughout the low-latitudes. The latter finding is clearly caused by the negative imbalance in net surface

radiative flux caused directly by stratospheric aerosol forcing. The winter and summer temperature response over eastern China is generally consistent with the response throughout the greater East Asian region (significant cooling); however, as noted earlier, the simulated cooling in southern China near the Vietnam boarder is uniquely weak for this latitude and this season. An explanation for this result is not clear.

As discussed in earlier Chapters, several previous studies have employed proxy-based paleoclimate reconstructions attempting to quantitatively estimate the actual magnitude of the global-scale cooling that occurs in response to historical eruptions, several of which were apparently much larger than recent 20th century eruptions. This question is particularly difficult to answer when the regional-, as opposed to global-, scale temperature response is of interest because well-calibrated proxies or direct measurements are rarely available in a particular area of interest. Yet this information is particularly desirable in the context of the present study because it provides a quantitative constraint on the actual regional-scale temperature response to exceptionally large historical eruptions.

Figure 6.23 plots the time series of seasonally averaged adjusted MAT anomalies from the SCS (Figure 5.15) compared with CSM-simulated seasonal mean surface air temperature anomalies from atmospheric grid-boxes over the model ocean in that region. This comparison represents an independent test on the reliability of regional-scale climate sensitivity to the SAOD forcing (Ammann et al., 2006) applied in the Millennium simulations. However, it should be emphasized that conclusions drawn from these results should be considered somewhat preliminary due to the fact that the SCS is only one

global region and because of quality control problems with the original MAT measurements (Chenoweth, 2000).

Still, results presented in Figure 6.23 illustrate that the modeled temperature response to exceptionally large Tambora era eruptions is remarkably realistic. While the model seems to slightly underestimate the magnitude of the observed cooling, simulated temperature variations throughout this era are generally well within the range of inter-seasonal variability in the observed MAT record. Interestingly, both the model and the observed MAT record also appear to have responded on comparable orders of magnitude to two other tropical eruptions (1812 and 1823) during this period, the latter of which is estimated to have been roughly the same size at the Agung and El Chichón eruptions (peak SAOD = ~ 0.15).

6.4.3.2. Hydroclimatic and atmospheric circulation anomalies

Figure 6.24 shows summer season composite anomalies of simulated East Asian precipitation along with three associated diagnostic variables during 13 high forcing summers between 850 and 1999 AD. The precipitation response throughout this analysis domain (a) and over eastern China, in particular, is generally one of drying, especially along the southern coast of China, in the lee of the Tibetan Plateau and in areas west of 110°E. The eastern parts of the YRV and NEC, which have been the primary focus of most hydroclimate analyses in this study, were relatively less responsive. Still, in all four composite plots statistically significant results are apparent, particularly in 500 hPa GPHs (c), which responded with very large (>30 m) negative anomalies in southern China and in the vicinity of the climatological West Pacific subtropical high. Meanwhile negative

pressure height anomalies were relatively less apparent in the north, thus creating a weakening in the south-north atmospheric pressure gradient and likely contributing to negative anomalies in the strength of the East Asian subtropical jet (d). At lower atmospheric levels, composite anomalies in 850 hPa zonal winds in the western Pacific region also reflect the noted weakening of the WPSH at 500 hPa: westerly anomalies at 10°N and easterly anomalies at 30°N. The climatologic westerly low-level jet over southern India, the Bay of Bengal and the Indochina peninsula is also weakened in response to this forcing.

6.4.3.3. Regional-scale monsoon indices

To further explore the regional-scale dynamical mechanisms that are likely contributing to the simulated drying over parts of eastern China, monthly composite anomalies are computed for each of the regional monsoon indices during high forcing years. Figure 6.25 presents the results from this analysis and may be compared with observational composite analyses, both before and after the SOI signal was removed from the indices (Figures 5.9 and 5.10, respectively). Focusing first on the winter season response, a weakening of the WPSHz is clearly evident (a), which is consistent with the simulated dampening of the NH Hadley circulation during this season. Higher SMI values are also simulated in winter (d), thus supporting evidence for a stronger winter monsoon and regional cooling during this season (Figure 6.22).

During summer months, the WPSHz is slightly weakened (a), which is consistent with significant pressure height anomalies at 500 hPa (Figure 6.24a), discussed in the previous section. Consistent with Figure 6.24d, the EAJSI is also significantly weakened

during summer. Based on the spatial correlation patterns between summer precipitation in eastern China and the EAJSI and the WPSHz indices (discussed earlier; Figures 6.10 and 6.11), some general inferences can be made regarding the implications of these findings for regional precipitation. First of all, both of these *simulated* indices are positively correlated with JJA precipitation over the YRV and NEC regions. Thus, the simulated drying response over northern China (Figure 6.25) may be at least partially attributable to dynamical mechanisms: negative anomalies in the WPSHz and EAJSI during summer.

On the other hand, the EAJSI and WPSHz indices are slightly inversely correlated with precipitation in southeastern China (in the model and observations). Thus, it might be expected that negative anomalies in these indices could lead to relatively wetter conditions in the south. However, this is not the simulated (or observed) result. In fact, as noted in the previous section, the precipitation composite (Figure 6.24a) indicates that drying occurs in the southern coastal region and throughout the adjacent SCS. Thus, it is possible that the simulated response over SEC may be less attributable to dynamical mechanisms and more indicative of a direct radiative response, associated with weakened evaporation in a cooler troposphere. This explanation would also be consistent with a weaker ITCZ and the dampened Hadley cell mechanism.

As a final note, it is worth mentioning that although many of the error bars in the Figure 6.25 composites are relatively small compared to observations (Figures 5.9), they remain quite large in many cases, despite the much larger sample size and higher average forcing in the model composites. This point is important because it illustrates that the signal-to-noise ratio in this monsoon index analysis is quite substantial, which could be

an indicator of two things. First, it may be a confirmation that regional-scale volcanic signals are generally noisier (Wagner and Zorita, 2005) and thus more ensemble members are necessary to properly resolve a clear signal.

Alternatively, these results may well reflect the fact that most of the regional monsoon indices examined here are simply not very sensitive to volcanic forcing. After all, the statistically significant simulated results noted in earlier sections reflect dynamical mechanisms that are either indicative of a global zonally-oriented response (e.g., positive AO) or are well represented by global zonal mean climate anomalies (e.g., Hadley cell dampening). In both cases the zonal structure of the global-scale forcing creates a global-scale zonal response. Meanwhile, the monsoon indices collectively reflect a complex regional-scale system containing significant zonal and meridional components.

6.5. Synopsis

Simple assessments of CSM biases (Figures 6.1 – 6.4) suggest that the CSM1.4 simulates the mean state of JJA general circulation reasonably well for the East Asia region. Primary model biases include, 1) high rainfall in the lee of the Tibetan Plateau, 2) dry conditions in southern China, 3) a strong WPSH and, 4) a strong East Asian Jet. In terms of simulated interannual rainfall variability, the loading patterns from the first and second principal components of regional precipitation shared much in common with results from similar analyses from the observations. Model skill with respect to regional scale hydroclimate was also considered using wet-minus-dry maps, regional monsoon indices and from the perspective of large-scale ocean and atmosphere variability. Overall, this assessment found that the CSM demonstrates reasonable skill with regard to

local- and regional-scale atmospheric circulation patterns that contribute to observed interannual precipitation variability in eastern China. This finding is particularly true for the YRV and SEC regions, suggesting that more confidence can be placed on subsequent modeling analyses in those regions.

However, regional-scale analyses uncovered some potentially significant CSM1.4 deficiencies as well. In particular, there is a strong anti-correlation between rainfall and surface air temperatures over E. China in nature, but this basic relationship is not captured well by the CSM. Whether or not the ReCM is more skillful in this regard will be tested in the following chapter. Also, while the CSM generally captured the basic spatial patterns of correlations between summer rainfall variability and most of the regional monsoon indices, the LSTD index was an exception. This is unfortunate given this study's specific interest in the EAM response to changes in radiative forcing. The model's demonstrably poor skill at simulating observed relationships between hydroclimate in eastern China and local SSTs or the LSTD index, an important thermodynamic index (Wu and Chan, 2005), is a cause for some concern. Combined, these results suggest that necessary parameterizations used for clouds and radiation could inhibit this global model's ability to realistically simulate a direct radiative response to volcanic forcing.

Not surprisingly, the CSM also has some difficulty accurately simulating atmospheric pressure-related teleconnection patterns beyond the immediate vicinity of East Asia, such as those with respect to the Okhotsk High (Figures 4.4 and 4.5). This confirms findings from several earlier global model assessments, wherein teleconnections linked to the EAM (Liang et al., 2002) and other mid-latitude climates (Kunkel et al.,

2006), are shown to be generally not well simulated by GCMs. Furthermore, as discussed in section 6.1.3, coupled AOGCMs have a particularly difficult time simulating teleconnections with observed modes of SST variability, as the spatial structure and temporal frequency of these modes are generally not well replicated by the ocean model. In contrast, atmosphere-alone GCMs typically perform slightly better in this regard (Liang et al., 2002) because prescribed SSTs are, by definition, based on observed – as opposed to modeled – ocean conditions. On the other hand, it is also worth recalling, from Chapter 4, that interrelationships between regional-scale monsoon indices and surface climate in China are not always stationary through time. Thus, portions of the observed global-scale teleconnections patterns presented in Figure 4.19, for example, may be somewhat tenuous and the inability of the model to replicate all of them in detail does not necessarily reflect severe model deficiencies with respect to regional-scale climate simulation.

A thorough summary of the CSM-simulated response to volcanic forcing is included in the conclusions section of this report (Chapter 8), along with a discussion comparing these results with the observed response studied in Chapter 5.

Table 6.1. Correlation matrix comparing interannual variability in CSM1.4 *simulated* regional and global climate indices during JJA, 1948 – 1999 AD. Note that linear trends were removed from all indices prior to calculation of r-values. Bold R-values that are significant at the 95th and 99th percent confidence levels are italicized and underlined, respectively (not accounting for autocorrelation or stationarity). See text, Table 4.1 and Figures 4.8 and 4.9 for details regarding index definitions.

Variable	WPSHz	LSTD	WNPMI	SMI	OKHI	EAJSI	GJSI	HCIN-sf	HCIN-vs	HCIS-sf	HCIS-vs	SOI	SOI-DJF	AO	PDO	CSMnec	CSMyrv	CSMsec
WPSHz	1	0.12	**-0.75**	0.17	-0.13	0.21	0.16	**0.35**	-0.15	**-0.36**	0.22	**-0.47**	***-0.27***	-0.03	0.24	0.20	**0.55**	**-0.63**
LSTD		1	-0.25	**0.44**	0.20	***0.28***	0.12	0.14	0.00	-0.05	0.18	0.25	-0.15	0.18	-0.01	**0.66**	0.18	-0.15
WNPMI			1	-0.14	-0.08	-0.14	-0.16	0.00	0.10	0.05	-0.23	0.14	0.17	0.17	0.00	-0.18	**-0.50**	**0.70**
SMI				1	***-0.27***	0.22	-0.01	0.21	0.22	0.03	0.23	0.16	0.00	0.21	0.10	**0.34**	**0.48**	-0.10
OKHI					1	0.06	0.15	-0.10	-0.18	0.05	-0.06	0.01	0.04	**-0.34**	-0.12	0.13	-0.12	-0.16
EAJSI						1	**0.46**	0.22	0.02	-0.13	0.18	**-0.41**	-0.04	-0.24	0.27	0.17	***0.27***	-0.28
GJSI							1	0.03	-0.04	-0.16	-0.11	***-0.28***	-0.06	**-0.55**	***0.28***	0.18	0.10	***-0.30***
HCIN-sf								1	**0.33**	-0.14	0.07	-0.08	0.17	0.23	0.11	0.05	***0.27***	-0.22
HCIN-vs									1	**0.34**	0.15	**0.43**	**0.33**	0.16	-0.11	-0.21	0.19	0.20
HCIS-sf										1	0.18	**0.56**	**0.36**	0.14	-0.26	-0.15	0.17	0.02
HCIS-vs											1	0.08	-0.24	0.03	-0.03	0.06	***0.31***	-0.15
SOI												1	0.26	**0.43**	***-0.30***	-0.03	-0.05	0.24
SOI-DJF													1	0.03	-0.14	-0.26	0.01	0.14
AO														1	0.04	0.04	0.12	0.15
PDO															1	0.17	0.24	-0.11
CSMnec																1	0.18	-0.12
CSMyrv																	1	**-0.44**
CSMsec																		1

Table 6.2. Same as Table 6.1, except for DJF, from 1948 – 1999 AD.

Variable	WPSHz	LSTD	WNPMI	SMI	OKHI	EAJSI	GJSI	HCIN-sf	HCIN-vs	HCIS-sf	HCIS-vs	SOI	DJF	PDO	NEC	YRV	SEC
WPSHz	1	-0.03	0.08	**-0.38**	0.08	***-0.28***	0.20	**0.52**	-0.10	**-0.35**	-0.09	**-0.56**	***0.31***	0.02	0.13	0.24	0.09
LSTD		1	***0.31***	**-0.53**	***0.31***	-0.17	***-0.31***	-0.15	0.11	0.15	0.05	**0.36**	0.12	0.04	0.07	***0.30***	**0.34**
WNPMI			1	**-0.50**	-0.06	**-0.44**	-0.24	0.16	-0.01	-0.15	-0.08	-0.10	0.26	0.02	-0.09	0.27	**0.44**
SMI				1	0.11	***0.41***	0.12	***-0.46***	-0.25	0.25	0.18	0.12	-0.23	-0.11	-0.21	**-0.57**	-0.21
OKHI					1	0.11	0.07	0.02	-0.01	0.07	0.11	0.15	-0.07	-0.17	0.15	-0.03	-0.07
EAJSI						1	**0.56**	**-0.40**	-0.11	0.00	-0.14	0.04	**-0.52**	-0.02	-0.01	**-0.38**	-0.25
GJSI							1	-0.12	-0.17	-0.19	***-0.28***	**-0.44**	**-0.43**	***0.32***	0.05	-0.16	-0.13
HCIN-sf								1	***0.31***	**-0.45**	-0.06	-0.20	**0.38**	-0.01	0.20	***0.30***	-0.10
HCIN-vs									1	-0.02	0.08	**0.41**	0.17	-0.16	0.17	0.13	0.04
HCIS-sf										1	**0.71**	0.20	-0.01	-0.20	-0.04	-0.19	0.11
HCIS-vs											1	0.14	0.18	**-0.33**	0.01	-0.11	0.10
SOI												1	0.17	***-0.32***	0.12	0.19	0.15
AO													1	-0.16	0.15	**0.48**	0.11
PDO														1	-0.13	-0.06	-0.23
NEC															1	**0.34**	0.17
YRV																1	0.27
SEC																	1

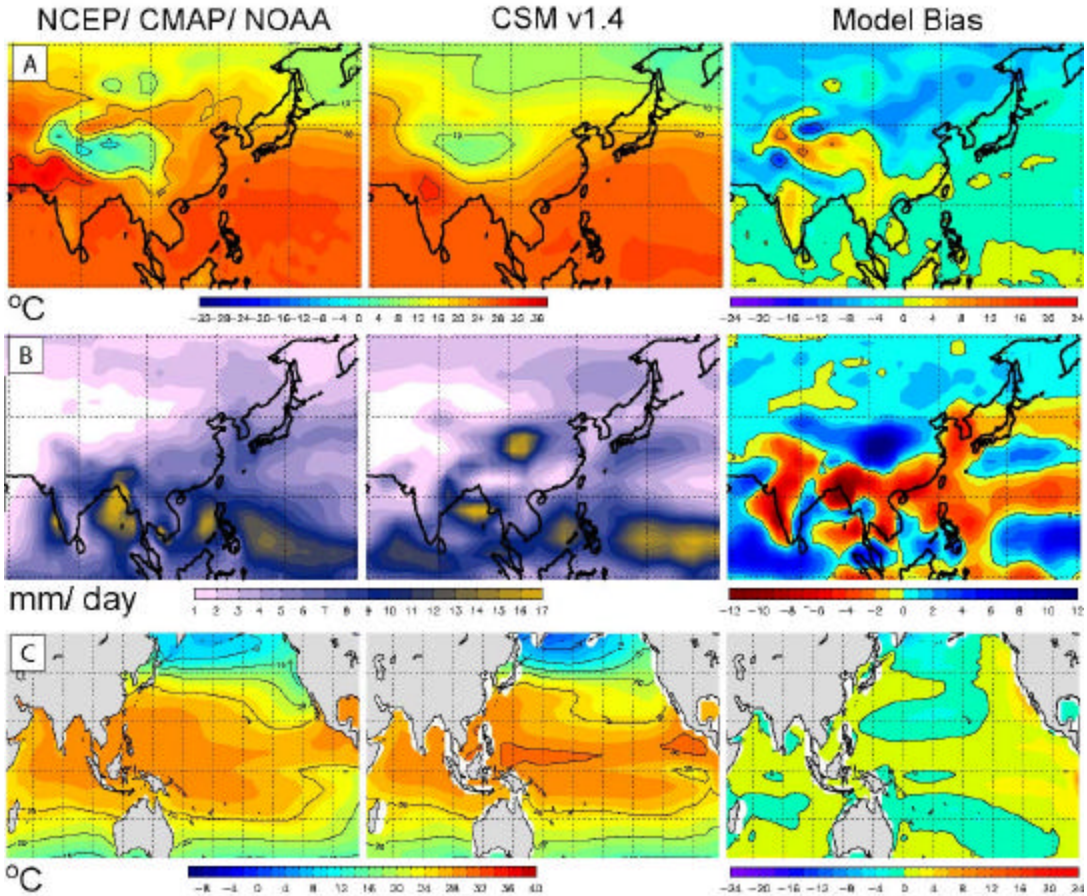

Figure 6.1. Summer season climatologies of surface conditions based on observations and results from the CSM1.4 Millennium simulation (1961 – 1990). Panels show (a) reference height temperature (NCEP), (b) precipitation (CMAP), and (c) sea-surface temperature (NOAA-ER SST). The model biases (right panels) were computed by subtracting the observations (left panels) from the model values (center panels), after model data were interpolated to the same grid as observations.

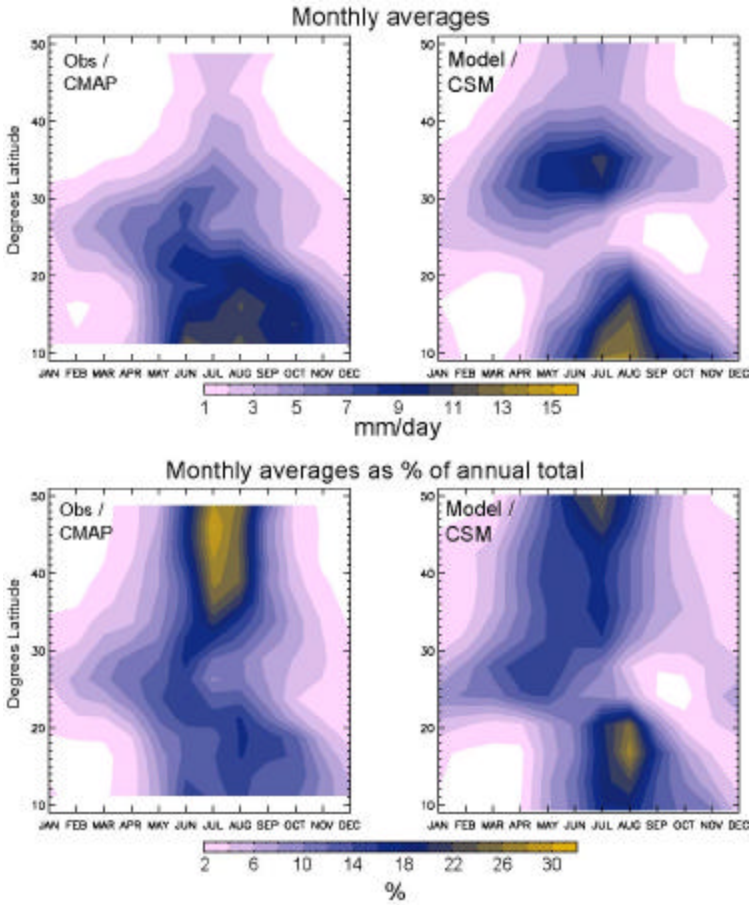

Figure 6.2. Comparing CMAP (left panels) with CSM1.4 (right panels) output, Hovmoller diagrams show the annual cycle of monthly precipitation, zonally averaged at each latitude across eastern China (105° – 122°E; 1961 – 1990 AD). Latitude-month precipitation values are presented as averages (top; mm/day) and as percentages of annual means (bottom), to highlight the seasonality of precipitation at each latitude.

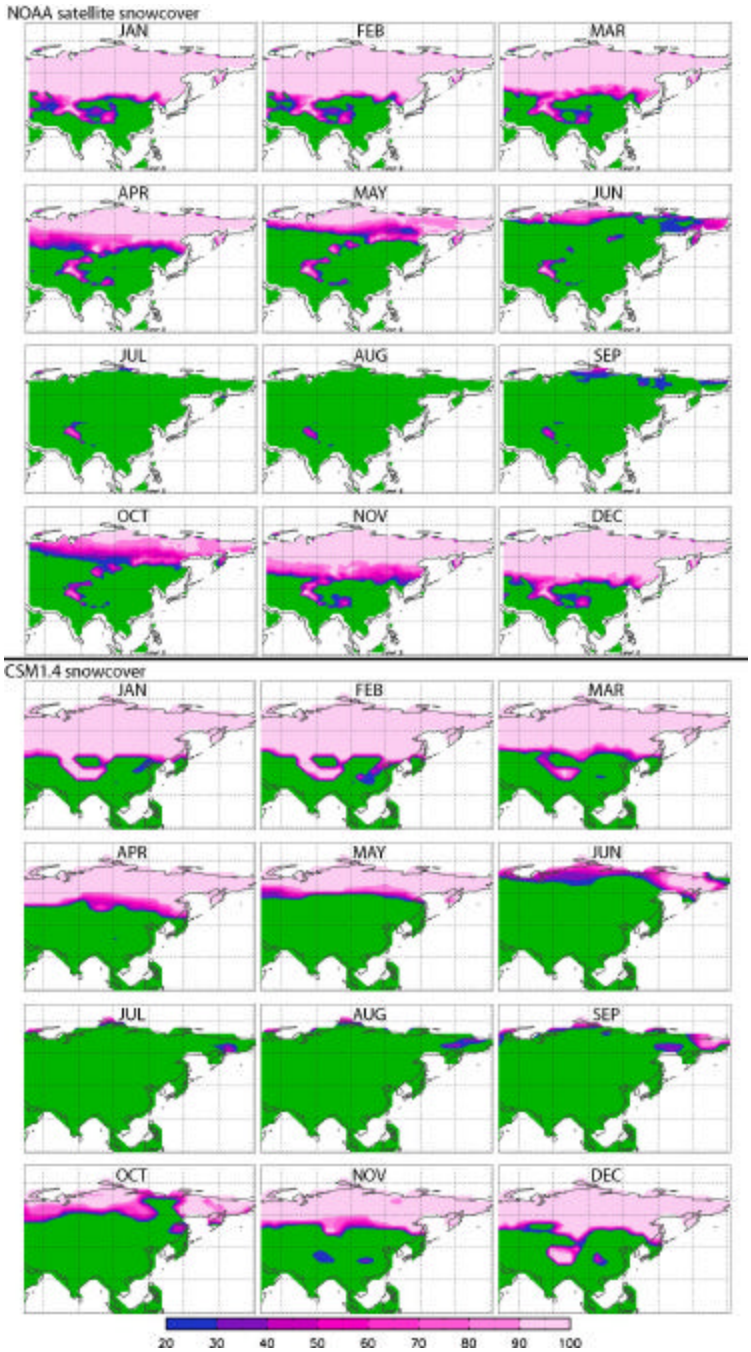

Figure 6.3. Comparing monthly snowcover from observations (top 12 panels) with CSM1.4 output (bottom 12 panels), in percent units. Observations are derived from weekly NOAA satellite data (Robinson et al., 1993) and model data were iteratively estimated from daily values of water equivalent snow depth (see text for details).

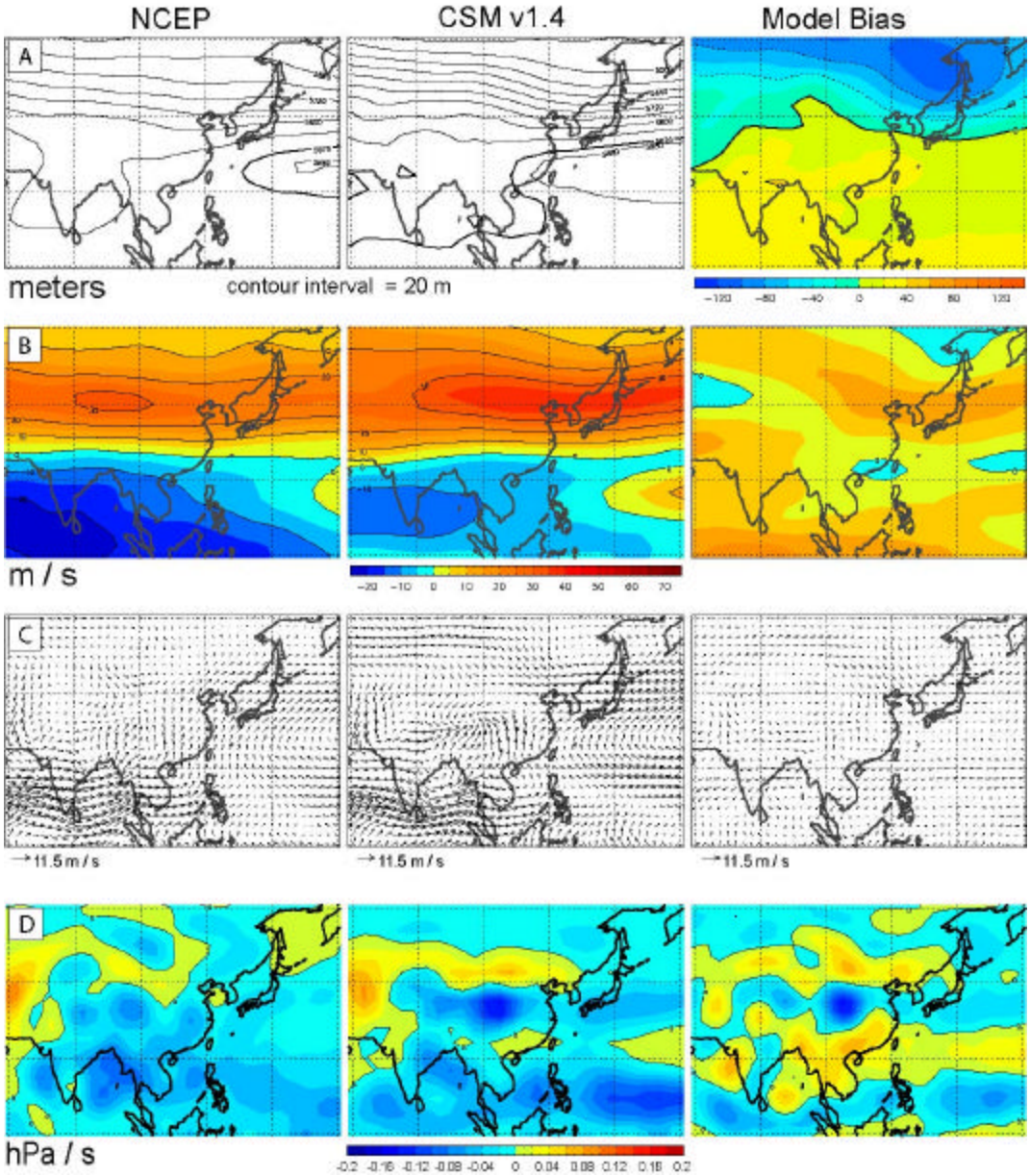

Figure 6.4. Upper-air plots are comparable to Figure 6.1 but for (a) 500 mb geopotential heights, (b) 200 mb zonal wind, (c) 850 mb wind, and (d) 500 hPa vertical velocity, or Omega, from 1961 to 1990 AD.

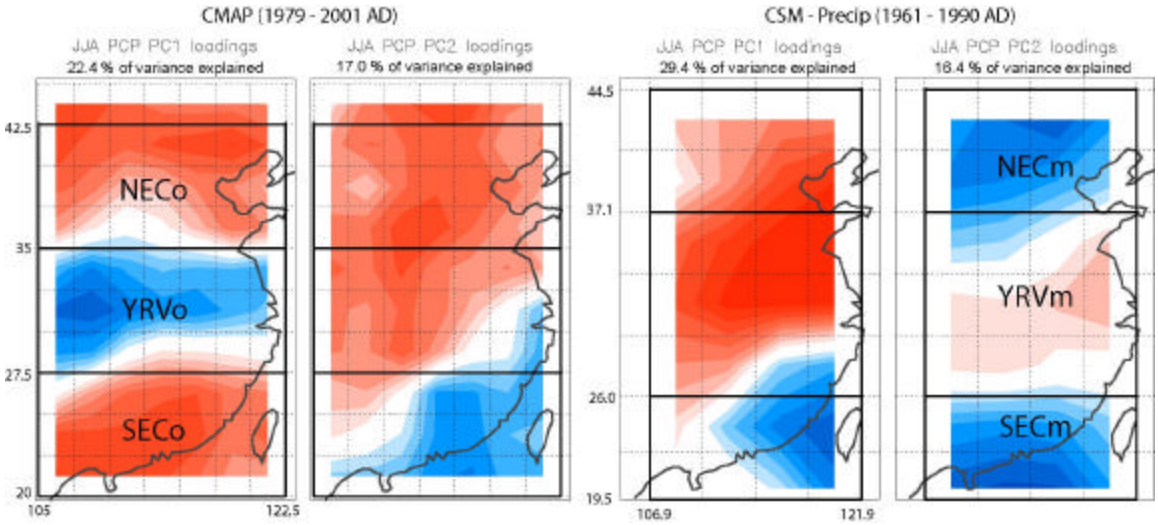

Figure 6.5. Loading patterns for the first and second principal components of interannual summer rainfall variability over eastern China (~20° – 45°N, 105° - 123°E) from the CMAP dataset (left two panels; 1979 - 2001) and CSM1.4 millennium simulation output (right two panels, 1961 - 1990). Grid cells are marked by light dashed lines. The boxes delineated in bold outline three zonal regions (labeled: NECm, YRVm, and SECm) with relatively coherent modes of interannual variability based on the first and second principal components of regional precipitation in CMAP and CSM output, respectively.

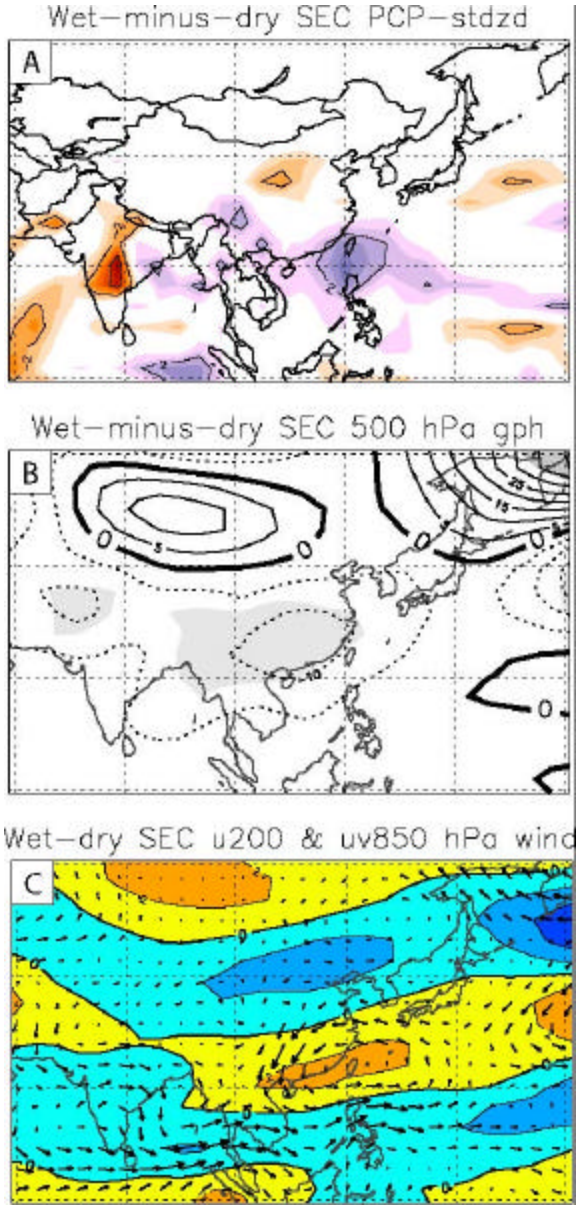

Figure 6.6. Wet-minus-dry maps based on SECm conditions showing (a) standardized precipitation, (b) 500 hPa geopotential heights, and (c) 200 hPa zonal winds (color contours) and 850 hPa wind vectors. Each plot reflects differences between model-simulated conditions during the 5 wettest and the 5 driest summers (JJA) between 1977 and 1999. (a) Precipitation color contours occur at 0.5 standardized unit intervals while line contours occur at 2 standardized unit intervals (only differences exceeding one standard deviation are shown). (b) 500 hPa geopotential height contours occur at five meter intervals (solid = positive; dashed = negative; zero = bold) with lightly shaded regions highlighting differences less than one standard deviation below zero, while dark shading highlights differences greater than one standard deviation above zero. (c) 200 hPa zonal wind color contours occur at 2 m/s intervals with warm colors reflecting positive difference values while cool colors are negative.

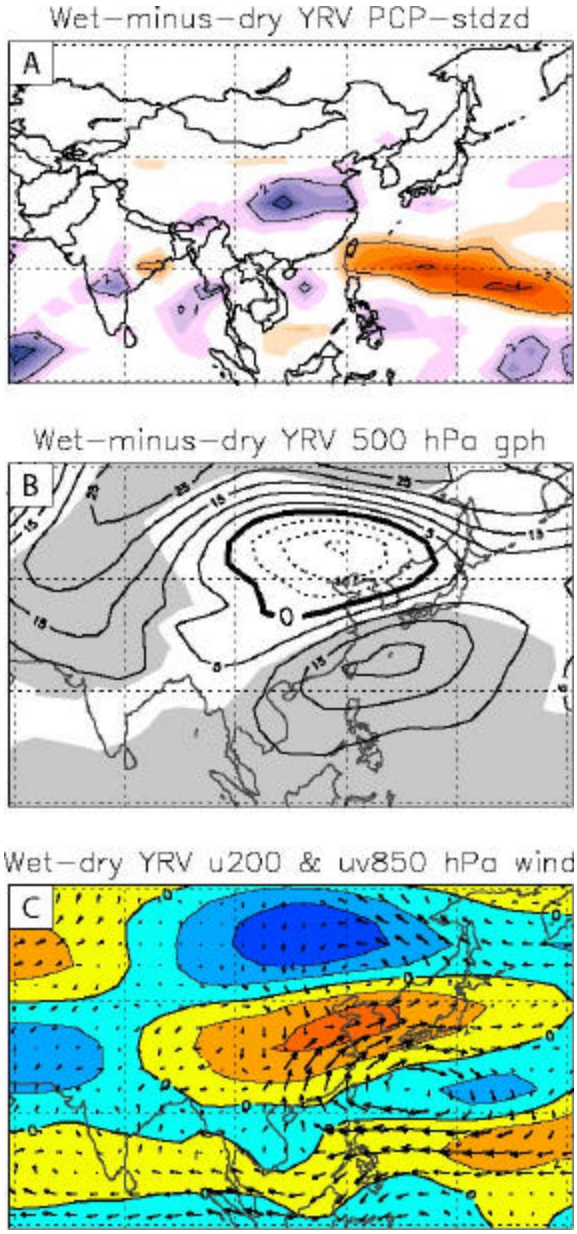

Figure 6.7. Same as Figure 6.6, except for model-simulated YRVm rainfall.

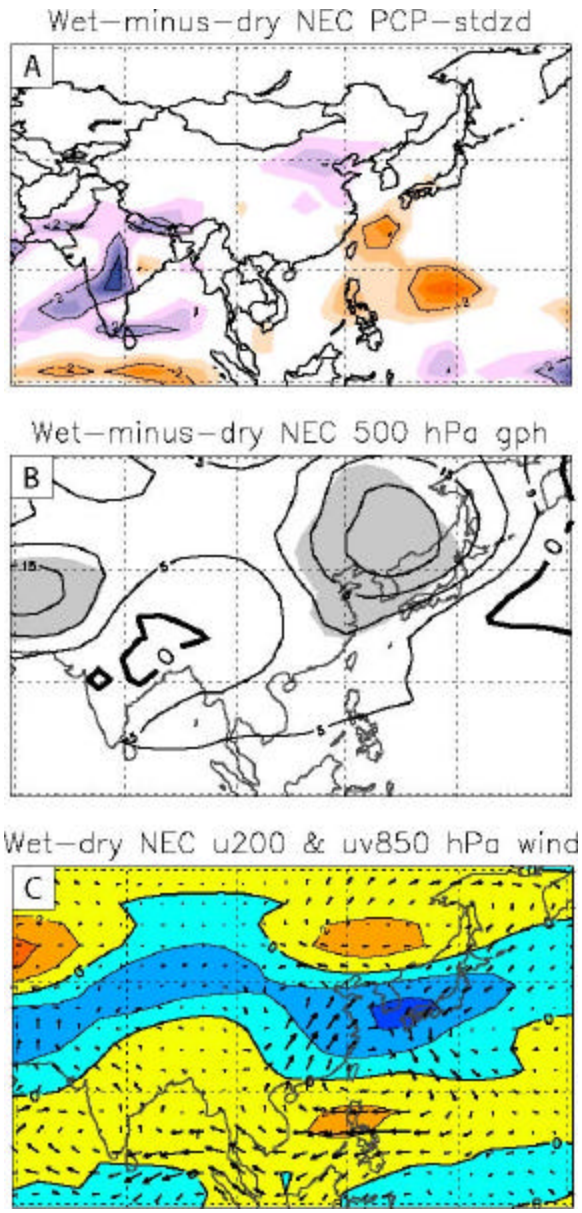

Figure 6.8. Same as Figure 6.6, except for model-simulated NECm rainfall.

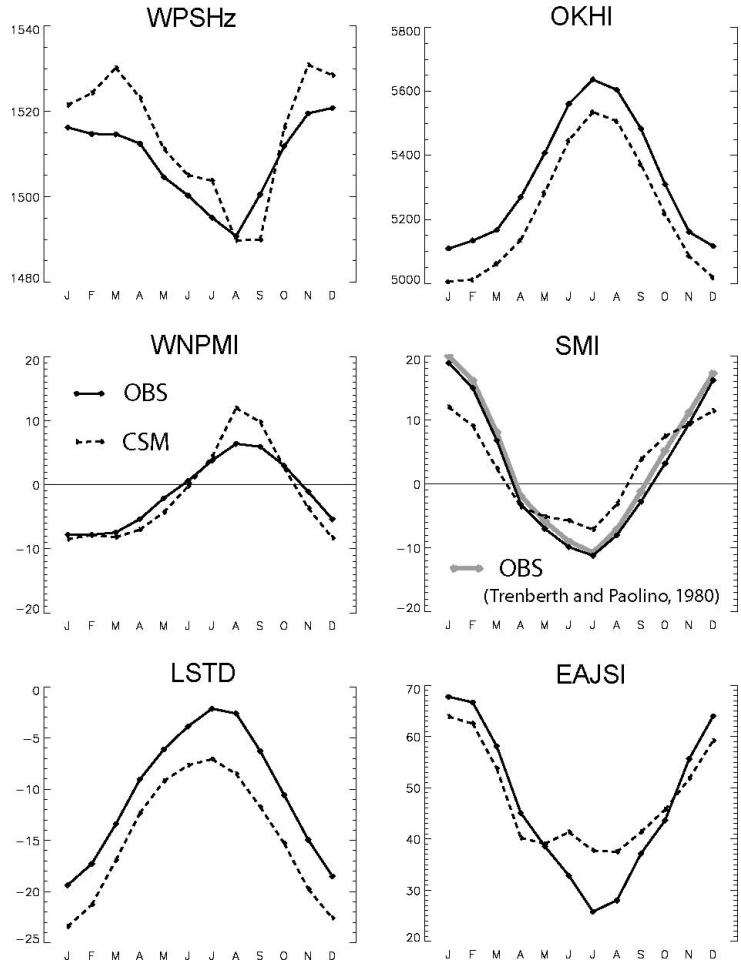

Figure 6.9. Long-term mean monthly climatologies for each of the regional climate indices. Results from both observations (solid) and the CSM (dashed) are shown, each averaged over the period from 1961 – 1990 AD. Also, note that the SMI includes two climatologies based on observational data, one derived from NCEP reanalysis (dark) and one from Trenberth and Paolino (1980; grey). Units: WPSHz (m), OKHI (m), WNPMI (m/s), SMI (mb), LSTD (°C), EAJSI (m/s).

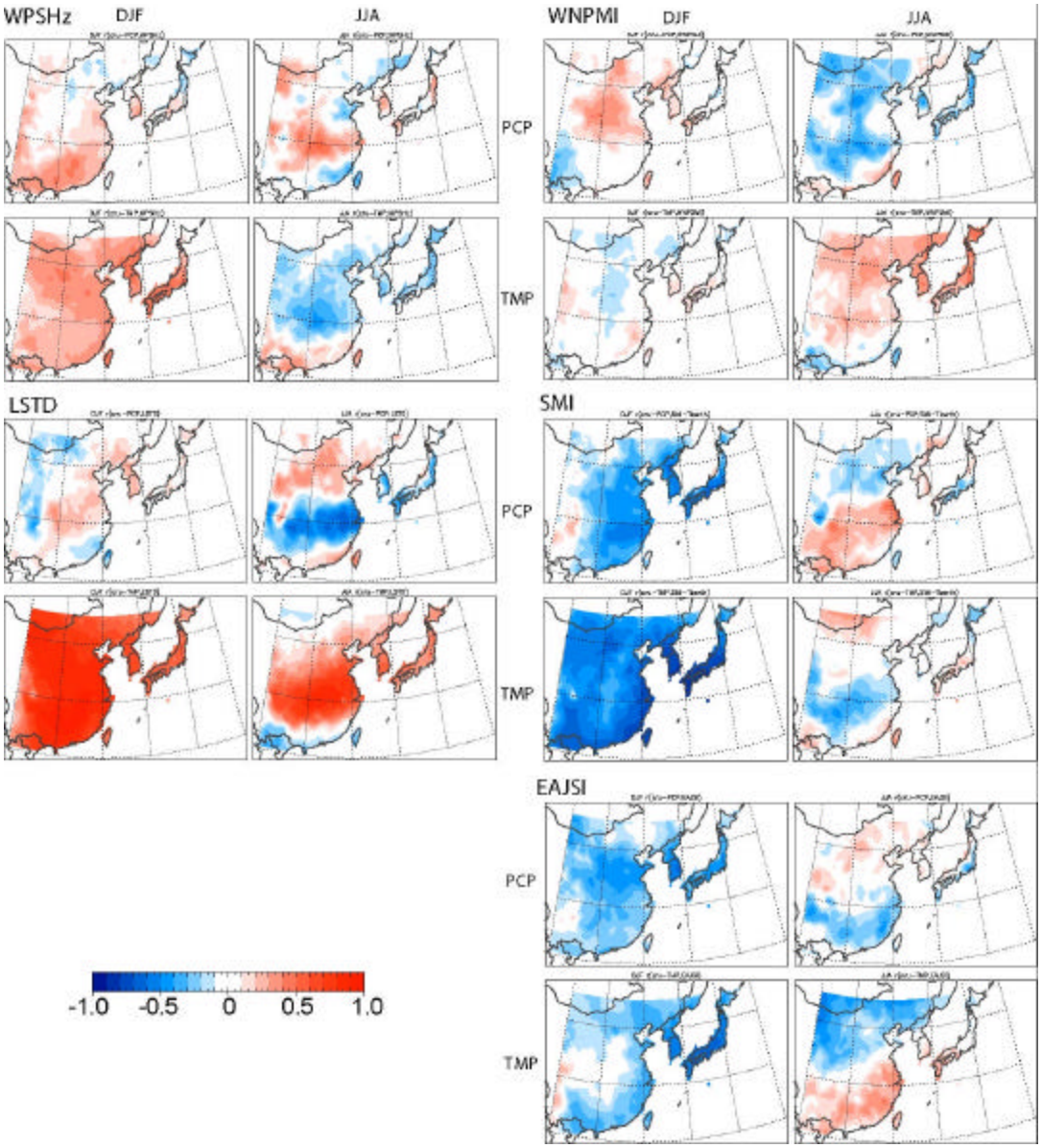

Figure 6.10. Observed spatial correlations between regional monsoon indices and surface air temperature and precipitation in the East Asia region (CRU, 1948 – 2002; replicated from Chapter 4, Figures 4.10 – 4.15). Seasons (DJF, JJA), variables (TMP, PCP) and indices are all appropriately labeled. Individual correlation values greater than 0.3 (or less than -0.3) are significant with roughly 95% confidence (not accounting for multiplicity, the testing of multiple hypotheses). See text for further details.

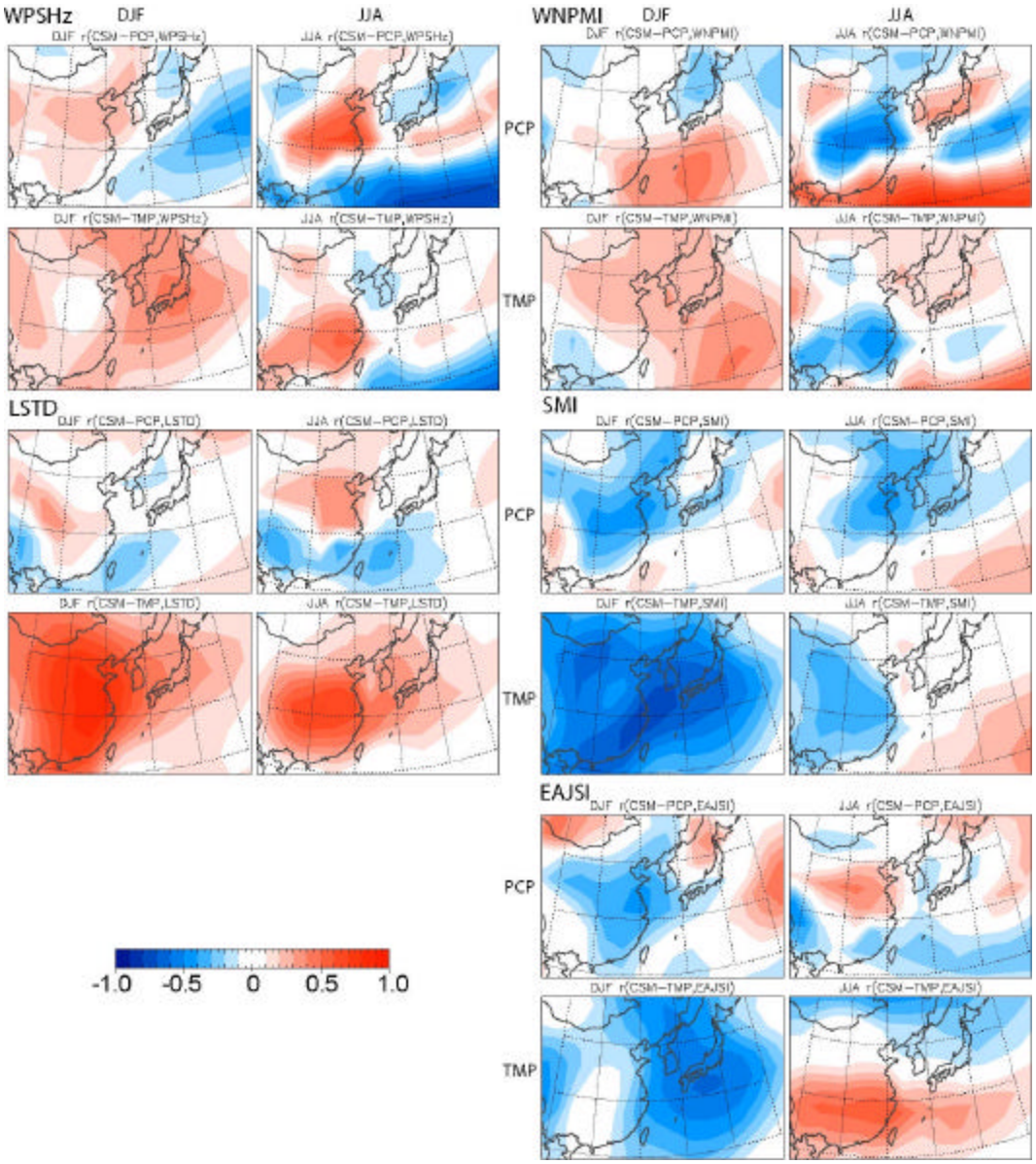

Figure 6.11. Same as Figure 6.10, except for the CSM1.4 Millennium simulation (1950-1999).

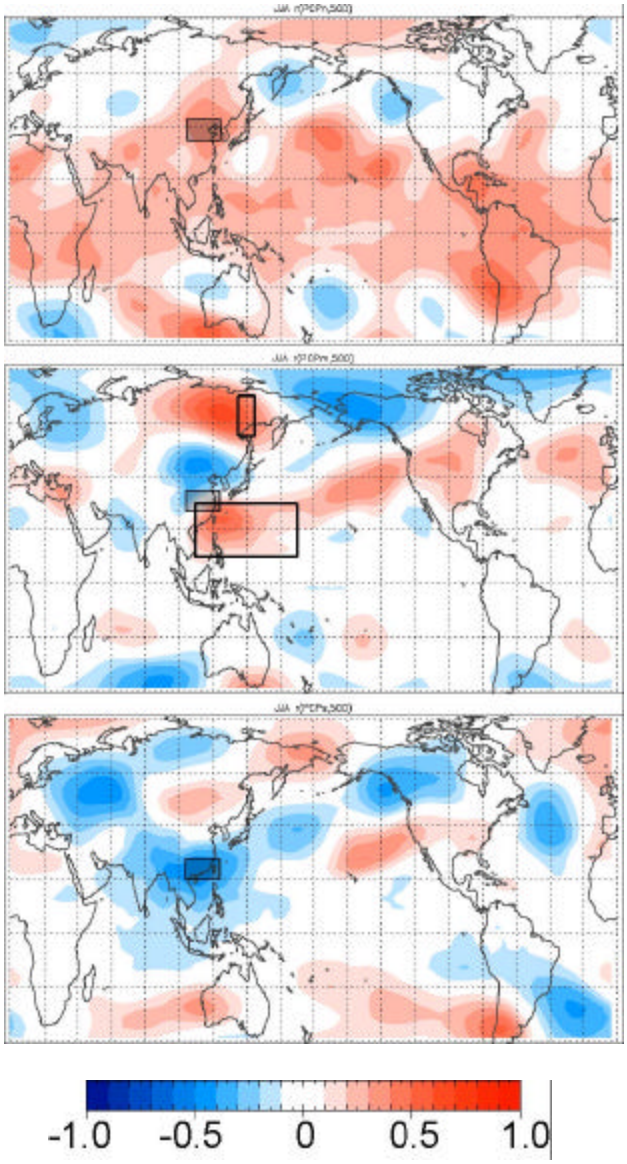

Figure 6.12. Map of correlations between CSM1.4-simulated 500 hPa geopotential heights and standardized regionally averaged precipitation in NEC (top), YRV (center) and SEC (1961 – 1990). For reference, precipitation regions are marked by translucent grey boxes while the Okhotsk High and WPSHz index domains are shown in the center plot. Individual correlation values greater than 0.4 (or less than -0.4) are significant with roughly 95% confidence (not accounting for multiplicity, the testing of multiple hypotheses).

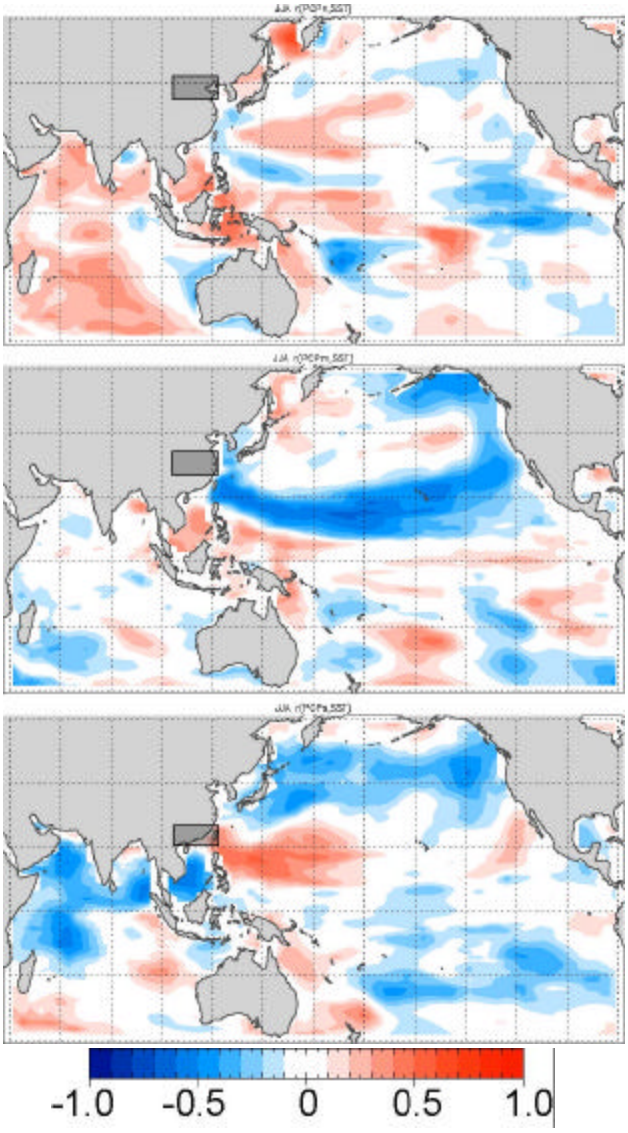

Figure 6.13. Map of correlations between CSM1.4-simulated SSTs and standardized regionally averaged precipitation in NEC (top), YRV (center) and SEC (1961 – 1990). For reference, precipitation regions are marked by translucent grey boxes. Individual correlation values greater than 0.4 (or less than -0.4) are significant with roughly 95% confidence (not accounting for multiplicity, the testing of multiple hypotheses).

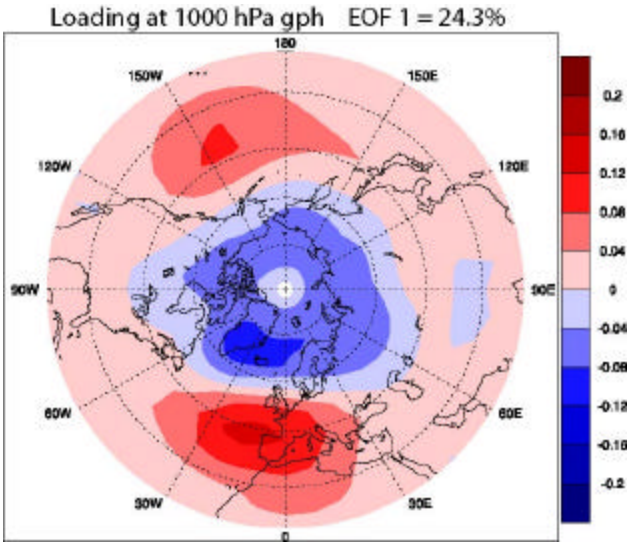

Figure 6.14. Loading patterns for the AO, based on the first principal component of the covariance matrix of monthly 1000 hPa geopotential height anomalies north of 20°N. Results from the CSM1.4 Millennium simulation, including all months between 850 – 1999 AD.

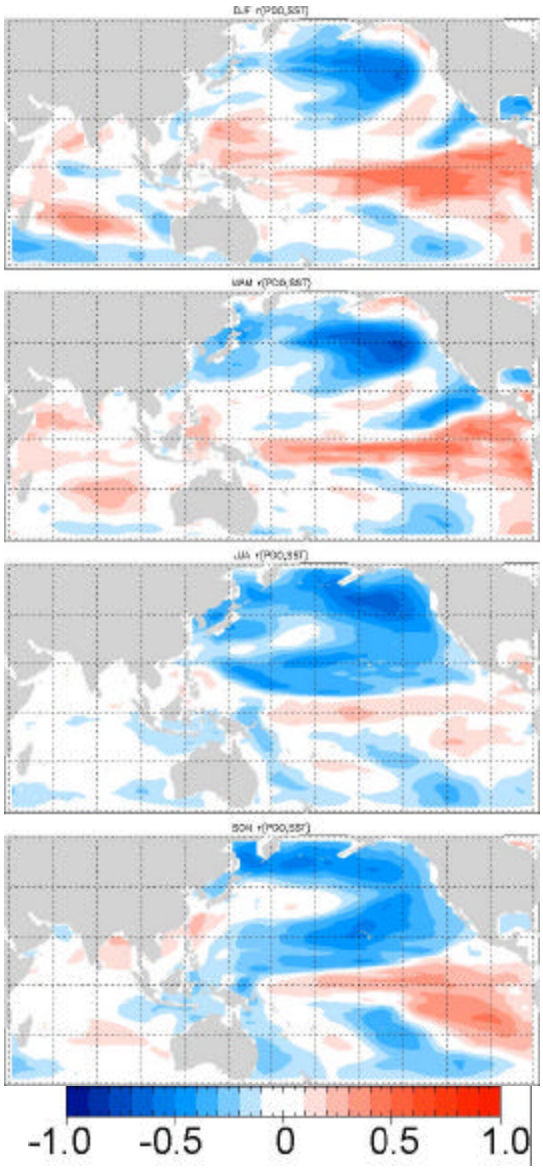

Figure 6.15. The seasonally averaged PDO indices correlated with respect to CSM1.4 Millennium simulation SST anomalies (850 – 1999 AD). Rows represent the seasons, from top to bottom respectively: DJF, MAM, JJA, and SON.

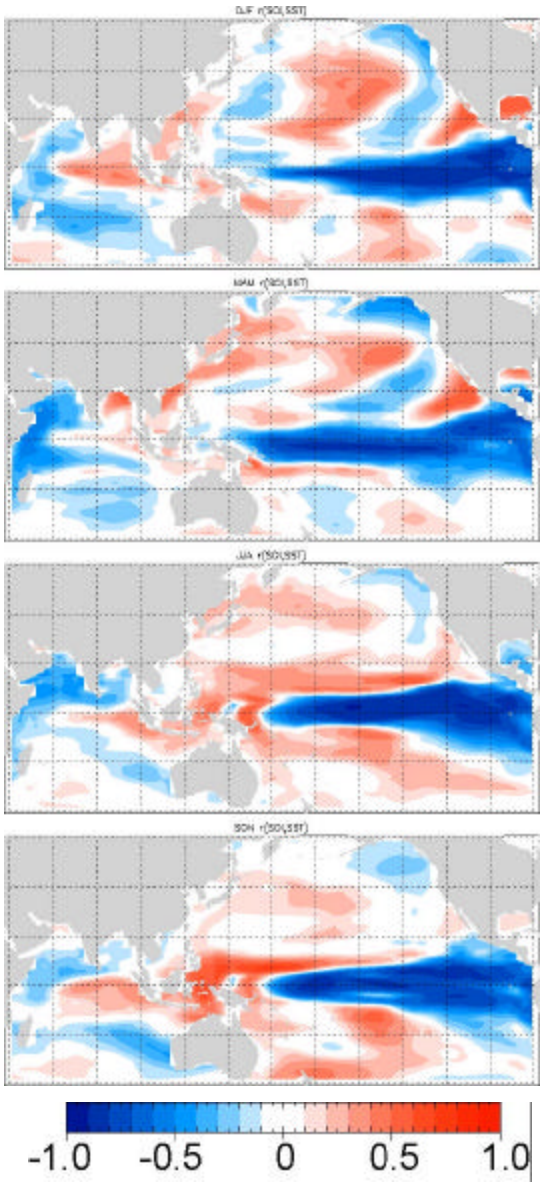

Figure 6.16. Similar to Figure 6.15, except that CSM1.4-simulated SSTs are correlated with respect to SOI values (850 – 1999 AD).

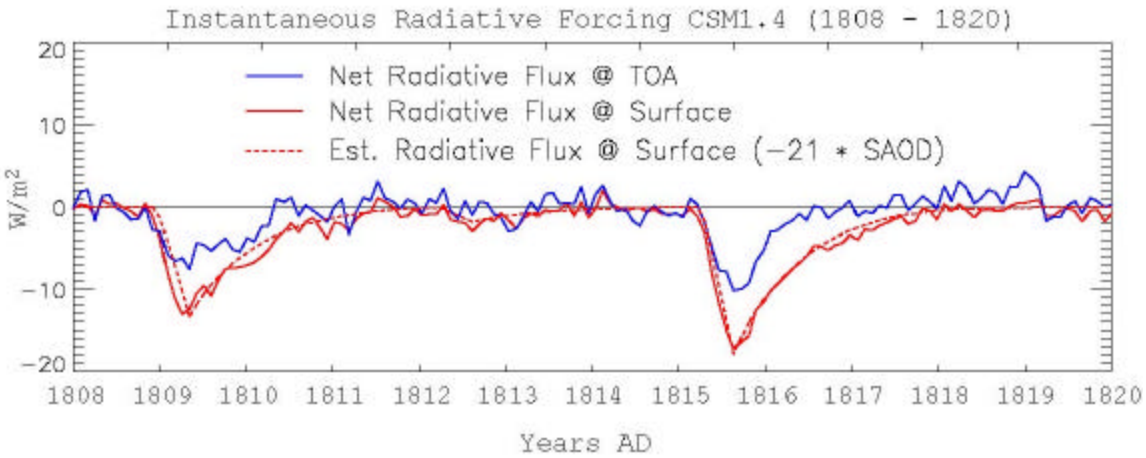

Figure 6.17. Calculated average instantaneous net radiative flux at the top of the atmosphere (TOA) and at the surface for all longitudes and all latitudes between 40°N and 40°S (1808 – 1820). Results are based on CSM1.4 output from one full forcing and one control simulation. For comparison, net radiative flux at the surface (red dashed line) was also estimated directly from the SAOD data using the simple empirical relationship (Equation 2.2) published by Hansen et al. (2002).

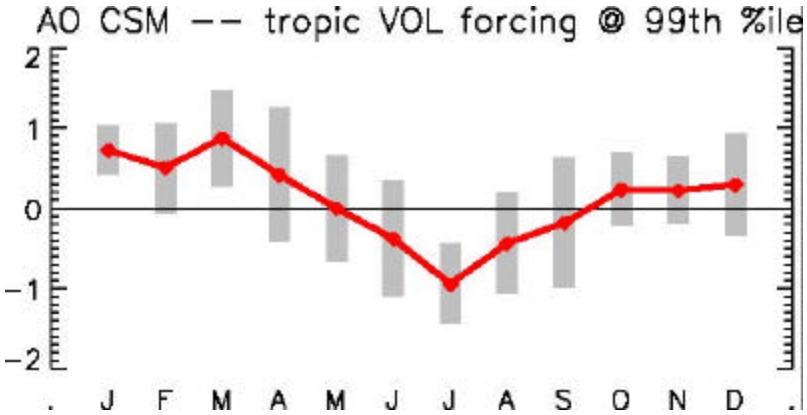

Figure 6.18. Composite of monthly AO index values simulated by the CSM during high volcanic forcing months (850 - 1999; n = 13/month). Gray vertical bars represent the 95% confidence interval of the true mean for each month. Compared to Figure 5.3, the model realistically captures the observed wintertime AO response to volcanic eruptions.

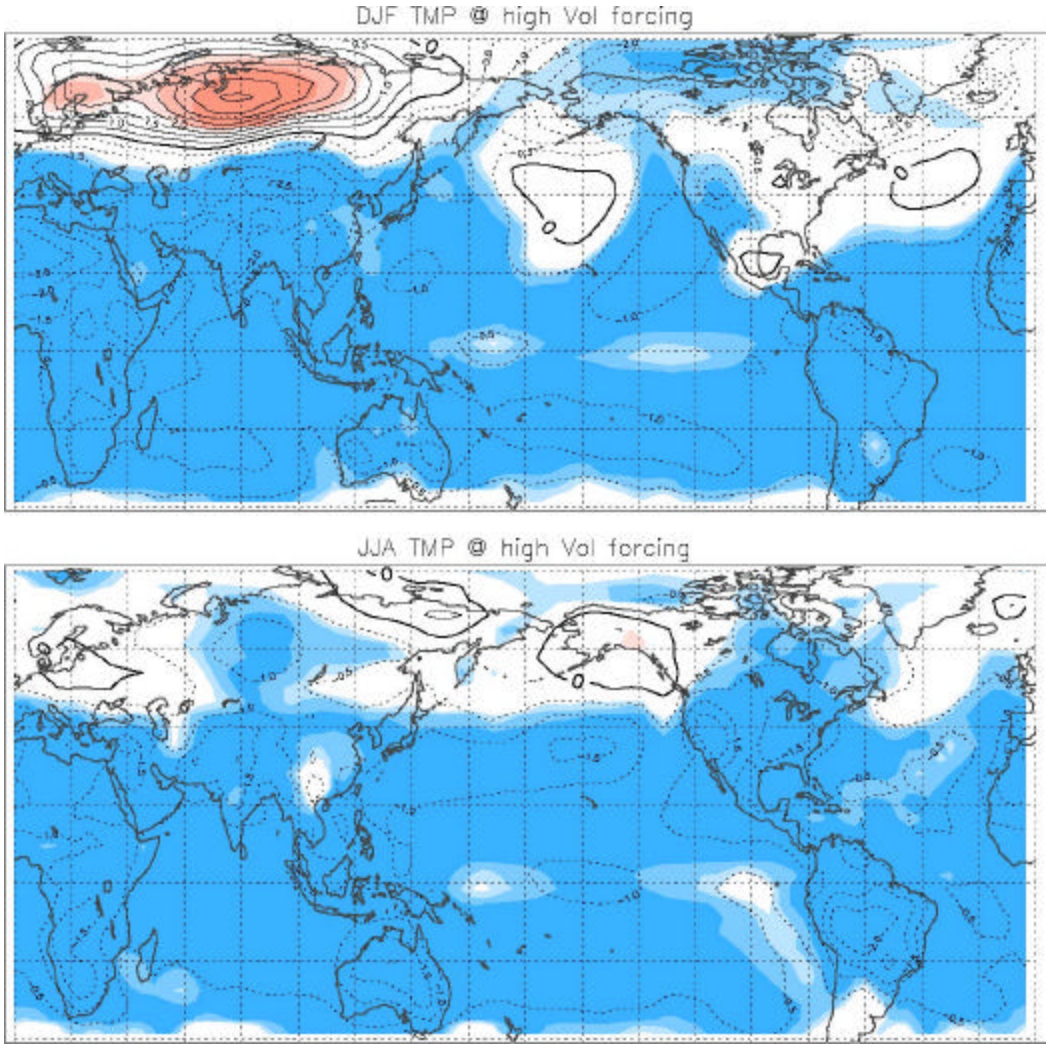

Figure 6.19. Contour plots show composites of simulated winter (top) and summer (bottom) surface air temperature anomalies during the 13 top volcanic forcing years from 850 to 1999. Positive, negative and zero anomalies correspond with solid, dotted and solid bold contours, respectively (intervals = 0.5°C). Based on individual student's t-tests, statistically significant positive and negative anomalies are highlighted with red and blue shading, respectively. The 90, 95 and 99 % confidence levels are associated with the lightest, medium and darkest color shading, respectively.

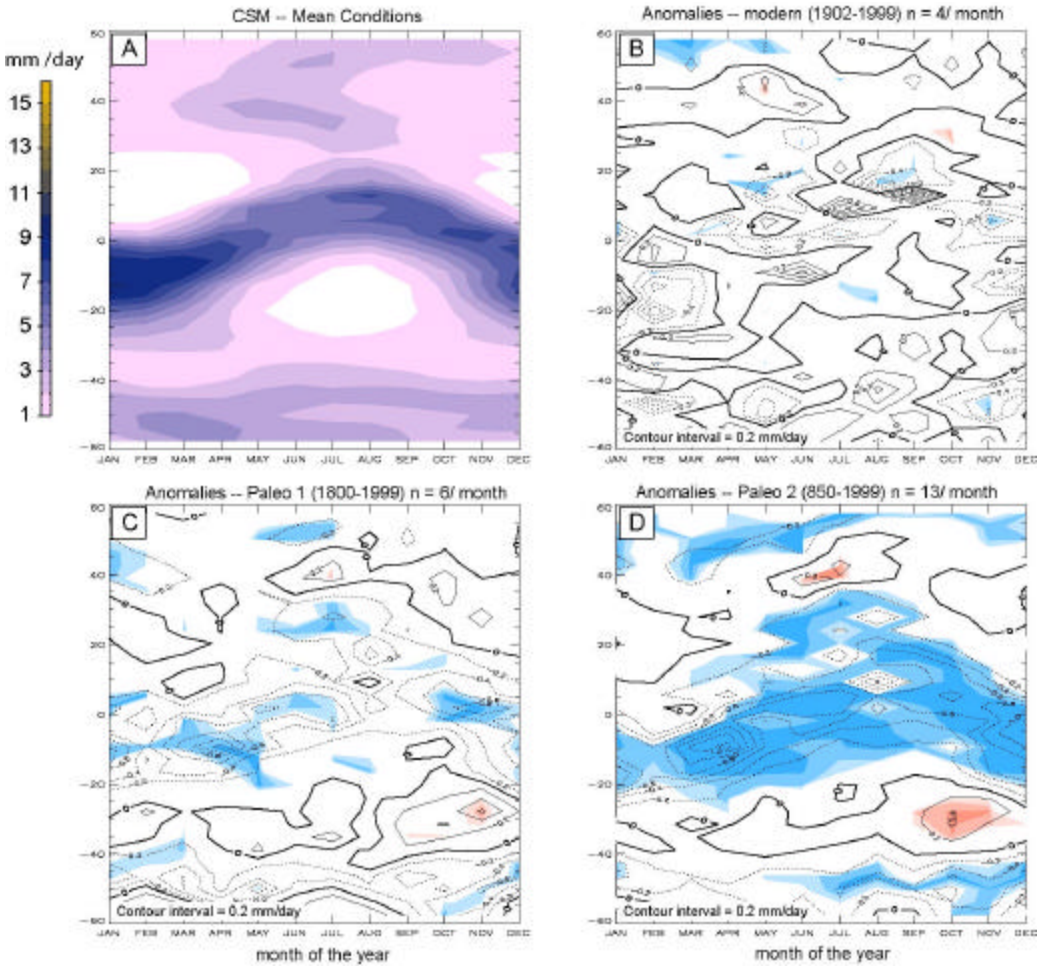

Figure 6.20. (a) Global, monthly, zonally averaged land precipitation rate (mm/day) from 60°N to 60°S (CSM1.4). (b-d) Composites of monthly precipitation-rate anomalies during high forcing conditions for three select eras: (b) modern, (c) Paleo1, and (d) Paleo2. The time periods considered in each analysis and the number of years in each composite is written in the respective panel headings. Compare panels (a) and (b) with Figure 5.4. Statistically significant anomalies are highlighted by red and blue shading, as in Figure 6.19.

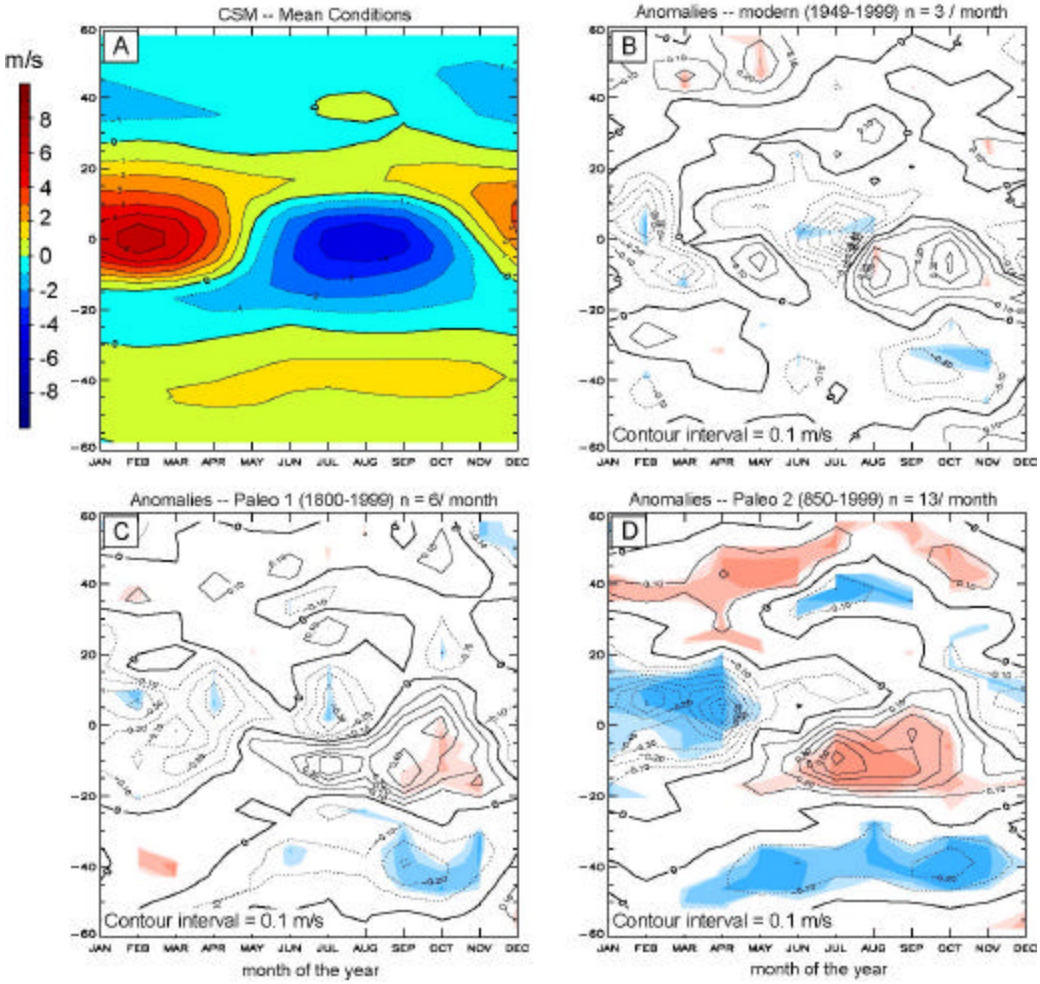

Figure 6.21. Same as Figure 6.20, except for zonal mean vertical wind shear, in m/s units. Vertical wind shear is defined as the difference between meridional wind velocity at 200 hPa and the same at 850 hPa. Compare Panels (a) and (b) with Figure 5.4.

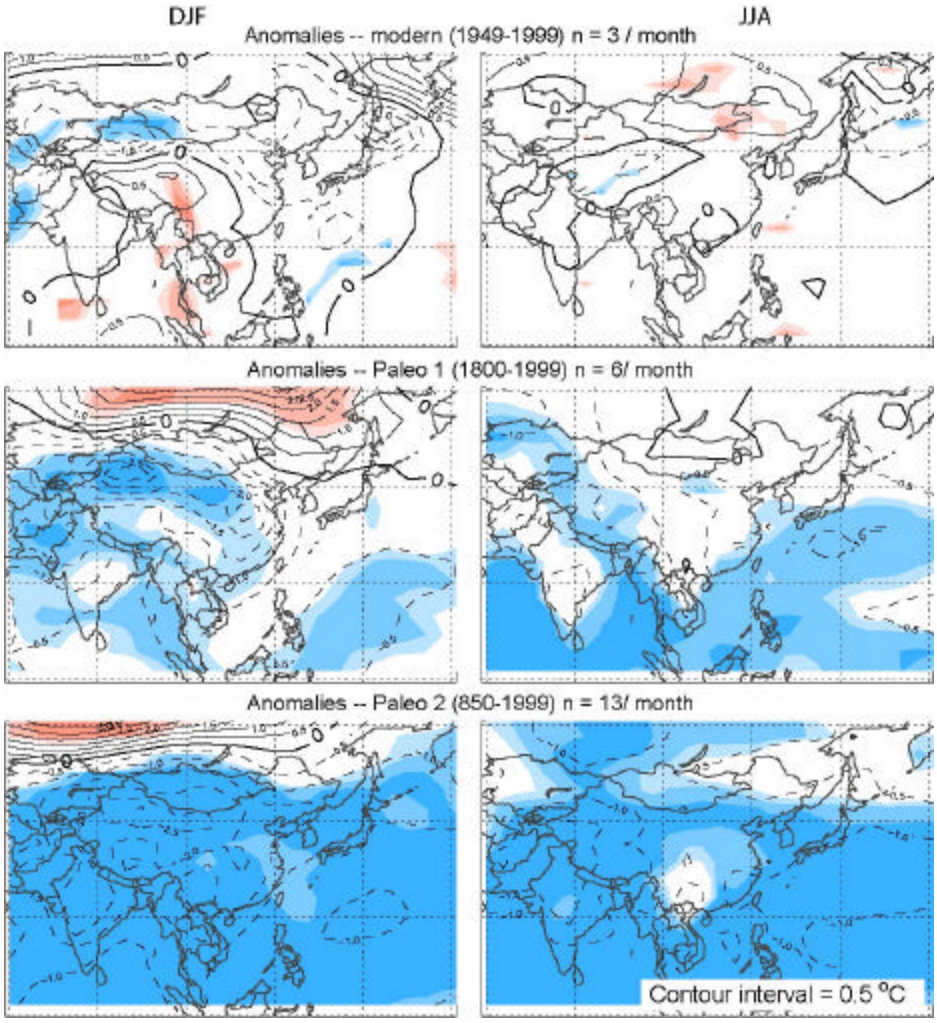

Figure 6.22. Contour plots show composites of simulated winter (left) and summer (right) surface air temperature anomalies during high volcanic forcing years. As in Figures 6.20 and 6.21, composites include high forcing conditions during three separate eras: modern, Paleo1, and Paleo2. The time periods considered in each analysis and the number of years in each composite is written in the respective row headings. Positive, negative and zero anomalies correspond with solid, dashed and solid bold contours, respectively (intervals = 0.5°C). Statistically significant anomalies are highlighted by red and blue shading, as in Figure 6.19.

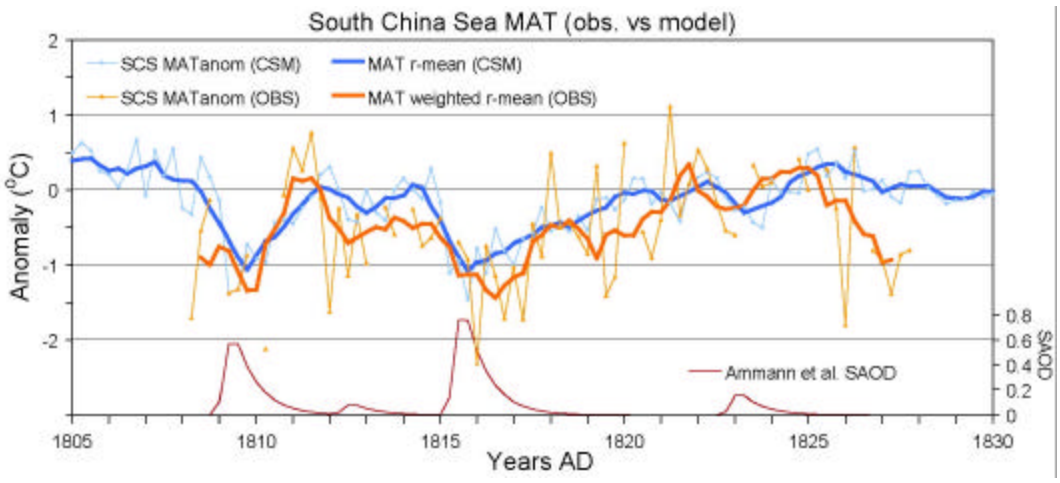

Figure 6.23. Comparison between seasonally averaged South China Sea MAT anomalies from observations (orange) and the CSM1.4 (blue). Individual va lues and 5-season running means are shown for both, as labeled. As in Figure 5.15, MAT anomalies are expressed in degrees Celsius relative to long-term mean anomalies during the period from 1820 and 1825 AD. See Chapters 3 and 5 for more details regarding the observed MAT record. The Ammann et al. (2006) SAOD data are also shown, seasonally averaged, to visually illustrate the estimated magnitude and timing of forcing from tropical (24°N – 24°S) volcanic eruptions during this era

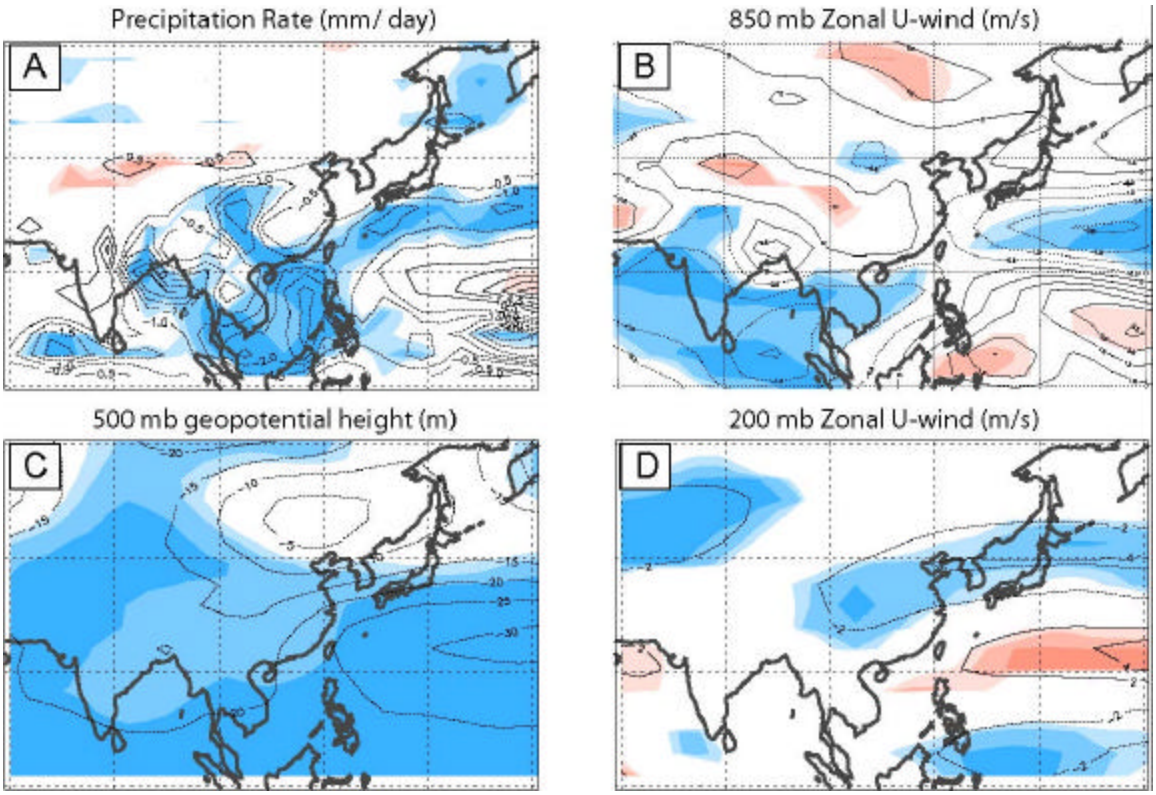

Figure 6.24. Contour plots show composites of simulated summer (a) precipitation rate, (b) 850 hPa zonal wind, (c) 500 hPa geopotential height, and (d) 200 hPa zonal wind anomalies during the 13 top volcanic forcing years between 850 and 1999. Contour intervals are (a) 0.5 mm/day, (b) 0.5 m/s, (c) 5 m, and (d) 2 m/s. Statistically significant anomalies are highlighted by red and blue shading, as in Figure 6.19.

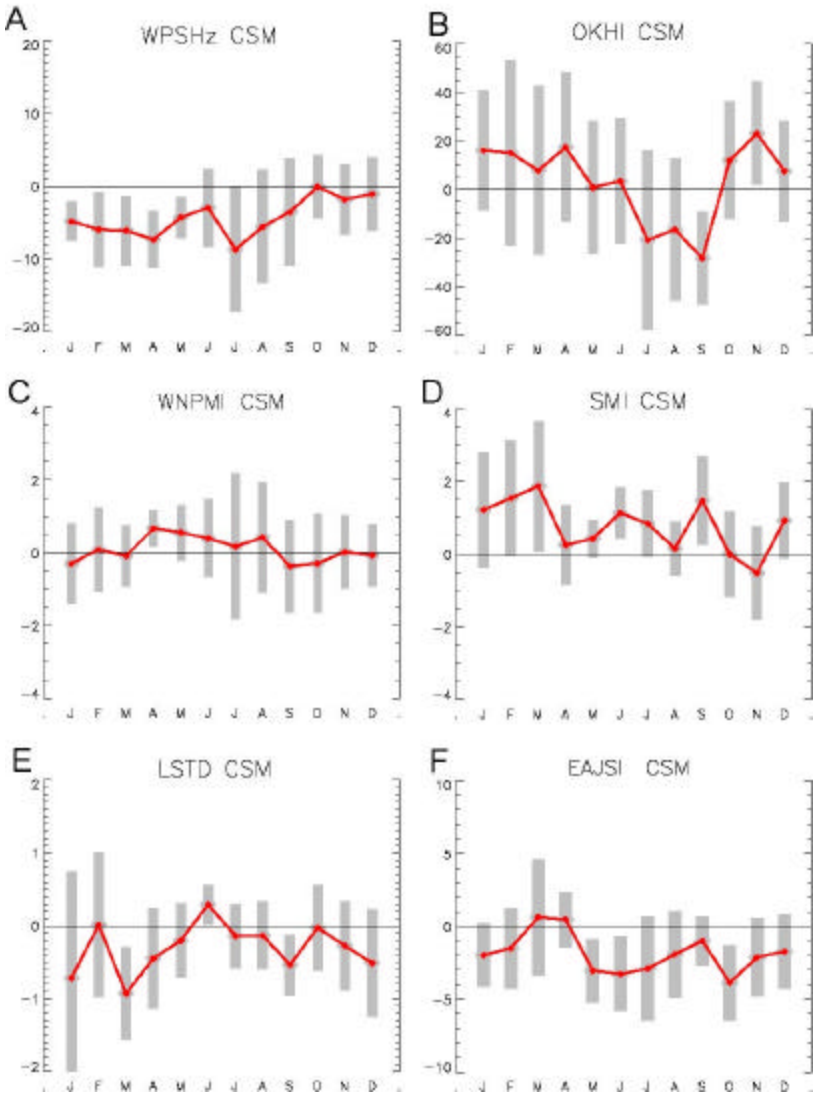

Figure 6.25. CSM1.4-simulated composite monthly regional monsoon index anomalies throughout the annual cycle (January - December) during high volcanic forcing conditions. Composites are computed during months concurrent with the top one percentile of SAOD during the period from 850 - 1999 (n = 13/ month). Vertical grey error bars represent the 95 percent confidence intervals for the true mean during each month.

CHAPTER 7

REGIONAL CLIMATE MODEL VALIDATION

This Chapter focuses wholly on the validation of the SUNYA regional climate model (ReCM) based on a 4-year simulation of modern climate with lateral boundary conditions prescribed by CSM1.4. Prior to this study, climate simulations with the SUNYA ReCM had been limited to dynamical downscaling of reanalysis data. For the present study, however, output from the CSM Millennium simulation was used as the driving field to assess the skill of the ReCM with a coupled AOGCM as lateral boundary conditions. This model validation strategy serves two primary purposes. First and foremost, it tests ReCM skill when CSM1.4 output is used as the model driver. This provides a model validation and control for subsequent analyses of output from a (pending) paleoclimate simulation of Tambora-era climate. Second, the modern validation and paleoclimate simulations could, together, provide a basis for considering this regional model's suitability for future climate change impact assessment studies, which necessarily require input from coupled AOGCMs with prognostic SSTs and strong radiative forcing.

Currently, collaborators at SUNYA are running a paleoclimate simulation of Tambora-era climate in East Asia with the ReCM – with CSM "Millennium simulation" boundary conditions – during the period from 1808 to 1819 AD. Once that model run is complete, analyses will build on the results from the assessment presented here.

7.1. Model validation

As explained in Chapter 2 there are a growing number of complementary efforts to downscale AOGCM output, using both dynamic and statistical techniques, to increase the spatial resolution of climate model projections (Leung et al., 2003). Yet, both empirical and dynamical downscaling tools necessarily require that AOGCM simulations are accurate on synoptic to global scales. Previous chapters have addressed the apparent strengths and weaknesses of the CSM1.4 model under modern and paleoclimate conditions. This chapter focuses on the skill of the regional model through comparisons with observational data and, in particular, with respect to the CSM1.4 *output* that was used as *input* to drive the ReCM for this simulation. Note that the period chosen for this modern climate simulation (January, 1986 to November, 1989) was a volcanically inactive time period; however realistic forcings (e.g., anthropogenic tropospheric aerosols, greenhouse gases, solar irradiance) were included in the simulation.

7.1.1. Upper-air general circulation

Figure 7.1 is a 6-panel plot comparing CSM and ReCM simulations of summer (JJA) mean climate with respect to three key diagnostic variables: 500 hPa GPHs, 200 hPa zonal winds and 850 hPa wind vectors. The general patterns of upper-air circulation that were simulated by the CSM are basically replicated in the ReCM regional climate simulation. This includes regional-scale patterns and structural features, such as 1) the WPSH at 500 hPa, 2) the East Asian westerly Jet at 200 hPa, 3) the location of the south-to-north transition from westerlies to easterlies at 200 hPa and 4) southerlies over SEC at 850 hPa that deliver the bulk of tropical moisture into eastern China during the summer

monsoon season. The location and strength of these features does not seem to have been noticeably altered by the ReCM; thus, confirming results from previous simulations, in which reanalysis data were used as the driving field (Wang W-C et al., 2000; Gong and Wang, 2000). This suggests that the one-way nesting scheme used within the ReCM's so-called "buffer zone" provides a reliably smooth transition from the lateral boundaries to the regional climate simulation (Wang et al., 2004), regardless of the realism of the driving field.

7.1.2. Surface climate

The remaining sections in this chapter consider 1) spatial biases in surface temperature and precipitation, 2) trends and variations in these variables over the course of the 4-year modern simulation and 3) the interrelationships between these variables in summer. First, spatial biases in precipitation are of paramount interest to this study because the global model was shown to have rather severe biases over eastern China. Thus, it is useful to know whether or not dynamically downscaling CSM output with the ReCM results in any improvement in terms of the spatial distribution of simulated summer rainfall over this region. Second, trends in simulated surface temperature must be tested because previous studies (Leung et al., 1999; Wang and Gong, 2000) have noted that the SUNYA ReCM displays significant cold biases at the surface that grew to roughly 5°C over the course of a 3-month simulation. Wei Gong has since made adjustments to the land model to make it more suitable for the longer simulations and the efficacy of those changes must be tested. Third, the interrelationship between surface air temperature and rainfall became a topic of interest during prior analyses after the CSM1.4

evidently failed to realistically simulate the observed strong anti-correlation that exists between these variables throughout eastern China during the summer season.

7.1.2.1. Regional rainfall

Focusing on precipitation biases, this section considers the spatiotemporal distribution of regional rainfall. Figure 7.2 plots average summer (JJA) mean rainfall over eastern China, comparing CMAP observations with CSM and ReCM simulations. A basic visual inspection of these plots clearly shows that the overall spatial distribution of summer rainfall simulated by the RCM does not differ much from CSM1.4 output. This runs somewhat contrary to the hypothesized result, based on the fact that higher resolution versions of the CSM are more realistic in that they do not simulate the same severe positive precipitation bias in the lee of the Tibetan Plateau (Ping Lu, personal communication). While this result is somewhat disappointing, it is also not very surprising given the choice of model domain. Figure 7.2b shows that the primary precipitation bias in the global model sits squarely within the ReCM buffer zone, thus virtually guaranteeing that the ReCM would replicate it. Perhaps a larger ReCM domain that is shifted west and includes the Tibetan Plateau inside the simulation area would produce more realistic precipitation patterns across eastern China. However, such a model configuration would create a prohibitively large computational demand given the time-scales of interest in this study. Hence, it might be worth testing this in a more limited 30-day simulation.

For comparison with earlier analyses, Hovmoller diagrams of the time-latitude evolution of regional precipitation is generated from ReCM output. Figure 7.3(a-c) plots

the mean annual cycle of monthly precipitation in eastern China, generated by averaging data from 105 – 122°E at each individual latitude between 10 and 50°N (for the ReCM, only data inside the simulation region, from 20 – 40°N, are shown). Also, Figure 7.3(d-f) plots the same monthly values in percentage units, relative to the annual total at each latitude, thus highlighting the seasonal distribution of precipitation throughout the average year. Note that the CMAP and CSM climatologies in Figure 7.3 are based on long-term means from at least 20 years of data, while ReCM climatologies are relatively noisier, having been derived from only three years of data (1986 – 1988). Figure 7.4 (left columns) provides another perspective, also comparing precipitation climatologies from the models with observations. There, simulated (CSM, ReCM) and observed (GHCN) monthly precipitation rates in the NEC, YRV and SEC regions were regionally averaged and plotted as raw values beside monthly climatologies of model biases, relative to GHCN data. Note that in Figure 7.4, the CSM data are from the same model output that was used to drive this ReCM simulation (both were also averaged over roughly the same three regions; see Figure 6.5, right panels, for regional delineations), so their climatologies should be directly comparable.

Visual inspection of Figures 7.3 and 7.4 suggest that ReCM-simulated precipitation has much more in common with CSM1.4 output than with observations. Like CSM, the ReCM under-predicts rainfall in the south: both models unrealistically simulate the majority of annual rainfall during late summer months. In reality, rainfall in the south is relatively more evenly distributed throughout the year (Figure 7.3d and Figure 7.4, bottom left panel). In NEC, both models also share very similar biases throughout the year, with a summer monsoon onset up to 3-months too early and

withdrawal also occurring slightly prematurely. However, in the YRV, the ReCM is relatively dry, compared to CSM, and has smaller biases relative to observations in this region.

As a final test of ReCM skill with respect to precipitation, it is useful to know if 1) inter-monthly and inter-annual variations generally occur in parallel with variations simulated by the CSM and 2) if there are any long-term trends in the ReCM simulation. Thus, Figure 7.5 compares observed (GHCN) and modeled (CSM and ReCM) monthly time series of regionally averaged precipitation from NEC, YRV and SEC, during the period from January, 1985 – December, 1989. Panels on the left illustrate raw regional averages with the seasonal cycles intact, while panels on the right plot anomalies, with long-term monthly means subtracted from each month. From Figure 7.5 it is apparent that inter-monthly and inter-annual variations in both models generally track in parallel.

7.1.2.2. Regional temperature

As noted earlier, significant cold surface temperature biases had been observed in the ReCM due to radiative imbalances caused by problems with the "force restore" land surface physics scheme (Leung et al., 1999). These biases grew rapidly over the course of a 90-day summer climate simulation and called into question the suitability of this model – under its then-current configuration – for long-term climate simulations. However, Wei Gong has subsequently modified the land surface physics of the ReCM and results from these simulations indicate that his adjustments were generally effective.

Firstly, the right two columns of Figure 7.4 plot monthly climatologies of regionally averaged temperature, illustrating the typical seasonal cycle along with model

biases relative to GHCN data from the same three eastern China regions. Figure 7.6, similar to Figure 7.5, plots time series of regionally averaged monthly temperatures – along with monthly anomalies. Figures 7.4 and 7.6 illustrate that 1) ReCM biases are similar to those in the CSM and 2) while there is significant interannual variability in ReCM temperature, these variations generally track in parallel with changes in the CSM driving field and, most importantly, no long-term trends are apparent (Figure 7.6, right panels). However, in SEC year-round regional temperature biases range from -2 to -8 compared to CSM and GHCN monthly means (Figure 7.4, bottom right panel).

7.1.2.3. Interrelationship between summer temperature and rainfall

A final assessment of ReCM skill with respect to surface climate simply tests if regional summer precipitation is realistically anti-correlated with surface air temperature. Figure 7.7 spatially plots r-values from correlation analyses between seasonally (JJA) averaged precipitation and surface air temperature at each grid point. Here, two observational datasets are used: GHCN station data (1961 – 1990) and CRU gridded data (1902 – 2002). GHCN station data were first interpolated to a 0.5 x 0.5 degree grid prior to this correlation analysis. CSM correlations were computed based on Millennium simulation output from 1950 -1999. However, due to the limited availability of ReCM data, correlations between temperature and precipitation anomalies were tested on a monthly – as opposed to seasonal – basis during the wet-season only. "Wet-season" was defined as the months of April to August, based on visual inspection of Figures 7.3c and 7.4. Dry season months were excluded from this analysis. Also, to test the sensitivity of these results to relatively low-frequency trends in the temperature data (Figure 7.6, right

panels) 3-year time series of monthly temperature and precipitation anomalies at each grid-point were first subjected to linear trend removal and a high-pass filter. After filtering, the dry-season months were discarded and wet-season monthly data were complied into a continuous time-series (as above); then the correlation analysis was repeated.

From the top two panels of Figure 7.7, the observed relationship between summer rainfall and temperature is clear. Throughout eastern China, anomalously wet summers are also cold summers, since rain clouds block short-wave radiation and thus dampen solar heating. However, as deduced from earlier analyses, the CSM (bottom left panel) does not consistently, realistically capture this relationship and actually simulates positive correlations between these surface climate variables over the middle to lower reaches of the YRV. In areas south, north and west of the YRV, the CSM does relatively better in this regard. The ReCM, on the other hand, accurately simulates the observed anti-correlation between summer rainfall and temperature, particularly over the YRV and NEC regions. However, this relationship is non-existent in SEC – or even reversed when the data are subjected to trend removal and high-pass filtering prior to analysis (Figure 7.7, bottom right panel).

7.2. Synopsis

While some biases in the CSM1.4 are evident, the global model demonstrates reasonable skill in its ability to capture large-scale atmospheric circulation patterns as well the seasonal cycle of all regional monsoon indices. This suggests that most boundary conditions and synoptic-scale dynamics that are fundamental to the EAM

system are somewhat realistic in the CSM. By not substantially altering general circulation from the CSM driving field, the ReCM shows signs of being a reliable dynamical downscaling tool for regional climate simulations. However, analyses conducted in this assessment indicate that the downscaled simulation of upper-air circulation is not necessarily any more realistic than the input provided by a global-scale coupled model, at least in terms of the mean-state climate. This generally confirms results from earlier studies, finding that if the lateral boundary conditions prescribed by global models are not realistically simulated, climate projections downscaled from these models will contain the same fundamental flaws.

Hence, it is not surprising that some of the primary surface mean-state climate biases in the CSM are simulated by the ReCM, as well. One apparent exception is over the YRV, where spring and summer precipitation biases are smaller, relative to observations. Also, the ReCM has significant (-2 to -8 °C) year-round cold biases over SEC, despite the fact that SATs in the CSM driving field are relatively skillful in this region. Also, there appear to be significant differences between the CSM and ReCM in terms of the simulated interrelationships between rainfall and surface air temperature. The ReCM realistically simulates the inverse relationship between these variables in NEC and the YRV – however, not over SEC – and is thus more similar to observations in this regard. This discrepancy between the global and regional models likely results from differences in how they parameterize radiation, clouds and rainfall. This result provides one indication that the ReCM-simulated hydroclimatic response to radiative forcing from increased SAOD could be significantly different from the CSM1.4 response and is thus worthy of further investigation.

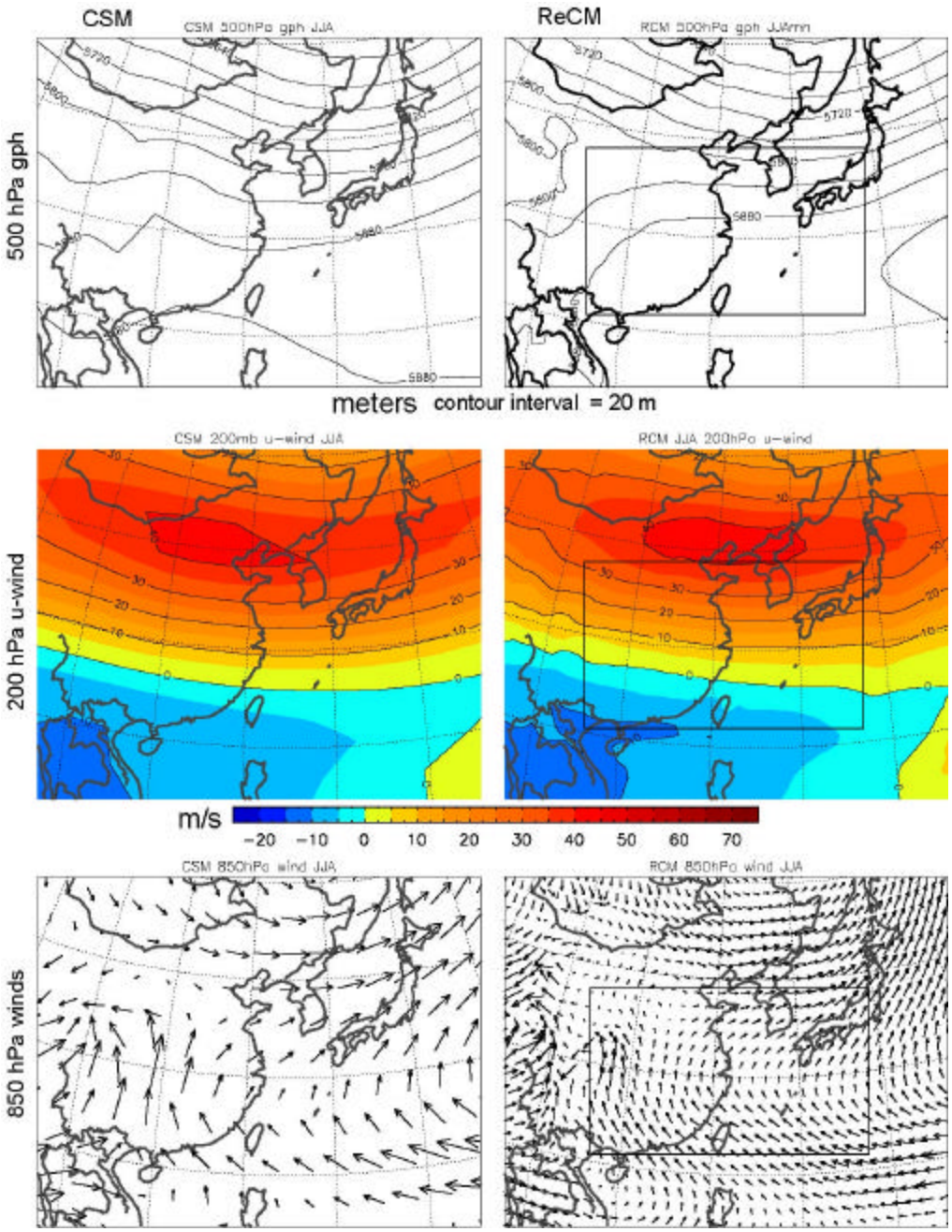

Figure 7.1. Summer (JJA) mean 500 hPa geopotential heights (top panels), 200 hPa zonal winds (center panels) and 850 hPa wind vectors (bottom panel). Averages from the CSM1.4 (left panels) and the ReCM (right panels) are based on their respective simulations for the period from 1986 – 1989. The rectangles in the panels on the right delineate the location of the inner edge of the ReCM buffer zone (values outside of that box should be discounted). Note that the CSM1.4 and ReCM wind vectors do not share a common scale. Also, ReCM wind vectors were first interpolated to a 1.5° x 1.5° grid for better visual presentation.

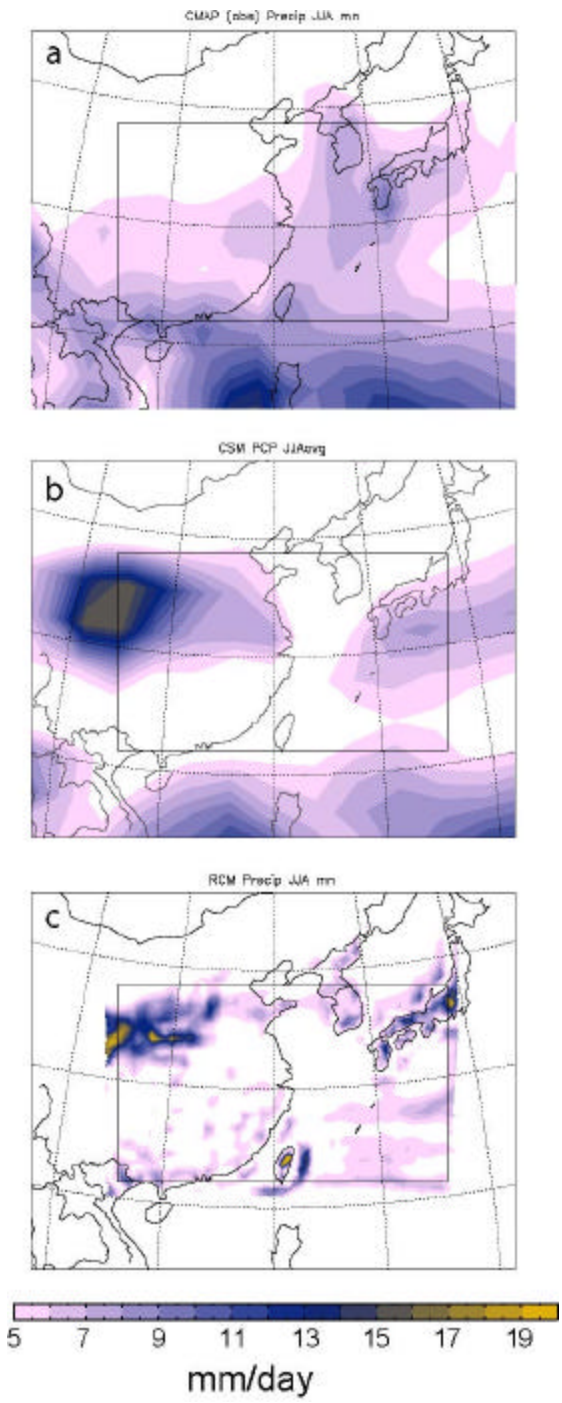

Figure 7.2. Summer (JJA) mean precipitation rates based on (a) CMAP observations (1979 – 2001), (b) CSM output (1950 – 1999) and (c) ReCM output (1986 – 1989). Note that only values greater than 5 mm/day are shown. For reference, rectangles in each panel delineate the location of the inner edge of the ReCM buffer zone.

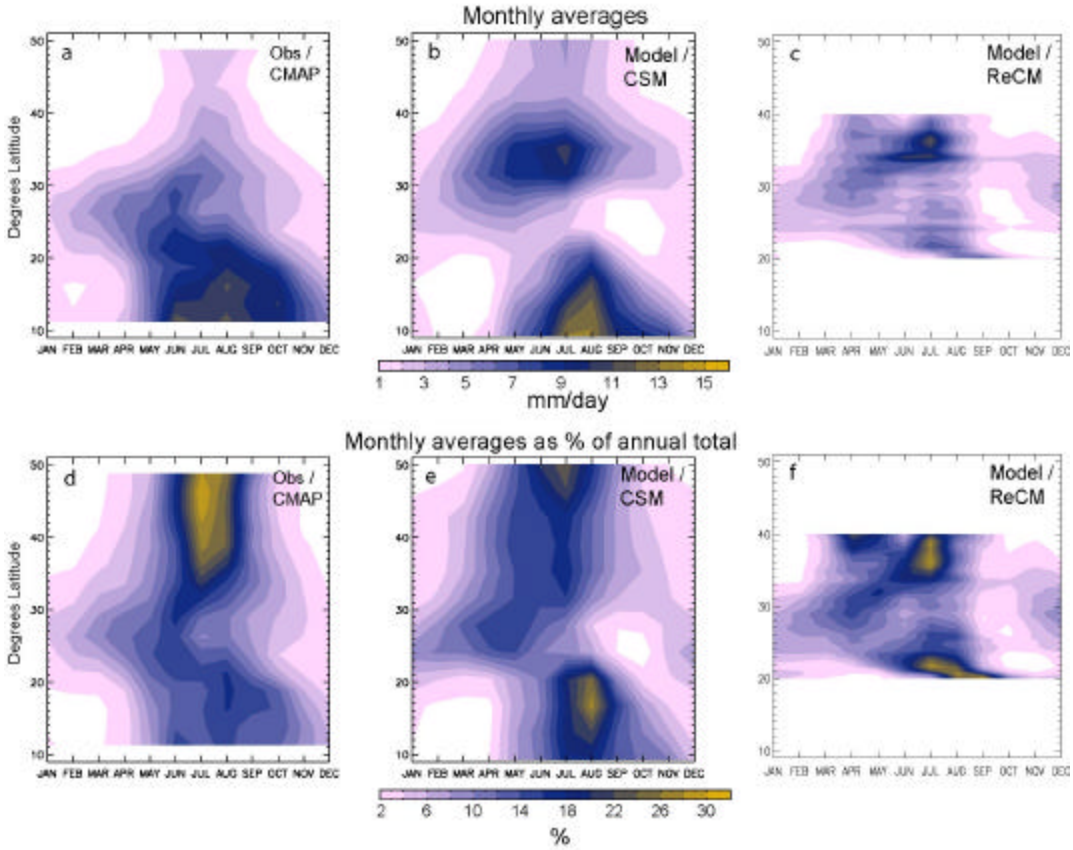

Figure 7.3. Hovmoller diagrams of the annual cycle of monthly precipitation, zonally averaged at each latitude across eastern China (105° – 122°E). Panels represent (a,d) CMAP observations (1979 – 2001), (b,e) CSM output (1950 – 1999) and (c,f) ReCM output (1986 – 1989). Latitude-month precipitation values are presented as averages (top row; mm/day) and as percentages of annual means (bottom row), to highlight the seasonality of precipitation at each latitude.

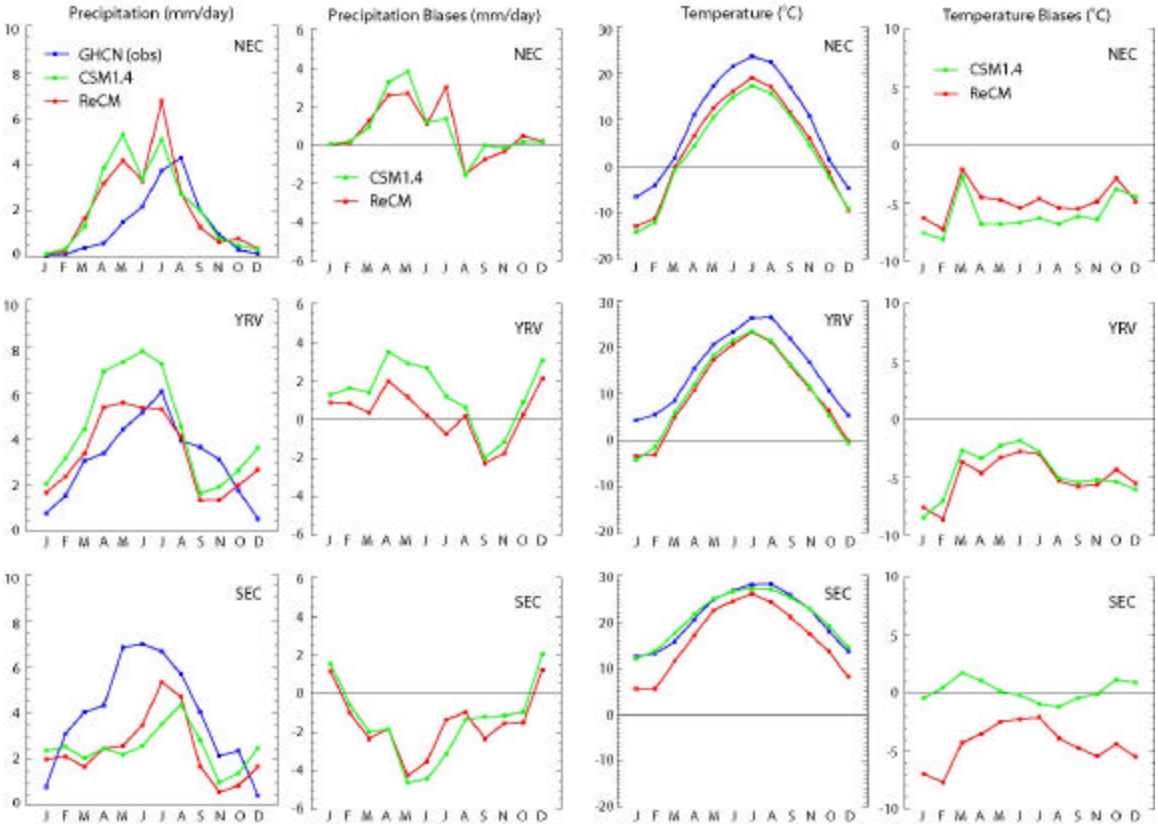

Figure 7.4. Monthly climatologies of observed and simulated precipitation (mm/day) and temperature (°C) regionally averaged for NEC (top row), YRV (center row) and SEC (bottom row) during the 3-year period from 1986 – 1988 AD. Climatologies from GHCN (blue), CSM1.4 (green) and ReCM (red) are expressed as monthly means and as biases (as labeled) relative to GHCN observations.

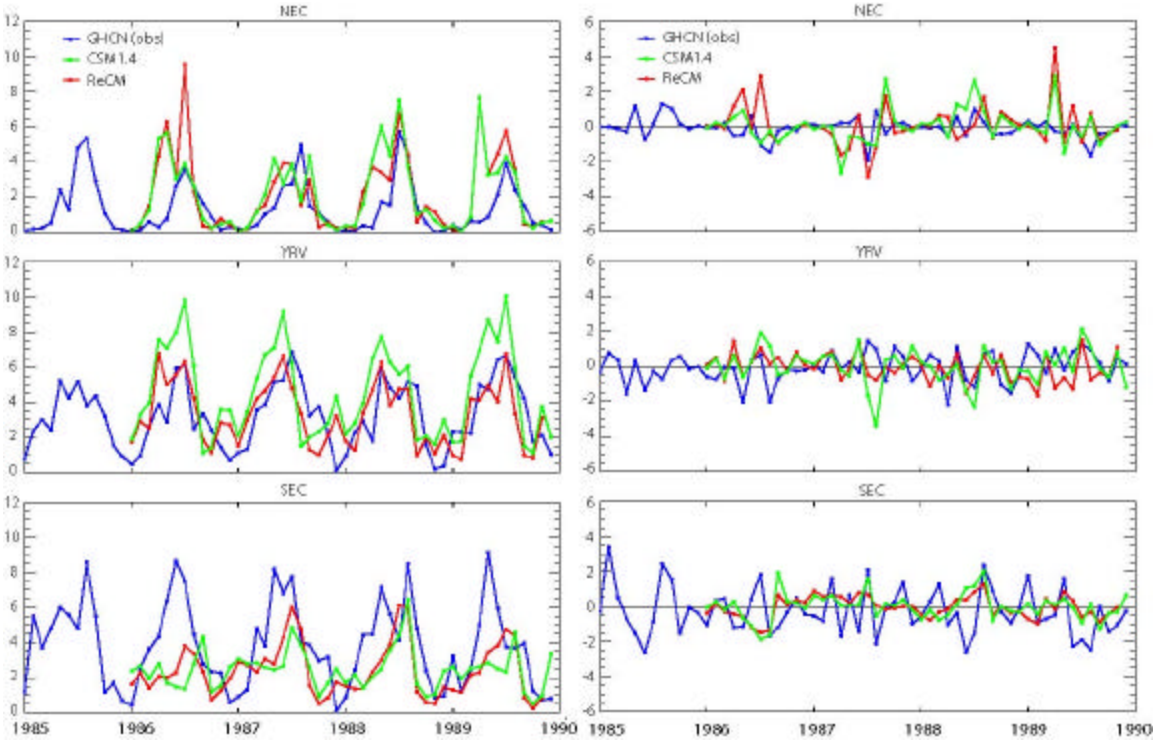

Figure 7.5. Regionally averaged precipitation time series from the NEC, YRV and SEC during the period from 1985 – 1990 AD. Data are expressed as monthly mean values (left) and as monthly mean anomalies, with respective monthly means subtracted at each time step (right), in mm/day units. See Figure 6.5 for spatial delineations of the NEC, YRV and SEC regions.

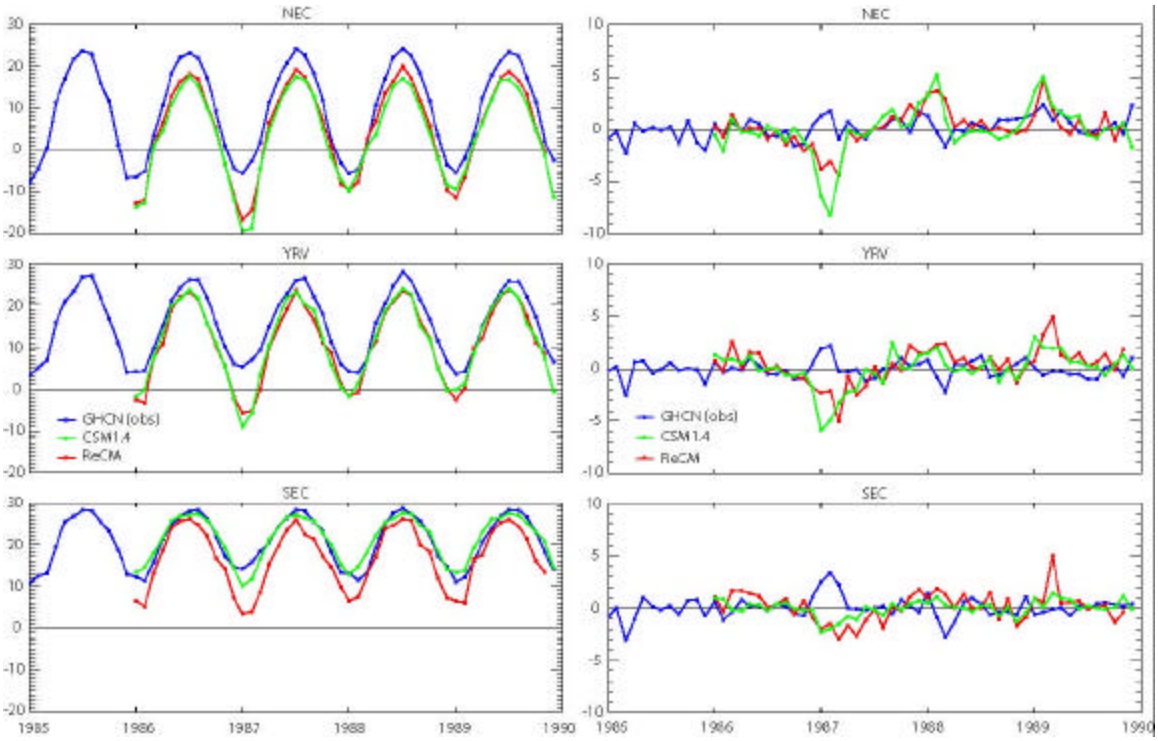

Figure 7.6. Same as Figure 7.5, except for temperature, in degree C units.

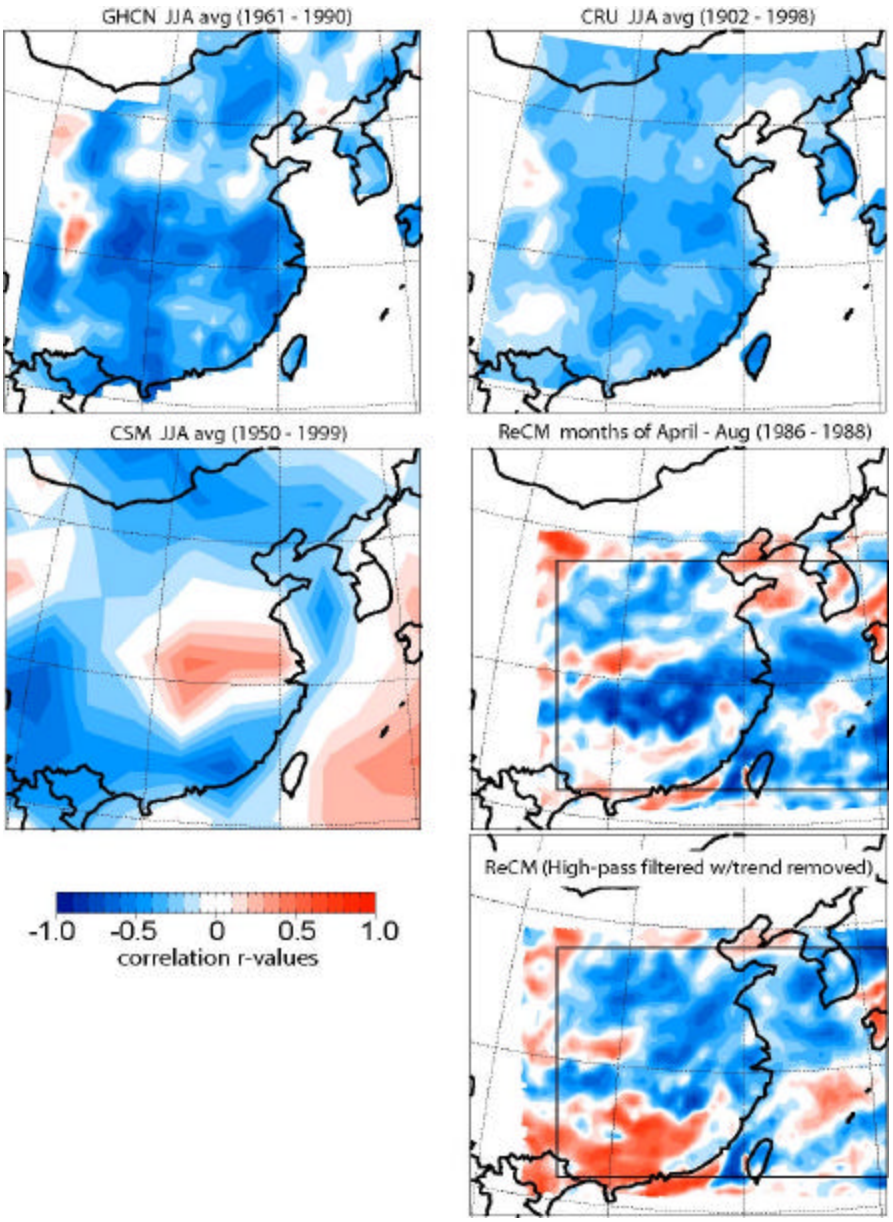

Figure 7.7. Spatial correlation patterns between summer temperature and precipitation at each grid point. For GHCN, CRU and CSM, r-values were computed based on annual resolution summer (JJA) mean time series during the periods listed at the top of each panel. GHCN station data were first interpolated to a 0.5 x 0.5 degree grid prior to analysis. Due to the limited available ReCM data, these analyses were conducted on wet-season (April – August) monthly (as opposed to seasonal) anomalies from 1986 – 1988. In the bottom ReCM panel, monthly temperature and precipitation anomalies from each grid-point were subjected to linear trend removal and a high-pass filter prior to extracting wet-season data for analysis. For reference, the rectangles in the bottom right panels delineate the location of the inner edge of the ReCM buffer zone.

CHAPTER 8

SUMMARY AND CONCLUSIONS

This summary and conclusions section focuses mostly on results from analyses of the hydroclimate response to volcanic forcing. Here, relatively less attention is focused on East Asian climate independent of forcing, or on model validation efforts, which were primarily aimed at laying a framework for subsequent analyses. Thus, this chapter begins with a review of the original *a priori* expectations, based on previous findings and hypotheses put forth in the literature. Next, the primary results from analyses of the observed climatic response – both from instrumental and paleoclimate studies – are reviewed and discussed. Then, the modeled response from eruptions in the Millennium simulation are considered and compared with observations, while also going into greater detail regarding possible mechanisms for the observed response. Next, an attempt is made to comprehensively review the primary strengths and limitations of the data and methods used in this study, in the context of the major findings. Also, some thoughts are offered on the societal implications of this study's results for the East Asia region. Finally, a synopsis of the key qualitative and quantitative conclusions is provided.

8.1. The hypothesized response

Before proceeding with a discussion of the observed response, this section revisits a few of the hypothesized mechanisms for a possible regional-scale response, with the benefit of hindsight and new knowledge of the actual observed and model-simulated results. From the literature, one previous study (Qun, 1988) had found that many of the coldest summers in eastern China during the past 500 year had occurred within two years

following major volcanic eruptions. Given the established inverse relationship between observed summer rainfall and temperatures, an accompanying increase in regional moisture could be tentatively inferred from Qun's findings. Meanwhile the clearest direct evidence for a hydroclimatic response came from Huang (1992), who noted exceptionally wet conditions in NEC and the YRV during the summer of 1816, attributing this response to a weakened WPSH throughout this decade (Huang and Wang, 1985). Thus, from the regional perspective, prior research had provided reasons to expect a detectible hydroclimatic response in East Asia, particularly to larger pre-instrumental eruptions, such as Tambora.

On larger spatial scales, results from Robock and Liu (1994) suggested that reduced shortwave radiation from SAOD forcing causes a decrease in surface evaporation, drying of the troposphere and decreased tropical precipitation. This result was basically supported by the findings of Gillett et al. (2004) and Lambert et al. (2004), which indicated that shortwave radiative forcing from 20th century volcanic eruptions caused noticeable reductions in global-scale precipitation. Based on results from these global-scale studies, it was hypothesized in the present study that a 10% dampening of global Hadley circulation could occur in response to increased SAOD from tropical eruptions on a scale comparable to Tambora. It is further noted that the present study found significant inverse correlations between seasonal indices for the NH Hadley cell and summer rainfall in the YRV and, to a lesser extent, NEC (Table 4.2).

The AO was also initially considered as a possible mechanism for a regional hydroclimate response in East Asia, given the role that it has been shown to play in causing regional-scale climatic change over the Eurasian continent (Shindell et al., 2004).

However there are a few reasons why the AO mechanism became less plausible before the Chapter 5 analyses of the observed response. First and foremost, the AO response to SAOD forcing occurs primarily during the winter season while the summer monsoon is the core focus of the present study. While one study (Gong and Ho, 2003) had found statistical evidence for a 1-3 month lagged relationship between YRV summer (JJA) rainfall and the May AO index, a mechanism for this link has not yet been clearly established. Furthermore, a significant AO response to volcanic forcing is not apparent in May. Finally, analyses in Chapter 4 found that the AO has no statistically significant zero-lag relationships with regional rainfall in eastern China or with the various East Asian monsoon indices. Thus, it is concluded with reasonable certainty that the AO is an unlikely dynamical mechanism for a regional-scale summer hydroclimatic response in East Asia.

8.2. The observed hydroclimatic response; the instrumental record

The conclusions of this study are generally consistent with conclusions from a great number of previous studies in finding that deducing a volcanic signal in regional climate is significantly hindered by the occurrence of simultaneous El Niño events (Kelly et al., 1996; Robock and Mao, 1995). For example, monthly composites of East Asian monsoon indices were suggestive of a possible regional-scale dynamical response but after the ENSO factor was accounted for these apparent volcanic signals disappeared. On the other hand, spatial composite plots of regional temperature and precipitation anomalies in the East Asia region provide evidence for some ENSO-independent regional climate signals. For example, a slightly stronger winter monsoon and cooler region-wide

temperatures during the cold season are evident in CRU temperature composites (1902 – 1999). This finding is also generally confirmed by historical records documenting a strong winter monsoon response to the Tambora eruption (Zhang et al., 1992). Also, results from similar composite analyses of summer rainfall offered hints of a regional hydroclimate signal (discussed in the next section).

Composite analyses of global land precipitation and vertical wind shear anomalies provide some support – in the instrumental record – for the hypothesized Hadley cell dampening mechanism. On the one hand, strong El Niño conditions apparently dominated over volcanic influences in the aftermath of the El Chichón and Pinatubo eruptions in 1982 and 1991, respectively. On the other hand, the Agung eruption occurred during a relatively weak El Niño year (1963) and a substantial weakening of Hadley circulation was apparent following that eruption. In that specific case, negative vertical wind shear anomalies were most apparent during the NH winter, when global Hadley cell overturning is generally driven by convection south of the equator. Interestingly, stratospheric sulfate aerosol loading from the Agung eruption was disproportionately limited to the Southern Hemisphere. The conceptual model to explain this response is that SH radiative forcing from Agung aerosols caused surface cooling, decreased local evaporation, weakened convection and dampened meridional overturning. This issue will be revisited in the context of the CSM simulated response, which provides further support for this hypothesis.

8.2.1. Observed hydroclimatic response; the paleoclimate record

Exceptional efforts were made to conduct a rigorous set of tests for exploring the observed hydroclimatic response based on the DI and WI records. For example, both Ammann et al. (2006) SAOD data and the Robock and Free (1995, 1996) IVI data were used to independently identify past high volcanic forcing years to include in composite analyses. Also, the stationarity and significance of the DI signal was tested with the WI data during their period of record-overlap (1470 – 1979), for the prior ~500 year period (950 – 1469 AD) and over the entire past millennium. While the statistical significance of results from these analyses was somewhat marginal, the general pattern that emerged in each of these separate analyses was remarkably consistent. Throughout SEC, summers concurrent with high SAOD forcing were generally drier and more prone to the occurrence of drought or severe drought, while the opposite is true for NEC. Over the entire YRV the response is basically neutral because the pattern is roughly split across the region: with wetter conditions in the north and drier conditions in the south. It is also important to note that these findings, based on the paleoclimate record (Figure 5.12 and 5.13), are entirely consistent with the historically documented response to the Tambora event (Huang, 1992) and with composite analyses based on the CRU instrumental record (1902 – 2002; Figures 5.8c & d). These results are also consistent with low-frequency regional temperature signals suggesting higher forcing brings colder (wetter) conditions to the north while the dry south, which would presumably have less cloud cover, generally does not respond with as much surface cooling.

Other paleoclimate data were also used to deduce the response from local to global-scale climatic boundary conditions that are apparently influential – or at least

related – to the East Asian summer monsoon system. For example, marine air temperature measurements from the SCS revealed significant year-round regional cooling following the 1809 and 1815 eruptions. This result provides a useful measure of the regional-scale climate sensitivity to these eruptions, but little can be said about what it means for regional hydroclimate over eastern China since quantitative land temperature estimates are poorly constrained on annual time-scales and, thus, an LSTD index anomaly cannot be reliably computed. The occurrence of a La Niña event during the winter of 1815/1816 (Chenoweth, 1996) may well have contributed to the wet conditions throughout NEC during the summer of 1816, however it seems unlikely to have been solely responsible for the exceptional flooding (Huang, 1992) that occurred during that year.

Cooler and generally drier conditions over the Tibetan Plateau can be deduced from slightly lowered annual net accumulation (A_n) and $d^{18}O$ values from the Dunde Ice core, during years with high volcanic forcing between 1801 and 1979. Extrapolating from the findings of Qian et al. (2003b) and assuming that the Dunde A_n record represents a reliable index for regional snowcover and snow depth over the entire northwestern Tibetan Plateau, negative snow accumulation anomalies would theoretically be linked to greater precipitation in NEC and SEC and drier conditions over the YRV. However, this is not the typical rainfall anomaly pattern that is shown in the present study to be associated with explosive tropical eruptions. The reliability of these ice-core records as regional climate indices is revisited later in this chapter.

8.3. Results from the CSM

Like many global models, the coupled CSM1.4 captures well large-scale features of the climate system while shortcomings become much more evident on regional-scales. For example, the exaggerated strength of tropical Hadley circulation appears to compound into other regional biases, such as anomalously strong subsidence in the subtropical region and an exceptionally fast subtropical jet in summer. The coarse resolution of the CSM1.4 also appears to be a significant drawback with respect to the climate of eastern China, due to this region's close proximity to the Tibetan Plateau. The smoothed spectral representation of topography has been blamed for exceptionally large positive precipitation biases in northern China (Kobayashi and Sugi, 2004; Ping Lu, personal communication). Also, unrealistically low elevations over the plateau result in regional warm biases, which apparently lead to a significantly shortened snowcover season. Some regional and global-scale teleconnection patterns are also absent or not realistically reproduced by the model.

However, perhaps more importantly, there are a few apparent model shortcomings that may have substantially inhibited CSM1.4's ability to realistically reproduce the observed response to volcanic forcing in the East Asian region, specifically. One such concern is that the model does not reliably reproduce all of the interrelationships between surface hydroclimate and the regional monsoon indices. In particular, the CSM does not realistically simulate the observed inverse correlation between the NH Hadley cell index and summer rainfall in the YRV and NEC, suggesting that there is little chance that it will effectively translate the simulated Hadley Cell dampening response into a realistic hydroclimatic response in eastern China. Finally, the CSM does not realistically capture

the observed inverse relationship between surface air temperature and summer rainfall, which is prevalent region-wide in nature.

8.3.1. Comparing the observed and modeled responses

Despite the various model shortcomings listed above, there are several important and valuable advantages to using global climate model simulations for the present study. First, since the CSM1.4 generally captures well all large-scale atmospheric circulation patterns and most regional-scale features, it provides a very useful tool for exploring possible mechanisms for a regional-scale response to global-scale forcing. In other words, even if the surface climate is not accurate on detailed regional-scales, the large-scale patterns are generally quite realistic and results are therefore informative.

Another significant advantage is that the Millennium simulation contains multiple large volcanic eruptions, several of which are larger than 20th century eruptions by a factor of three or more. Thus, model composites contain a greater number of samples with greater average forcing, significantly increasing the signal-to-noise ratio when statistically testing the results. This point was clearly illustrated by analyses of the "modern," Paleo1" and "Paleo2" composite plots. In particular, it is striking that the simulated response under modern forcing conditions is frequently very similar to the observed modern-era response; common patterns are apparent but neither displays statistically significant results. In contrast, the Paleo1 and Paleo2 composites revealed much clearer anomaly patterns with much higher levels of statistical significance.

In terms of the global-scale response, it is encouraging to note that the radiative forcing that is simulated at the surface by the CSM1.4 is very consistent with published

estimates based on similar assumptions regarding aerosol properties and stratospheric optical depth (e.g., Hansen et al., 2002). Furthermore, the CSM-simulated SAT response in the South China Sea to the 1809 and 1815 eruptions is in very good agreement with the observed MAT response in that region. The CSM1.4 also realistically captures the basic pattern of the observed positive AO response as well as the associated changes in Eurasian SAT in winter, although, as noted by Stenchikov et al. (2006), all AOGCMs underestimate the magnitude of this response and they consistently fail to capture all of the regional-scale details.

With consideration to the Hadley circulation, the model proves useful for gaining a better understanding of global-scale response to forcing from tropical eruptions. As noted above, results from observations certainly suggest that the Hadley cell dampening mechanism may have occurred in response to the Agung eruption. However, those findings were largely anecdotal and so the model provides a chance to investigate this further. This question is mostly interesting for its global-scale climatic implications. Analyses of CSM-simulated global land precipitation and vertical wind shear reflect a roughly 10% Hadley cell weakening in response to the 13 largest tropical eruptions between 850 and 1999. This result clearly quantitatively and qualitatively supports the hypothesized Hadley Cell dampening mechanism put forth in Chapter 2. It is also of interest that the CSM simulated wetter global conditions at roughly 40°N during NH summers under high volcanic forcing. This result was also in qualitative agreement with the observed response – based on CRU land precipitation (Figure 5.4) – and is therefore suggestive of a mechanism for the actual observed response in NEC. Still, this global-

scale result does not necessarily directly translate to a regional signal in NEC and should thus be treated as somewhat preliminary.

In terms of the regional response, under very high forcing (Paleo2) the model simulates some very significant changes in a few critical regional diagnostic variables. In particular, there is a significant weakening of the WPSH and the regional East Asian jet in summer and these results are dynamically consistent (Figure 6.11) with the model's simulated drying throughout NEC. Unfortunately, due to the ENSO factor the instrumental record (1948 – 1999) provides no clear indication of a dynamic response; however results from paleoclimate analyses by Huang and Wang (1985) agree with the model that the WPSH is significantly diminished under high SAOD forcing conditions. So, while the NEC surface hydroclimatic response in observations (wetter) is in complete disagreement with the model (drier), the observed response is dynamically consistent with a weakened WPSH, according to observational analyses in this (e.g., Figure 4.10; Figure 4.19) and previous studies (Huang et al, 1992).

Over SEC, there is general agreement between observations and the CSM that high volcanic forcing causes drying in that region. Interestingly, the model and observations also agree that this response runs contrary to the expected response given a diminished WPSH and weakened EASJI, the latter of which is simulated by the model (Figure 6.24d). Thus, the hydroclimatic response in the south appears to be dynamically inconsistent with both observed and simulated changes in atmospheric circulation. It is inferred from these results that the summer drying in SEC is likely to have resulted from direct radiative forcing, which is also the inferred mechanism for the simulated and observed drying response throughout the tropics (e.g., Hadley cell dampening). Lending

further support to this interpretation, it is also noted that in the model, as in observations (Figure 5.1), peak SAOD forcing immediately following tropical eruptions is generally strongest at low-latitudes. Thus, low-latitude regions may be especially susceptible to decreased surface evaporation caused directly by reduced shortwave radiation, while subtropical and extra-tropical regions may be more likely to respond to indirect or dynamical effects.

8.4. Strengths and limitations of data and methods

The inherent strengths and limitations of the present study, some of which were outlined in Chapter 3, are worth reiterating and discussing further in the context of the results presented above. Many problems stem from the very nature of paleoclimate research, where sources for error and uncertainty in proxy-based records and reconstructed estimates of radiative forcing typically grow larger in the more distant past. It follows that uncertainties in the magnitude of the radiative forcing directly affect the realism of the response simulated by the models. Finally, the time and spatial-scales of interest are of critical importance when weighing uncertainties in the above findings.

8.4.1. The paleoclimate record

With regard to the radiative forcing, reconstructions of the timing and magnitude of pre-instrumental volcanic eruptions is much more reliable during the second half of the last millennium compared to the first half. This conclusion is highlighted by the fact that the source for only one of the major tropical eruptions prior to 1500 AD has been positively identified (Briffa et al., 1998, Gao et al., 2006; also see Table 2.1).

Furthermore, based on comparisons between forcing from various independent reconstructions (e.g., Robertson et al., 2001; Ammann et al., 2006), Hansen et al. (2002) subjectively estimated that at least 50% uncertainty should be associated with proxy-based estimates of eruption magnitude prior to 1915 AD.

The present study's focus on the EAM summer hydroclimate response on seasonal to annual time-scales is considered viable for a number of different reasons. Primarily, the DI and WI paleo-hydroclimate records contain unique qualities that make them exceptionally well suited for examining the climatic response to volcanic forcing. For example, the annual resolution and multi-century coverage of the flood/drought indices provide the excellent opportunity to increase the sample size of composite analyses and to consider the climatic response to much larger, pre-instrumental eruptions. However, this data characteristic alone is not exceptionally unique, since multi-century annual-resolution proxy-based climate reconstructions have been used by several previous studies to investigate the observed climatic response to volcanic forcing (e.g., Briffa et al., 1998, Shindell et al., 2004). The DI data are particularly valuable in the context of this study because they are annually resolved *and* they are available from multiple independent sites across a broad continental region (Figure 3.5). This makes them particularly well suited for exploring spatial details of the regional-scale climate response and for providing unique insights into *both* direct/radiative and indirect/dynamical mechanisms for the hydroclimate response. Also, since the China region includes both tropical and extratropical land areas, results from this analysis have the potential to provide insights into the general nature of the observed climatic response to large-scale radiative perturbations in other global regions as well.

However, paleoclimate reconstructions derived from historical records also contain significant limitations. In particular, low-frequency climatic variations on decadal or longer time-scales are sometimes very difficult to quantitatively derive based on subjective writings in historical documents (Jones et al., 1998). Of course, the quality of the climate proxy is also not equal for all time periods or for all regions. Spatio-temporal data coverage is unsurprisingly inconsistent due to variable record keeping practices throughout history. Also, certain types of information are more reliable for the purpose of calibration with respect to instrumental records. For example, an explicitly quantitative form of daily precipitation record keeping, known as "Yu-Xue-Fen-Cun," was included in thousands of memos to the Emperor during the period from 1736 to 1911 (Ge et al., 2005). However, during other periods in history climate reconstructions were more reliant on relatively subjective hydroclimatic information derived from descriptive writings in gazettes or national and provincial official histories. Thus, composite analyses based on the observed response to 18th, 19th and 20th century eruptions should be considered relatively more reliable and perhaps more comparable to results from the instrumental record.

It should also be reiterated that the most reliable and consistently archived historical records contain relatively more hydroclimatic data – such as references to drought, flooding, precipitation and soil moisture – but relatively little explicit information with direct relevance to temperature (Zhang et al., 1992). Thus, proxy-based regionally representative temperature reconstructions are based on relatively fewer, more subjective data points and are generally only available at decadal or longer time-scales (e.g., Wang and Wang, 1991; Ge et al., 2003). To improve the chances of reliably

capturing the actual observed temperature response to volcanic forcing, a broad range of available temperature indices were used in the present study. Furthermore, these included temperature reconstructions that were derived through a variety of methodologies, using historical records from several different regions across eastern China.

A word of caution is warranted regarding the interpretation of results from ice core records from the Dunde Ice Cap. First of all, it should be emphasized that environmental conditions recorded from any single point – particularly one that sits over 2,000 meters above the nearest inhabited region – do not necessarily represent conditions from the broader region. Furthermore, climate proxy records must first be well calibrated and validated with respect to independent modern observations (Jones et al., 1998) and this was only marginally accomplished with respect to the Dunde A_n record. Finally, the Dunde ice-core records are relatively short (1801 – 1986), analyses revealed only subtle evidence for a climatic response and there were no means by which to independently confirm the findings. Thus, for the purpose of the present study, results from analyses of the Dunde records should be treated as strictly preliminary and generally inconclusive.

Finally, it should noted that while there are inherent uncertainties associated with calibrating and interpreting paleoclimate records, on their own proxy-data can also provide useful information. For example, they can be used as a qualitative constraint on general boundary conditions because the presence of long-term trends or abrupt shifts in the records may be indicative of local or regional environment changes during a given period of interest.

Thus, it is noted that the somewhat-limited two-century ice-core records from the Dunde Ice Cap contain little evidence for any significant trends or dramatic shifts (Davis et al., 2005). Furthermore, decadally averaged $d^{18}O$ records from Dunde, covering the past millennium, show long term trends that are indicative of colder conditions during the LIA, but otherwise no exceptional abrupt changes or trends are evident (Thompson et al., 2003). From the various multi-century reconstructed PDO indices there is some evidence for low-frequency changes in large-scale SST patterns, but the poor agreement between the various reconstructions indicate that 1) the actual spatio-temporal variability of those boundary conditions remain somewhat poorly constrained and 2) teleconnection patterns relating Pacific SST variability with surface climate over continental regions may not be entirely stationary over time.

The final boundary condition that has displayed significant changes during the past millennium is land cover throughout eastern China. Growing populations and changing land-use practices (Fu, 2002) along with long-term changes in orbital forcing have contributed to a slow but steady decline in vegetation cover as well as an associated change in the geographical extent of the monsoon system over eastern China (Gao et al., 2003; Wang, H. et al., 2003). The extent to which these changes could have influenced the observed dynamical or direct radiative response to volcanic forcing was not explored or taken into account in the present study. However, given that the time-scales associated with land use change are very different from the time-scale of volcanic eruptions, changes in the land surface seem unlikely to have qualitatively affected the outcome of analyses presented here. On the other hand, in the case of any significant change in large-scale boundary conditions it is certainly possible that indirect impacts could result,

such as in changes in the spatio-temporal stationarity of regional and large-scale teleconnection patterns.

8.4.2. Climate model simulations

In addition to specific biases and model shortcomings described above, there are a few other issues inherent to the specific model configuration used for this study that are worth reviewing in this section. For example, following up on the previous section, using a dynamic land-surface/ vegetation component in the coupled model may provide insights into the extent to which changes in this boundary condition influence the character and magnitude of the regional-scale response to volcanic forcing (in the context of gradual orbitally induced changes in the greater monsoon system). Another important problem with large-scale to boundary conditions in the CSM1.4 is basically applicable to most modern AOGCMs and it relates to the realism of the simulated patterns of SST variability. First of all, the CSM1.4 does not realistically capture all details of observed spatio-temporal variability in the ENSO system (Meehl and Arblaster, 1998) and therefore associated atmospheric teleconnection patterns are somewhat unrealistic in the model (Figure 6.16).

It follows that any direct comparison between AOGCM output and observed climate will always be imperfect. Part of this is due to model deficiencies but another important factor stems from the basic fact that much of observed climate variability occurs due to internal processes in the coupled ocean-atmosphere system. Thus, even with perfect knowledge of external radiative forcing, observed climate changes could never be exactly replicated by a model. This is particularly important in the context of

this study's direct comparisons between observed and simulated Tambora-era climate. Thus, multiple climate simulations with identical forcing (several ensemble members) would have been ideal for exploring that specific time period in greater detail. Instead, this study focused on composite analyses based on both observed and model-simulated climate, which is probably the best that could have been done with the available data.

One final point regarding the global model: there may be fundamental problems with the practice of validation a climate model for paleoclimate simulations on the basis of comparisons with respect to the modern record. Granted, the modern record is all that is available and hence must be used for such an exercise. Yet, it is important to remember that recent global and regional climate changes have been noticeably influenced by increasing greenhouse gas concentrations and associated global warming (IPCC, 2001). Furthermore, in East Asia the problem of industrial pollution and tropospheric aerosols is particularly acute and apparently has had far reaching impacts on the way that clouds are formed, how and when precipitation occurs and possibly even on meso-scale dynamical meteorology (e.g., Menon et al., 2002; Ramanathan et al., 2001). Thus the modern record is literally polluted by these complex anthropogenic influences and, as a result, is not necessarily directly comparable with pre-industrial climate.

With regard to the viability of dynamical downscaling from coupled AOGCM simulations, the analyses presented here suggest that the ReCM does not introduce any particularly noteworthy additional biases, beyond those that already exist in the CSM1.4 driving field. Thus, the ReCM apparently provides a reasonably suitable downscaling tool. However, improved results could be expected under the following circumstances. First, existing biases in the spatial distribution of precipitation over Eastern China may be

lessened if the ReCM included the entire Tibetan Plateau within the inner region of its climate simulation domain. This would result in a more realistic representation of surface topography and, thus, the significant mismatch in topography between the global and regional models would not have to be reconciled within the ReCM's buffer zone. Also, as a general rule, a higher resolution global model would likely be better suited as a driving field for the regional model (Wang et al., 2004). Finally, it would be ideal to drive the ReCM with output from a suite of several different global models to generate a multi-model ensemble mean response. This would provide a wider range of lateral boundary conditions for the regional model and the averaged solution would likely create the most realistic dynamically downscaled product (Déqué et al., 2005).

8.5. Societal implications of results

Based on a survey of existing paleoclimate data and published literature, it is evident that 20th century volcanic eruptions did not cause major climatic changes or socioeconomic impacts on a par with disruptions caused by earlier, much larger events. For example, colder temperatures and shorter growing seasons following Tambora and the preceding unknown eruption of 1809 caused significantly diminished harvest yields in spring and summer, particularly in north and central China. Crop reductions during this and other cold periods during the past millennium in China led to civil strife, rebellion, state wars and even dynastic change (Zhang et al., 2006).

However, shortened growing seasons and resulting crop reductions caused by future eruptions on the scale of Tambora are certainly within the realm of possibility. Furthermore, the future socioeconomic impacts of such an event could be dramatically

exasperated by the tripling of population that has occurred in China since the early 19th century. It should also be noted that it is not clear to what extent crop reductions following major eruptions are entirely attributable to colder conditions vs. reduced radiation caused by increased concentrations of stratospheric aerosols. Unfortunately, the course temporal resolution of available temperature reconstructions significantly limits the possibility of resolving this question in the near future.

8.6. Synopsis

Global and regional-scale climatic changes caused by volcanic eruptions are difficult to discern conclusively based on limited 20th century climate records. The occurrence of El Niño episodes during the years immediately following the two most recent explosive tropical eruptions (Pinatubo and El Chichón) is chiefly responsible for complicating efforts to identify and interpret the hydroclimatic response (Adler et al., 2003). However, analyses of paleoclimate records and results from the CSM1.4 Millennium simulations offer helpful clues and collectively indicate that a significantly increased volcanic signal occurs in East Asia in response to historical eruptions, many of which were much larger than those experienced in the 20th century. However, due to uncertainties in the precise magnitude of the forcing that drives the model and in the paleoclimate reconstructions themselves, most results and conclusions drawn from analyses in this study are necessarily qualitative.

For instance, the 80% confidence error bars on Ge et al. (2003) temperature reconstructions for northeastern China from 1500 to 1990 typically exceed the magnitude of the temperature anomaly in each decade. Thus, those records are mostly useful for

qualitatively assessing which regions may be relatively more or less sensitive to variations in volcanic forcing. It is concluded from simple pair-wise correlation analyses between a SAOD index and several decadally averaged regional temperature reconstructions that decades with greater volcanic activity are generally cooler in the north, while the southeast is relatively less temperature sensitive. To qualitatively summarize the regional-scale hydroclimate response in eastern China, it can be said with roughly 95% confidence that major eruptions over the past half millennium have generally led to a relatively wet north and a dry south. It is further noted that these temperature and hydroclimate responses are in qualitative agreement with one another, given the established inverse relationship between summer rainfall and surface air temperatures in China.

More quantitative assessments were also attempted with some success. In particular, comparisons between simulated and directly recorded MAT observations from the SCS during the early 19th century have provided the best direct measurement of model skill in the tropical Southeast Asia region. While the limited time and spatial scale of this model-data comparison precludes the possibility of drawing broad conclusions from these results, excellent agreement between the simulated and observed temperature response to Tambora-era volcanism has a couple of important, though somewhat tentative, implications. Primarily, it suggests that the sensitivity of the CSM1.4 to volcanic forcing is realistic and that estimates of the SAOD forcing from Tambora are reasonably accurate. Of course, it is useful to also have a reliable control on at least one of these factors, because, for example, if the model is too sensitive and the forcing is underestimated, then the same result could occur. As a constraint on model sensitivity it

is worth noting that Ammann et al. (2003) found that the NCAR-PCM – a very similar AOGCM with identical volcanic forcing – realistically simulated the global-scale temperature response to relatively reliable, modern estimates of time-evolution anthropogenic and natural radiative forcing during the period from 1890 – 2000 AD. Also, Ammann et al. (2006) found that results from the CSM1.4 Millennium simulation were similarly skillful (Figure 1.1).

Another relatively quantitative conclusion that may be drawn form this study relates to the good agreement between the theoretical estimate and model-simulated magnitude of Hadley cell dampening in response to large tropical eruptions. As predicted in Chapter 2, the CSM1.4 simulates a 10% reduction in the strength of tropical Hadley circulation (and equivalent decreases in precipitation throughout the tropics) under Tambora-like volcanic forcing conditions. This result suggests that a reduction in radiative forcing caused by simulated explosive tropical eruptions causes an immediate and linear simulated decrease in the surface solar radiation gain that drives Hadley cell overturning. However, while there is some anecdotal evidence in modern observations to generally support this model result, recent instrumental records and reanalysis data provide no robust quantitative confirmation. Nevertheless, theory, observational evidence and robust model-simulation results all support a dampened Hadley circulation response and thus provide a convenient qualitative explanation for one final noteworthy conclusion. An associated decrease in tropical precipitation caused by volcanic forcing, reduced incoming solar radiation and lower evaporation rates is hypothesized to have caused both observed and model-simulated decreases in summertime precipitation in southeastern China.

BIBLIOGRAPHY

Adams, J. B., M. E. Mann, and C. M. Ammann, 2003. Proxy evidence for and El Nino-like response to volcanic forcing. *Nature*, **426**, 274-278.

Adler, R. F., G. J. Huffman, A. Chang, R. Ferraro, P.-P. Xie, J. E. Janowiak, B. Rudolf, U. Schneider, S. Curtis, D. Bolvin, A. Gruber, J. Susskind, P. A. Arkin and E. Nelkin. 2003. The Version-2 Global Precipitation Climatology Project (GPCP) monthly precipitation analysis (1979-Present). *Journal of Hydrometeorology*, **4**(6), 1147-1167.

Ammann, C., 2001. Volcanic eruptions and climate, a data and model intercomparison. Ph.D. Dissertation, University of Massachusetts Amherst, 313 pp.

Ammann, C.M., G.A. Meehl, W.M. Washington and C.S. Zender, 2003. A monthly and latitudinally varying volcanic forcing dataset in simulations of 20th century climate. *Geophysical Research Letters*, **30**, doi:10.1029/2003GL016875RR.

Ammann, C. M., F. Joos, D. S. Schimel, B. L. Otto-Bliesner, and R. A. Thomas, 2006. Solar influence on climate during the past millennium: results from transient simulations with the NCAR Climate System Model. Submitted to *Proceedings of the National Academy of Science*s.

Ammann, C. M., and P. Naveau, 2003. Statistical analysis of tropical explosive volcanism occurrences over the last 6 centuries, *Geophysical Research Letters*, **30**(5), 1210, doi:10.1029/2002GL016388.

Andronova N.G., E. Rozanov, F. Yang, M.E. Schlesinger, and G.L. Stenchikov, 1999. Radiative forcing by volcanic aerosols from 1850 through 1994. *Journal of Geophysical Research*, **104**, 16807-16826.

Bard E., G. Raisbeck, F. Yiou, J. Jouzel, 2000. Solar irradiance during the last 1200 yr based on cosmogenic nuclides. *Tellus B*, **52**(3) 985-992.

Baron, W. R., 1992. 1816 in perspective: the view from the northeastern United States. In: The year without a summer? World climate in 1816. Edited by: Harrington, C. R., Canadian Museum of Nature, Ottawa, pg. 124-144.

Barnes J. E. and D. J. Hofmann, 1997. Lidar measurements of stratospheric aerosol over Mauna Loa Observatory. *Geophysical Research Letters*, **24**, 1923-1926.

Bauer, E., M. Claussen, V. Brovkin, 2003. Assessing climate forcings of the Earth system for the past millennium. *Geophysical Research Letters*, **30**(6), 1276, doi:10.1029/2002GL016639.

Bluth, G. J. S., S. D. Doiron, S. C. Schnetzler, A. J. Krueger, and L. S. Walter, 1992. Global tracking of the SO_2 clouds from the June 1991 Mount Pinatubo eruptions. *Geophysical Research Letters*, **19**, 151–154, 1992.

Biondi, F., A. Gershunov, and D. R. Cayan, 2001. North Pacific decadal climate variability since 1661. *Journal of Climate Letter*, **14**, 5 – 10.

Bonan, G., 1998. The land surface climatology of the NCAR Land Surface Model (LSM 1.0) coupled to the NCAR Community Climate Model (CCM3). *Journal of Climate*, **11**, 1307–1326.

Boville, B. A., J. T. Kiehl, P. J. Rasch, and F. O. Bryan, 2001: Improvements to the NCAR CSM-1 for transient climate simulations. *Journal of Climate*, **14**, 164-179.

Boville, B. A., and P. R. Gent, 1998. The NCAR climate system model, version one. *Journal of Climate*, **11**, 1115–1130.

Bradley, R. S., 1988. The explosive volcanic eruption signal in Northern Hemisphere continental temperature records, *Climatic Change*, **12**, 221–243.

Bradley, R. S., 1999. Paleoclimatology: Reconstructing Climates of the Quaternary. Academic Press, San Diego, 610 pp.

Briffa, K. R., P. D. Jones, F. H. Schweingruber and T. J. Osborn, 1998. Influence of volcanic eruptions on Northern Hemisphere summer temperature over the past 600 years. *Nature*, **393**, 450-455.

Briffa, K.R., T. J. Osborn, F. H. Schweingruber, I. C. Harris, P. D. Jones, S. G. Shiyatov, and E. V. Vaganov, 2001. Low-frequency temperature variations from tree ring density network, *Journal of Geophysical Research*, **106**, 2929-2941.

Bryan, F. O., B. G. Kauffman, W. G. Large, and P. R. Gent, 1996. The NCAR CSM flux coupler. NCAR Tech. Note 424, 50 pp.

Cane, M. A., A. C. Clement, A. Kaplan, Y. Kushnir, D. Pozdnyakov, R. Seager, S. E. Zebiak, R. Murtugudde, 1997. Twentieth-century sea surface temperature trends. *Science*, **275**, 957 –960.

Central Meteorological Bureau, 1981: Atlas of flood and drought in China in the last 500 years. Cartological Press, Beijing, China, 332 pp.

Chang, C.-P., Y. Zhang, and T. Li, 2000a: Interannual and interdecadal variations of the East Asian summer monsoon and tropical Pacific SSTs. Part 1: Role of the Subtropical Ridge. *Journal of Climate,* **13**, 4310-4325.

Chang, C.-P., Y. Zhang, and T. Li, 2000b: Interannual and interdecadal variations of the East Asian summer monsoon and tropical Pacific SSTs. Part 2: Southeast China rainfall and meridional structure. *Journal of Climate*, **13**, 4326-4340.

Chen, T.-C., S.-Y. Wang, W.-R. Huang, M.-C. Yen, 2004. Variation of the East Asian Summer Monsoon Rainfall. *Journal of Climate,* **17**, 744-762.

Chenoweth, M, 1996. Ships' Logbooks and "TheYear without a Summer." *Bulletin of the American Meteorological Society.* **77**(9), 2077-2093.

Chenoweth, M, 2001. Two major volcanic cooling episodes derived from global marine air temperature, AD 1807-1827. *Geophysical Research Letters*, **28**(15), 2963-2966.

Cohen, J., and M. Barlow, 2006. The NAO, AO, and global warming: how closely related? *Journal of Climate,* **18**, 4498-4513.

Crowley, T. J., and K.-Y. Kim, 1999: Modeling the temperature response to forced climate change over the last six centuries, *Geophysical Research Letters*, **26**, 1901–1904.

D'Arrigo, R., E. R. Cook, R. J. Wilson, R. Allan, and M. E. Mann, 2005. On the variability of ENSO over the past six centuries. *Geophysical Research Letters*, **32**, L03711, doi:10.1029/2004GL022055.

D'Arrigo, R., and R. Wilson, 2006. On the Asian Expression of the PDO. *International Journal of Climatology* (in press) DOI: 10.1002/joc.1326.

Dai, J., E. Mosley-Thompson, and L. G. Thompson, 1991. Ice core evidence for an explosive tropical volcanic eruption 6 years preceding Tambora. *Journal of Geophysical Research,* **96**, 17,361 – 17,366.

Dai., A. and T. M. L. Wigley, 2000. Global patterns of ENSO-induced Precipitation. *Geophysical Research Letters*, **27**(9), 1283-1286.

Dai., A., G. A. Meehl, W. M. Washington, and T. M. L. Wigley, 2001a. Climate Changes in the 21st century over the Asia-Pacific region simulated by the NCAR CSM and PCM. *Advances in Atmospheric Sciences*, **18**(5), 639-658.

Dai., A., T. M. L. Wigley, B. A. Boville, J. T. Kiehl, and L. E. Buja, 2001b. Climates of the twentieth and twenty-first centuries simiulated by the NCAR Climate System Model. *Journal of Climate*, **14**, 485-519.

Davis, M. E. L. G. Thompson, T. Yao and N. Wang, 2005. Forcing the Asian Monsoon on the Tibetan Plateau: Evidence from high-resolution ice core and tropical coral records. *Journal of Geophysical Research*, **110**, D04101, doi:10.1029/2004JD004933.

Déqué, M., D. P. Rowell, D. Lüthi, F. Giorgi, J. H. Christensen, B. Rockel, D. Jacob, E. Kjellström, M. de Castro, and B. van den Hurk, 2005. An intercomparison of regional climate models for Europe: assessing uncertainties in model projections. (WP2 contribution) PRUDENCE Final Report: 1 November 2001 – 31 October 2004, EVK2-CT2001-00132.

Dewey K.F., Heim R. Jr., 1982. A digital archive of Northern Hemisphere snow cover, November 1966 through 1980. *Bulletin of the American Meterological Society*, **63**, 1132–1141.

Ding, Y.H., 1994: Monsoons Over China, 419 pp, Kluwer Academic Publishers.

Ding, Y., C. Li, Y. Liu, 2004. Overview of the South China Sea Monsoon Experiment. *Advances in Atmospheric Sciences*, **21**(3), 343-360.

Duchon, C. E., 1979. Lanczos filtering in one and two dimensions. *Journal of Applied Meteorology*, **18**, 1016-1022.

Eddy, J., 1992. Before Tambora: The sun and climate. In: The year without a summer? World climate in 1816. Edited by: Harrington, C. R., Canadian Museum of Nature, Ottawa, 11.

Elvin, M., 2004. The Retreat of the Elephants: an Environmental History of China. Yale University Press, New Haven, CT, 564 pp.

Free, M. and A. Robock, 1999. Global warming in the context of the Little Ice Age. *Journal of Geophysical Research*, **104**(D14), 19,057-19,070.

Fu, C., 2002. Chapter 25: Can human induced land-cover change modify the monsoon system? In: Challenges of a changing earth. Edited by: W. Steffan, J. Jager, D. J. Carson C. Bradshaw, Springer-Verlag, Berlin, Germany, 133-136.

Fu, C., S. Wang, Z. Xiong, W. J. Gutowski, D.-K. Lee, J. L. McGregor, Y. Sato, H. Kato, J.-W. Kim and M.-S. Suh, 2005. Regional Climate Model Intercomparison Project for Asia. *Bulletin of the American Meteorological Society*, **86**(2), 257-266.

Gao, C., L. Oman, A. Robock, and G. L. Stenchikov, 2006: Atmospheric volcanic loading derived from bipolar ice cores accounting for the spatial distribution of volcanic deposition. Submitted to *Journal of Geophysical Research*, doi:10.1029/2006JD007461.

Gao, X., Y. Lou, W. Lin, Z. Zhao, F. Giorgi, 2003. Simulation of effects of land use change on climate in China by a regional climate model. *Advances in Atmospheric Sciences*, **20**(4), 583-592.

Ge, Q., J. Zheng, X. Fang, Z. Man, X. Zhang, P. Zhang, and W.-C. Wang. 2003. Winter half-year temperature reconstruction for the middle and lower reaches of the Yellow River and Yangtze River, China, during the past 2000 years. *The Holocene*, **13**(6), 933-940.

Ge, Q.-S., J.-Y. Zheng, Z.-X. Hao, P.-Y. Zhang and W.-C. Wang, 2005. Reconstruction of Historical Climate in China: High-Resolution Precipitation Data from Qing Dynasty Archives. *Bulletin of the American Meteorological Society*, **86**(5), 671–679.

Gedalof Z. and D. Smith, 2001. Interdecadal climate variability and regime-scale shifts in Pacific North America. *Geophysical Research Letters*, **28**, 1515–1518.

Gent, P. R., F. O. Bryan, G. Danabasoglu, S. C. Doney, W. R. Holland, W. G. Large, and J. C. McWilliams, 1998. The NCAR Climate System Model global ocean component. *Journal of Climate*, **11**, 1287–1306.

Gillett, N. P., H. F. Graf, T. J. Osborn, 2003. Climate change and the NAO. Chapter 9. In: The North Atlantic Oscillation. Edited by: J. Hurrell, Y. Kushnir, G. Ottersen and M. Visbeck, American Geophysical Union, Washington, DC.

Gillett, N. P., A. J. Weaver, F. W. Zwiers, and M. F. Wehner, 2004. Detection of volcanic influence on global precipitation. *Geophysical Research Letters*, **31**, L12217, doi:10.1029/2004GL020044.

Giorgi, F. and R. Francisco, 2000. Evaluating uncertainties in the prediction of regional climate change. *Geophysical Research Letters*, 27, 1295-1298.

Gleckler, P. J., T. M. L. Wigley, B. D. Santer, ,J. M. Gregory, K. AchutaRao, K. E. Taylor, 2006. Brief Communications: Krakatoa's signature persists in the ocean. *Nature*, **439**, 675.

Gong, D.-Y., and C.-H. Ho, 2002. Shift in the summer rainfall over the Yangtze River valley in the late 1970s. *Geophysical Research Letters*, **29**(10), doi:10.1029/2001GL014523.

Gong, W. and W.-C. Wang, 2000. A regional model simulation of 1991 severe precipitation event over Yangtze-Huai river valley. Part II: Model bias. *J. Climate* **13**, 93-108.

Gong, D.Y., S.-W. Wang, J.-H. Zhu, 2001. East Asian winter monsoon and Arctic Oscillation. *Geophysical Research Letters*, **28**(10), 2073-2076.

Gong, D. and S. Wang, 2003. Influence of Arctic Oscillation on winter climate over China. *Journal of Geographical Sciences*, **13**(2), 208-216.

Gong, D.-Y., and C-H. Ho, 2003. Arctic Oscillation signals in the East Asian summer monsoon. *Journal of Geophysical Research*, **108**(D2), 4066, doi:10.1029/2002JD002193.

Gordon L. J., W. Steffen, B. F. Jonsson, C. Folke, M. Falkenmark, A. Johannessen, 2005. Human modification of global water vapor flows from the land surface. *Proceedings of the National Academy of Sciences*. **102**(21), 7612–7617.

Gu, L., D. D. Baldocchi, S. C. Wofsy, J. W. Munger, J. J. Michalsky, S. P. Urbanski, and T.A. Boden, 2003. Response of a Deciduous Forest to the Mount Pinatubo Eruption: Enhanced Photosynthesis. *Science*, **299**, 2035-2038.

Hamill, P., E. J. Jensen, P. B. Russell, and J. J. Bauman, 1997. The life cycle of stratospheric aerosol particles, *Bulletin of the American Meteorological Society*, **78**, 1395–1410.

Hansen, J., R. Ruedy and M. Sato, 1996. Global surface air temperature in 1995: Return to pre-Pinatubo level. *Geophysical Research Letters*, **23**(13), 1665-1668.

Hansen, J., M. Sato, L. Nazarenko, R. Ruedy, A. Lacis, D. Koch, I. Tegen, T. Hall, D. Shindell, B. Santer, P. Stone, T. Novakov, L. Thomason, R. Wang, Y. Wang, D. Jacob, S. Hollandsworth, L. Bishop, J. Logan, A. Thompson, R. Stolarski, J. Lean, R. Willson, S. Levitus, J. Antonov, N. Rayner, D. Parker, and J. Christy, 2002. Climate forcings in Goddard Institute for Space Studies SI2000 simulations. *Journal of Geophysical Research*, **107**(D18), 4347, doi:10.1029/2001JD001143.

Hansen, J., M. Sato, R. Ruedy, L. Nazarenko, A. Lacis, G. A. Schmidt, G. Russell, I. Aleinov, M. Bauer, S. Bauer, N. Bell, B. Cairns, V. Canuto, M. Chandler, Y. Cheng, A. Del Genio, G. Faluvegi, E. Fleming, A. Friend, T. Hall, C. Jackman, M. Kelley, N. Kiang, D. Koch, J. Lean, J. Lerner, K. Lo, S. Menon, R. Miller, P. Minnis, T.

Novakov, V. Oinas, Ja. Perlwitz, Ju. Perlwitz, D. Rind, A. Romanou, D. Shindell, P. Stone, S. Sun, N. Tausnev, D. Thresher, B. Wielicki, T. Wong, M. Yao, and S. Zhang, 2005. Efficacy of climate forcings, *Journal of Geophysical Research*, **110**, D18104, doi:10.1029/2005JD005776.

Harrington, C. R. 1992. The year without a summer? World climate in 1816. Canadian Museum of Nature, Ottawa, 575 pp.

Hirono, M., 1988. On the trigger of El Niño–Southern Oscillation by the forcing of early El Chichón volcanic aerosols, *Journal of Geophysical Research*, **93**, 5365–5384.

Hoerling, M.P. and A. Kumar, 2000. Understanding and Predicting Extratropical Teleconnections Related to ENSO. In: El Niño and the Southern Oscillation, Multiscale Variability and Regional Impacts. Edited by Diaz, H.F. and V. Markgraf, Cambridge University Press, New York, N.Y., 57-88.

Hou, A.Y., 1998: Hadley Circulation as a modulator of the extratropical climate. *Journal of Climate*, **55**, 2437-2457.

Hu, Z.-Z., R. Wu, J. Kinter, S. Yang., 2005. Connection of summer rainfall variations in South and East Asia: Role of El Nino-Southern Oscillation. *International Journal of Climatology*, **25**, 1279-1289.

Huang, R., Zhou Liantong and Chen Wen, 2003. The Progresses of recent studies on the variabilities of the East Asian Monsoon and their causes. *Advances in Atmospheric Sciences*, **20**(1), 55-69.

Huang, J., 1992. Was there a colder summer in China in 1816? In: The year without a summer? World climate in 1816. Edited by: Harrington, C. R., Canadian Museum of Nature, Ottawa, pg. 436-447.

Huang, J.-Y. and S.-W. Wang, 1985. Investigations on variations of the subtropical high in the western Pacific during historic times. *Climatic Change*, **7**, 427-440.

Hurrell, J.W., 1995: Decadal trends in the North Atlantic Oscillation regional temperatures and precipitation, *Science*, **269**, 676-679.

IPCC, 2001. Climate change 2001: The Scientific Basis, Intergovernmental Panel on Climate Change. Cambridge University Press, Cambridge, UK, 388 pp.

Jones, P.D., K.R. Briffa, T.P. Barnett and S.F.B. Tett. 1998. High-resolution palaeoclimatic records for the last millennium: interpretation, integration and comparison with General Circulation Model control-run temperatures. *The Holocene*, 8(4), 455-471.

Jones, P. D., and A. Moberg, 2003. Hemispheric and large-scale surface air temperature variations: An extensive revision and an update to 2001. *Journal of Climate,* **16**, 206–223.

Jones, P.D. and M. E. Mann, 2004. Climate over past millennia. *Reviews of Geophysics*, 42(2), RG2002, doi: 10.1029/2003RG000143.

Kang, I.-S., K. Jin, B. Wang, K.-M. Lau, J. Shukla, V. Krishnamurthy, S.D. Schubert, D.E. Wailser, W.F. Stern, A. Kitoh, G.A. Meehl, M. Kanamitsu, V.Y. Galin, V. Satyan, C.-K. Park, and Y. Liu, 2002: Intercomparison of the climatological variations of Asian summer monsoon precipitation simulated by 10 GCMs. *Climate Dynamics*, **19**, 383-395.

Kelly, P. M., P. D. Jones,. and J. Pengqun, 1996. The spatial response of the climate system to explosive volcanic eruptions. *International Journal of Climatology,* **16**(5), 537-550.

Kiehl, J. T., J. J. Hack, G. Bonan, B. A. Boville, D. Williamson, and P. Rasch, 1998. The National Center for Atmospheric Research Community Climate Model: CCM3. *Journal of Climate*, **11**, 1131–1149.

Kinter, J. L., K. Miyakoda, and S. Yang, 2002. Recent change in the connection from the Asian monsoon to ENSO. *Journal of Climate*, **15**(10), 1203-1215.

Kirchner, I., and H.-F. Graf, 1995: Volcanoes and El Niño: Signal separation in Northern Hemisphere winter. *Climate Dynamics*, **11**, 341–358.

Kirchner, I., G. L. Stenchikov, H.-F. Graf, A. Robock and J. C. Antuña, 1999. Climate model simulation of winter warming and summer cooling following the 1991 Mount Pinatubo volcanic eruption. *Journal of Geophysical Research*, **104**, 19,039-19,055.

Koch, P., H. Wernli, H.C. Davies, 2006: An event-based jet-stream climatology and typology. *International Journal of Climatology*, **26**, 283-301.

Kunkel, K. E., X.-Z. Liang, J. Zhu and Y. Lin, 2006. Can CGCMs simulate the Twentieth century "warming hole" in the central United States? *Journal of Climate, in press.*

Labitzke, K. and M. P. McCormick, 1992. Stratospheric temperature increases due to Pinatubo aerosols. *Geophysical Research Letters*, **19**, 207-210.

Lamb, H. H., 1970. Volcanic dust in the atmosphere with a chronology and assessment of its meteorological significance. *Philosophical Transactions of the Royal Society of London*, **266**, 425-533.

Lambert, F. H., P. A. Stott, M. R. Allen, and M. A. Palmer, 2004. Detection and attribution of changes in 20th century land precipitation. *Geophysical Research Letters*, 31, L10203, doi:10.1012/2004GL019545.

Lamarche Jr., V. C. and K. K. Hirschboek, 1984. Frost rings in trees as records of major volcanic eruptions. *Nature*, **307**, 121 - 126

Langway Jr., C. C., H. B. Clausen, C.U. Hammer, 1988. An inter-hemispheric volcanic time-marker in ice cores from Greenland and Antarctica. *Annals of Glaciology*, **10**, 102-108.

Lau, K.-M. and W. Bua, 1998: Mechanisms of monsoon-Southern Oscillation coupling: insights from GCM experiments. *Climate Dynamics*, **14**, 759-779.

Lau, N. G. and B. Wang, 2006. Interactions between the Asian monsoon and the El Nino/Southern Oscillation. In: The Asian Monsoon. Edited by: B. Wang, Praxis, Springer Berlin Heilberg, 479 - 512.

Lean, J., J. Beer, and R. Bradley. 1995. Reconstruction of solar irradiance since 1610. *Geophysical Research Letters*, **22**, 3195-3198.

Leung L. R., L. O. Mearns, F. Giorgi, and R. L. Wilby. 2003. Regional climate research: needs and opportunities. *Bulletin of the American Meteorological Society*, **84**(1), 89-95.

Leung, L. R., S. J. Ghan, Z.-C. Zhao, Y. Luo, W.-C. Wang, and H.-L. Wei, 1999. Intercomparison of regional climate model for simulation of the 1991 Summer Monsoon in eastern Asia. *Journal of Geophysical Research*, **104**, 6425–6454.

Li, C., J. He, J. Zhu, 2004. A Review of Decadal/ Interdecadal Climate Variation Studies in China. *Advances in Atmospheric Sciences*, **21**(3), 425-436.

Liang, X.-Z., A. Samel., W.-C. Wang, 1995. Observed and GCM simulated decadal variability of monsoon rainfall in east China. *Climate Dynamics*, **11**, 103-114.

Liang, X.-Z., W.-C. Wang, and A. Samel, 2001. Biases in Amip model simulations of the east China monsoon system. *Climate Dynamics*, **17**, 291-304.

Lim, Y.-K., K.-Y. Kim, and H.-S. Lee, 2002. Temporal and spatial evolution of the Asian Summer Monsoon in the seasonal cycle of synoptic fields. *Journal of Climate*, **15**, 3630-3644.

MacCracken, M.C., 2006. Geoengineering: Worthy of Cautious Evaluation? *Climatic Change*, doi: 10.1007/s10584-006-9130-6.

MacDonald, G. M., and R. A. Case, 2005. Variations in the Pacific decadal oscillation over the past millennium, *Geophysical Research Letters*, **32**, L08703, doi:10.1029/2005GL022478.

Mann, M. E., R. S. Bradley, and M. K. Hughes, 1998. Global-scale temperature patterns and climate forcing over the past six centuries. *Nature*, **392**, 779–787.

Mann, M.E., M.A. Cane, S. E Zebiak, and A. Clement, 2005: Volcanic and Solar Forcing of the Tropical Pacific over the Past 1000 years. *Journal of Climate*, **18**, 447-456.

Mantua, N. J., S. R. Hare, Y. Zhang, J. M. Wallace, and R. C. Francis, 1997. A Pacific inter-decadal climate oscillation with impacts on salmon production. *Bulletin of the American Meteorological Society*, **78**(6), pp. 1069 -1079.

Mantua N, Hare S. 2002. The Pacific Decadal Oscillation. *Journal of Oceanography*, **58**, 35–44.

Meehl, G. A., and J. M. Arblaster, 1998. The Asian–Australian monsoon and El Niño–Southern Oscillation in the NCAR Climate System Model. *Journal of Climate*, **11**, 1356–1385.

Menon, S. J. Hansen, L. Nazarenko, Y. Luo, 2002. Climate effects of black carbon aerosols in China and India. *Science*, **297**, 2250

Mitas, C.M. and A. Clement, 2005. Has the Hadley Cell been strengthening in recent decades? *Geophysical Research Letters*, **32**, L03809, doi:10.1029/2004GL021765.

Mitchell, J. M., 1970. A preliminary evaluation of atmospheric pollution as a cause of the global temperature fluctuation of the past century. In: Global effects of environmental pollution. Edited by: Singer, S. F., Springer, New York, pp.139-155.

Mitchell, T. D., P. D. Jones, 2005. An improved method of constructing a database of monthly climate observations and associated high resolution grids. *International Journal of Climatology*, **25**, 963 – 712.

Newhall, G. C. and S. Self, 1982. The Volcanic Explosivity Index (VEI): an estimate of explosive magnitude for historical volcanism. *Journal of Geophysical Research*, **87**, 1231–1238.

Niu, T., L. Chen., and Z. Zhou, 2004. The characteristics of climate change over the Tibetan Plateau in the last 40 years and detection of climatic jumps. *Advances in Atmospheric Sciences*, **21**(2),193-203.

Oort, A. H., and J. J. Yienger, 1996. Observed interannual variability in Hadley Circulation and its connection to ENSO, *Journal of Climate*, **9**(11), 2751-2767.

Oman, L., A. Robock, G. Stenchikov, G. A. Schmidt, and R. Ruedy, 2005. Climatic response to high latitude volcanic eruptions, *Journal of Geophysical Research*, **110**, D13103, doi:10.1029/2004JD005487.

Oman, L., A. Robock, G. L. Stenchikov, T. Thordarson, D. Koch, D. T. Shindell, and C. Gao, 2006. Modeling the distribution of the volcanic aerosol cloud from the 1783–1784 Laki eruption, *Journal of Geophysical Research*, **111**, D12209, doi:10.1029/2005JD006899.

Oppenheimer, C., 2003, Climatic, environmental and human consequences of the largest known historic eruption: Tambora volcano (Indonesia) 1815, *Progress in Physical Geography*, **27**, 230-259.

Ortlieb, L., 2000: The documented historical record of El Niño events in Peru: An update of the Quinn record (Sixteenth through Nineteenth centuries). In: El Niño and the Southern Oscillation, Multiscale Variability and Regional Impacts. Edited by: Diaz, H.F. and V. Markgraf, Cambridge University Press, New York, N.Y., 207-295.

Pang, K. D., 1991. The legacies of eruption: matching traces of ancient volcanism with chronicles of cold and famine. *The Sciences*, **31**, 30-35.

Písek, J. and R. Brázdil, 2006. Responses of large volcanic eruptions in the instrumental and documentary climatic data over central Europe. *International Journal of Climatology*, **26**, 439-459.

Qian, W., Q. Hu, Y. Zhu, D.K. Lee, 2003a. Centennial-scale dry-wet variations in East Asia. *Climate Dynamics*, **21**, 77-89.

Qian Y. F., Y. Q. Zheng, Y. Zhang, M. Q. Miao, 2003b. Responses of China's summer monsoon climate to snow anomaly over the Tibetan Plateau. *International Journal of Climatology*. **23**(6), 593-613.

Quan, X.-W., H. F. Diaz, and M. P. Hoerling, 2004. Changes in the tropical Hadley cell since 1950. In: The Hadley Circulation: Present, Past and Future. Edited by: H. F. Diaz and R. S. Bradley, Kluwer Academic Publishers, 85-120.

Quinn, W. H, V. T. Neal and S. E. Antunez de Mayolo, 1987: El Niño occurrences over the past four and a half centuries. *Journal of Geophysical Research*, **92**, 14,449-14,461.

Qun, X., 1988. The abnormally cold summers of central China and their relation to volcanic eruptions. In: *Aerosols and Climate.* Edited by: . Hobbs, P.V., and M. P. McCormick, Deepak publishing, Hampton, VA, pp. 223-231.

Ramanathan, V., P.J. Crutzen, J. T. Kiehl, D. Rosenfeld, 2001. Aerosols, climate and the hydrologic cycle, *Science*, **294**, 2119 -2124.

Rasmusson, E.M., 1985. El Niño and the Variations in Climate. *American Scientist*, **73**, 168-177.

Rind, D., J. Perlwitz, and P. Lonergan 2005. AO/NAO response to climate change: 1. Respective influences of stratospheric and tropospheric climate changes. *Journal of Geophysical Research*, **110**, D12107, doi:10.1029/2004JD005103.

Riyu, L., 2002. Indices of the Summertime Western North Pacific Subtropical High. *Advances in Atmospheric Sciences*, **19**(6), 1004-1028.

Robertson, A., J. Overpeck, D. Rind, E. Mosley-Thompson, G. Zielinski, J. Lean, D. Koch, J. Penner, I. Tegen, and R. Healy. 2001. Hypothesized Climate Forcing time series for the last 500 years. *Journal of Geophysical Research*, **106**(D14): 14,783-14,803.

Robinson D.A., Dewey K.F., Heim R.R., 1993: Global snow cover monitoring: an update. *Bulletin of the American Meteorological Society*, **74**, 1689–1696.

Robock, A., and J. Mao, 1992. Winter warming from large volcanic eruptions. *Geophysical Research Letters*, **19**, 2405–2408.

Robock, A., and Y. Liu, 1994. The volcanic signal in Goddard Institute for Space Studies three-dimensional model simulations. *Journal of Climate*, **7**, 44–55.

Robock, A. and J. Mao, 1995. The volcanic signal in surface temperature observations. *Journal of Climate*, **8**, 1086-1103.

Robock, A., K. E. Taylor, G. L. Stenchikov, and Y. Liu, 1995. GCM evaluation of a mechanism for El Nino triggering by El Chichon ash cloud. *Geophysical Research Letters*, **22**(17) 2,369-2,372.

Robock, A., and M. P. Free, 1995. Ice cores as an index of global volcanism from 1850 to the present. *Journal of Geophysical Research*, **100**, 11549- 11567.

Robock, A., and M. P. Free, 1996. The volcanic record in ice cores for the past 2000 years. In: Climatic Variations and Forcing Mechanisms of the Last 2000 Years. Edited by: P. D. Jones, R. S. Bradley, and J. Jouzel, Springer-Verlag, New York, pp. 533–546.

Robock, A., 2000. Volcanic eruptions and climate. *Reviews of Geophysics*, **38**, 191-219.

Robock, A., 2001a. Volcanic eruption, Tambora. In: Encyclopedia of Global Environmental Change, vol. 1. Edited by: Ted Munn, John Wiley and Sons, London, 737-738.

Robock, A., 2001b. Volcanic eruption, Mt. Pinatubo In: Encyclopedia of Global Environmental Change, vol. 1. Edited by: Ted Munn, John Wiley and Sons, London, 737.

Robock, A., 2001c. Volcanic eruption, El Chichón. In: Encyclopedia of Global Environmental Change, vol. 1. Edited by: Ted Munn, John Wiley and Sons, London, 736.

Robock, A. 2001d. Stratospheric forcing needed for dynamical seasonal prediction. *Bulletin of the American Meteorological Society*, 82(10), 2,189-2,192.

Robock, A., 2005. Cooling following large volcanic eruptions corrected for the effect of diffuse radiation on trees. *Geophysical Research Letters*, **32**, L06702, doi:10.1029/2004GL022116.

Robock, A., and C. Mass, 1982. The Mount St. Helens volcanic eruption of 18 May 1980: Large short-term surface temperature effects. *Science*, **216**, 628–630.

Ropelewski, C. F. and M.S. Halpert, 1987. Global and regional scale Precipitation Patterns Associated with the El Niño/Southern Oscillation. *Monthly Weather Review*, **115**, 1606-1626.

Ropelewski, C. F. and P. D. Jones, 1987. An extension of the Tahiti-Darwin Southern Oscillation Index. *Monthly Weather Review*, **115**, 2161-2165.

Rogers, J.C., 1984. The Association between the North Atlantic Oscillation and the Southern Oscillation in the Northern Hemisphere. *Monthly Weather Review*, **112**, 1999-2015.

Rutherford, S., M. E. Mann, T. L. Delworth, and R. Stouffer, 2003. Climate field reconstruction under stationary and nonstationary forcing, *Journal of Climate*, **16**, 462– 479.

Samel, A. N., W.-C. Wang and X.-Z. Liang, 1999. The monsoon rainband over China and relationships with Eurasian Circulation. *Journal of Climate*, **12**, 115 - 131.

Samel, A. N. and X.-Z. Liang, 2003. Understanding relationships between the 1998 Yangtze River flood and northeast Eurasian blocking. *Climate Research*, **23**, 149-158

Sato, M., J. E. Hansen, M. P. McCormick and J. B. Pollack, 1993. Stratospheric optical depth, 1850 – 1990. *Journal of Geophysical Research*, **98**(D12), 22,987 – 22,994.

Scaife, A., J. Knight, G. Vallis, and C. Folland, 2005. A stratospheric influence on the winter NAO and North Atlantic surface climate, *Geophysical Research Letters*, 32, L18715, doi:10.1029/2005GL023226.

Self, S., Zhao,J-X, Holasek, R.E., Torres, R.C., and. King, A.J., 1996. The atmospheric impact of the 1991 Mount Pinatubo eruption. In: Fire and Mud: Eruptions and Lahars of Mount Pinatubo, Philippines. Edited by: C. Newhall and Punongbayan, University of Washington Press, Seattle.

Shen, C., W.-C. Wang, W. Gong, and Z. Hao, 2006. A Pacific Decadal Oscillation rainfall over eastern China, *Geophysical Research Letters*, **33**, L03702, doi:10.1029/2005GL024804.

Shindell, D. T., G. A. Schmidt, R. L. Miller, and D. Rind, 2001a. Northern Hemisphere winter climate response to greenhouse gas, ozone, solar, and volcanic forcing. *Journal of Geophysical Research*, **106**, 7193– 7210.

Shindell, D.T., G.A. Schmidt, M.E. Mann, D. Rind, and A. Waple 2001b. Solar forcing of regional climate change during the Maunder Minimum. *Science*, **294**, 2149-2152.

Shindell, D. T., G. A. Schmidt, R. Miller, and M. E. Mann, 2003. Volcanic and Solar Forcing of Climate Change during the Preindustrial Era. *Journal of Climate*, **16**, 4,094-4,107.

Shindell, D. T., G. A. Schmidt, M. E. Mann and G. Faluvegi, 2004: Dynamic winter climate response to large tropical volcanic eruptions since 1600. *Journal of Geophysical Research*, **109**, D05104, doi:10.1029/2003JD004151.

Shiyan, T., F. Congbin, Z. Zhaomei, Z. Qingyun, 1997: Two Long-Term Instrumental Climatic Data Bases of the People's Republic of China. Prepared by: D. P. Kaiser, Carbon Dioxide Information Analysis Center, Oak Ridge, Tennessee.

Simkin, T., and L. Siebert, 1994. Volcanoes of the World: A Regional Directory, Gazetteer, and Chronology of Volcanism During the Last 10,000 Years, 2nd ed., Geoscience Press, Tucson, Ariz, 349 pp.

Smith, S. R., D. M. Legler, and K. V. Verzone, 2001. Quantifying uncertainties in NCEP Reanalysis using high-quality research vessel observations. *Journal of Climate*, **14**, 4062-4072.

Smith, T. M., and R. W. Reynolds, 2004. Improved Extended Reconstruction of SST (1854-1997). *Journal of Climate*, **17**, 2466-2477.

Song, J., 1998. Reconstruction of the Southern Oscillation from Dryness/wetness in China for the last 500 years. *International Journal of Climatology*, **18**, 1345–1355.

Song, J., 2000. Changes in Dryness/Wetness in China during the last 529 years. *International Journal of Climatology*, **20**, 1003–1015.

Stenchikov, G. L., I. Kirchner, A. Robock, H.-F. Graf, J. C. Antunã, R. G. Grainger, A. Lambert, and L. Thomason, 1998. Radiative forcing from the 1991 Mount Pinatubo volcanic eruption, *Journal of Geophysical Research*, **103**, 13,837–13,857

Stenchikov, G., A. Robock, V. Ramaswamy, M. D. Schwarzkopf, K. Hamilton, and S. Ramachandran, 2002. Arctic Oscillation response to the 1991 Mount Pinatubo eruption: Effects of the volcanic aerosols and ozone depletion. *Journal of Geophysical Research*, **107**, ACL 28-1 - ACL 28-16.

Stenchikov, G., K. Hamilton, A. Robock, V. Ramaswamy, and M. D. Schwarzkopf, 2004. Arctic Oscillation response to the 1991 Pinatubo eruption in the SKYHI GCM with a realistic Quasi-Biennial Oscillation. *Journal of Geophysical Research*, **109**, D03112, doi:10.1029/2003JD003699.

Stenchikov, G., K. Hamilton, R. J. Stouffer, A. Robock, V. Ramaswamy, B. Santer, and H.-F. Graf, 2006. Arctic Oscillation response to volcanic eruptions in the IPCC AR4 climate models, *Journal of Geophysical Research*, **111**, D07107, doi:10.1029/2005JD006286.

Stothers, R. B., 1996. Major optical depth perturbations to the stratosphere from volcanic eruptions: Pyrheliometric period, 1881 – 1960. *Journal of Geophysical Research*, **110**(D2), 3901 – 3920.

Stommel, H. and E. Stommel, 1983. Volcano Weather: The Story of 1816, The Year Without a Summer. *Seven Seas Press*, Newport, RI., 177.

Stott, P. A., J. F. B. Mitchell, M. R. Allen, T. L. Delworth, J. M. Gregory, G. A. Meehl and B. D. Santer, 2006. Observational Constraints on Past Attributable Warming and Predictions of Future Global Warming. *Journal of Climate*, **19**(13), 3055–3069.

Tanka, M., 1997. Interannual and interdecadal variations of the western North Pacific monsoon and Baiu rainfall and their relationship to the ENSO cycles. *Journal of the Meteorological Society of Japan*, **75**(6), 1109-1123.

Tanka, H. L., N. Ishizaki, and A. Kitoh, 2004: Trend and interannual variability of walker, monsoon and Hadley circulations defined by velocity potential in the upper atmosphere. *Tellus*, **56A**, 250-269.

Teller, E., R. Hyde, and L. Wood, 2002. Active Climate Stabilization: Practical Physics-Based Approaches to Prevention of Climate Change. UCRL-JC-148012, Lawrence Livermore National Laboratory, Livermore, California, USA, 11 pp.

Thompson, D.J.W., and J. M. Wallace, 1998. The Arctic Oscillation signature in the wintertime geopotential height and temperature fields. *Geophysical Research Letters*, **25**(9), 1297-1300.

Thompson, D. J. W., and J. M. Wallace, 2000. Annual modes in the extratropical circulation. Part I: Month-to-month variability. *Journal of Climate*, **13**, 1000-1016.

Thompson, D. J. W., and J. M. Wallace, 2001. Regional climate impacts of the Northern Hemisphere annular mode. *Science*, **293**, 85-89.

Thompson, L. G., E. Mosley-Thompson, M. E. Davis, P.-N. Lin, K. Henderson and T. A. Mashiotta, 2003. Tropical glacier and ice core evidence of climate change on annual to millennial time scales. *Climatic Change*, **59**, 137-155.

Trenberth, K. E., and D. A. Paolino Jr., 1980. The Northern Hemisphere sea-level pressure data set: Trends, errors and discontinuities. *Monthly Weather Review*, **108**, 855-872.

Trenberth, K. E. and J. W. Hurrell, 1994. Decadal atmosphere-ocean variations in the Pacific. *Climate Dynamics*, **9**, 303-319.

Trenberth, K. E., D. P. Stepaniak, and J. M. Caron, 2000. The global monsoon as seen through the divergent atmospheric circulation. *Journal of Climate*, **13**, 3969-3993.

Trenberth, K. E., and J. M. Caron, 2000. The Southern Oscillation revisited: Sea level pressures, surface temperatures and precipitation. *Journal of Climate*, **13**, 4358-4365.

Wagner, S., E. Zorita, 2005. The influence of volcanic, solar and CO_2 forcing on the temperatures in the Dalton Minimum (1790-1830): a model study. *Climate Dynamics*, **25**, 205-218.

Wang, B., R. Wu, X. Fu., 2000. Pacific-East Asian Teleconnection: How does ENSO Affect East Asian Climate? *Journal of Climate*, **13**, 1,517-1,536.

Wang, B., R. Wu, and K. M. Lau, 2001. Interannual variability of the Asian summer monsoon: contrasts between the Indian and the western North Pacific–East Asian monsoons. *Journal of Climate*, **15**, 4073–4090.

Wang, H., A. J. Pitman, M. Zhao, and R. Leemans, 2003. The impact of land-cover modification on the June meteorology of China Since 1700, simulated using a regional climate model. *International Journal of Climatology*, **23**, 511-527.

Wang, S.-W., 1988. Wetness variation in China over the last 500 years. In: The reconstruction of climate in China for historical times. Edited by: Zhang, J., Science Press, Beijing China, 66 –78.

Wang, S.-W. 1991. Reconstruction of temperature series of North China from 1380s to 1980s. *Science in China (Series B)*, **6**, 751–759.

Wang, S. and Wang, R. 1990. Variations of seasonal and annual temperatures during 1470–1978 AD in eastern China. *Acta Meteorologica Sinica*, **48**(1), 26–35 (in *Chinese*).

Wang, S., and W.-C. Wang, 1994. Application of historical documentary records in reconstruction of the Paleo-climate series in China. *TAO*, **5**(3), 373-381.

Wang, W.-C., W. Gong, H. Wei, 2000. A regional model simulations of 1991 severe precipitation event over Yantze-Huai River valley. Part I: Precipitation and circulation statistics. *Journal of Climate*, **13**, 74-92.

Wang, S., J. Cai, Q. Mu, Z. Xie, J. Zhu and D. Gong. 2002. Modeling and Diagnostics Studies on the Variations of the Subtropical High over the Western Pacific from 1880 to 1999. *Advances in Atmospheric Sciences*, **19**(6), 1148-1152.

Wang, Y., F. Yasushi, and K. Kuranoshin, 2003. A teleconnection pattern related with the development of the Okhotsk High and the Northward Progress of the Subtropical High in East Asian Summer. *Advances in Atmospheric Sciences*, **20**(2), 237-244.

Wang, B., I.-S. Kang, and J.-Y. Lee, 2004. Ensemble Simulations of Asian-Australian Monsoon Variability by 11 AGCMs. *Journal of Climate*, **17**, 803-818.

Waple, A. M., M. E. Mann, and R. S. Bradley, 2002. Long-term patterns of solar irradiance forcing in model experiments and proxy based surface temperature reconstructions. *Climate Dynamics*, **18**, 563-578.

Weatherly, J., B. Briegleb, W. G. Large, and J. Maslanik, 1998. Sea ice and polar climate in the NCAR CSM. *Journal of Climate*, **11**, 1472–1486.

Webster, P., 2005: The elementary Hadley circulation. In: The Hadley Circulation: Present, Past and Future. Edited by: H. F. Diaz and R. S. Bradley, Kluwer Academic Publishers, 9-60.

Wigley, T. M. L., C. M. Ammann, B. D. Santer, and S. C. B. Raper, 2005. Effect of climate sensitivity on the response to volcanic forcing, *Journal of Geophysical Research*, **110**, D09107, doi:10.1029/2004JD005557.

Wu, M. C. and J. C. L. Chan, 2005a. Observational relationships between summer and winter monsoons over East Asia. Part 1: Basic Framework. *International Journal of Climatology*, **25**, 437-451.

Wu, M. C. and J. C. L. Chan, 2005b. Observational relationships between summer and winter monsoons over East Asia. Part 2: Results. *International Journal of Climatology*, **25**, 453-468.

Wu, R., and B. Wang, 2002. Contrast of the East Asian summer monsoon–ENSO relationship between 1962–77 and 1978–93. *Journal of Climate*, **15**: 3266–3279.

Wu. S., Y. Yin, D. Zheng and Q. Yang. 2006. Moisture conditions and climate trends in China during the period 1971-2000. *International Journal of Climatology*, **26**: 193-206.

Xie, P. and P. A. Arkin, Global Precipitation: A 17-year monthly analysis based on gauge observations, satellite estimates, and numerical model outputs. *Bulletin of the American Meteorological Society*, **78**, 2539-2558 (1997).

Yang, F. and K.-M. Lau, 2004. Trend and variability of China precipitation in spring and summer: linkage to sea-surface temperatures. *International Journal of Climatology*, **24**, 1625-1644.

Yang, F. 2000. Radiative forcing and climatic impact of the Mount Pinatubo volcanic eruption. Ph.D. dissertation, University of Illinois, Urbana Champaign, 219 pp.

Yang, F. and M. E. Schlesinger, 2001: Identification and separation of Mount Pinatubo and El Nino-Southern Oscillation land surface temperature anomalies. *Journal of Geophysical Research*, **106**(D14), 14,757-14,770.

Yang, F. and M. E. Schlesinger, 2002. On the surface and atmospheric temperature changes following the 1991 Pinatubo volcanic eruption: a GCM study. *Journal of Geophysical Research*, **107**(D8), 10.1029/2001JD000373.

Yang, B., A. Braeuning, K. R. Johnson, and S. Yafeng, 2002. General characteristics of temperature variation in China during the last two millennia. *Geophysical Research Letters*, **29**(9), 1324, 10.1029/2001GL014485.

Yu, R., W. Li, X. Zhang, Y. Liu, Y. Yu, H. Liu, and T. Zhou, 2000. Climate features related to eastern China summer rainfalls in the NCAR CCM3. *Advances in Atmospheric Sciences*, **17**, 503-518.

Yu, R., M. Zhang, Y. Yu, and Y. Liu, 2001. Summer monsoon rainfalls over Mid-Eastern China lagged correlated with Global SSTs. *Advances in Atmospheric Sciences*, **18**(2), 179-196.

Zhang, P.-Y., W.-C. Wang, and S. Hameed, 1992. Evidence for anomalous cold weather in China 1815-1817. In: The year without a summer? World climate in 1816. Edited by: Harrington, C. R., Canadian Museum of Nature, Ottawa, 436-447.

Zhang, Y., K. R. Sperber and J. S. Boyle, 1997. Climatology and Interannual Variation of the East Asian Winter Monsoon: Results from the 1979-95 NCEP/NCAR Reanalysis. *Monthly Weather Review*, **125**, 2605-2619.

Zhang, D. D., C. Y. Jim, G. C.-S. Lin, Y.-Q. He, J. J. Wang, and H. F. Lee, 2006. Climatic change, wars and dynastic cycles in China over the last Millennium. *Climatic Change Online First*, DOI: 10.1007/s10584-005-9024-z.

Zheng Y.Q., G. Yu, S.M. Wang, B. Xue, D. Q. Zhuo, X. M. Zeng, and H. Q. Liu, 2004. Simulation of paleoclimate over East Asia at 6 ka BP and 21 ka BP by a regional climate model. *Climate Dynamics*, **23**(5), 513 –529.

Zhu, C., W.-S. Lee, H. Kang, and C.-K. Park, 2005: A proper monsoon index for seasonal and interannual variations in the East Asian monsoon. *Geophysical Research Letters*, **32**, L02811, doi:10.1029/2004GL021295.

Zhu, J. and S. Wang, 2002. 80 yr oscillation of summer rainfall over North China and East Asian Summer Monsoon. *Geophysical Research Letters*, **29**(14), doi:10.1029/20001GL013997.

Zhu, J., and S. Wang, 2001. 80a-oscillation of summer rainfall over the east part of China and East Asian summer monsoon. *Advances in Atmospheric Sciences*, **18**(5), 1043-1051.

Zielinski, G.A., 2000. Use of paleo-records in determining variability within the volcanism-climate system. *Quaternary Science Reviews*, **19**, 417-438.